Performance of the HADES Spectrometer for Dilepton Identification in the Reaction C+C at 1-2 AGeV

Inaugural-Dissertation
zur Erlangung des Doktorgrades der Naturwissenschaften
der Justus Liebig Universität Giessen
Fachbereich 07 (Mathematik und Informatik, Physik, Geographie)

vorgelegt von

ALBERICA TOIA

aus Mailand (Italien)

II. Physikalisches Insitut
der Justus Liebig Universität Giessen
March 2004

SONGS OF INNOCENCE

INTRODUCTION

Piping down the valleys wild,
Piping songs of pleasant glee,
On a cloud I saw a child,
And he laughing said to me:

"Pipe a song about a Lamb!"
So I piped with merry cheer.
"Piper, pipe that song again;"
So I piped: he wept to hear.

"Drop thy pipe, thy happy pipe;
Sing thy songs of happy cheer:!"
So I sang the same again,
While he wept with joy to hear.

"Piper, sit thee down and write
In a book, that all may read."
So he vanish'd from my sight;
And I pluck'd a hollow reed,

And I made a rural pen,
And I stain'd the water clear,
And I wrote my happy songs
Every child may joy to hear.

(William Blake)

Contents

III PERFORMANCE OF THE HADES DILEPTON TRIGGER 147

Zusammenfassung

Eines der Hauptziele der Kernphysik in den letzten Jahren ist das Verständnis des Verhaltens von Hadronen und ihren Konstituenten im Vakuum und unter den extreme Bedingungen in hießenr und dichter Kernmaterie. Solche Bedingungen lassen sich experimentell in pion-, proton- und schwerioneninduzierten Reaktionen herstellen. Vektormesonen sind eine ideale Sonde für diese Untersuchungen, da ihre Lebensdauer in derselben Größenordnung liegt wie diejenige des in der Reaktion erzeugten "Fireballs". Die elektromagnetischen Zerfallsmoden der Vektormesonen stellen das beste Werkzeug zur ungestörten Untersuchung stark wechselwirkender Materie, da die Zerfallsprodukte (Dileptonen) im Endzustand keiner starken WEcheselwirkung unterliegen.

Die Analyse und Interpretation von Dileptonenspektren führte in den letzten Jahren zu einem kontroversen Bild: während verschiedene Experimente (unter anderem DLS am LBNL, CERES am SPS) wiederholt einen deutlichen Dileptonenüberschuss relativ zu den hadronischen Quellen feststellten, versuchten verschiedene theoretische Modelle versucht, dies entweder als eine Signatur der Wiederherstellung der chiralen Symmetrie zu interpretieren oder alternativ als eine Wechselwirkung mit dem dichten hadronischen Medium.

Das "High Acceptance DiElectron Spectrometer" (HADES) wurde gebaut zur Untersuchung der elektromagnetischen Struktur und der Mediummodifikationen von Hadronen mittels der elektromagnetischen Zerfälle der leichten Vektormesonen.

Zu diesem Zweck muß das Spektrometer eine Massenauflösung von 1% erreichen, was mit Hilfe von je zwei Driftkammern vor und hinter dem Feld eines supraleitenden Toroidmagneten erreicht wird, während die für Elektronen optimierte Teilchenidentifizierung durch einen hadronenblinden Cherenkov-DeteKtor, eine Flugzeitwand und einen Preschauer-Detektor gewährleistet ist..

Da der Wirkungsquerschnitt für Vektormesonen sehr klein ist und ihr Verzweigungsverhältnis in den Dileptonenkanal sehr niedrig, wird ein schneller und sehr selektiver Trigger benötigt zur Reduktion von Untergrundereignissen.

In einem ersten Schritt bestimmen "Image Processing Units" Leptonensignaturen in den einzelnen PID-Detektoren; im zweiten Schritt werden diese in einer "Matching Unit" korreliert, um Trackkandidaten zu ermitteln sowie deren Ladung und Impuls zu bestimmen. Damit ist es möglich, Leptonenpaare in einem vorgegebenen Bereich invarianter Massen auszuwählen.

Im Rahmen der vorliegenden Arbeit wurde eine detaillierte Untersuchung der Leistungsfähigkeit des HADES-Triggersystems durchgeführt.

Um die Funktionalität des Triggers zu verifizieren und weitergehende Untersuchungen durchführen zu können, wurden Software-Emulationen für alle in Hardware implementierte Triggeralgorithmen erstellt. Der selektivste Algorithmus des Second Level Triggers ist die Identifizierung der durch Elektronen erzeugten Cherenkov-Ringe in einem RICH-Detektor. Allein hierdurch kann in C+C-Kollisionen eine Ereignisreduktion um einen Faktor größer als 10 erreicht werden. Das Verhalten der Online-Ringerkennung wurde mit Hilfe von Simulationen untersucht. Eine Effizienz im Bereich von 85% wurde ermittelt, auch das Verhalten im Vergleich zum Offline-Algorithmus wurde charakterisiert. Sowohl Online- als auch Offline-Ringerkennung werden von fehlidentifizierten Ringen dominiert, die vor einem aussagekräftigen Vergleich der beiden Algorithmen verworfen werden müssen. Dies geschieht durch die Auswahl von Leptonenkandidaten unter Verwendung der vollständigen Detektorinformation in einer Analyse, die im Rahmen dieser Arbeit entwickelt und durchgeführt wurde.

Abhängig von den Bedingungen ist die Online-Ringkerkennung in der Lage, bis zu 80% der in der Offline-Analyse bestimmten Leptonenkandidaten zu identifizieren.

Der Second Level Trigger wurde während der Strahlzeit im November 2002 betrieben und erreichte eine Ereignisreduktion um einen Faktor 12. Es wurde abgeschätzt, daß ein Reduktionsfaktor bis zu 20 ohne weiteren Effizienzverlust möglich ist. Aufgrund einer restriktiven Einstellung des Online-Ringerkennungsalgoritmus wurde eine integrale Leptoneneffizienz von 62% gemessen, eine Effizienz von 84% für Dileptonen mit einem Öffnungswinkel größer als 4°, und 92% für Öffnungswinkel größer als 8°. Durch den Vergleich von Leptonen- und Dileptonenspektren für die getriggerten sowie für ungetriggerte Ereignisse kann gezeigt werden, daß der Trigger keinen Bias einführt. In den getriggerten Ereignissen ist der Leptonengehalt um einen Faktor 7,5 angereichert, der Gehalt an offenen Dileptonenpaaren um eine Faktor 11 im Vergleich zu den ungetriggerten Ereignissen.

Introduction

We shall not cease from exploration
And the end of all our exploring
Will be to arrive where we started
And know the place for the first time.
(T. S. Eliot)

One of the main goals of the last years in the field of nuclear physics research is the understanding of the behavior of hadrons and their constituents in vacuum and under extreme conditions of hot and dense matter. These conditions are experimentally realized by pion, proton and heavy ion induced reactions. Vector mesons are ideal probe for those investigations, since their life-time is compatible with the life-time of the fireball produced in a collision. Electromagnetic decays of vector mesons are the best tool for the studies of strongly interacting matter, since they do not undergo strong force in the final state.

The analysis and the interpretation of dilepton spectra has been controversial in the last few years: while different experiments (among others DLS at LBNL, CERES at SPS) repeatedly observed a strong dilepton enhancement over the hadronic sources, theoretical models have tried to interpret it either as a signature of chiral symmetry restoration or as interaction with the dense hadronic medium. The **H**igh **A**cceptance **Di**E**lectron **S**pectrometer (HADES) has been built to investigate the electromagnetic structure and the in medium modification of hadrons, with the analysis of decays of light vector mesons.

For this purpose the magnetic spectrometer has to reach a mass resolution of 1% thanks to two pairs of drift chamber in front and behind the field produced by a superconducting toroidal magnet, while the particle identification, with a special care dedicated to leptons, is guaranteed by a hadron blind Cherenkov detector, a Time of Flight wall and a Pre-Shower detector. Since the vectors meson cross section is very small and the branching ratio for the dilepton decays very low, a fast selective trigger is needed in order to reduce background events. In the first step Image Processing Units find

lepton signatures in each of the corresponding PID detectors; in the second step a Matching Unit correlates these signatures to identify a common track, and calculates the charge and the momentum of the particle depending upon the deflection in the magnetic field. It is then possible to select lepton pairs within a given invariant mass range.

In the framework of the present thesis a detailed study of the performance of the HADES trigger is presented. To investigate and characterize the functionality of this trigger, all hardware components have been emulated with software. The most selective algorithm of the second level trigger is the identification of Cherenkov rings from electrons traversing the RICH, which alone can provide an event reduction factor higher than 10 for C+C collisions. The behavior of the online ring recognition has been studied with the help of simulations, where an efficiency of around 85% has been measured, and by comparing it to the offline analysis algorithm.
Both online and offline ring recognition algorithms are dominated by misidentified rings, which have to be rejected in order to make a proper comparison. The rejection is done with the selection of a lepton candidate sample with an analysis, developed and performed in the framework of the present thesis, which makes used of the information collected by the full detector. Depending upon the conditions, the online ring finder is capable to recognize up to 80% of the lepton candidates reconstructed with the offline analysis.
The second level trigger was fully operational during the beamtime of November 2002 with an event reduction by a factor 12. It has been estimated that higher reduction, up to a factor 20 are achievable without further loss of efficiency. Due to a more restrictive implementation of the ring recognition algorithm, a lepton efficiency of 62% was measured, while 84% efficiency was estimated for dileptons with opening angle larger than $4°$, and 92% for opening angle larger than $8°$. However no physical bias was introduced in the data, as the agreement between leptons and dileptons spectra for triggered and untriggered events shows. In the triggered events an enhancement by a factor 7.5 is found in the lepton yield, and by a factor 11 in the open pairs dilepton yield with respect to the untriggered ones.

Part I

HADES: THE DETECTOR AND ITS PHYSICS PROGRAM

In this part of the thesis the physics motivations which led to the conception of the HADES detector is briefly discussed. The HADES detector, as well as other pioneering dielectron experiments are presented. The obtained results are reviewed and discussed. The experimental challenge of the HADES detector are presented. Major focus is put on the second level trigger of HADES, and especially to its algorithms as event selection criteria.

The main aspect of the HADES physics program is the investigation of the properties (e.g. mass, lifetime) of the light vector mesons ρ, ω and ϕ in pion, proton and heavy ion induced reactions up to 2 AGeV. This is treated in Chapter 1. The purpose of heavy ion reactions is the understanding of the modification of the fundamental hadron properties due to the presence of a hadronic medium, where theoretical models predict different possible scenarios. The focus of elementary reactions is to study the electromagnetic structure of vector mesons via their transition form factor, and to provide an important normalization for A+A spectra.
Pioneering dielectron experiments, and in particular CERES and DLS, are revisited in Chapter 1 (Section 1.5).

The requirements of statistics and resolution for the physics program puts lots of constraints on the detector: HADES, described in Chapter 2, is designed to achieve a mass resolution of 1% and a geometrical acceptance for lepton pairs of 45%. The momentum is measured by tracking the particles with two pairs of Multiwire Drift Chambers (MDCs), before and after the coils of a superconducting magnet. Particle identification is performed with a Ring Image CHerenkov detector (RICH) provided with a hadron blind radiator gas, a Time Of Flight (TOF) wall, which can select fast particles, and a Pre-Shower detector, which can distinguish electrons from hadrons.

Since the dielectron yield from vector meson decays is in the order of 10^{-6}, a large geometrical acceptance, high rate capability as well as a highly selective multilevel trigger system for efficient online event reduction have to be guaranteed. The second level trigger is based on two consecutive steps: in the first step Image Processing Units look for electron candidates in different Particle Identification detectors (RICH, TOF, Pre-Shower).
In the second step the Matching Unit combines the angle information from the IPUs signatures before and after the magnetic field to select lepton candidates, estimates their momentum depending upon the deflection in the magnetic field and then combines electrons with positrons. Thus it is possible to select lepton pairs within a given invariant mass range. The second level trigger is presented in Chapter 3.

Chapter 1

Physics Motivations

EXPERTS

*Experts have
their expert fun
ex cathedra
telling one
just how nothing
can be done.*

(Piet Hein - Grooks)

1.1 Quantum Chromo Dynamics

Quantum Chromo Dynamics (QCD) is the gauge theory of the strong force, and it describes the interaction of color-charged particles via the exchange of bosons (gluons), which play a similar rule as photons in QED. Like photons in QED, gluons are massless, as demanded by gauge symmetry, but unlike photons, the gluon field is self-interacting resulting in the property of *asymptotic freedom* at small distances or equivalently at large momenta, when the color coupling goes to zero. No theoretical assumption but only phenomenological models can described the other important property which characterize the QCD, namely the *confinement* which appears when the color coupling goes to infinity at large distances, thus making color-neutral states (SU(3) singlets) the only stable structures at such scales.

1.1.1 Asymptotic Freedom

Inelastic electron scattering at very high momentum transfer demonstrated the existence of a substructure inside the nucleon, consisting out of objects, named quarks. These experiments indicate that quarks inside the nucleon behave under such conditions as point like, non-interacting particles.

(a) fermion loop   (b) boson loop
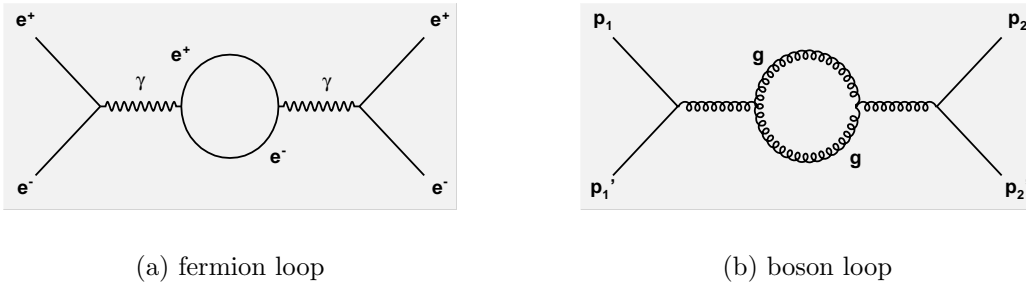
Figure 1.1: *Loops between a) fermion and b) boson propagators. Boson loops, typical only of QCD, lead to contributions to the coupling constant opposite in sign to fermion loops.*

This property, known as *asymptotic freedom*, can be understood with the self-interaction of gluons, resulting in boson loops between boson propagators (shown in Figure 1.1 (b)). The vacuum polarizations in QED consisting out of fermion loops in the boson propagator result in a screen of the electrical charge. At high momentum transfer the electron, penetrating the e^+e^- cloud of the fermion loops, experience a higher effective charge. On the contrary, boson loops in QCD result in an anti-screening of the strong charge. If the number of gauge bosons is large enough, the contribution from boson loops is stronger than from fermion loops; since the bosons contributions to the coupling constant are opposite in sign to those coming from the fermion ones, the coupling constant then decreases with decreasing distances, i.e. with increasing momentum transfer and quarks appear as non interacting particles [1]. A good approximation for the *running* coupling constant is:

$$\alpha_S = \frac{12\pi}{(33 - 2N_f)\ln(q^2/\Lambda^2)} \tag{1.1}$$

where N_f is the number of flavors, Λ is the QCD scale parameter[1], and q is the momentum transfer: the QCD potential has almost the shape of a

---

[1]experimentally $\Lambda_{QCD} \approx 200 MeV$

"Coulomb" potential:

$$V(r) = -\frac{\alpha_S}{r} \tag{1.2}$$

For high momentum transfer, α_S is very small, and methods of perturbation theory can be applied.

1.1.2 Confinement

When α_S approaches unity, i.e. at small momentum transfer, a perturbative treatment can no longer be justified, and no analytical solution of the QCD equations can be derived. Therefore to study the evolution of the system, phenomenological[2] or numerical methods[3] have to be used while only an approximate shape of the QCD potential can be given as

$$V(r) \approx \lambda r \tag{1.3}$$

Figure 1.2 shows that the QCD potential can be expressed, up to an $\mathcal{O}(\Lambda_{\mathrm{QCD}}^3 r^2)$
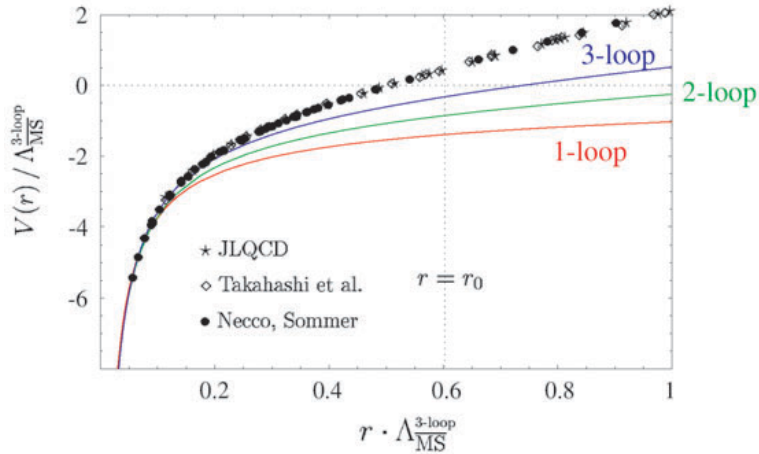
Figure 1.2: *Comparison of the "Coulomb+linear" approximation corresponding to the cases with one, two, or three loops running and the lattice data [11]: Takayashi et al. ($\diamond$), Necco/Sommer ($\bullet$). and JLQCD ($\star$) [12].*

uncertainty, as the sum of a "Coulomb" potential (with logarithmic corrections at short distances) and a linear potential, within an approximation based on perturbative expansion in α_S.

---

[2]Bag Model: relativistic Bogolyubov [2], MIT model[3, 4, 5, 6], chiral bags [7, 8, 9] String Model, Lund Model [10], etc
[3]Lattice QCD [11]

In QED the vacuum fluctuations, corresponding to fermion loops in the photon propagator, lead to a screening of the electric charge at large distance, i.e. an electric-dipole looks like a charge-neutral object from large distances. In QCD boson loops, which are more abundant than fermion loops, produce the opposite effect. The consequent anti-screening of the charge at large distances due to the boson loops results in the increasing of the running coupling constant. The force which binds quarks together increases with the distance and any effort to separate quarks would result then in the creation of a $q\bar{q}$ pair, i.e. a meson. It is virtually impossible, since it costs infinite energy, to free a colored quark; only color singlets which are color-neutral are observed [1].

1.2   The QCD Lagrangian and its Symmetries

QCD is described in terms of its Lagrangian and its symmetries which, according to Noether's theorem, correspond to conserved currents and charges. The QCD Lagrangian is expressed as:

$$\mathcal{L}_{QCD}(x) = \bar{\psi}_q(x)(i\gamma^\mu D_\mu - \hat{M}^0)\psi_q(x) - \frac{1}{4}G^a_{\mu\nu}(x)G^{\mu\nu a}(x) \qquad (1.4)$$

where ψ_q is the quark field, $\gamma_\mu(\mu = 0, 1, 2, 3)$ are the Dirac matrices and $G^a_{\mu\nu}(x)$ is the gluon tensor

$$G^a_{\mu\nu}(x) = \partial_\mu \tilde{A}^a_\nu(x) - \partial_\nu \tilde{A}^a_\mu(x) + gf^{abc}\tilde{A}^b_\mu(x)\tilde{A}^c_\nu(x) \qquad (1.5)$$

$D_\mu = \partial_\mu - igt^a \tilde{A}^a_\mu(x)$ is the covariant derivative which generates the coupling between quarks and the gauge potentials $\tilde{A}^a_\mu$, g is the strong coupling constant and f^{abc} are the structure constants of the symmetry group SU(3) [13]. This Lagrangian is invariant under the global symmetry $U(1)$, i.e. a phase constant; this corresponds to the conservation of the baryonic current and the baryon number.
The axial component of this symmetry $U_A(1)$ is not conserved in Nature: this phenomenon is known as the *axial anomaly* and it is responsible of the large mass of the $\eta\prime$ $(m_{\eta\prime} = 958\,MeV/c^2)$.

1.2.1   Chiral Symmetry

Assuming $m_u = m_d = m_s$, the QCD Lagrangian is invariant under gauge transformation $SU(3)_{colour}$, i.e. does not depend on the color of quarks.

When the momentum transfer is about 1 GeV/c, the quark masses are [14]

$$
\begin{aligned}
m_u &= (5 \pm 2)\,\mathrm{MeV/c^2} \\
m_d &= (9 \pm 3)\,\mathrm{MeV/c^2} \\
m_s &= (175 \pm 55)\,\mathrm{MeV/c^2}
\end{aligned}
\tag{1.6}
$$

and therefore can be considered small or even zero compared to the hadronic scale. Another symmetry then appears, namely the *chiral symmetry*. Defining the right and left component of a fermion fields as

$$
\psi_{R,L} = \frac{1}{2}(1 \pm \gamma_5)\psi
\tag{1.7}
$$

the chiral symmetry is represented by $SU(3)_R \times SU(3)_L$, where

$$
SU(3)_R : \psi_R \to R\psi_R = \exp\left(i\theta_R^a \frac{\lambda_a}{2}\right)\psi_R \simeq \left(1 + i\frac{\lambda_a}{2}\theta_R^a\right)
$$

$$
SU(3)_L : \psi_L \to L\psi_L = \exp\left(i\theta_L^a \frac{\lambda_a}{2}\right)\psi_L \simeq \left(1 + i\frac{\lambda_a}{2}\theta_L^a\right)
\tag{1.8}
$$

According to Noether's theorem, these conservations correspond to the separate conservation of right and left currents which, properly combined, lead to the conservation of the vector and the axial current and charge.

The chiral symmetry is already broken in the fundamental hadronic state, where the value of the scalar quark condensate is [15]

$$
\Delta\mathcal{L}_{massa} = -\hat{M}^0\langle\bar{\psi}\psi\rangle = -m_u\bar{u}u - m_d\bar{d}d - m_s\bar{s}s = -(230 \pm 25)\mathrm{MeV}
\tag{1.9}
$$

The chirality is expressed as the projection of the spin along the momentum direction. In a pictorial bag model, where hadrons are bags where quarks are confined, the chirality is not conserved when the quark is confined into a hadron, for instance once the parton hits the surface of the bag where the momentum direction is reversed, while the spin is not. In a more and more deconfined state, where the bags expand to disappear, the quark never hits the wall of the bag and the chiral symmetry is restored.

The non-zero value of the quark condensate leads to a spontaneous breaking of chiral symmetry. The chiral symmetry is *spontaneously* broken even in the vacuum. This means that the axial charge does not leave the fundamental state invariant $(Q_a^A|0\rangle \neq 0)$, but there are eigenstates of the Hamiltonian $H|\phi_a\rangle = Q_a^A H|0\rangle = 0$: these states correspond to the octet of pseudo-scalar mesons $(\pi^\pm, \pi^0, k^\pm, k^0, \bar{k}^0, \eta)$, with a small mass. For each broken symmetry in fact, when the Nature "choose" a defined state and the potential is no

longer symmetric, any deviation from this configuration, leads to excitations, namely the *Goldstone bosons*, which correspond to massive or massless particles, depending whether the excitation costs energy or not.

The small, but still non-zero, mass of the pseudo-scalar mesons is due to the *explicit* breaking of the chiral symmetry, which reflects the fact that the mass of the quarks is small, but non-zero. This can be understood thanks to a mechanical analogy [16, 17].

Noether's theorem states that for every symmetry conserved, there is a conserved current and a conserved charge. Goldstone264s theorem on the other hands states that for every symmetry breaking there are massless and massive excitations which dynamically generate the mass of the known hadrons.

The potential

$$V(\phi \dagger \phi) = \mu^2 \phi \dagger \phi + \lambda(\phi \dagger \phi)^2 \qquad (1.10)$$

can have two different shapes, which are shown in Figure 1.3, depending upon the sign of the first term [16, 17].

For $\mu^2 > 0$ the potential and its ground state $\phi = 0$ are rotationally invariant; for $\mu^2 < 0$ there is an infinite number of degenerate ground states, while $\phi = 0$ is a local maximum, i.e unstable. The potential has the so called *mexican hat* shape. If Nature chooses one particular state, the rotational symmetry is *spontaneously* broken and any deviation away from the chosen ground state would result in excitations which, according to Goldstone264s theorem, correspond to particles, so called *Goldstone bosons*. The particles are massless in case they correspond to the rotational deviations along the π field which do not cost energy[4], or massive for radial excitations which do cost energy along the field σ[5].

The experimental observation of the small, however non-zero, mass of the pseudoscalar mesons is explained with the *explicit* breaking of the chiral symmetry. As Figure 1.4 shows, this corresponds to a small tilting of the mexican hat potential in the pictorial model of the rotational symmetry, which defines a minimum in f_π, even before the choice of a ground state with the explicit breaking. In this configuration even rotational excitations along the π field do cost some energy, and the corresponding bosons have a small, yet non-null mass, proportional to the explicit symmetry breaking parameter.

Different theoretical calculations (see Section 1.3) indicate the chiral symmetry restoration as responsible of modification of fundamental hadron prop-

---

[4]the pseudoscalar mesons octet
[5]vector mesons and nucleons
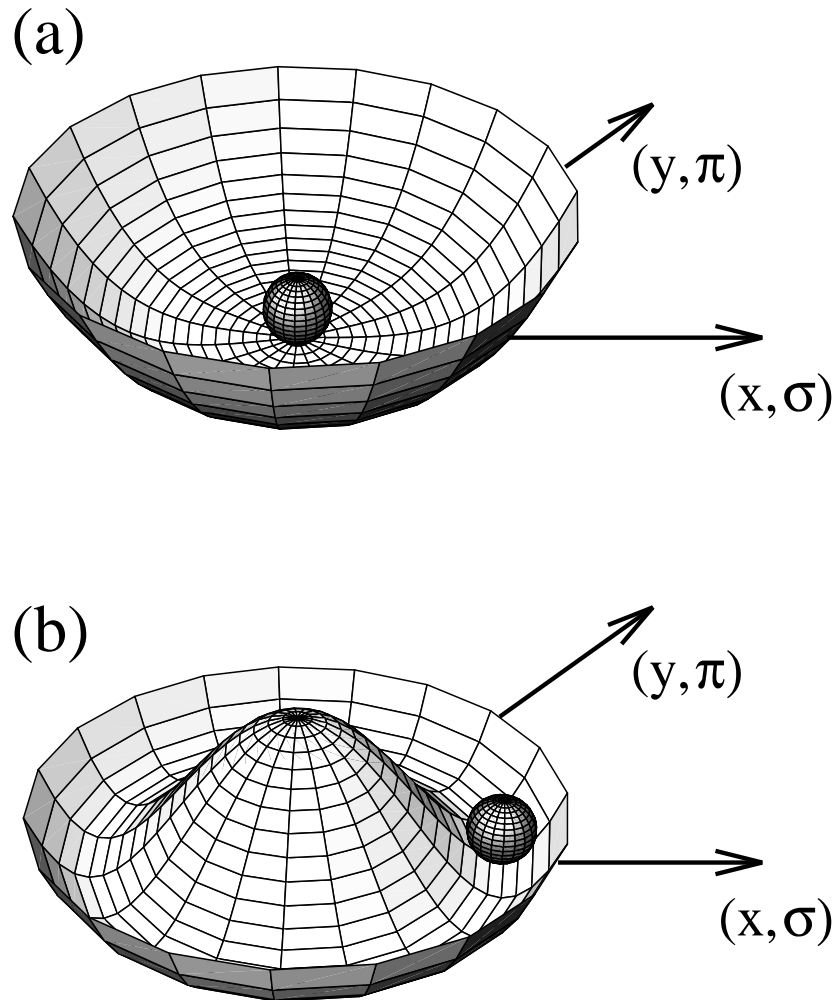
Figure 1.3: *Mexican-hat potential expressed ad a function of the σ and π fields. In the case when $\mu^2 > 0$ (top figure) $\phi = 0$ is the ground state, in the case when $\mu^2 < 0$ (bottom figure) there is an infinite number of degenerate ground states, while $\phi = 0$ is a local maximum.*

(a) symmetric potential   (b) tilted potential
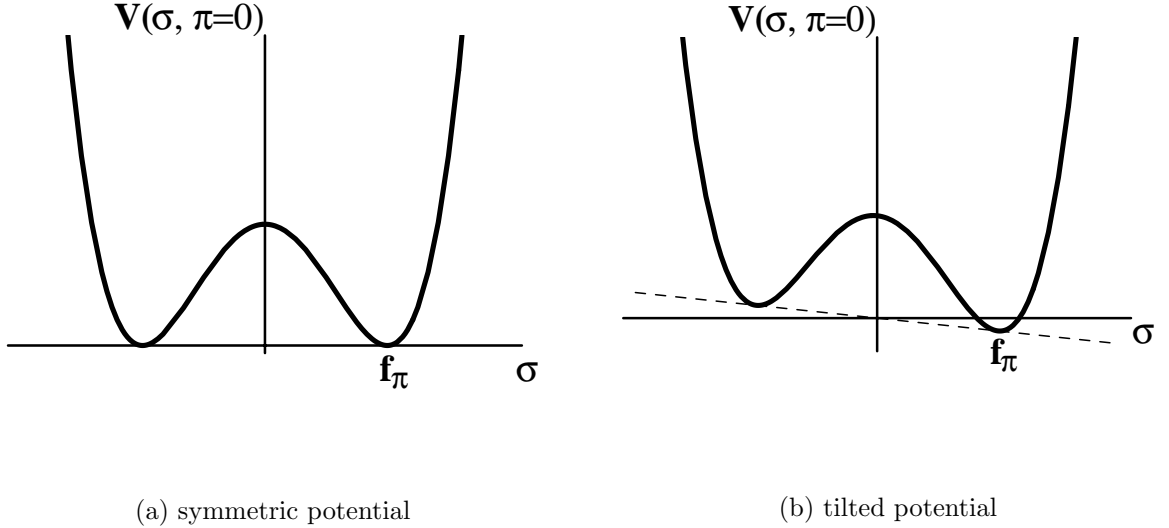
Figure 1.4: *1D Mexican Hat potential with the field σ and π instead of the cartesian axes x and y. In the case b) the potential is tilted along the σ field direction: the chiral symmetry is* explicitly *broken.*

erties. A restoration of chiral symmetry would happen in a deconfined state, i.e. when the mass of quarks approaches a zero value, while a partial restoration would already start when reaching condition of a hot and dense medium. The tool to experimentally achieve such conditions of high temperature and density are relativistic heavy ion collisions.

1.2.2   Heavy Ion Collisions

Heavy ion collisions are tools experimentally used for probing properties of hadronic matter under extreme conditions of temperature and density, and therefore studying and understanding the phase diagram of nuclear matter. Experiments carried out at various incident energies, ranging from 1 AGeV (BEVALAC, SIS) to 200 AGeV (SPS) have generated systems of large density but moderate temperature (SIS, BEVALAC), systems with both large density and temperature (AGS), and systems of low density and high temperatures (SPS), so that a large region of the QCD diagram can be explored. Depending upon the energy regime, the collisions are defined

- Ultra Relativistic Heavy Ion Collisions: up to 3 ATeV, (RHIC, LHC)

- Relativistic Heavy Ion Collisions at high energy: up to 158 AGeV, (AGS, SPS)

- Relativistic Heavy Ion Collisions at low energy: 1-2 AGeV, (SIS)
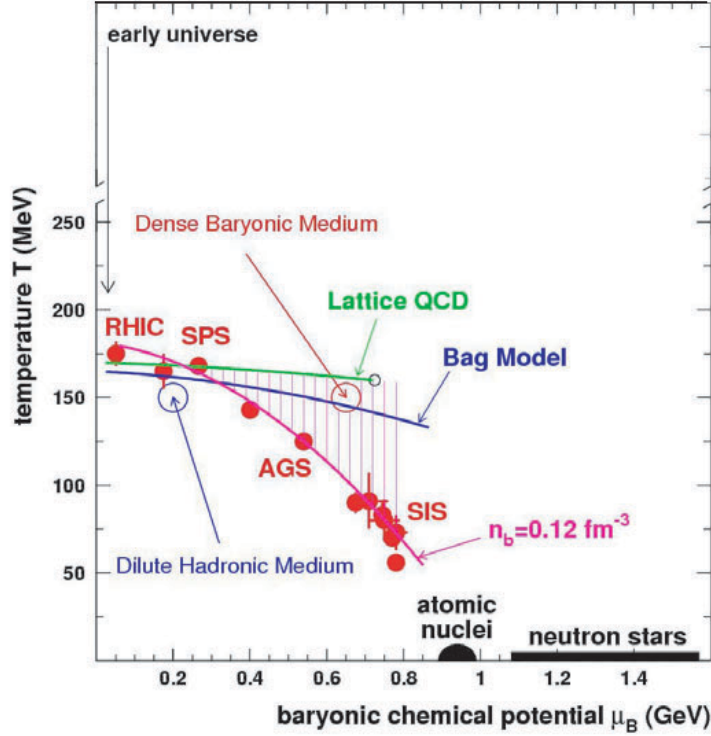
Figure 1.5: *The phase diagram of strongly interacting matter plotted as a function of baryochemical potential and temperature. Indicated are the phase-space regimes accessible by different experiments (SIS-GSI, AGS-BNL, SPS-CERN) [24]. The full symbols represent freeze-out points obtained with a statistical model analysis from particle ratios measured in heavy ion collisions [25, 26, 27]. The curve labeled with "$n_b = 0.12 fm^{-3}$" connecting the data points refer to a calculation of the chemical freeze-out which occurs at the constant density of $n_b = 0.12 fm^{-3}$ [28]. The curve labeled with "Lattice QCD" represents the phase boundary between the quark-gluon plasma and the hadronic phase as obtained with a QCD lattice calculation with a critical point at $T = 160 \pm 3.5 MeV$ and $\mu = 725 \pm 35 MeV$ [29].*

These studies are not only for the knowledge of the nuclear matter itself, but also to characterize the phase of the early universe, immediately after the Big

Bang when, between the first nanosecond and the first microsecond of the Universe, all particles known today were already present and quarks started to be confined in hadrons due to the strong interaction.

Ultra Relativistic Heavy Ion Collisions

Ultra-relativistic heavy ion reactions are performed to probe the phase transition which brought the original deconfined phase (Quark Gluon Plasma) of the early universe, which might be re-created in the nuclear collision, to the confined phase of Hadron Gas. The present understanding about the phase diagram of strongly interacting matter is shown in Figure 1.5 in terms of the temperature and the baryochemical potential 240[24]. From the measurements obtained in heavy ion collisions at different energies[6] values for temperature and the baryonic chemical potential are extracted from the particle ratios and inverse mass slope with a statistical model analysis.
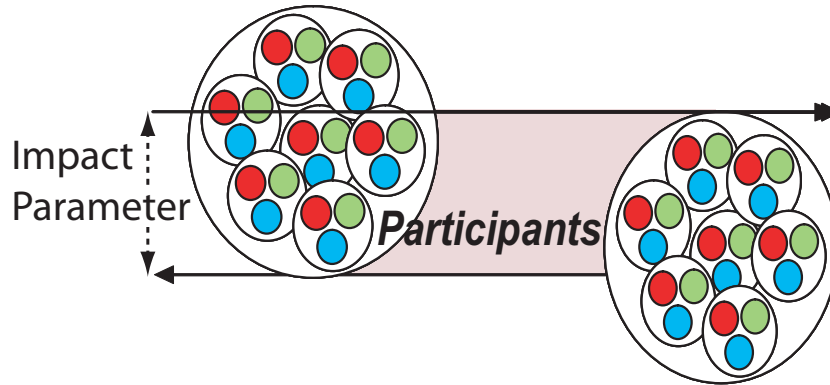
Figure 1.6: *Pictorial view of a heavy ion nuclei collision [30]. After the collision, spectators, not involved in the reaction, leave the collision area without a significant change in their momenta, while participants fuse in a fireball.*

As Figure 1.6 shows, the nuclei collide with an impact parameter b. A highly excited zone (*fireball*) is created between the colliding nucleons (*participants*) while the nucleons not involved in the collision (*spectators*) keep their

---

[6]As Figure 1.5 shows, the SIS energy as quite below the energy required to reach the fully deconfined phase. However it seems to lie on the transition are and therefore a general brief description is provided of the phenomenology, as it is known so far, of a full transition as the ones produced in ultra relativistic heavy ion collisions.

original momentum and fly away from the hot zone. According to different
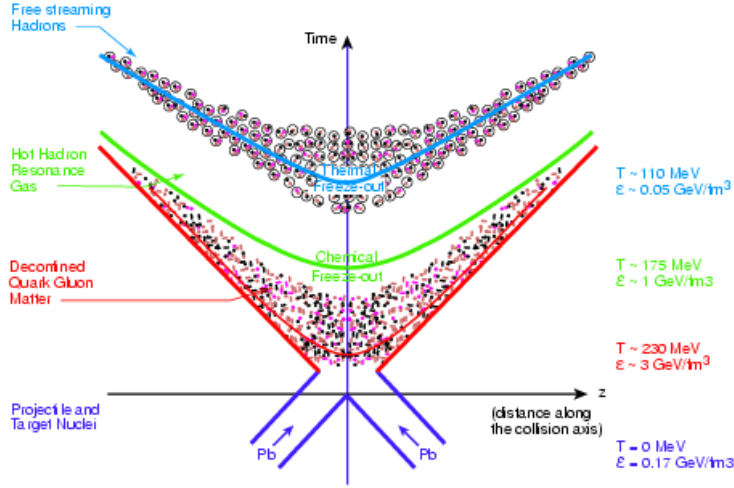
Figure 1.7: *Space-Time evolution of a fireball produced in a ultra relativistic heavy ion collision [30].*

theoretical calculations for central collisions [30, 24], the evolution of the fireball, depicted schematically in Figure 1.7 foresees an expansion and a cooling process, where the pressure from the reaction is released. After a proper time of 1 fm/c, the system is predicted to be in a thermalized QGP. During the following expansion of the system, emission, absorption, and scattering of bosons equilibrate the different hadron species until, after few tens of fm/c ($\approx 3 \times 10^{-23} s$), the system is dilute enough that the mean free path of the formed hadrons is of the order of the size of the system and the hadrochemical composition of the system is then frozen: this point is called *freeze-out* and can be analyzed from the hadronic products detected to provide important parameters which describe the system at this stage (temperature and densities) [30].

Relativistic Heavy Ion Collisions at Low Energy

While RHIC, LHC and SPS address a region of the phase diagram with a high temperature and virtually baryon-free, with the energy regime of Relativistic Heavy Ion Collisions at Low Energy it is possible to investigate a high baryonic density and low temperature region. These energies, around a few AGeV, are for instance the ones produced by the SIS, the Synchrotron for Heavy Ions installed at GSI Darmstadt. GSI (Gesellschaft für Schwereionen-
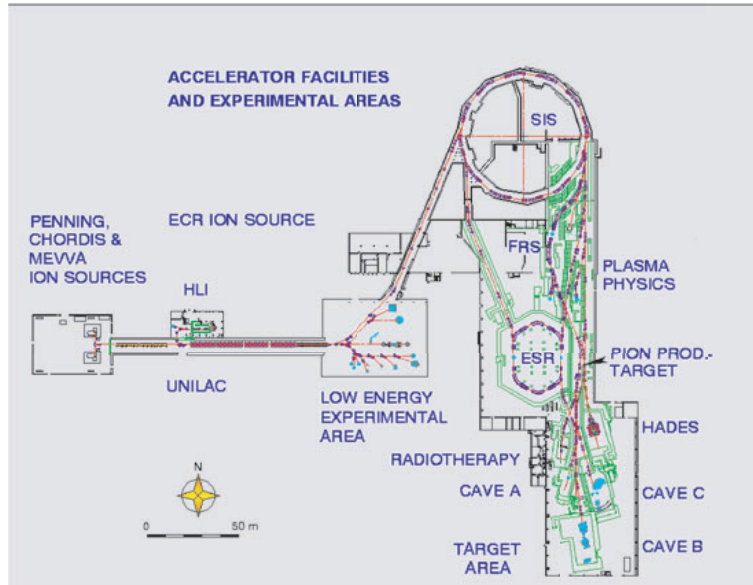
Figure 1.8: *Schematic view of the GSI facility [34].*

forschung) is a heavy ion research center located in Darmstadt. GSI with its about 30 experimental set-ups operates a heavy ion accelerator facility consisting of the Universal Linear Accelerator UNILAC (energy of 2 - 20 AMeV), the Synchrotron for Heavy Ions SIS 18 (1 - 2 AGeV) with a diameter of 60 meters, the Experimental Storage cooler Ring ESR (0.5 - 1 AGeV), and a Fragment Separator (FRS), as shown in Figure 1.8.

This permits to accelerate ions of all elements (up to U) up to a maximum energy of 1 and elements up to Ne to 2 GeV per atomic mass unit with an energy resolution of 10^{-3} without any significant particle loss. The cycle length can be selected between 1 and 10 seconds, bringing around 10^{10} ions per cycle [34].

For all the energy regimes discussed above, different calculations, described in some details in the following Section, suggest that properties of the light hadrons, such as masses and couplings, change considerably in the nuclear environment. By studying medium effects on hadronic properties one can directly test the understanding of those non-perturbative aspects of QCD responsible for the light hadronic states.

Considering various hadronic probes, the best way to investigate the change of hadronic properties is to study of particles, preferably those with a suffi-

ciently short life time, such that their decay or at least part of it occurs the hot dense hadronic medium, i.e. on a time scale of a few 10 fm/c. Another important criterion is that those particles are not obscured by strong interaction in the final state, i.e. leptons and photons.

Pseudo-scalar mesons (π^0, η^0, K) cannot be used since their life-time is much longer and their decay therefore mainly happens outside the reaction zone. Suitable probes which meet both criteria are vector mesons (ρ, ω, ϕ) which decay directly into dileptons; a change in their mass can be seen in the dilepton invariant mass spectrum.

1.3 Vector Mesons

Vector mesons, whose main characteristics are summarized in Tab. 1.1, are hadrons with spin 1 and isospin 0 (isoscalars) or 1 (isovectors). According

meson	mass (MeV/c^2)	FWHM (MeV/c^2)	$c\tau$ (fm)	main decay	e^+e^- branching ratio
ρ	768	152	1.3	$\pi\pi$	4.4×10^{-5}
ω	782	8.43	23.4	$\pi^+\pi^-\pi^0$	7.2×10^{-5}
ϕ	1019	4.43	44.4	K^+K^-	3.1×10^{-4}

Table 1.1: *Main characteristics of vector mesons [51]*

to the Vector Mesons Dominance Model (VMD), the coupling between hadrons and leptons at low energy is carried by the vector mesons which therefore determines the electromagnetic form factor, as shown in Figure 1.9. The quantum numbers of the vector mesons in fact are the same as for the photons $(J^{PC} = 1^{--})$, then the off shell photon can convert to a vector meson. The coupling between vector mesons and photons is proportional to an amplitude [35]

$$f_V = \frac{eM_V^2}{2g_V} \tag{1.11}$$

where M_V is the mass of the vector meson, g_V a normalization constant. f_V are also experimentally determined by the partial widths of electromagnetic decays $\Gamma_{V \to e^+e^-}$. A good agreement (in the order of 20%) for the ratio $\frac{f_\rho}{f_\omega}$ is found between experimental values determined by the partial decay widths and theoretical values based on the SU(3) quark model. The produc-

(a) ρ (b) ω
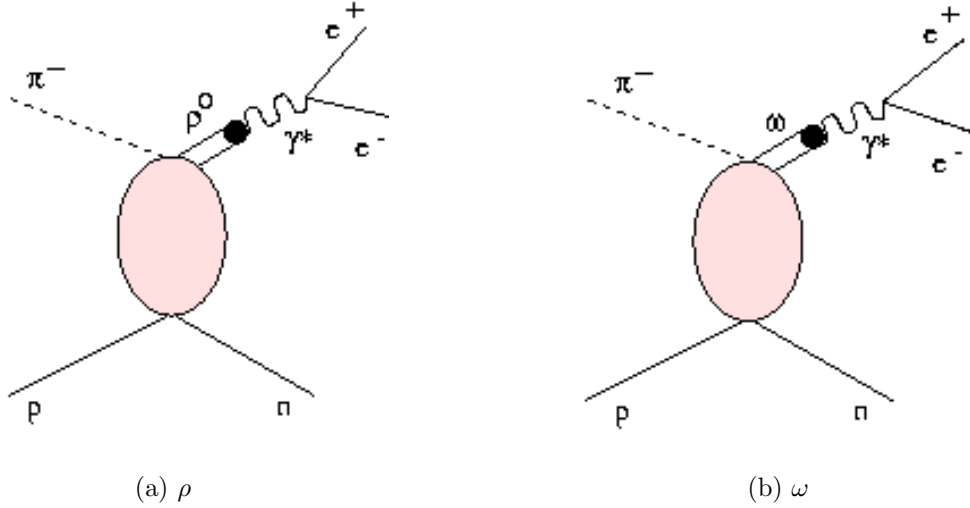
Figure 1.9: *Feynman diagrams of production and decay of ρ and ω vector mesons.*

tion cross section, proportional to this ratio squared is an order of magnitude larger for the conversion of the virtual photon in ρ than in ω [35].

1.3.1 Form Factors

The importance of form factors is directly related to the studies of the electromagnetic structure of hadrons. An effective tool to probe it consist in the scattering of a charged probe in the electromagnetic field of the object under investigation.

The scattering of high energy pions on electrons in a H_2 target, the cross-section for the process $\pi^\pm + e^- \rightarrow \pi^\pm + e^-$ is directly measured; as Figure 1.10 shows, the mechanism to describe it involves the exchange of a virtual photon with energy ω and momentum q; in the center of mass reference frame of the colliding particles, the energy of the electron remains unchanged and only the direction of its momentum is affected: the virtual photon transfers momentum but not energy:

$$q^2 = (\Delta E_e)^2 - (\Delta p_e)^2 = -4p_e^2 \sin^2(\theta/2) < 0 \qquad (1.12)$$

It corresponds to the region of space-like energy-momentum transfer.

The differential cross section for the scattering between an electron and a
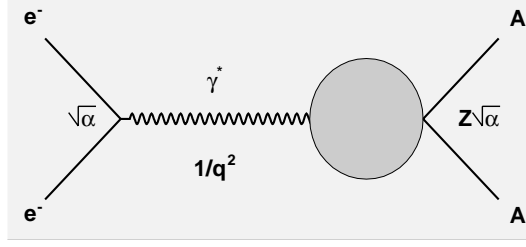
Figure 1.10: *Feynman diagram of the interaction between an electron and a non-point-like generic hadron. The internal electromagnetic structure of the particle, represented in figure by the grey circle, is described by the form factor.*

non-point-like particle is expressed[7] in the form [38]

$$\frac{d\sigma}{d\Omega} = \left[\frac{d\sigma}{d\Omega}\right]_{Mott} \cdot \left[\frac{G_E^2(Q^2) + G_M^2(Q^2)}{1 + \tau} + 2\tau G_M^2(Q^2)\left(\tan\frac{Q}{2}\right)^2\right] \quad (1.13)$$

where $\left[\dfrac{d\sigma}{d\Omega}\right]_{Mott}$ is the Mott differential cross section, $Q^2 = -q^2 = \left(\dfrac{E}{c}\right)^2 - p^2$ is the 4-momentum transfer $\tau = \dfrac{Q^2}{4M^2c^2}$, G_E^2 is the electric and G_M^2 is the magnetic form factor of the non-point-like particle. The form factor can be non-relativistically interpreted as the Fourier transform of the spatial electromagnetic charge[8] distribution of the particle: it represents then the internal electromagnetic structure of the particle.

A different kinematical region can be explored with the annihilation process $e^+e^- \to \pi^+\pi^-$: in this case the squared 4-momentum of the virtual photon is positive and corresponds to the squared total energy of the colliding particles

$$q^2 = (2E)^2 - (p - p)^2 = (2E)^2 = s > 0 \quad (1.14)$$

The virtual photon transfers energy but not momentum and corresponds to the time-like region of the energy-momentum transfer. However the time-like processes shows a kinematically forbidden region $0 < q^2 < 2m_\pi^2$ since the energy transfer is not enough to generate the two outgoing pions [36]. Experimental results show that the form factor of the pion in the space-like region decreases with increasing q^2, because the region where scattering takes

---

[7]taking into account the spin of the electron
[8]i.e electric charge and magnetic moment.
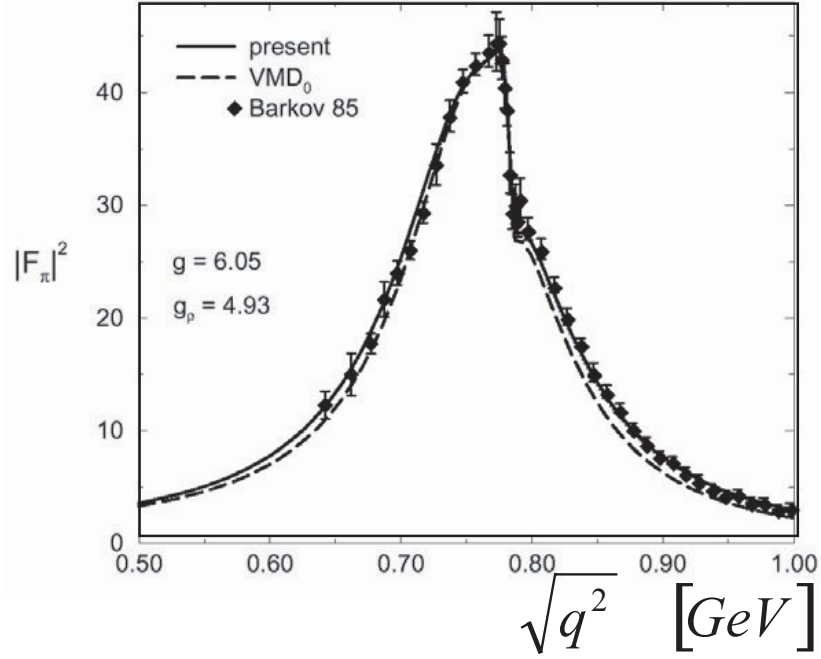
Figure 1.11: *Form Factor of pion in the time-like region, i.e. measured un the $e^+e^- \rightarrow \pi^+\pi^-$ annihilation process. The resonance at ρ and ω vector meson mass can be explained withe the Vector Meson Dominance Model and the $\rho - \omega$ mixing [37].*

place diminishes and the virtual photon "sees" the smaller and smaller inner region of the hadron. A good parameterization is given by

$$F(q^2) = \left[1 - \frac{q^2}{\Lambda_\pi^2} \right]^{-1}. \qquad (1.15)$$

This argument might be valid also in the time-like region (shown in Figure1.11) at high values of q^2, but here another phenomenon plays an important role, since the virtual photon interacts with hadrons, not only directly but also with a transition to a vector-meson (ρ, ω, ϕ). This phenomenon becomes dominant (and therefore it is known as *Vector Mesons Dominance model* (VMD) when q^2 approaches the values of the squared mass of the vector mesons. This explains the resonant q^2 dependence of the pion form factor in the time-like region [39, 40]. The sudden fall of the curve around the ω mass (780 MeV/c^2) are explained with the interference between the ρ and the ω meson and it is known as $\rho - \omega$ mixing, due to the coupling of the ω meson with two pions which happens only in presence of hadronic matter.

$$F_\pi(q^2) = \frac{m_\rho^2}{m_\rho^2 - q^2 - im_\rho\Gamma_\rho(q^2)}. \tag{1.16}$$

In general, the VMD describes a form factor as

$$F(q^2) = \frac{M_V^2}{M_V^2 - q^2} \tag{1.17}$$

so that the mass of the vector meson is directly proportional to the form factor and by analyzing this last one, information is derived about the electromagnetic structure of the meson.

1.3.2 Transition Form Factors

For neutral pseudoscalar mesons like $\pi^0, \eta, \eta\prime$, processes of single-photon exchange are forbidden due to the conservation of charge-conjugation parity. They can however undergo *internal conversion* processes, i.e. radiative decays $A \to B\gamma* \to Be^+e^-$, where the particle A is converted into the particle B with the sign-reversed value of A charge-conjugation parity.

(a) N

(b) η
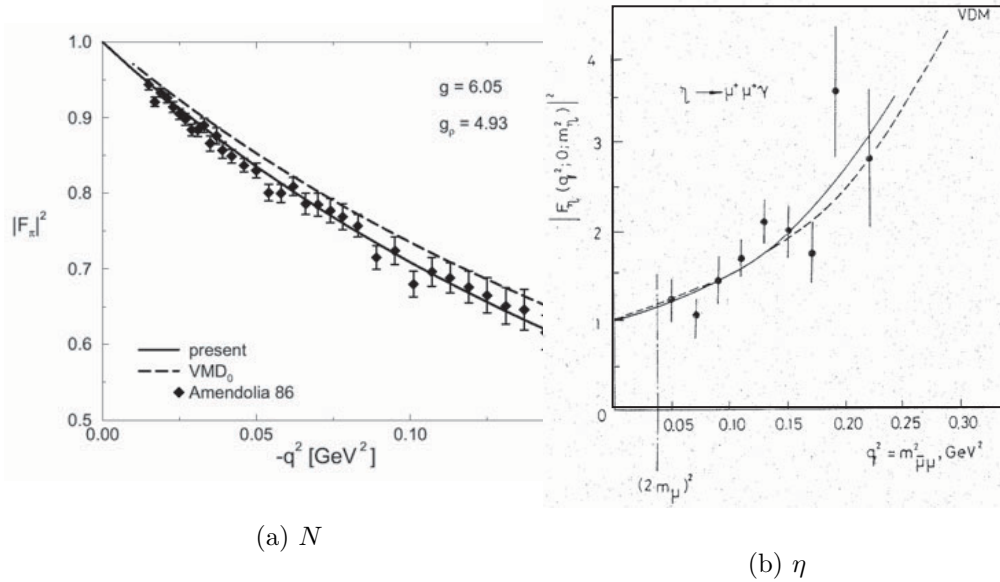
Figure 1.12: *Transition form factors of N (a), η (b). The theoretical calculations based on the Vector Meson Dominance model are in good agreement with the experimental data [36].*

The probability for such a radiative decay depends on the internal electromagnetic structure arising at the vertex $A \rightarrow B$, namely on the *transition form factor* $[F_{A \rightarrow B}(q^2)]$, where the 4-momentum transfer q^2 is the invariant mass squared of the lepton pair $q^2 = m_{e^+e^-}^2 = (E_{e^+} + E_{e^-})^2 - (p_{e^+} + p_{e^-})^2$. While the VMD model seems to be a good approximation for transition form factors of N, $\eta, \eta\prime, \pi^0$, as Figure 1.12 shows, it does not reproduce instead the transition form factor of ω shown in Figure 1.13. Here data collected in Dalitz decays ($\omega \rightarrow \pi^0 \mu^+ \mu^-$) and in annihilation processes ($e^+ e^- \rightarrow \pi^0 \omega$), not numerous and with large errors, are not reproduced by theoretical models based on VMD and $\phi - \omega$ mixing.

A detailed knowledge about form factors is not only important for the understanding of the internal structure of hadrons, but it also plays an important role in the interpretation of dilepton spectra from heavy ion experiments [18].
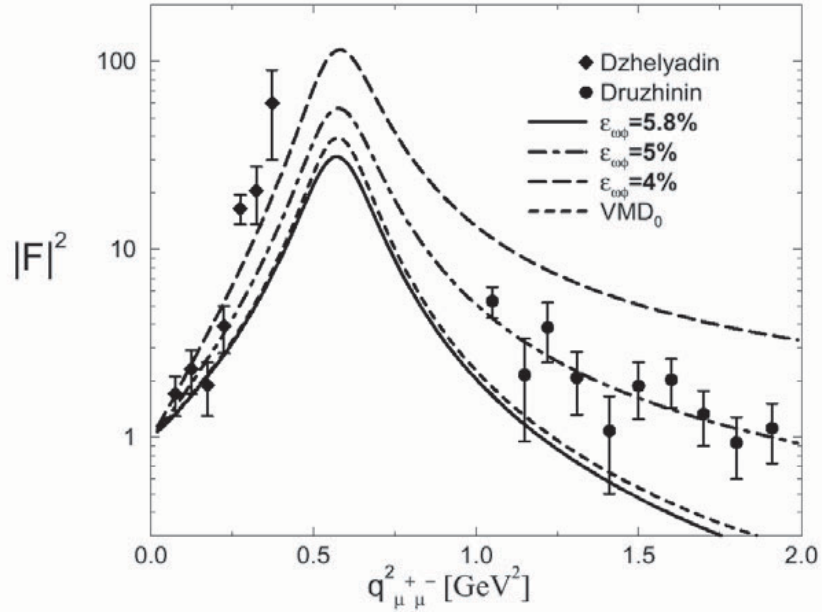
Figure 1.13: *Form Factor of omega in time-like region, i.e. measured from the Dalitz decays $\omega \rightarrow \pi^0 \mu^+ \mu^-$ [41] and in annihilation processes $e^+ e^- \rightarrow \pi^0 \omega$ [42]. Calculations based on Vector Meson Dominance model and possible variation including $\omega - \phi$ mixing (depending upon the parameter $\epsilon_{\omega\phi}$) [37] are not in agreement with data.*

1.3.3 Properties of the Vector mesons in Nuclear Matter

Vector mesons are suitable probes for investigating the hot dense states of nuclear matter, since their life time is compatible with the life time of the hot and dense fireball they are produced in and can therefore provide information about it. In addition the atomic nucleus itself represents a system at zero temperature and finite density. At nuclear density the quark condensate is estimated to be reduced by about 30%, so that effects due to the change of chiral order parameter may be measurable in elementary reactions induced by pions or protons on the nucleus, where no fireball is produced.
Different prediction have been drawn for the fundamental properties of vector mesons, such as their mass distribution, when they are embedded in nuclear matter. They are mainly related with the assumption of two different scenario: one which considers the restoration of chiral symmetry, another which deals with hadronic interaction [16, 19, 20, 21, 22, 23, 43, 44, 45, 46, 47, 48, 49].

As mentioned in Section 1.2.1, the chiral symmetry breaking generates an effective mass of the quarks, known as *constituent mass*; in dense and hot nuclear matter, when the quarks deconfine, the quark condensate decreases, while the symmetry gets restored, and the fundamental properties of hadrons, like the mass, change.
The remarkable Gell-Mann, Oakes, Renner relation relates the values of the experimentally known mass and decay constant of the pion($f_\pi = 93$ MeV) with the expectation value of the quark condensate

$$\langle \bar{q}q \rangle_{\rho=0} = -\frac{m_\pi^2 f_\pi^2}{m_0} \tag{1.18}$$

with $m_0 = \frac{1}{2}(m_u + m_d)$.

Calculations within the instanton liquid model [20] as well as results from phenomenological models for hadrons [21] suggest that the properties of vector mesons are controlled by chiral symmetry and its spontaneous and explicit breaking. According to these models, the hadronic properties should depend on the value of the chiral condensate $\langle \bar{q}q \rangle$, and they are predicted to significantly change in the nuclear environment where the condensate is reduced.
Based on restoration of chiral symmetry, within a mean-field approach, Brown and Rho [23] have argued that masses of non-strange hadrons would scale with the quark condensate and therefore decreasing for increasing density

and temperature of the nuclear medium. For increasing density

$$\frac{\langle\bar{q}q\rangle_\rho}{\langle\bar{q}q\rangle_{\rho=0}} = 1 - m_0\frac{\partial M_N}{\partial m_0} \cdot \frac{1}{m_\pi^2 f_\pi^2}\rho + ... \qquad (1.19)$$

So already at normal densities ($\rho = \rho_0 = 0.17 fm^{-3}$) with the experimental value $\Sigma_N = 45$ MeV, the value of the condensate is expected to decrease of about 35% with respect to the vacuum value, and the mass of vector mesons ρ and ω and reduced by

$$M_\rho = M_{\rho_0}(1 - 0.35(\rho/\rho_0))^{1/2} \qquad (1.20)$$

i.e. 16%, corresponding to about 130 MeV [19, 16].
The temperature dependency of the scalar quark condensate is predicted to be quadratic [19, 16]

$$\frac{\langle\bar{q}q\rangle_T}{\langle\bar{q}q\rangle_{T=0}} = 1 - \frac{T^2}{8f_\pi^2} + ... \qquad (1.21)$$

Therefore, with the assumption of the equations above, one can derive a prediction for the value of the scalar quark condensate $\langle\bar{q}q\rangle$ as a function of ρ and T, shown in Figure 1.14 [22].
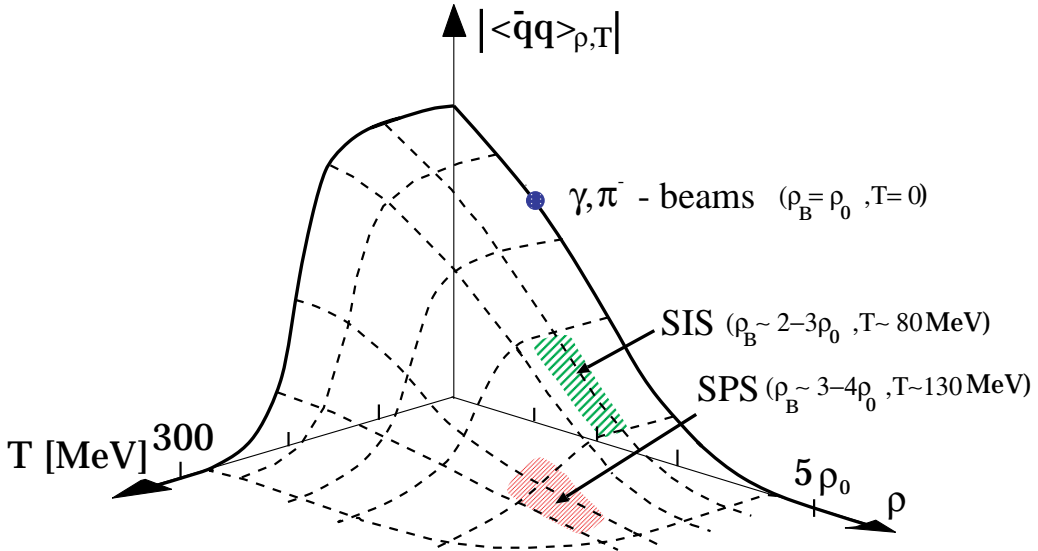
Figure 1.14: *The dependency of the quark condensate on temperature and density of the nuclear matter, predicted by the Nambu-Jona-Lasinio model [22].*

Thanks to the connection between the value of the quark condensate and the hadron masses drawn in [23], a reduction of the hadron masses is expected at finite densities, for example a reduction of the ρ meson mass by about 15-20%.

Another scenario is considered by different models [43, 44, 45, 46, 47] to explain in medium modification of vector mesons, namely the hadronic scenario. In this case the modifications arise from the fact that for the ρ and ω mesons many additional channels are opened in a hot dense medium. These models predict a broadening of the peak as a consequence of the additional channels opened and of the shortening of the the life time of the particle inside the nuclear matter, due to interactions with the medium.

The ρ Meson

The ρ meson is constituted of a quark - antiquark pair of equation

$$\rho^0 = \frac{1}{\sqrt{2}}(u\bar{u} - d\bar{d}) \tag{1.22}$$

The distance it propagates into nuclear matter, derived from its life time is about 1.3 fm, so it decays inside the fireball which has a life time of about 10 fm/c. Nevertheless, if it has a large momentum then the formation time as well as the life time are Lorentz dilated by and therefore heavy ions (Au or Pb) have to be chosen in order to get the decay still inside the fireball. Being a two-pion resonance for the conservation of the G-parity, a broadening of the peak is expected due to the additional channels opened in the hot and dense matter, like $\pi - N - hole$ and $\pi - \Delta - hole$ [43, 44, 45, 46].

Figure 1.15 shows the *spectral function* of the ρ meson. The spectral function, defined as the imaginary part of the propagator, due to the presence of the medium which breaks the Lorentz invariance, depends on the energy ω and the 3-momentum q of the meson

$$A(\omega, q) = \frac{1}{\pi} \frac{Im\Sigma(\omega, q)}{(\omega^2 - q^2 - m^2 + Re\Sigma(\omega, q))^2 + Im\Sigma(\omega, q)^2} \tag{1.23}$$

and can be interpreted as the mass distribution of the ρ meson. The figure shows the ρ spectral function for transverse and longitudinal polarization of the ρ meson as a function of momentum and invariant mass of the ρ. This calculation is performed in a low density approximation where the $D_{13}(1520)$ resonance dominates the $\rho - N$ scattering [47].

(a) transverse polarization   (b) longitudinal polarization
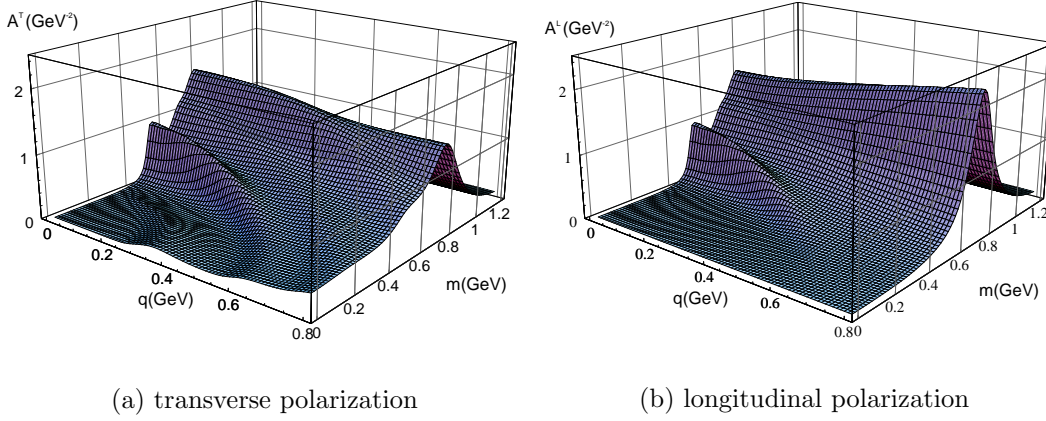
Figure 1.15: *3-d plots of the ρ spectral function a) for transverse and b) for longitudinal polarization of the ρ meson. The spectral function is shown as a function of momentum and invariant mass of the ρ [47].*

The ω Meson

The ω meson is also a composition of u and d quarks

$$\rho^0 = \frac{1}{\sqrt{2}}(u\bar{u} + d\bar{d}) \tag{1.24}$$

but has a much longer life time of about 23.4 fm, resulting in a narrow three pions resonance for the G-parity conservation. The two pion decay can be explained with the mixing with the ρ meson, which is also responsible of the sharp edge in the pion form factor resonance [48].

To enhance the amount of those mesons which decay inside the fireball the use of heavy ions (Au or Pb) is forseen. Figure 1.16 shows the ω spectral function for two different momenta, at rest and with a relative momentum of 0.4 GeV with respect to the nuclear medium, based on a VMD model calculations and the coupling of baryon resonances to the photon-nucleon system [49].

Figure 1.17 shows results for the spectral function of the ρ and ω mesons, calculated assuming an effective chiral Lagrangian and taking into account 2-body processes of nucleon, pion and vector meson [50].

In addition for the measurement of the ωtransition form factor, the usage of pion beams is forseen, with proton beams ($pp \to pp\omega$), i^- beams ($\pi^-p \to \omega()$ and π^+ beams ($\pi^+p \to \pi^+p\omega$), which combines the advantages of pion beams (high cross sections, low background, low single rates in the detectors)
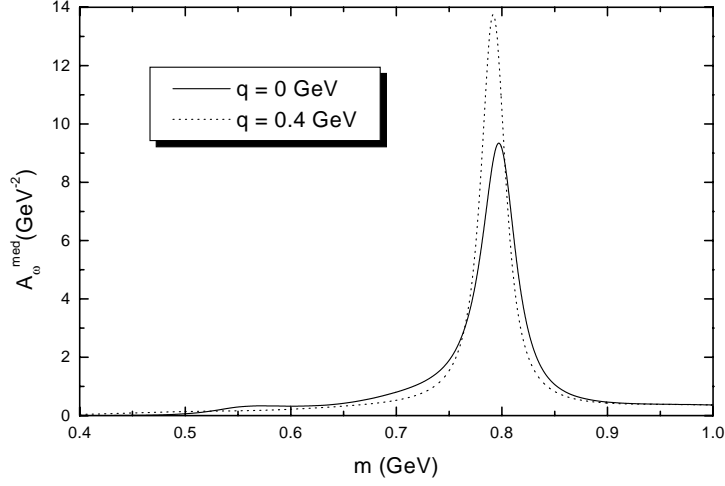
Figure 1.16: *ω spectral function as a function of its invariant mass for two different momenta, at rest and with a relative momentum of 0.4 GeV [49].*
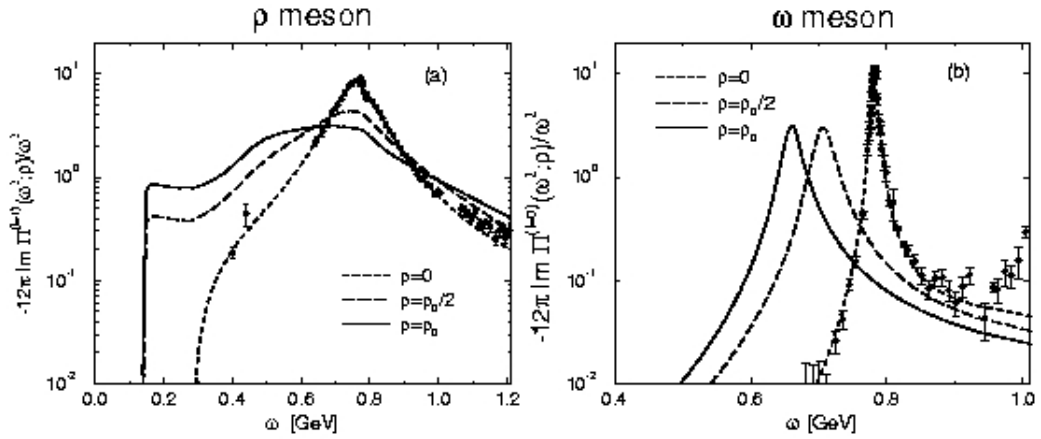
Figure 1.17: *In medium modification of the ρ and ω mesons calculated for different densities of the nuclear matter [50].*

and of the proton beams (fully exclusive kinematics) [54].

Vector mesons have a dileptonic decay channel (see 1.1). This is an ideal tool for the investigation on the expansion phase of the system and interaction of hadrons with the hot and dense environment, since after being

created, e^+e^- do not interact any longer with the medium, because they do not undergo strong interaction.

1.4   The Dielectron Spectroscopy

Heavy ion and elementary reactions are a good environment to investigate in medium modification in a hot and dense nuclear matter, as well as to measure electromagnetic properties of vector mesons,. Heavy ion reactions in fact allow to investigate fireballs of different sizes and to study the properties of hadrons when they are embedded in dense nuclear matter. Elementary reactions instead, since they can offer complete kinematics channels, provide good reference for heavy ion reactions and measurement of electromagnetic properties of hadrons via the estimation of their form factor.
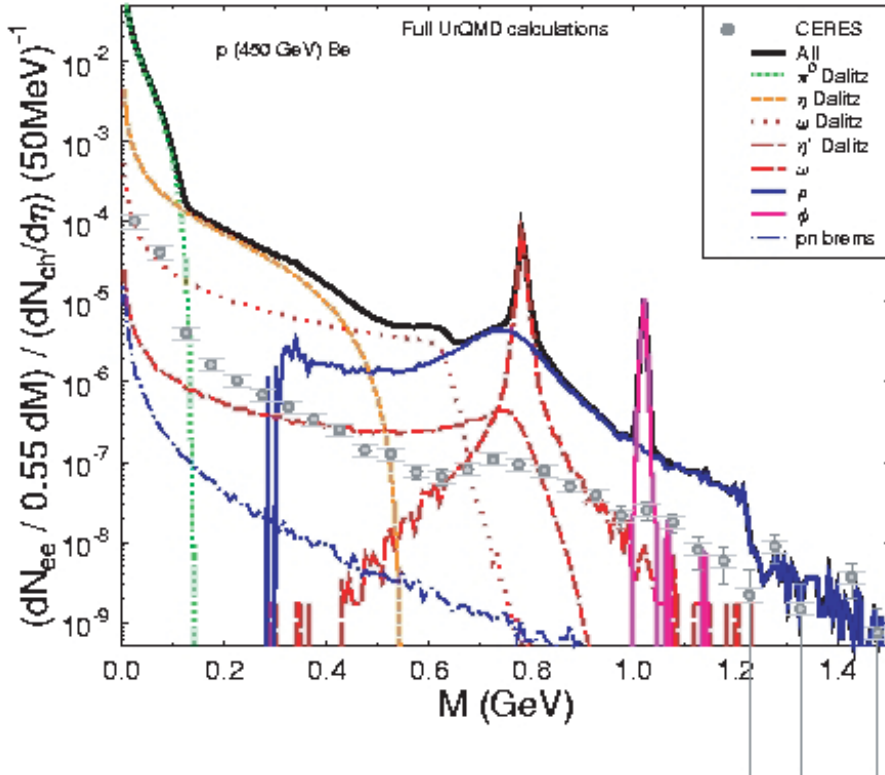
Figure 1.18: *Dilepton spectrum for p+Be at 450 GeV. The UrQMD results are not filtered and the (CERES) data points are for orientation only [55].*

The electromagnetic decay channel (e^+e^-) is an ideal probe to investigate vector mesons in hot and dense nuclear matter as well as the electromagnetic properties of hadrons, since leptons do not undergo strong interaction in the final state and leave undisturbed the collision area to reach the spectrometer preserving the characteristics at the formation.

Unfortunately the branching ratio of the e^+e^- decay of ρ, ω, ϕ is on the order of $10^{-5} - 10^{-6}$ putting lots of challenge in the construction of the detector, as well as in the data analysis. On the other hand the background is often dominant with respect to the signal, and as Figure 1.18 shows, it is mainly constituted by

- Dalitz decay of neutral mesons $\pi^0 \rightarrow \gamma e^+ e^-$; $\eta \rightarrow \gamma e^+ e^-$

- Proton-Neutron bremsstrahlung: $pn \rightarrow NN e^+ e^-$

- Dalitz decay of Δ resonance: $\Delta \rightarrow N e^+ e^-$

- Pionic annihilation: $\pi^+ \pi^- \rightarrow e^+ e^-$.

1.5 The Pioneering Experiments

Different experimental set-ups have been built to investigate modifications of the hadron properties due to the interaction with hot and dense matter; several experiments have obtained interesting and sometimes controversial results.

In the present context it is worth to mention two experiments which have performed studies of nuclear matter via the dileptonic decay, respectively at medium and ultra-relativistic collision energy: the DiLepton Spectrometer (DLS) at LBNL Berkeley, and ChErenkov Ring Electron Spectrometer (CERES) at SPS CERN.

1.5.1 DLS

The DiLepton Spectrometer (DLS), shown in a schematic view in Figure 1.19, ran at LBNL from 1987 to 1993 with different systems (from p-p, to p-A, to A-A, up to the heaviest studied system Nb-Nb) at different energies (from 1 up to 5 AGeV) and collected a significant amount of about 3×10^4 dilepton pairs with small values of mass ($m = 0.1 - 1$ GeV) and tranverse momentum ($p_T \leq 0.8$ GeV).

The results provide important indications like the existence itself and the

measurability of a dilepton signal in elementary and heavy ion reactions at intermediate collision energies, a contribution from Dalitz decay and bremsstrahlung, and a contribution from pionic annihilation resulting in high mass pairs.

However no clear conclusion can be drawn on the agreement with theoretical calculations, partly due to the limitations of the spectrometer (low statistics caused by the small geometrical acceptance of the detector (0.5-1%) and low mass resolution (10-15%)). This was worth the title "DLS puzzle".

The Spectrometer

The DLS detector consists of a two arms magnetic spectrometer at positive and negative azimuthal angles with respect to the beam line, movable but normally placed in the region of mid rapidity. The segmented target allows an increase of the interaction probability minimizing the multiple scattering and re-absorption probability.

The momentum reconstruction, as well as the tracking of the particles, is
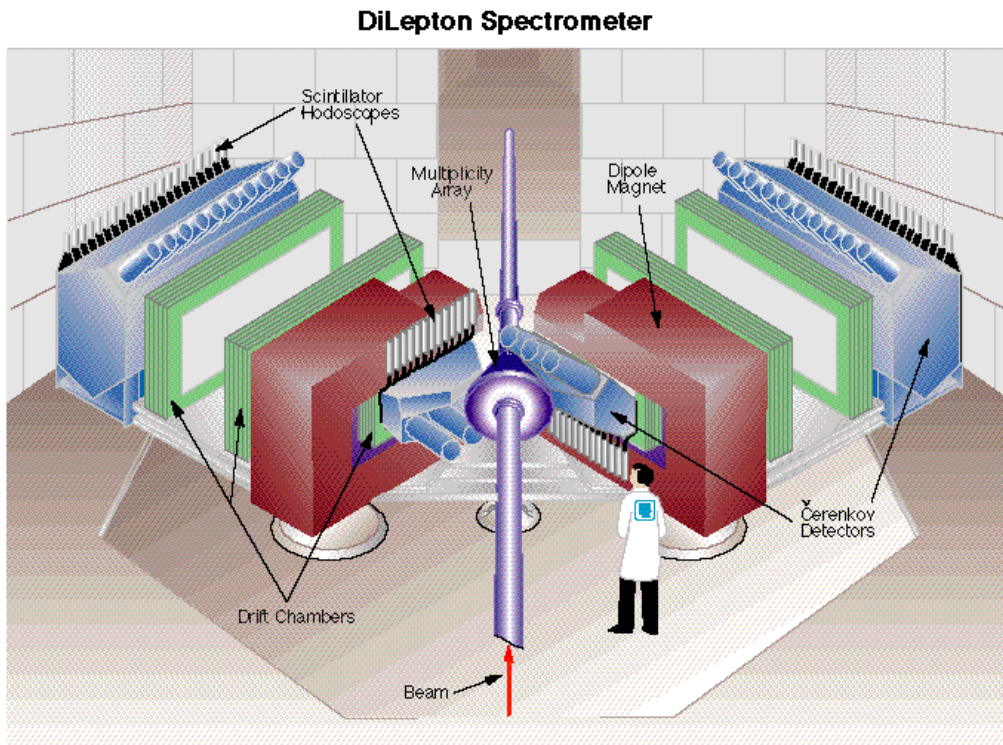
Figure 1.19: *Schematic top view of the DLS spectrometer in which each of the primary spectrometer components are identified.* [56].

provided by a set of 3 drift chambers, each constituted of 6 (+1 added in the upgrade of the spectrometer) wire planes with a different orientation in order to optimize the resolution, one placed upstream and two downstream of the nearly uniform vertical dipole field of about 1.5 kG. Lepton-hadron discrimination is provided by two arrays of threshold Cherenkov gas radiators (Isobutane and Freon) coupled to phototubes and placed upstream and downstream of the dipole field and two sets of segmented plastic scintillator, also used as trigger.

In the upgrade of the spectrometer a segmented multiplicity array, to select the centrality of the reaction, was placed around the target and a scintillator hodoscope were placed at the end of each arm in order to improve the lepton-hadron discrimination [56].

The Results

The small geometrical acceptance puts an upper limit to the tranverse momentum of the single leptons and a lower limit to the invariant mass of the reconstructed pair, so that the mass spectra below $0.2\,\mathrm{GeV/c^2}$ is affected as well as the entire range of the transverse momentum and rapidity spectra. In the first generation of experiments light systems were measured [60] and the spectra are explained with a dominance of pion annihilation for mass values larger than $0.4\,\mathrm{GeV/c^2}$ and by p-n bremsstrahlung and Dalitz decay of π^0, η, Δ for mass values below $0.4\,\mathrm{GeV/c^2}$. The spectra, within the error bars, are reproduced by theoretical calculations and no evidence for in medium modification is found [63].

The second generation of data was taken after the upgrade of the experimental set-up, better event statistics and an improved data analysis, all in all resulting in a significant improvement of the statistical and systematic error: light systems (C-C, Ca-Ca) were revised, keeping the elementary reactions (p-p, p-d) as reference system, and heavier systems (up to Nb-Nb) were explored. In these data, the discrepancy with theoretical calculation in the lepton yield led to a dilepton cross section up to a factor 7 larger than the predictions, especially in the mass region $(0.2 - 0.6\,\mathrm{GeV/c^2})$, as Figure 1.20 shows for the Ca+Ca reaction and Figure 1.21 shows for the C+C reaction [57][58].

Several attempts ([62] and references therein) have been made to reduce this discrepancy including in-medium effect on the ρ spectral function, which gives an enhancement but a factor 2-3 too low, or dropping the η mass, which gives a scenario however incompatible with the η photo-production. Other attempts have used ultra relativistic transport calculations with the explicit

(a) "free" spectral function

(b) "full" spectral function
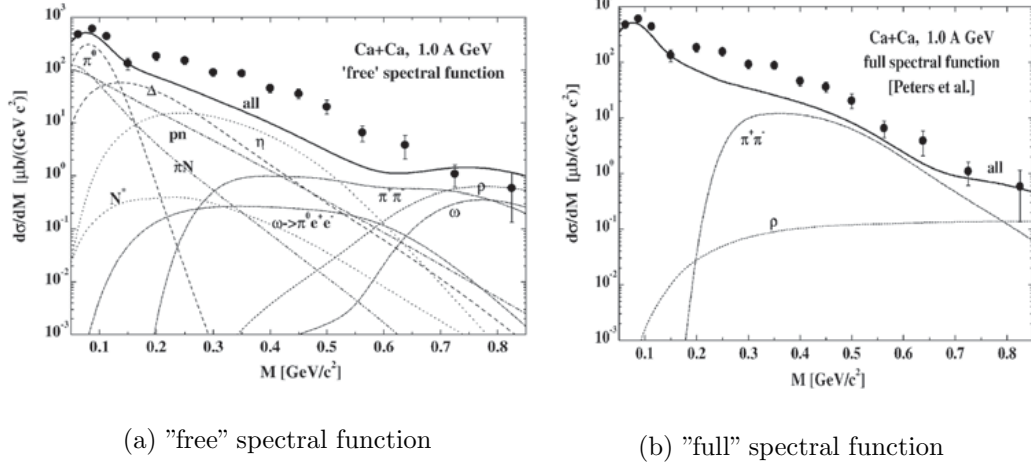
Figure 1.20: *Dilepton invariant mass spectrum dσ/dM measured for Ca+Ca reaction at 1AGeV [57][58] (full circles), compared with BUU transport calculation. The figures on the left include the individual contributions from the different production channels and a "free" ρ spectral function. In the right the ρ spectral function has been calculated with an extended approach [59], using in-medium modifications for the $\pi^+\pi^-$ annihilation.*

(a) "free" spectral function

(b) "full" spectral function
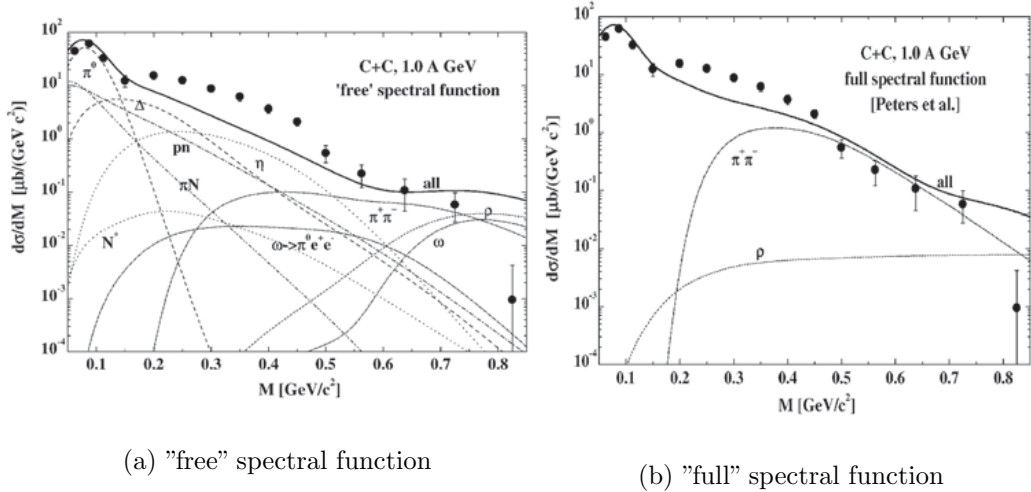
Figure 1.21: *Same as Figure 1.20 for the C+C reaction.*

dropping of the ρ mass according to the Brown-Rho m_T scaling [23], or subthreshold production of N(1520) [61], which increases, but not sufficiently,

the total yield in the medium mass range. Up to now no model has found a satisfactory solution for the dilepton enhancement and the DLS-puzzle is still unresolved.

1.5.2 CERES

The ChErenkov Ring Electron Spectrometer (CERES) has collected data from collisions of different beams produced by the Super Proton Synchrotron (SPS) at CERN on to a fixed target, for different systems (p-A and A-A up to the heaviest Pb-Au) at different collision energies (up to some hundreds AGeV).

At these energies, which are far above the energies achieved at SIS, several other processes contribute to the dilepton spectra, such as the Drell-Yan process ($q\bar{q} \rightarrow e^+e^-$) for masses larger than $1.5\,\mathrm{GeV/c^2}$, and thermal emission which would allow to classify the origin of the pairs as a partonic or a pionic annihilation, signatures respectively for different phase of nuclear matter (Quark-Gluon Plasma or Hadron Gas).

For mass values smaller than $1\,\mathrm{GeV/c^2}$ the dominant contribution is provided by the electromagnetic or Dalitz decay of hadrons and virtual photon bremsstrahlung. The dilepton production has been studied in the mid rapidity region within a broad range of transverse momenta.

The Spectrometer

The CERES spectrometer [64], shown in Figure 1.22, consists of two azimuthally symmetric Ring Imaging Cherenkov (RICH) detectors one inside the other one surrounded by the coils of a superconducting double solenoid. Due to the threshold $\gamma_{thr} = 32$, the RICH detectors are essentially blind to protons, while all electrons produce Cherenkov rings of asymptotic radius; pions are seen with momentum larger than $4.5\,\mathrm{GeV/c}$, but are distinguished from electrons from the much smaller angle of the Cherenkov cone.

The magnetic field produced by the solenoid provides an azimuthal momentum kick for momentum and charge determination. Additional correction coils are added to eliminate magnetic field from the first RICH and from the Time Projection Chamber (TPC) added in 1998 at the end of the spectrometer to improve the tracking and the mass resolution.

Furthermore for the heaviest systems a Silicon Drift chamber before the first RICH allows particle tracking to the interaction point, vertex reconstruction, identification and rejection of close pairs, and a Silicon Pad detector is used for a coarse multiplicity evaluation, which is the base for the centrality
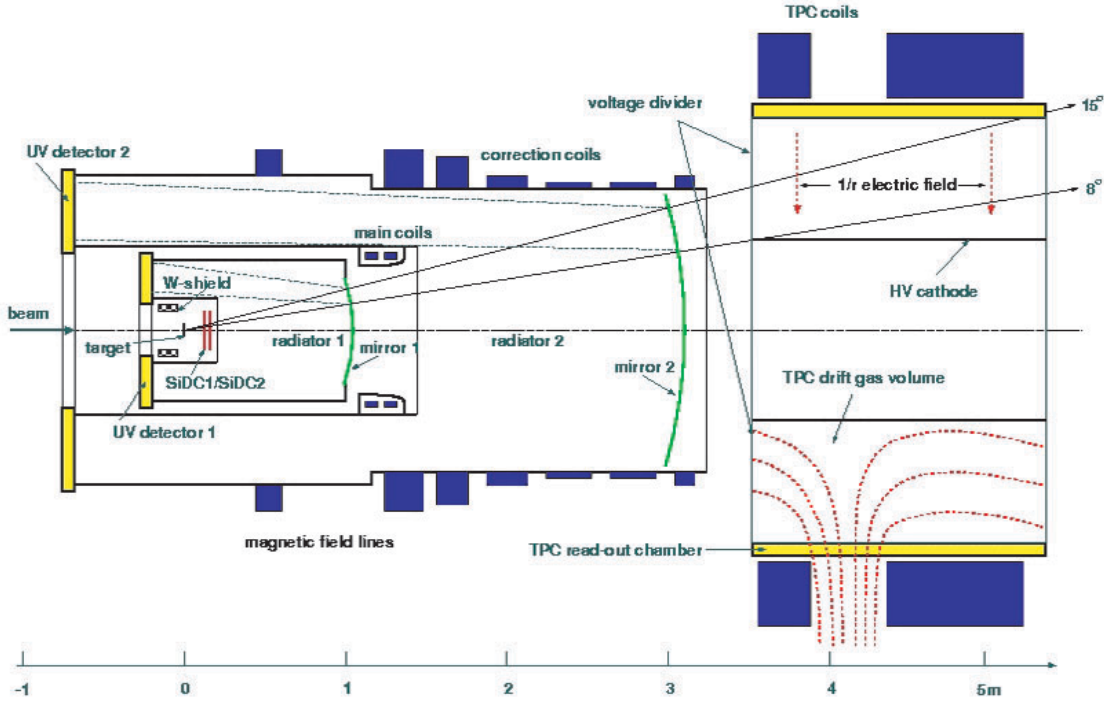
Figure 1.22: *Schematic top view of the CERES spectrometer with the upgrade of the TPC (to the right). The outline of the various detectors are visible: the RICH1 inside the RICH2, with their respective mirrors and radiators, the main and correcting coils. In addition the TPC field lines for the electric and magnetic field are shown [64].*

trigger. Moreover for high multiplicity reactions, the lepton identification capability is increased with the employ of a TPC after the second RICH.

The Results

The first generation of data studied by CERES used proton beams of different energies (up to 450 GeV) with different targets (p-p, p-A from Be to Au) and are in agreement with theoretical calculations which include all the known dilepton sources within $< 20\%$ [67].
Discrepancies come with the second generation of experiments, where ion beams (up to Pb) of different energies ($30 AGeV < E_{beam} < 200 AGeV$) are used, especially in the mass region $0.2 - 1.5 \, \mathrm{GeV/c^2}$, correlated to the low p_T region, where an enhancement factor is present depending on the collision system and the mass region, larger for heavier systems.

Figure 1.23 a) shows the invariant mass spectrum for the Pb+Au re-
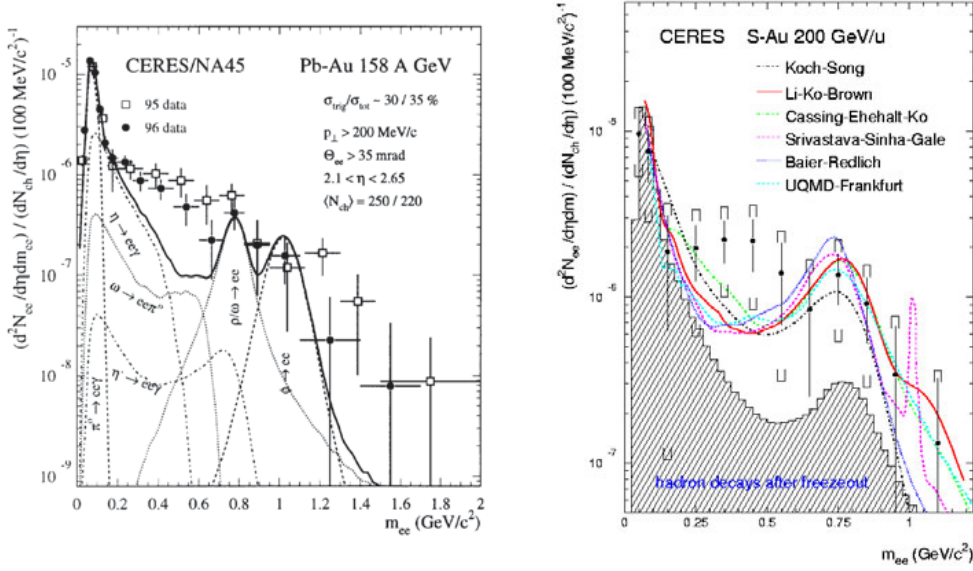
(a) Pb+Au @ 158 AGeV

(b) S+Au @ 200 AGeV

Figure 1.23: *Inclusive e^+e^- mass spectrum measured by CERES for the reaction a) Pb+Au at 158 AGeV and b) S+Au at 200 AGeV. Data are compared to different theoretical calculations obtained with the sum of the expected contributions from hadron decays [65, 66].*

action at 158 AGeV [68] with calculations including all the contribution known so far [69]: integration of the measured yield of pairs with mass above $m_{ee} > 250 MeV/c^2$ renders a relative enhancement by a factor of $3.0 \pm 1.3(stat.) \pm 1.2(syst.)$ with respect to the expected hadronic cocktail. Figure 1.23 b) shows the invariant mass spectrum for the S-Au at 200 AGeV: the conventional hadronic scenario could reproduce the results with a probability of 35% [70]. The analysis of Pb+Au at 40 AGeV shows an enhancement of dilepton pairs with mass above $m_{ee} > 200 MeV/c^2$ of a factor $5.1 \pm 1.3(stat.) \pm 1.0(syst.)$ [71].

The data in general demonstrate that the hadronic cocktail [69] does not explain the observed dielectron yield. The rise of the enhancement with the number of charged particles in the final state point to a two-body annihilation process, most likely of pions: $\pi^+\pi^- \rightarrow \rho \rightarrow e^+e^-$. Theoretical calcu-

lations (for a review see [72]) try to explain the enhancement starting from different approaches: hydrodynamical ([73, 74, 75, 76]), transport models ([77, 78, 79, 80, 81]), and thermal fireball models ([46, 83, 84, 85, 86]). Attempts to explain the CERES invariant mass spectra have been carried with different theoretical scenarios: with the dropping ρ mass according to Brown-Rho scaling (based on phenomenological implementation of the restoration of chiral symmetry) [87], with the $\pi\pi$ annihilation with vacuum spectral functions, or with both the π and ρ properties modified in the medium due to rescattering (collisional broadening of the spectral function) [72, 61].
But up to now no conclusion has been drawn and the dilepton enhancement does not have a satisfactory explanation yet.

Another dielectron experiment which should be mentioned is the E325 at KEK-PS [48] observed a significant enhancement below the ω peak stronger with a Cu target than with a C target. In addition other experiments have measured di-muon spectra with the same purpose to investigate in medium properties of hadrons: the HELIOS-3 [88], which measured up to the J/Ψ region, the NA38/NA50 upgraded to NA60 [89] at CERN-SPS.

Chapter 2

The High Acceptance DiElectron Spectrometer

YOU DON´T BELIEVE

You don´t believe - I won´t attempt to make ye:
You are asleep - I won´t attempt to wake ye.
Sleep on! sleep on! wheil in your pleasant dreams
Of Reason you may drink of Life´s clear streams.
Reason and Newton, they are quite two things;
For so the swallow and the sparrow sings.
Reason says "Miracle": Newton says "Doubt".
Aye! that´s the way to make all Nature out.
"Doubt, doubt, and don´t believe without experiment":
That is the very thing that Jesus meant,
When He said "Only believe! believe and try!
Try, try, and never mind the reason why!".

(William Blake - The Rossetti Manuscript)

The **H**igh **A**cceptance **DiE**lectron **S**pectrometer (HADES), shown in Figure 2.1, is a second generation detector installed at the Heavy Ion Synchrotron SIS at GSI Darmstadt. It is built to measure and reconstruct the decay products of elementary (pion and proton) and heavy ion induced reactions, with beams up to the energies of a few AGeV, collided on a fixed target [90, 91, 92]. The main signal of interest HADES is optimized for are the products of dileptonic decays, which have a branching ratio of the order of 10^{-6} of light vector mesons, which have a low production cross section. The energy regime is the same as DLS (1-2 AGeV), but the mass resolution of HADES (1%) and the geometrical acceptance (50%) represent an improve-
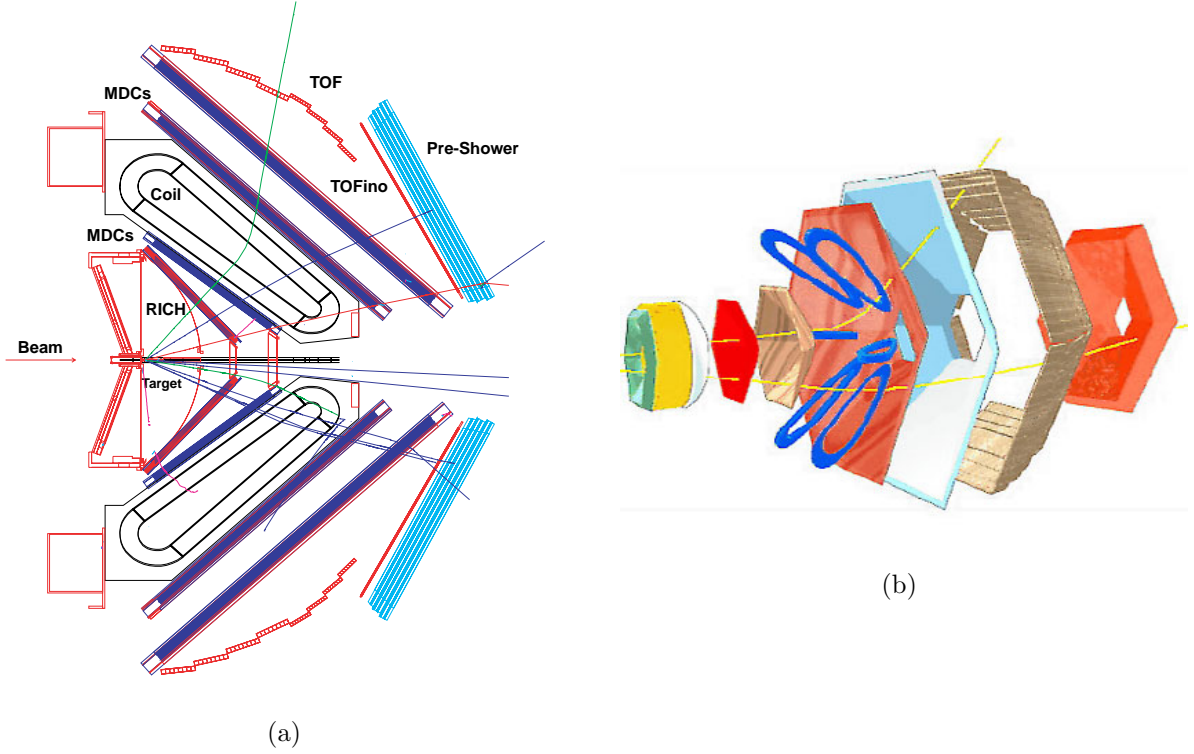
Figure 2.1: *Schematic view of the HADES detector. In fig (a) a cross section of the detector is shown. Particle tracks are from C+C simulations at 1.5 AGeV. In fig. (b) a 3D view is presented. The hexagonal structure is visible. From the target, the first detector visible is the RICH, followed by the first pair of MDC, the coils of the magnet, the second pair of MDC, Tof, Tofino and Pre-Shower.*

ment by a factor 10 compared to DLS which would provide the resolution and the statistics to resolve the ρ and ω peaks and interprete the dilepton spectra.

HADES, characterized by a six-fold geometry, has almost a full azimuthal acceptance and a polar acceptance between 15° and 85°, which leads to 45% coverage of the solid angle, and a geometrical acceptance for lepton pairs of about 45%-50%. In order to be able to distinguish the narrow ω signal from the broad contribution of the ρ, HADES has to provide a mass resolution, and therefore a momentum resolution of 1%. This is assured by two sets of Multiwire Drift Chambers (MDCs) before and two sets after a toroidal magnetic field, produced by a superconducting magnet. The particle identification is

guaranteed by the innermost detector, a Ring Imaging Cherenkov detector (RICH), completely hadron blind at the SIS energies, and by the outermost Multiplicity Electron Trigger Array (META), consisting of a Time of Flight Wall, which discriminates particles depending upon their time of flight, and a Pre-Shower detector in the small polar angle region ($18° - 45°$), which is able to discriminate electrons from pions depending upon the development of an electromagnetic shower which electrons produce, pions do not.

2.1 The Ring Imaging Cherenkov Detector

The Ring Imaging Cherenkov detector (RICH), shown in Figure 2.2 is the innermost detector, surrounding the target in the forward hemisphere, covering the full azimuthal range and a polar range between $18°$ and $85°$. It allows a very selective lepton identification thanks to the Cherenkov effect. When a particle traversing a medium has a velocity higher than the speed of light[1],$v_{part} > c/n$, where n is the index of refraction of the traversed medium, then Cherenkov light is emitted, under an angle θ_c, given by

$$\cos\theta_c = \frac{1}{\beta n} \tag{2.1}$$

Therefore particles are detected which have $\beta \geq 1/n$, i.e. [94]

$$\gamma \geq \sqrt{\frac{n^2}{(n^2 - 1)}} \tag{2.2}$$

The number of Cherenkov photons produced in a length L of radiator material is a function of the radiator material and the spectral distribution of the wave length [95]

$$\frac{dN_\gamma}{dL} = 2\pi\alpha Z^2 \int_{\lambda_1}^{\lambda_2} \left[1 - \frac{1}{\beta^2 n^2}\right] \frac{d\lambda}{\lambda^2} \tag{2.3}$$

This principle is used in the technique of Cherenkov counters and Ring Imaging Cherenkov detectors [96, 97], widely used in high energy and neutrino physics.

2.1.1 Radiator

The radiator gas of the HADES Rich [98] C_4F_{10} has an index of refraction $n = 1.00151$, which corresponds to a thresholds of $\gamma_{thr} \approx 18.3$. The threshold

---

[1]and therefore higher than the speed of the photons emitted by the particle itself

mounting frame

photodetector, with 6560 pads in each sector

photodetector gas

UV-mirror

radiator gas (C_4F_{10})

target

beam

connection to readout electronics

CsI photocathode

anode wires

cathode wires

CaF_2 window

e$^-$
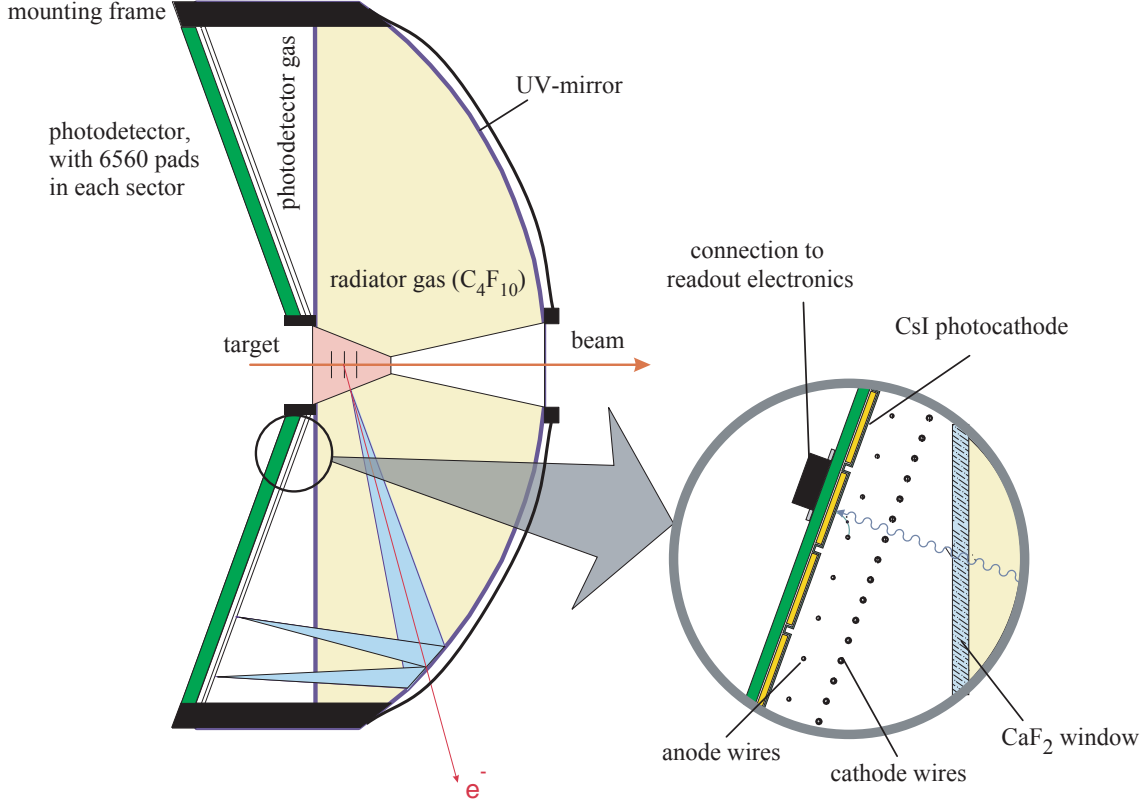
Figure 2.2: *Schematic side view of the RICH detector [93].*

energies to emit Cherenkov light in such a radiator gas are therefore $E^p_{thr} \simeq$ 15.9 GeV for protons, $E^\pi_{thr} \simeq$ 2.4 GeV for pions, both far above the SIS energies, whereas $E^e_{thr} \simeq 8.5$ MeV for electrons which, above $p = 100$ MeV/c, produce light at an asymptotic angle of $\theta_c = 3.18$.

Moreover the radiator gas is optimized to give the maximum of transparency and the minimum of scintillation; the density of the gas, kept at normal pressure, is optimized to give the best photon yield and the minimum photon conversion and multiple scattering.

2.1.2   Mirror

The Cherenkov light cone produced is reflected by a spherical mirror on to a photon detector. The mirror, composed of three trapezoidal segments per sector, has a curvature radius R = 870 mm and is placed at a distance of 402 mm = 0.45 · R from the target. The fact that the target is not in the center of the sferical mirror change the path length particles run in the radiator gas from 36 cm at small polar angle to 65 cm at large polar angle: this has consequences for the detection efficiency. A carbon fiber is chosen as constituent material of the mirror in order to minimize the radiation length to 1%, to prevent conversion and multiple scattering: on top of it a substrate of Al, covered by a thin layer of MgF_2 to prevent oxidation, is evaporated to guarantee an overall reflectivity larger than 85% in the Vacuum Ultra Violet (VUV) wavelength region[2]. To prevent distortion and smearing in the resulting rings, a roughness of maximum 2 nm is allowed. Still not all the carbon mirrors have been installed and the missing ones are replaced by glass mirrors which do not show any substantial difference in the optical properties.

2.1.3   Photon Detector

The photon detector [99], shown in Figure 2.3 is composed by Multi Wire Proportional Chambers (MWPC) with a segmented CsI photocathode: when Cherenkov photons in the VUV wavelength region reach the photocathode, electrons are emitted by photoelectric effect, are amplified by a factor 10^5 by the MWPC and induce electric charge on the photocathode, in one (or more neighboring) pads it is segmented into. Feedback effects can occur when electrons and ions recombine producing another photon in the VUV wavelength region which, emitted isotropically, could eventually hit the pad plane and initiate again a photoelectric avalanche. The photocathode is placed at an angle of 20° with respect to the normal to the beamline in order to cover the full mirror focal plane and the pads have varying dimensions in Y from $7.1\,\mathrm{mm} \times 6.6\,\mathrm{mm}$ and $4.6\,\mathrm{mm} \times 6.6\,\mathrm{mm}$ in order to compensate for the optical distortions due to the fact that the pad plane is only an approximation of the focal plane and keep the ring radius constant of 4 pads. The single photoelectron detection efficiency is around 95%. The photon detector gas CH_4 is chosen for the good transmittivity in the VUV region.

The photon detector is separated from the radiator gas by a window consisting out of 64 CaF_2 hexagonal crystals with diameter of 1.5 m, and thickness of 5 mm which provides an average transmission of 70% in the

---

[2]The wavelength region interesting for HADES is $145 < \lambda < 210$ nm.
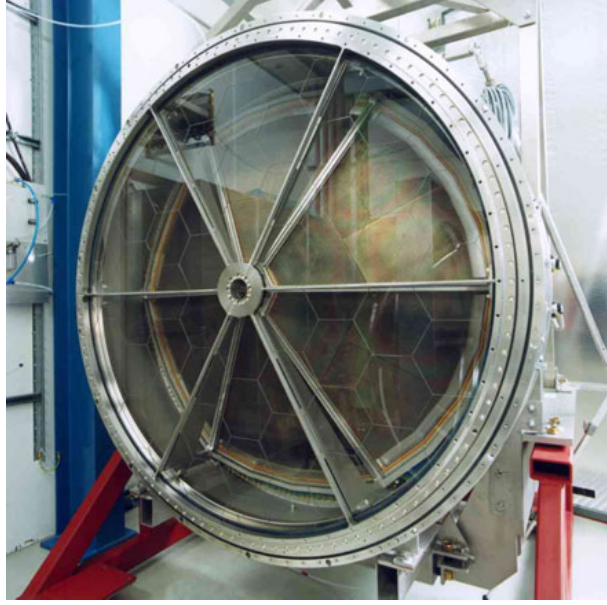
Figure 2.3: *The Rich front view with open radiator. The overall structure of the detector is visible. In addition the pad structure of the photon detector is shown on the background.*

VUV region. The number of detected photoelectrons is given by

$$N_{min,max} = N_0 \frac{L_{min,max}}{\gamma_{thr}^2} \qquad (2.4)$$

where $L_{min,max} = 0.36 - 0.65$m is the radiator path length and N_0 is the so called figure of merit given by

$$N_0 = 2\pi\alpha\,\epsilon_{se} \int_{\lambda_1}^{\lambda_2} R_{mirror}\,T_{C_4F_{10}}\,T_{CaF_2}\,T_{CH_4}\epsilon_Q\,d\lambda \qquad (2.5)$$

R_{mirror} is the average mirror reflectivity, $T_{C_4F_{10}}$ the transmission through the radiator gas, T_{CaF_2} the transmission through the window, T_{CH_4} the transmission through the photon detector gas, ϵ_{se} the single photoelectron efficiency, ϵ_Q is the CsI photocathode quantum efficiency. The figure of merit of $N_0 = 109$ shown in Figure 2.4 which is then deduced corresponds to 12-21 detected photons per ring [101]. However more recent studies [102] performed with Online Efficiency Measurements (OEM), provided more precise results, summarized in Table 2.1
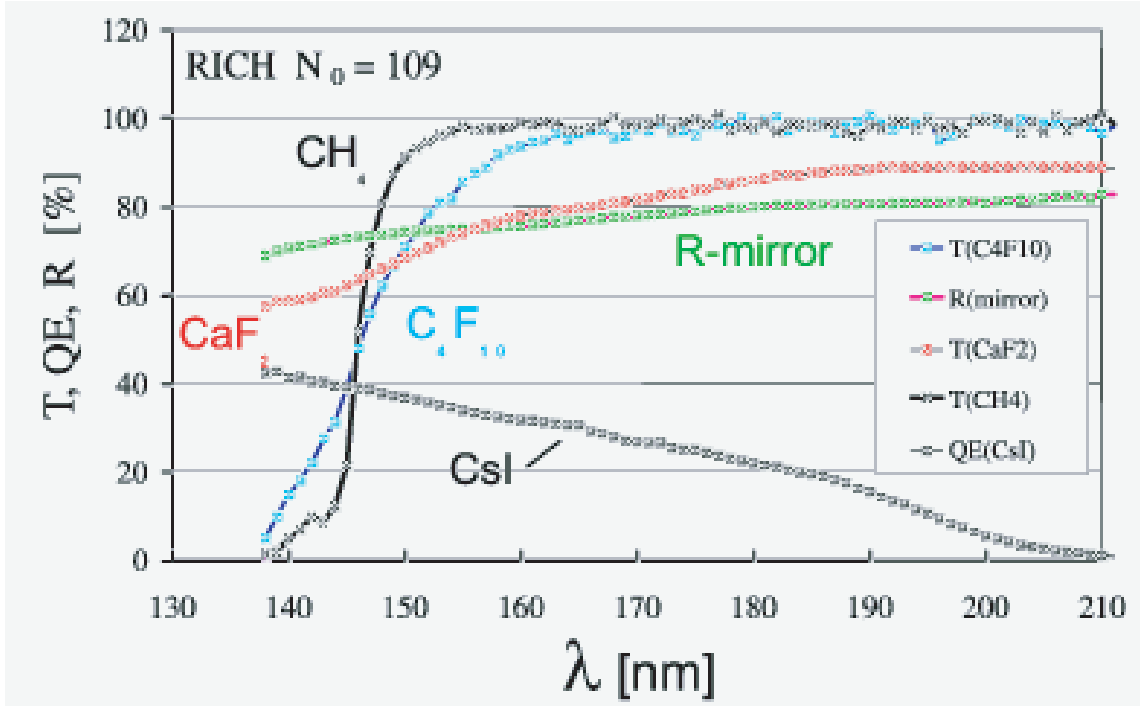
Figure 2.4: *Optical parameters of the different components of the RICH detector: transmission of radiator gas (C_4F_{10}), of the window (CaF_2), of the detector gas (CH_4), the mirror reflectivity (Mirror), and the photon detector (CsI). More recent results about the mirror reflectivity are shown in [100].*

Sector	1	2	3	4	5	6
$N_0^{Sim}[cm^{-1}eV^{-1}]$	112	112	112	112	112	112
$N_0^{Exp}[cm^{-1}eV^{-1}]$	69±7	70±7	80±9	85±8	80±10	75±7

Table 2.1: *Calculated values for the figure of merit N_0 for all the six sectors. For comparison expected values of the simulations are shown as well [102].*

2.2 The Magnetic Spectrometer

The Multiwire Drift Chambers (MDC) are responsible of the tracking of the particles and the determination of the momentum depending upon the deflection in the magnetic field. There are two planes of MDC in front and two planes behind the coils of a superconducting magnet in order to determine the direction of the particles before and after the deflection.

2.2.1   The magnet ILSE

The magnet (ILSE), shown in Figure 2.2.1, consisting of six superconducting coils surrounding the beam axis, producing a toroidal field which bends the particles in first approximation only in the polar direction. Due to inhomogeneity of the field, the deflection in azimuthal direction is though non neglectable, especially at the border of the sectors. The magnetic field reaches a maximum of 3 T, but not more than 0.7 T in the HADES acceptance, resulting in a momentum kick lower or in the order of 100 MeV/c, and higher at smaller polar angles, which allows to achieve a good momentum resolution without losing low momenta particles [103].

Figure 2.5: *The magnet ILSE, during the installation phase in the HADES cave.*

2.2.2   The Multiwire Drift Chambers

The MDCs cover the full azimuthal range, and the polar range between 18° and 85° and their distance from the target varies from 50 cm of the first plane up to 160 cm of the last. Each MDC module is composed of six layers of drift cells, oriented of $0°, \pm 20°, \pm 40°$ with respect to the normal on the symmetry axis of the module, as Figure 2.2.2, to get and improve a 2D resolution of the tracking. Each drift cell is realized by two aluminized MYLAR foils, which act as cathode planes with wires (made of aluminum,
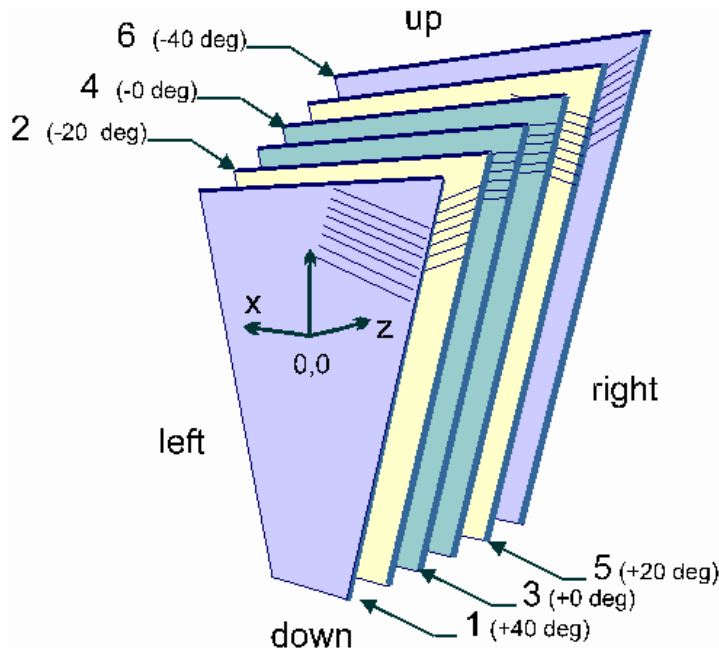
Figure 2.6: *Orientation scheme of the different cells layers of the MDCs. The layers are oriented of $0°, \pm20°, \pm40°$ with respect to the normal on the symmetry axis of the module.*

diameter 80 μm), sense wires (made of gold and tungsten, diameter of 20 μm) and field wires (made of aluminum, diameter of 100 μm) in the center of the cell.

A charged Minimum Ionizing Particle (MIP) traversing one of these cells randomly ionizes the gas (a mixture of 60% Helium and 40% Isobutane), producing about 50 clusters per centimeter per average pathlength in a drift cell (a 100MeV proton produces about 160 clusters/cm)[104] ; the sensitive wires collect the charge produced in the primary and secondary ionization in a time (typically $< 1\mu$sec) proportional to the distance of the track from the wire. The size of the cells varies from $5\,mm \times 5\,mm$ in the first plane up to $10\,mm \times 14\,mm$ in the last plane in order to keep constant the granularity and therefore the double hit resolution in the 4 detector planes.

This high granularity allows a maximum of 30% mean cell occupancy in the high multiplicity zones for a simulated Au+Au reaction, and therefore leads to a good ability in double track separation, which then minimizes the contribution of close pairs from γ conversion, the largest fraction of the background. The required momentum resolution of 1% is achieved thanks to a spatial resolution of 35-50 μm in polar direction and 85-125 μm in azimuthal direction [105, 106].

2.3   The Pre-Shower Detector

The passage of high energy charged particles through matter is characterized by a loss of energy due to inelastic collision with the atomic electrons of the material and to elastic scattering from nuclei, which causes ionization or excitation of the material. The energy loss decreases quadratically with the velocity of the particle and increases only logarithmically with the energy after reaching a minimum around 1 GeV/c^2, according to the Bethe-Bloch formula [107]

$$\frac{dE}{dx} = -4\pi \, N_A r_e^2 m_e c^2 z^2 \, \frac{Z}{A} \frac{1}{\beta^2} \left(\log\left(\frac{2m_e c^2 \gamma^2 \beta^2}{I}\right) - \beta^2 - \frac{\delta}{2} \right) \qquad (2.6)$$

where ze is the charge of a particle passing through material with atomic number Z and atomic weight A, N_A is Avogadro's number, r_e is the classical electron radius, m_e is the electron mass and β, γ are v/c and $1/\sqrt{1-\beta^2}$ respectively. The ionization constant I is approximately given by $16Z^{0.9}$ eV for $Z > 1$. δ represents the so called density effect. Figure 2.8 shows the Bethe-Bloch prediction of dE/dx as a function of the momentum for sev-
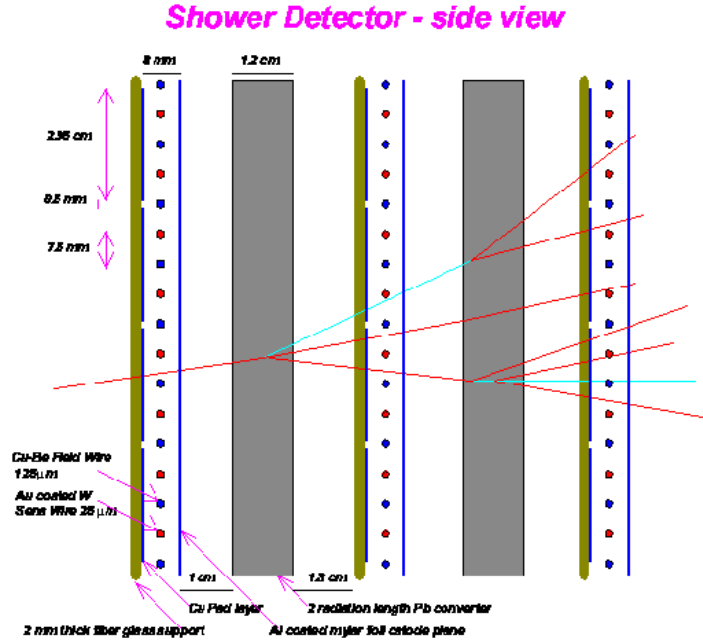
Figure 2.7: *A scheme of the shower detector: 3 MWPC with 2 Lead converters in between.*

eral particles. However high energy charged particles, when passing through
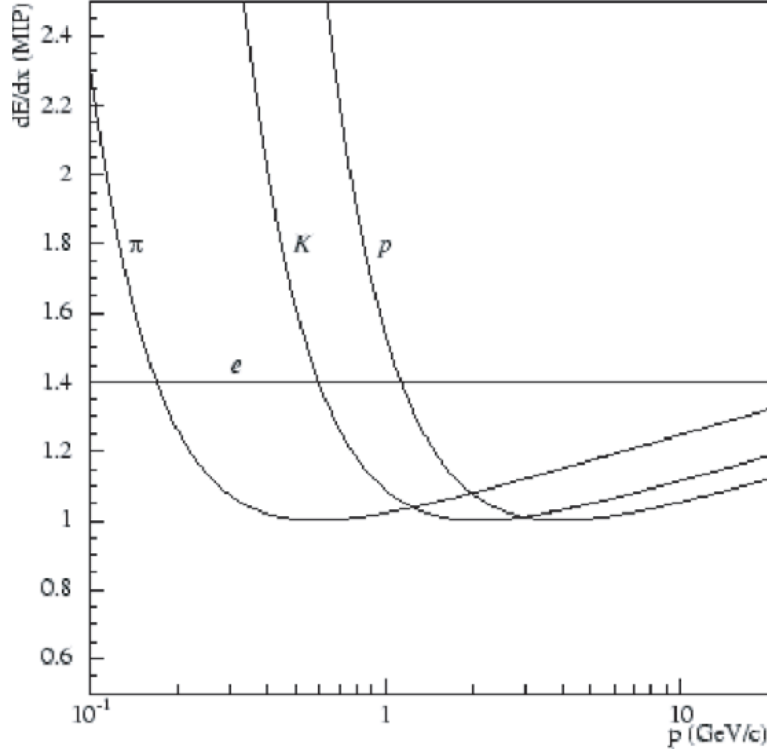
Figure 2.8: *The specific energy loss of kaons, protons, pions and electrons as a function of momentum according to the Bethe-Bloch equation [107].*

matter, also experience an energy loss due to the emission of electromagnetic radiation in the scattering with the electric field of a nucleus, the so called bremsstrahlung. The emission probability is proportional to the inverse mass squared $1/m^2$, with m the rest mass of the particle; bremsstrahlung therefore plays a particularly important role for light particles; up to energies of 100 GeV, bremsstrahlung contributes substantially to energy loss in matter only for electrons. Whereas the loss for ionization depends linearly on the Z of the material, the loss for bremsstrahlung increases quadratically with the Z: for each material a critical energy is defined as that energy where the average energy loss by radiation and by ionization is the same and can be approximated by $E_C = 550 \, \text{MeV}/Z$. The average energy loss by bremsstrahlung per unit length is [108]

$$\frac{dE}{dx} = -4\alpha N_A r_e^2 \frac{Z^2}{A} z^2 \left(\frac{1}{4\pi\epsilon_0} \cdot \frac{e^2}{mc^2} \right) E \ln \frac{183}{z^{1/3}} \tag{2.7}$$

where α is fine structure constant.

Photons with energy higher than 1.022 MeV interact with matter by pair production, i.e. the transformation of the photon into an electron-positron pair. The combined effect of bremsstrahlung and pair-production produces the so called electromagnetic shower: a high energy electron emits by bremsstrahlung a photon which then converts into an electron-positron pair; electron and positron emits again photons and so on, resulting in a cascade of electrons, positrons and photons until the energy of the electrons drops below the energy needed to emit a photon with 1.022 MeV.

The HADES Pre-Shower detector [109] uses this effect to distinguish electrons, which develop such a shower, from pions which do not, in the region of small polar angles, where, due to the Lorentz boost, electrons are not distinguishable from fast pions with the only help of time of flight.

The detector consist of three planes of Multi Wire Proportional Chambers (MWPC): in between the planes there is a layer of lead converter with a thickness of ≈ 1 cm (i.e. 2 radiation length). Each chamber is filled with a mixture of Ar and Isobutane gas, has one wire plane and two cathodes, one of which segmented into $3\,\text{cm} \times 3\,\text{cm}$ pads. There are 32 pads in Y direction and a varying number of pads, between 20 and 32 in the X direction, organized such that there is a 1:1 correspondence of pads in each of the three MWPC layers.

The passage of charged particles in the MWPC chamber ionizes the gas and the charge is then collected at the anode wire. The MWPC operate in a Self-Quenching Streamer mode [110, 111], such that the collected charge does not depend on the energy deposited but only on the number of particles traversing the chamber: this is achieved with the employ of quenching gases which absorb photons produced during the secondary ionization.

2.4 The Start-Veto Detector

The start and the veto diamond detector are two identical octagonal shaped polycrystalline diamonds synthesized using a Chemical Vapor Deposition (CVD) technique [112], shown in Figure 2.4. The thickness of the detector is 100 μm to minimize multiple scattering. Due to a band gap of 5.5 eV, a particle traversing the detector, produces a electron-hole pair; the signal is then amplified with low noise, digitized and processed; thanks to the fast rise time and the small pulse width, the time resolution achieved is about 30 ps which allows primary rates up to 10^8 Hz [113]. The start detector, as well as the veto, both of dimensions of $25\,\text{mm} \times 15\,\text{mm}$, placed 75 cm upstream and downstream the target position, are segmented into 8 strips,
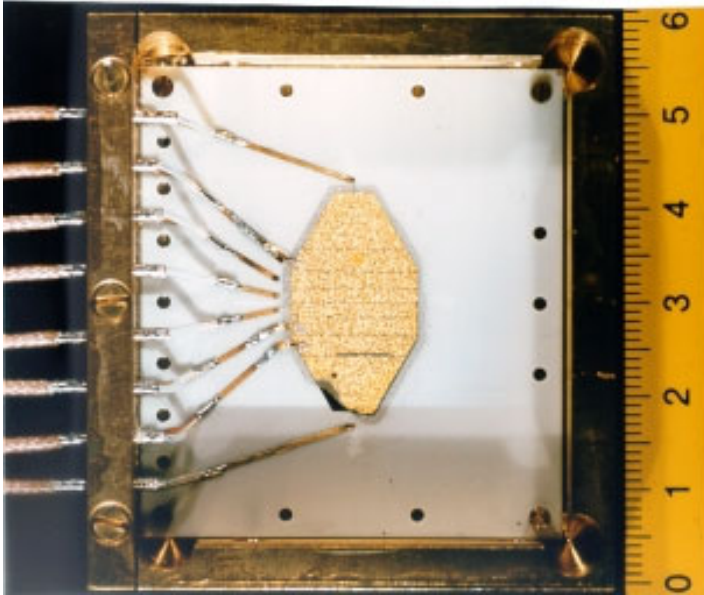
Figure 2.9: *A picture of the start detector: an octagonal shaped polycrystalline diamond constituted of 8 strips, connected to the amplifiers. The veto detector is identical.*

and work in anti-coincidence, such that when a signal is provided by both detectors the event is vetoed since the particle has not interacted with the target, having reached the detector downstream; the width of the strips is optimized to guarantee 96.5% efficiency with a start:veto coincidence of 1:3 strips. The start detector is also used as a spill monitor to check the quality and the focus of the beam, connecting a fast counter to each channel.

2.5 The Time of Flight Detector

The Time of Flight (TOF) detector [114] contributes, in the full HADES acceptance, to the particle identification by measuring the time between the start detector signal and the arrival signal and therefore, assuming a given path length, calculating the velocity of the particle.
The polar range from 45° to 85° is covered by 8 blocks of 8 bars each (therefore 64 bars per sector) of scintillator material (BC408) which uses the phenomenon of fluorescence to emit light when a charged particle passes by: the light travels in the scintillator bar with a group velocity given by

$$v_{group} = v\cos <\theta> = \frac{c}{n} \approx 16\,\mathrm{cm/ns} \qquad (2.8)$$

where $n = 1.6$ is the index of refraction of the material and $<\theta> \simeq 33°$ is the average angle of total reflection in the BC408 material. The light is collected at both ends by photomultipliers, connected to the scintillator bars via light guides, and it is then converted in a time signal by a TDC and in
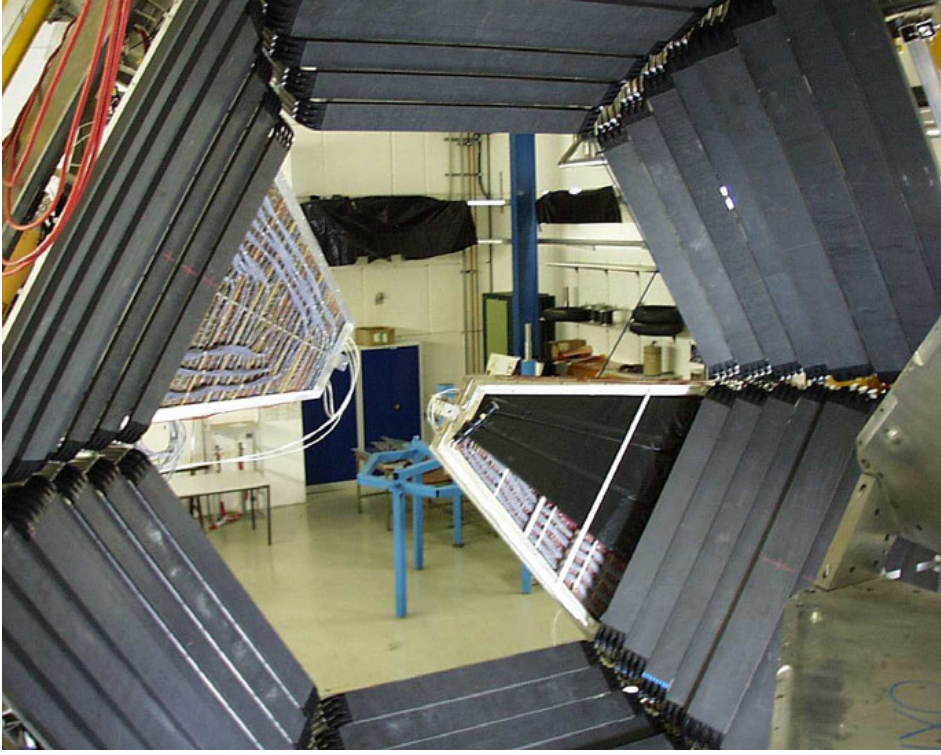
Figure 2.10: *A picture of the TOF wall from the target. All the 6 sectors are visible. In the left upper corner a sectors of the Pre-Shower detector is visible, and in the right lower corner a sector of the TOFino detector, mounted on the Pre-Shower.*

an amplitude signal by an ADC [115].

The τ_{left} and τ_{right} are the time measured by the left and right TDCs :

$$\tau_{left/right} = \tau + t_{left/right}, \tag{2.9}$$

where τ is the Time-of-Flight and $t_{left/right}$ are the time the light spends in the scintillator bar to reach the left/right TDC. The τ_{left} and τ_{right} are then combined to deduce the Time-of-Flight and the longitudinal coordinate of the impact position x according to

$$\text{ToF} = \tau = \frac{\tau_{right} + \tau_{left}}{2} - \tau_0 \tag{2.10}$$

where

$$\tau_0 = \frac{t_{right} + t_{left}}{2} = \frac{L}{2v_{group}} \tag{2.11}$$

is the time the light takes to run half a scintillator bar. and it is therefore constant, and

$$x = \frac{x_{right} - x_{left}}{2} = \frac{\tau_{right} - \tau_{left}}{2} \, v_{group} \qquad (2.12)$$

The amplitude information is used to apply a walk correction. Moreover the amplitude of the signal gives information about the energy loss of the particle in the scintillator, very helpful for the particle identification.

With the time resolution of about 150 ps, which corresponds to a spacial resolution of 2-3 cm, and a path length of about 2 m, it is possible, in the polar range between 45° and 85°, to distinguish electrons from protons up to momenta of 3 GeV/c and from pions up to 0.5 GeV/c.

Due to the Lorentz boost, this is not enough in the polar range between 15° and 45°, where pions reach much higer momenta, and where infact the Pre-Shower detector is installed to take care of the identification of fast pions. In this region the Time of Flight detector (TOFINO) is constitued only by 4 scintillator bars per sector, which are readout only at one end; this, together with the reduced granularity reduces very much the time and space resoution as well as the double hit capability.

TOF and TOFINO together are also used as multiplicity counter to give the first level trigger signal.

2.6 New Developments

For heavy system reactions, where a higher granularity is required, the substitution of TOFINO by a Resistive Plate Chamber (RPC) [116, 117] is forseen in the region with polar angle between 13° and 45°. The high granularity is needed in order to fulfill the LVL1 requirements, while for the LVL2 needs of lepton identification the hadron occupancy should be kept as small as possible. In particular a time resolution below 100 ps and a space resolution of a few centimeters (about 3 cm^2), as well as a good behaviour at rates of few hundreds Hz/cm^2 is foreseen.

A Resistive Plate Chamber is a gaseous parallel-plate detector that combines the spatial resolution of the wire chambers with the time resolution typical of a scintillation counter. It is therefore well-suited for fast space-time particle tracking. An RPC is built from a pair of parallel bakelite Glass plates separated by spacers. The outer surfaces of the plates are coated with layers of graphite paint connected to a high-voltage supply. An insulating film is glued on the graphite to shield external Al electrodes from the high voltage. The pick-up strips are fixed on a film of a plastic material which is pressed against the detector surface on both sides. Two sets of orthogonal strips al-

low for two-dimensional readout of the particle position. The gas admixture used is 98.5% of $C_2H_2F_4$, 1% of SF_6 and 0.5% of isobutane.

Tests on a prototype with a 2-layers configuration were performed and confirmed the parameters reuired for space-time resolution. The cross-talk is kept below a 0.4% level by shielding between cells, so that coincident hits in neighbour cells do not induce any degradation in time resolution. A global efficiency $\epsilon = 87 - 15\% \cdot \text{rate (kHz/cm}^2)$ has been achieved, where the inefficiency is compatible with the size of the dead zones among the cells.

2.7   The Data Acquisition

The architecture implemented for the HADES data acquisition system forsees the employ of two pipes: the first one to store the digitized data after a positive LVL1 trigger, the second one to store data after positive LVL2 trigger for the readout. When the LVL2 decision is negative, data is removed from the LVL1 pipe. The LVL2 pipe is typically implemented in the SRAM memory of VMEbus readout boards. From there data is read out by the CPU which acts as crate controller. This VMEbus interfaces are also used for configuration, test and error-handling operations.

From these local CPUs data from the subdetector read-out as well as for the seond level trigger is transferred either via ATM or ethernet to the common event builder, which is responsible of the final assembling of an event. The data taping speed achieved by the event builder is 10 MB/s, i.e. up to $5 \cdot 10^3$ events per second in a C+C reaction or about 10^2 events per second with heavier systems.

Chapter 3

The Trigger System

It is impossible to travel faster
than the speed of light,
and certainly not desirable,
as one's hat keeps blowing off.

(Woody Allen)

The main purpose of the HADES spectrometer is the measurement of dilepton decays of light vector mesons; since the production cross section of these are rather low, and the dileptonic decay branching ratio is on the order of $10^{-5} - 10^{-6}$, in order to collect enough statistics for these events a very high primary rate is needed. In this case the high amount of raw data (evaluated in some few kB/event, resulting in some GB/second) would not be stored and analyzed without the employ of an online selective mechanism which allows an enhancement of the signal-to-background ratio where signal is meant an event which *might* contain an electron-positron pair.

The SIS accelerator at GSI produces beams of intensities up to 10^8 particles per second; the interaction target has to be thin in order to minimize pair production of photons and multiple scattering as well as event pile-up: a segmented target is then forseen to increase the interaction probability up to 1% of interaction length. The resulting rate of nuclear reactions which might reach the spectrometer is therefore of the order of 10^6 events per second.

The first level trigger (LVL1) selects the most central collisions, based on the multiplicity of charged particles collected in TOF and TOFINO and reduces the event rate of typically a factor 10, down to 10^5 events per second.

The second level trigger (LVL2) searches signatures of dilepton decays first as leptons candidates in the RICH, TOF and Pre-Shower detector, and afterwards combined into opposite-sign pairs within a given invariant mass range [119, 120].

The third level trigger (LVL3) is meant to use MDC hit pattern to match
and verify the LVL2 decision and has been implemented only offline. Fig.
3.1 shows an overview of the Trigger concept.
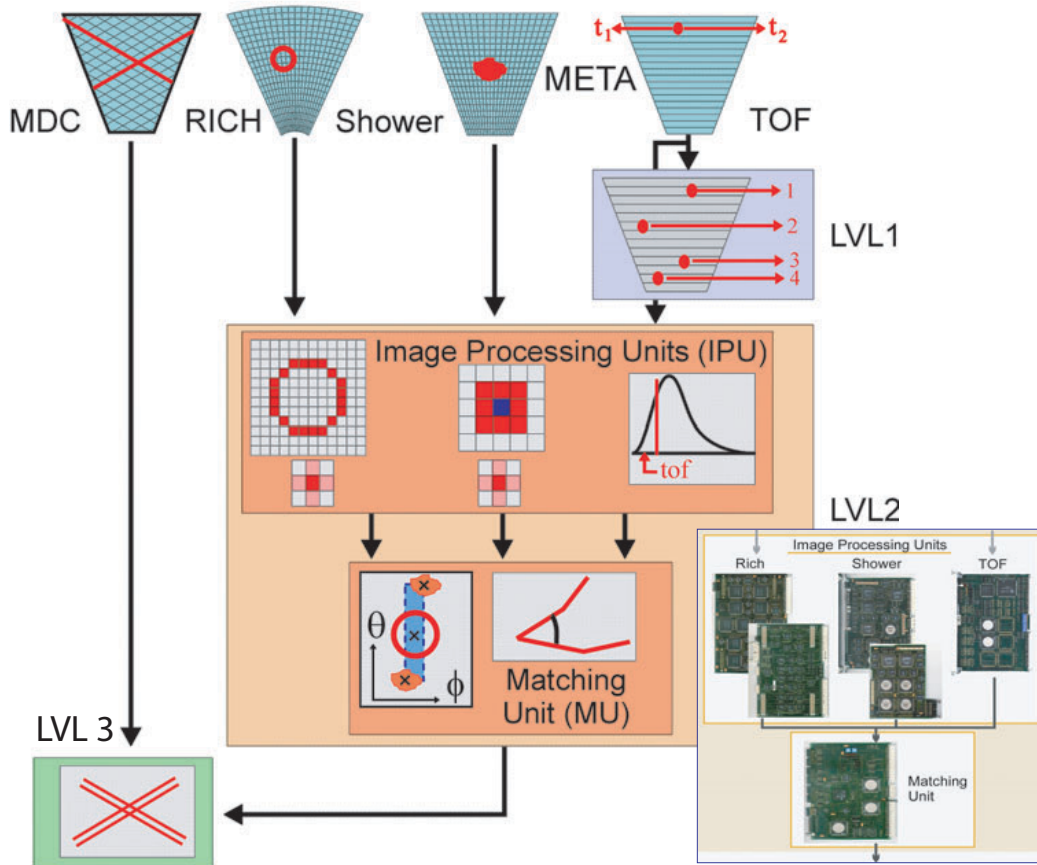
Figure 3.1: *Overview of th HADES Trigger. The flow diagram follows the
functionality of the Trigger. The first level trigger is based on the multiplicity
of charged particles in the TOF, signature for the centrality of the collision.
The second level trigger works in two steps: in the first one lepton signa-
tures from the different Image Processing Units (RICH, TOF, Pre-Shower)
are collected; in the second step they are combined by the Matching Unit to
identify a "lepton" track, combine electron with positron candidates, and cal-
culate the invariant mass. The third level trigger combines the hit pattern
information of the MDCs with the selected candidate. In the bottom right
corner the LVL2 scheme is reproduced with images of the hardware boards.*

3.1 The First Level Trigger

The production cross section of light vector mesons increases with density and temperature of nuclear matter; these conditions are met more often in central collisions, i.e. when the impact parameter of the reaction is small. The impact parameter is connected, via simple geometrical models to the number of participants in the reaction. Depending upon the energy of the colliding nuclei, in heavy systems the multiplicity of the products can be parameterized as a function of the number of participants, and therefore of the centrality of the reaction.

It is therefore possible to select a given percentage of the events, corresponding to the most central collisions, collecting the signals of the individual particles which hit TOF or TOFINO with a Multiplicity Trigger Unit (MTU) which discriminates the event and delivers the LVL1 trigger within a time interval of about 100-200 ns.

It has been estimated that a selection of events with impact parameter $b < 4$fm would reduce the events of a Au+Au reaction by a factor 10, therefore bringing the event rate down to 10^5 events per second. With C+C reactions, due to the small dimensions of the C nuclei, it is more difficult to directly relate the multiplicity to a given centrality [118].

3.2 The Second Level Trigger

The second level trigger searches directly for the signal of interest of the reaction: electron-positron decays of light vector mesons.

In a first step Image Processing Units (IPUs), receiving data from the read-out systems of the different particle identification detectors before and after the magnetic field, detect lepton signatures as Cherenkov rings in the RICH detector, as fast particles in the TOF detector, as development of electromagnetic showers in the Pre-Shower. Position and angle information is provided for each of these signatures and delivered to a Matching Unit (MU).

Assuming a magnetic deflection in polar direction and only a second order correction in azimuthal direction, the MU combines the detector signatures before and after the magnet into lepton candidate trajectories and determines the momentum and the charge of the lepton candidate depending upon the deflection. Lepton candidates are then combined into opposite-sign pairs, the opening angle is calculated, and therefore the invariant mass and finally the MU selects the *events* which contain a pair candidate in the invariant mass range of interest. The performance achieved with C+C reactions will be presented later.

3.2.1   The Rich IPU

The RICH Image Processing Unit [121, 122, 123] searches for lepton signatures as Cherenkov rings in the padplane of the RICH detector. The Lorentz factor thresholds for Cherenkov light production $\gamma_{thr} = 18.3$ of the C_4F_{10} gas radiator is such that all the electrons with momentum between 100 and 1500 MeV/c are in the asymptotic region, and therefore produce rings of a constant diameter of about 8 pad units. To keep the ring diameter constant over
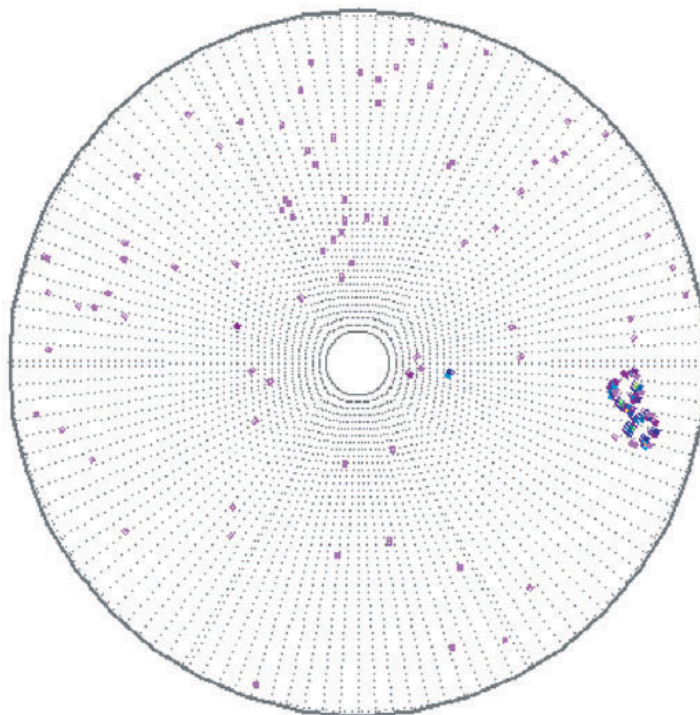
Figure 3.2: *Event Display in the Rich pad plane. Two rings (yet, not the typical case) are clearly identified in the bottom right corner of the figure. Additional rings might also be reconstructed thanks to noise depending upon the thresholds used.*

the full area of the pad plane, the pads have a varying size in Y to account for the shape distortion on the focal plane. The quality of the signal is influenced the low photon statistics (12-21 photons per ring) and the smearing of the ring pattern created by the pad response and by optical distortion.

In addition the ring recognition is disturbed by different sources of background, such as direct ionization of the photon detector, scintillating light

produced in the radiator gas, Cherenkov light produced even by hadrons in the window (made out of CaF_2 which has a Lorentz factor $\gamma = 1.4$), delta electrons, electronic noise. Fig. 3.2 shows an event where two rings are clearly identified in the bottom right corner.

The ring recognition is performed for the complete 96x96 pad plane (thus including also unphysical regions, not covered by the real detector) by one IPU per sector. Each IPU consists out of 2 6U-VME boards: one Pattern Reconstruction Card (PRC) which reconstructs the hit pattern on the pad plane, one Ring Recognition Unit (RRU) which performs the ring recognition algorithm. The position information of the fired pads are stored in three buffer FIFOs where each contains 32 columns of the pad plane. The data is then transferred into two SRAM which reconstruct the hit pattern. From the second port of the SRAM, the data are transferred to the RRU which performs the algorithm, which is implemented in 12 FPGAs each containing 8 dedicated ring recognition units for one column of the pad plane. The results are then collected on the PRC and transferred to the Matching Unit via a 20 MByte/s bus.

The IPU ring recognition is based exclusively on the hit pattern information which is transferred for all the pads from the Readout Controller to the IPU: no information about the amplitude of the signal is used, pedestals corrections are applied before the transfer happens.

Each pad is treated as a potential ring center, and for center candidates
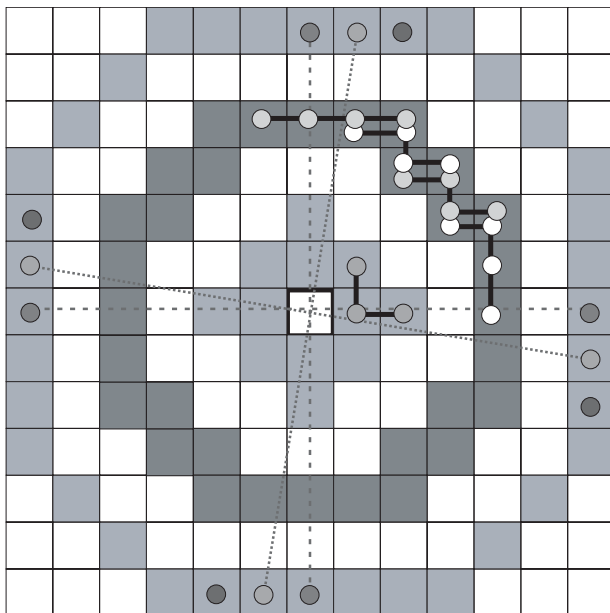
Figure 3.3: *Ring recognition searching mask. The ring region and the inner/outer veto regions are shown. Pads are not summed individually but grouped in order to save hardware resources.*

two regions contained in the 13x13 search mask shown in Figure 3.2.1 are evaluated: a ring region, corresponding to the purely geometrical mask of ring and a veto region, consisting of an inner and an outer circumference of respectively 4 and 12 pad units diameter. In between the ring and the veto region there is always a separation area of 1 pad unit thickness which is not evaluated. Neighboring or separate pads in these regions are grouped together and a logical OR is applied to the groups, such that when at least one pad in the group is fired, the group is considered valid. This has been proven to save logic resources in the hardware implementation, without efficiency loss. The groups in the ring region overlap, such that a fired pad validates two groups: in this way a double weight is assigned to pads in the ring region with respect to the ones in the veto, and therefore accounts for the high background. The overlap of groups in the ring region also increases the weight of single photons (pads) statistically distributed over the full ring circumference compared to clusters of pads which might come from cross talk of the same photon response [122]. Figure 3.4 shows some of the several
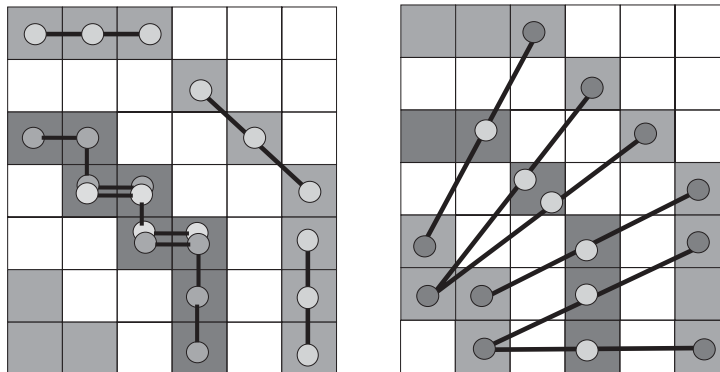
Figure 3.4: *Different variations in the pad grouping: neighboring or separated pads are connected in order to increase their weight in different ways [122].*

variation which have been tested in order to optimize the pads grouping for the performance of the algorithm. After all the groups of both regions are evaluated and summed up, two thresholds are independently applied on the sum of the ring and the sum of the veto region in order to determine a ring candidate. Thresholds can be set independently or combining the ring and the veto region, in different sectors or even in different areas of a sector, in order to account for a reduced photon statistics at low polar angle or a reduced photon acceptance at the border of the sector.

Since usually several neighboring pads fulfill the thresholds conditions, the best among neighboring candidates is selected with a local maximum search

on the 4 or 8 neighboring pads which uses the sum of the ring region as quality parameter, in order to prevent the IPU from reconstructing more than one ring corresponding to only one real lepton as a result of the ring smearing and the cross-talk. The resulting position in pad units of the ring centers is then sent sectorwise to the MU. The ring recognition is performed in parallel for all the columns, for the rows at 12 MHz requiring a fixed time of 10 μsec; together with the time required for the data transfer from the Readout Controller and to the MU (including the proper formatting for this last one), this results in a latency of the RICH IPU of 30-40 μsec, depending on the data (pattern, hits) load.

Different variations of the algorithm have been tested in order to optimize the performance of the algorithm, concerning the grouping of the pads, the thresholds cut and the local maximum condition. Performance of the different variations will be shown later (see Chapter 8).

3.2.2 The Tof IPU

The TOF Image Processing Unit [124] searches for lepton signatures as particles which reach the TOF Wall (45°-85°) with a given velocity. It has already been mentioned how the electron discrimination is possible in this polar angle range with the achieved time resolution. For each scintillator bar, the TOF IPU receives two signals from the TDC and two signals from the ADC. A number of operation has then to be performed in order to deliver to the MU angular information about lepton signatures:

- convert the TDC channel into a time: τ_{left} and τ_{right}

- calculate the Time-of-flight according to the formula 2.11

- apply the walk correction with the ADC values

- calculate the longitudinal coordinate of the hit position according to the formula 2.12

- calculate the polar and the azimuthal angle of the hit thanks to a look-up table

- apply a time of flight cut, which takes into account the start time which does not directly enter the trigger

All the hits (not only the ones selected as lepton signatures) are then sent to the MU sectorwise, with the full information of position in cartesian and angular coordinates, the time of flight and a flag set for the lepton signatures.

Since the complexity of this algorithm is high (higher for instance than the RICH IPU or SHOWER IPU ones), although the number of data to be processed is smaller, the algorithm, as well as the readout, is implemented on Digital Signal Processors (DSPs), able to operate with floating points, in a pipelined architecture. Data from ADCs and TDCs are transferred via a VME bridge on the VME bus by a chained block transfer. Data are then transferred to one DSP which performs part of the algorithm. After that it will transfer the event to the next DSP, and so on. One TOF IPU analyzes two sectors in parallel.

3.2.3 The Shower IPU

The SHOWER Image Processing Unit [125] searches for lepton signatures as development of electromagnetic showers in the Pre-Shower detector (polar range: $15° − 45°$), where the fast pions abundance compromises the lepton-pion discrimination which extends only up to 0.5 GeV/c with the time of flight. It has already been mentioned that, thanks to the Self Quenching Streamer Mode operation of the MWPC, the charge collected by these last ones depends only upon the number of charged particles traversing the chamber.
The IPU identifies, via a local maximum search on the 4 neighboring pads, the impact position of a particle on the first layer

$$Q_{Pad}^{L1}(m,n) > Q_{Pad}^{L1}(i,j) \tag{3.1}$$
$$with$$
$$(i,j) = (m, n-1), (m+1, n)$$

$$Q_{Pad}^{L1}(m,n) \geq Q_{Pad}^{L1}(i,j) \tag{3.2}$$
$$with$$
$$(i,j) = (m-1, n), (m, n+1)$$

Then the charge collected in the 8 neighboring pads, which corresponds to the area scanned by a circle with the Moliere radius, therefore the area where the cascade might have developed is sum up. Since there is a direct correspondence of pads in the three chambers, the sum of collected charge on the first layer Q_S^{L1} is then compared with the sum on the second Q_S^{L2} and the

third one Q_S^{L3} to search for an increase.

$$Q_S^{L2orL3} > Q_S^{L1} + Q^{Thres} \tag{3.3}$$

$$with$$

$$Q_S^{Lx}(m,n) = \sum_{i=m-1}^{m+1} \sum_{j=n-1}^{n+1} Q_{Pad}^{Lx}(i,j)$$

Figure 3.5 shows a schematic view of the shower principle.
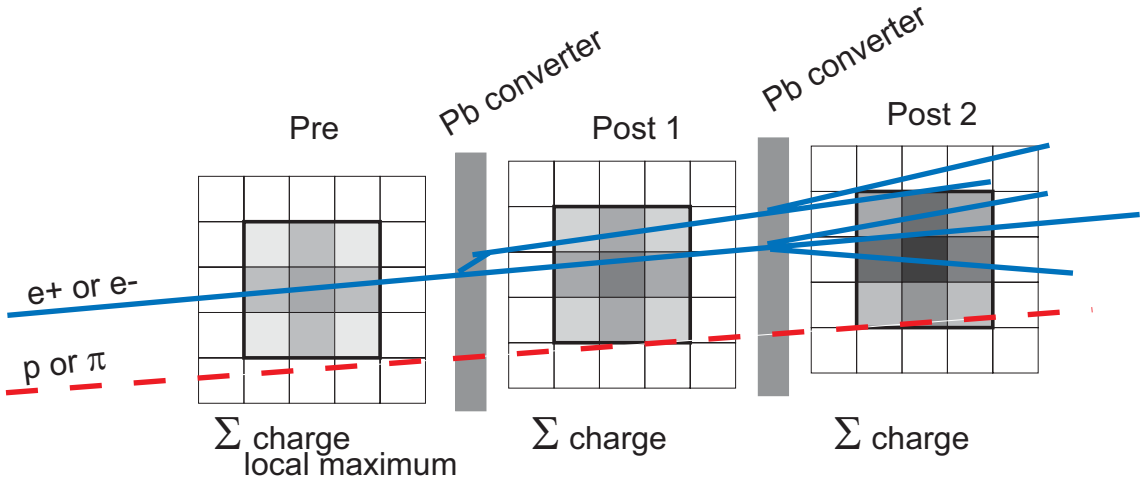
Figure 3.5: *Schematic description of the Shower algorithm. Electrons and positrons by bremsstrahlung emit photons which convert into e^+e^- originating a cascade of particles. Protons and pions do not.*

The position of the shower center in pad units is then sent sectorwise to the MU. One SHOWER IPU, which also performs the readout of the system which requires additional operations such as pedestal correction, zero suppression and data storage, analyzes half a sector. The realization of the board is similar to that of the RICH IPU. Data are processed in parallel by FPGAs, where the algorithm is implemented in a pipelined fashion, row by row.

3.2.4 The Matching Unit

The Matching Unit [126] is the responsible of the LVL2 final decision. Figure 3.6 shows the basic principle of the Matching Unit functionality.
In a first step it reads the information about lepton signatures from the inner and outer IPUs and combines them sectorwise. The RICH IPU and the
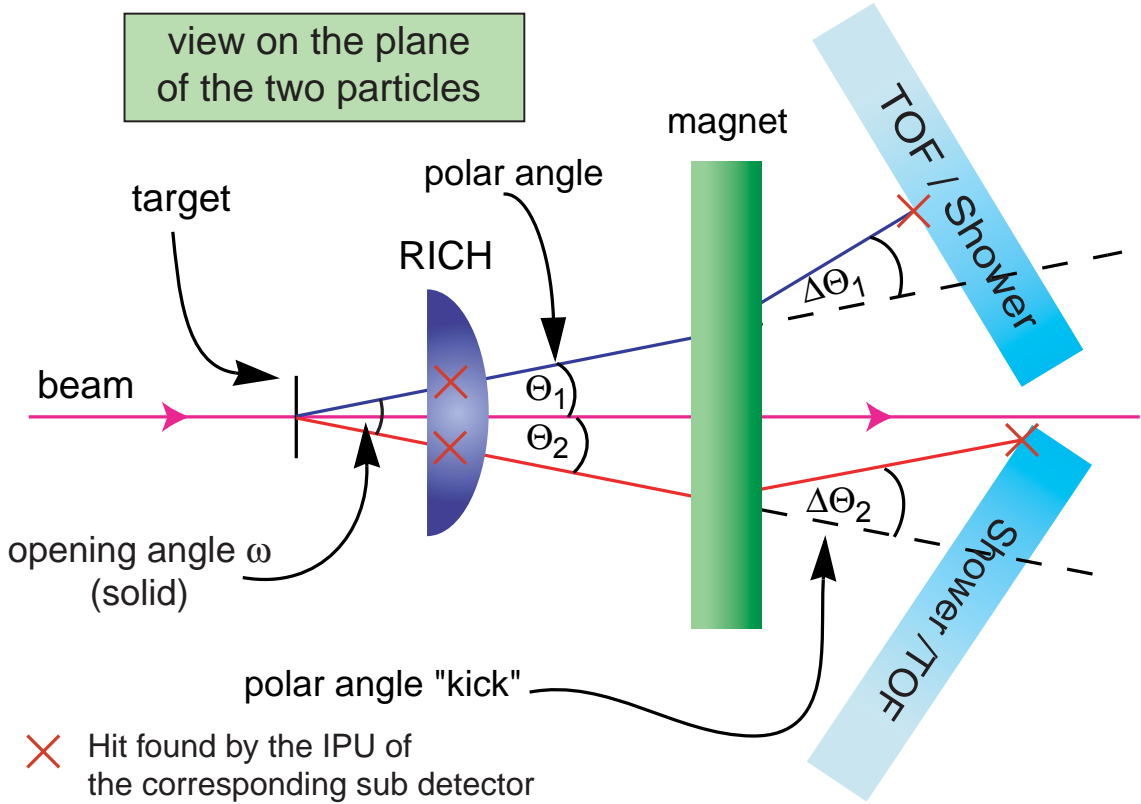
Figure 3.6: *The basic principle of the Matching Unit algorithm. Signatures from different IPUs are matched in azimuthal direction to find a lepton candidate, momentum is calculated from the deflection in polar direction.*

SHOWER IPU deliver the position information in detector specific units, and therefore have to be mapped by the MU into LAB angle coordinates via look-up tables. To identify a lepton candidate trajectory, the MU combines angular information of the RICH IPU signature with the one of the TOF IPU or the SHOWER IPU for the same sector; the window in polar angle has to account for the momentum dependent deflection in magnetic field, whereas the azimuthal window can be smaller in order to provide an event reduction, but has to be larger at the border of the sector to account for the second order deflection in azimuthal angle due to the inhomogeneity of the magnetic field, as well as for alignment problems.

In the C+C experiments analyzed in the framework of the present thesis, where the attention was on the low invariant mass range (π^0 Dalitz and η Dalitz) several azimuthal windows have been tested, while a polar window

has never been applied to avoid any cut on the momentum of the particles. Once a trajectory has been identified as a match between a hit in RICH and a hit in META (TOF or SHOWER), its momentum can be determined as a function of the position before the deflection and the polar deflection itself via a look-up table with the same granularity for the different detectors.

Thanks to a kickplane approach (fully described in Section 4.7.1), it is possible to calculate the direction of the particle before and after the deflection of the magnetic field while only two points are measured (one by the hit in RICH, one by the hit in META), and therefore calculate the momentum of the particle. All this information can be parameterized in a look-up table which provides the momentum of the particle in a range from 50 MeV/c to 1 GeV/c as a function of position and polar deflection. Moreover the sign of the polar deflection determines the charge of the lepton candidate.

In a second step, used for the full dilepton trigger, implemented and tested but not yet performed in real experiments, the MU combines opposite charge lepton candidates, calculates their opening angle and their invariant mass, according to the formula (fully equivalent to 6.2)

$$m_0^2 = \frac{4p_1 p_2 \left(\sin \frac{\omega}{2}\right)^2}{c^2} \tag{3.4}$$

where ω is the opening angle of the $e^+ e^-$ pair, and can then select pairs within a given invariant mass range.

Data from the IPUs are transferred to the MU via a standardized protocol. A CPLD receives the data , multiplexes it, and sends it to a dedicated DSP, which serves as scheduler, to collect data, check for consistency and build events, which are sent to other DSPs which perform the matching algorithm, and write the results to a FIFO which is then read out by the local VME-CPU. Via the VME backplane, the LVL2 decision is finally sent to the CTU.

3.3 The Third Level Trigger

The third level trigger is meant to correlate the LVL2 decision with the hit pattern of the MDCs. The hit positions in RICH, TOF and Pre-Shower of the trajectory reconstructed by the MU define regions of interests in the MDC planes, which are determined assuming an abrupt deflection of the trajectory due to magnetic field in a kick plane located in correspondence of the magnet: hits or clusters are searched in these regions. This would allow to discard lepton candidates arising from the match of a misidentified ring with a META hit coming from a different track, or those lepton candidates, typically with very low momentum which, after producing a ring in the RICH
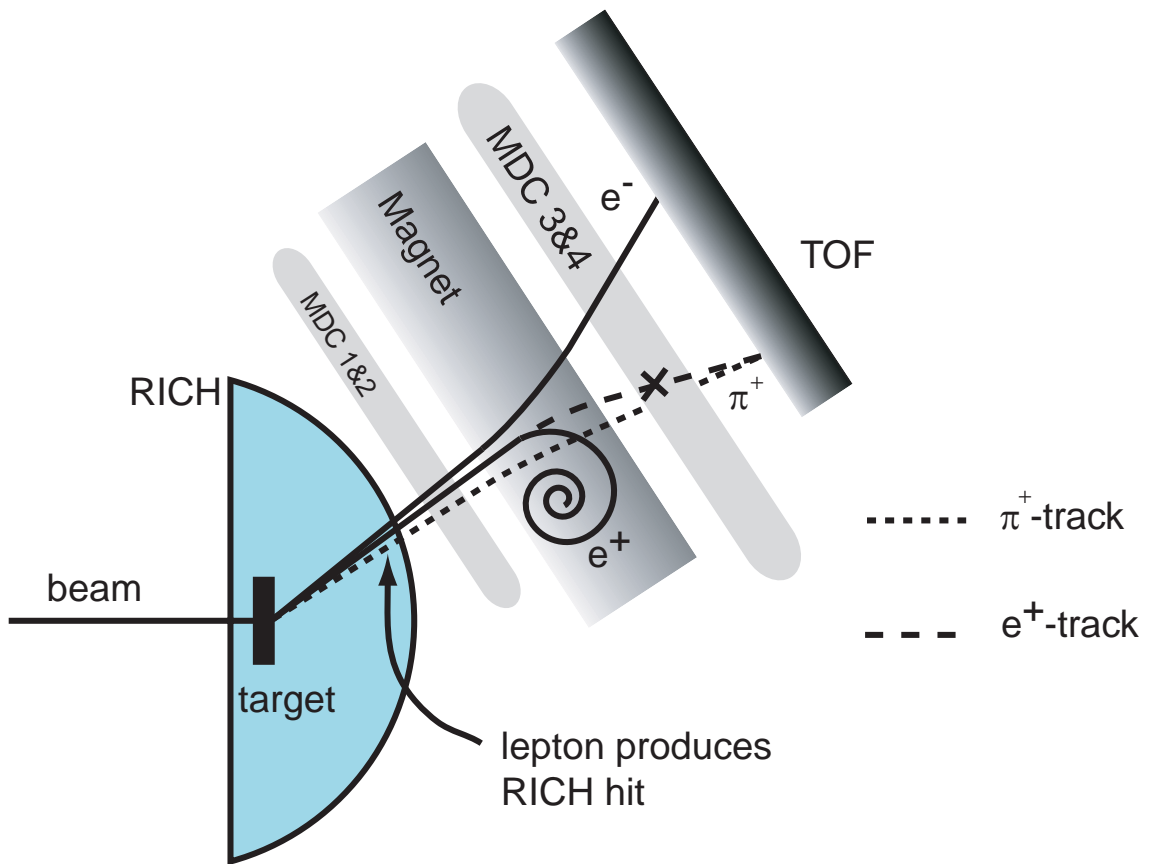
Figure 3.7: *The basic principle of the third level trigger. A lepton with low momentum, coming for instance from a γ conversion, is bended in the magnetic field, but can still be matched by a fast pion in coincidence. A match with MDC hit pattern information reduces these background events.*

and a tracklet in the first two MDCs are bended away by the magnetic field, but are still matched by a hit in META produced by another track.
With a C+C reaction the first part of such a trigger implemented offline (i.e. the matching with hit pattern in MDC1 or MDC2) reduces the LVL2 events by a factor 5.

3.4   The Trigger Distribution

The trigger decisions (LVL1, LVL2) are distributed to the different detectors by a trigger bus which brings the signal coming from a Central Trigger

Unit (CTU) to the Detector Trigger Units (DTUs) corresponding to the different detectors, which convert it into detector specific signals in order to interface the readout electronics of the different detectors.

The CTU distributes the LVL1 trigger from its source to the single detector systems which have to start their readout, and the LVL2 trigger from the MU. Different possible sources of LVL1 trigger are the MTU which gives information about the multiplicity of the event, or the Halo detector, or a coincidence multiplicity modules which would allow to trigger on charged particles detected in opposite sectors, in order to enhance the pp elastic signal with a coplanarity condition.

A unique trigger tag is attributed to each event, together with the trigger decision, a unique eventID, the event type, and error conditions in case of a LVL2 trigger [124].

Part II

THE RECONSTRUCTION SOFTWARE FOR DILEPTON ANALYSIS

In this part of the thesis the Software used for the HADES dilepton analysis is presented. Methods used for single subdetectors calibration and analysis, as well as for the full event reconstruction is explained. The software, explicitly developed in the framework of the present thesis, for the lepton and dilepton analysis is described.

In Chapter 4 the HADES software package (HYDRA) for reconstruction, simulation and analysis is presented. It provides the fundamental methods for data organization, streaming, histogramming. HYDRA is a modular structure whose basic unit is the *event*. It provides a set of base classes to store data, to define and perform reconstruction tasks, to organize parameters and detector structure.
This is realized in the different libraries HYDRA is comprised of, where Unpackers, Calibrators and different Hit Finder algorithms (ring recognition, tracking, time of flight calculation,...) fill the categories corresponding to the different subdetectors. Methods for Vertex reconstruction and Momentum determination are shortly described.

Chapter 5 and Chapter 6 present an analysis which was fully developed in the framework of the present thesis.
The analysis was performed for C+C reactions at 1 and 2 AGeV. Experimental data were collected during beamtime of November 2001 and November 2002. Simulated data are analyzed as well. Methods used for lepton identification are presented in Chapter 5. RICH rings are correlated to reconstructed tracks. A time of flight cut is applied. Cuts on RICH quality parameters are presented. In addition a condition on the Pre-Shower detector is used to reduce the pion contamination. Some important characteristics of the leptons are shown.

Chapter 6 presents the dilepton analysis for the experimental and simulated runs mentioned above. Leptons are combined into like and unlike sign pairs. Methods to reduce the combinatorial background by applying cuts on pairs are presented. Leptons which share the same ring or the same META hit are discarded. An opening angle cut is presented and motivated. Finally the combinatorial background is estimated and subtracted from the signal.

Chapter 4

The Event Reconstruction

ODE TO THE ATOM

Infinitesimal
star
you seemed
forever buried
in metal, hidden,
your diabolic fire.
One day
someone knocked
at your tiny
door:
it was man,
with one
explosion
he unchained you,
you saw the world?

(Pablo Neruda)

After the generation of a signal in the different detectors, several stages of acquisition and analysis, corresponding to different data levels, have been developed both in hardware and software, in order to organize the information content and structure the successive steps to get it. In this chapter general methods of the HADES analysis will be presented, necessary for the comprehension of the specific work developed in the framework of the present thesis.

4.1 The Software Overview

HYDRA (HADES sYstem for Data Reduction and Analysis) [127] is the HADES software package for reconstruction, simulation and analysis, an application written in C++, based on ROOT [128], an Object Oriented Data Analysis Framework, which provides the fundamental methods for data organization, streaming, histogramming.

HYDRA is a modular structure comprising independent libraries which can be dynamically linked, and whose basic unit is the *event*, either real or simulated. It provides a set of base classes which define the data source and data output, the detector structure, classes to manage parameters, classes to store different levels of data, classes to define and perform reconstruction tasks.

Parameters, with the proper run-dependent initialization, are stored and managed in an ORACLE database [129], including a version management, to refine and modify parameters, and a context management for different usage of the same parameter. Classes which store data are the so-called *Categories*, containers of objects within the same event, with the proper setting and retrieving methods.

Reconstruction and calibration are managed by so-called Reconstructors, which comprise initialization and finalization functions, executed at the beginning and at the end of the data processing, and an execute function, executed each event.

4.1.1 Experimental Data

The reconstruction of experimental data starts after an event, consisting of all the different sub-event, has been built and written out to mass storage in binary format. The event is first decoded by the so-called *Unpackers* and then simply stored in the first level of reconstruction, the Raw data level, which still contains all the hardware related information, structured into the HYDRA classes scheme.

The Cal data level is reached with the use of the so-called *Calibrators*, consisting of one or more calibration steps, where the hardware information is translated into physical values.

The Hit data level is filled via analysis procedures, generally called *Hit finder*, which have different meaning for each detectors, but finally correspond to the information of the impact of a particle on a given detector. Successive analysis steps will no longer refine or modify the data content, but simply extract and derive additional physical information, such as the momentum determination, with the three methods used so far of the Kickplane, the Reference Trajectories and the Spline Fitting, and finally the Particle Identification.

4.1.2 Simulated Data

Simulated events are normally generated with Quantum Transport Models (BUU or UrQMD) or with thermal models (PLUTO), and provide information about the impact parameter of the reaction, and the Energy-Momentum of the generated particles with their identity (see Appendix A, B).

The events are then "tracked" in the HADES detector by HGeant, the HADES simulation package based on Geant 3.21 [130]. HGeant contains all the information concerning the technical structure and the geometry of the detectors, and the physical information of interaction cross section of a given particle with a given material.

The reconstruction of simulated data starts at this level where the information coming from HGeant is digitized by the so-called *Digitizers* to fill the Sim Cal data level, which is essentially corresponding to the Cal data level of experimental data, and contains in addition the information to retrieve the known primary source in a procedure known as "track-number propagation". From this stage on, data are treated exactly in the same way as experimental data to develop the further steps of analysis.

4.2 The Rich Reconstruction

The Rich Raw container (HRichRaw) contains the information of all the pads fired: their sector, their position in sector coordinate system (row and column), the amplitude of the deposited charge, directly translated from ADC channels. No pedestal subtraction is performed yet. Nevertheless, in the Front End Electronics a pedestal comparison is performed and, even if pedestal values are not subtracted, only pads which overcome their pedestal thresholds are reconstructed.

The calibration process consists in the calibration of the ADC gain the pedestal subtraction, so that the pads information is the same as in the Raw level, except for the amplitude which in the Cal container (HRichCal) is pedestal-subtracted.

The Hit level (HRichHit) is filled after the ring finder analysis [131] has been performed, and therefore contains information about the rings found: their sector, their position in sector coordinate system (row and column), and different quality parameters which refer to the ring finding algorithm used. The ring finder performed after a cleaning of single pads which cannot contribute to a ring to remove noise or isolated hits and a labeling of connected pads in order to save time and resources, consists of two algorithms: the Pattern

Matrix and the Hough Transformation.

Figure 4.1 shows the Pattern Matrix: it is a mask of 13x13 pads, normal-
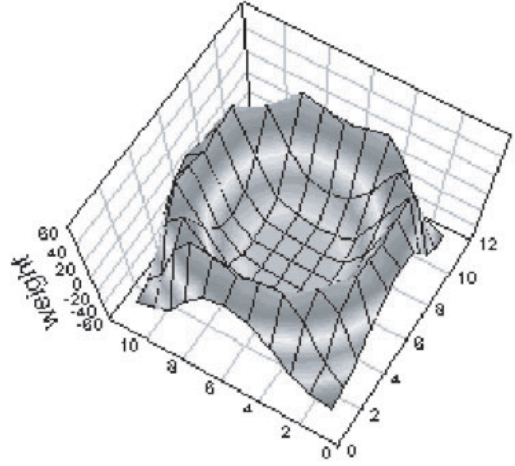
Figure 4.1: *The searching mask used by the Pattern Matrix algorithm. The important difference with respect to the Rich IPU mask is that in this one all the pads are evaluated, within a different weight.*

ized to 0, where every pad has assigned a weight depending on the position in the ring mask. The matrix is scanned over the full pad plane and pads are summed up depending upon the amplitude of deposited charge. Finally a threshold is applied and candidates are selected. In the Hough Transformation process, schematically shown in Figure 4.2, every combination of three pads is built to form a ring with the given fixed radius and the centers of the formed rings are cumulated in a two-dimensional local maxima. Candidates are then selected if their center overcome a given threshold.

The first, faster algorithm has limited accuracy in case of distorted or overlapped (closed pairs) rings, while the second, a kind of hough transformation, insensitive to shape distortions and independent of the ring radius has higher efficiency when the noise is not neglectable. The ring finder selects rings which fulfill both the algorithms, and on top of this additional tests are performed on the eccentricity and the asymmetry of the ring, on the distribution of pads in a so-called ring and veto region, on the density of pads, on the amplitude of the overall deposited charge.
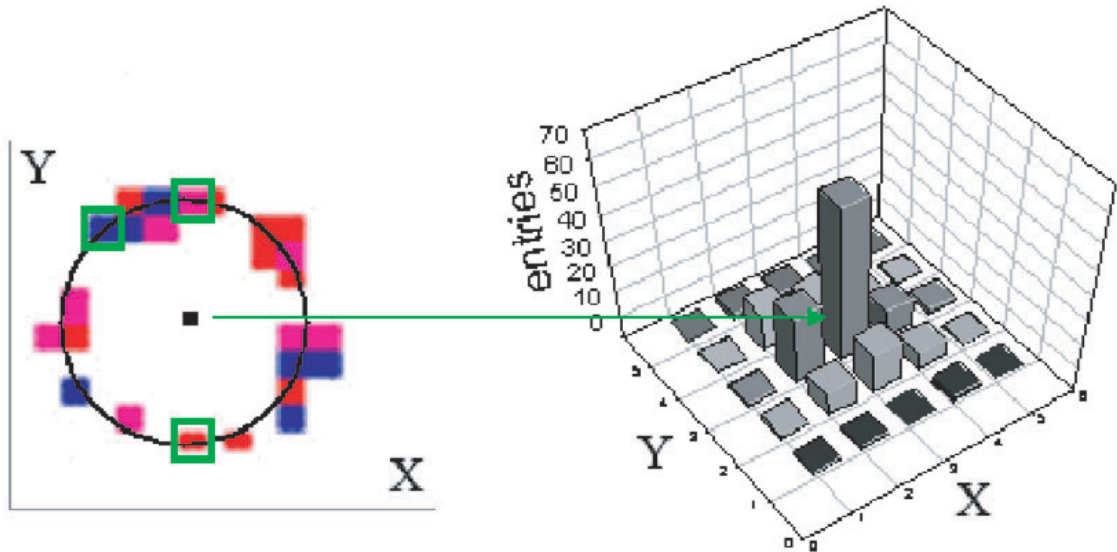
Figure 4.2: *Schematic view of the Hough Transformation algorithm. When three pads are found to lie on a ring with the required radius, the center of the ring is incremented. This algorithm is too slow to be implemented in hardware.*

4.2.1 The Rich Digitizer

t to mention and shortly describe the RICH digitizer [102], since it turns out to be important also for the Rich IPU analysis when tested on simulated data. In a so called *Online Efficiency Measurement* (OEM) the response of the detector to a single photon hit is studied. Figure 4.3 (a) shows the set-up for such an experiment.

A Carbon beam of 600 or 800 AMeV is deflected to hit, instead of the target, the cylindric solid radiators (SiO_2 and MgF_2) which surround the beam pipe. These produce rings at θ around $50°$ and $70°$ (so called superrings, shown in Figure 4.3 (b)) which a relatively low occupancy, such that the single photon hit can be identified.

Since the overall photon yield is well known $N_{photons} = N_0 \cdot Z^2$, the figure of merit can be estimated. Moreover, once the hit of a single photon is identified among the different types of hit which include cluster of more photons and photons coming from feedback effects, the response of the central pad (where the photon has reached the detector) and the neighboring pads (which are also reached by the electron avalanche) can be parameterized and modeled with an heuristic method implemented in the digitizer.
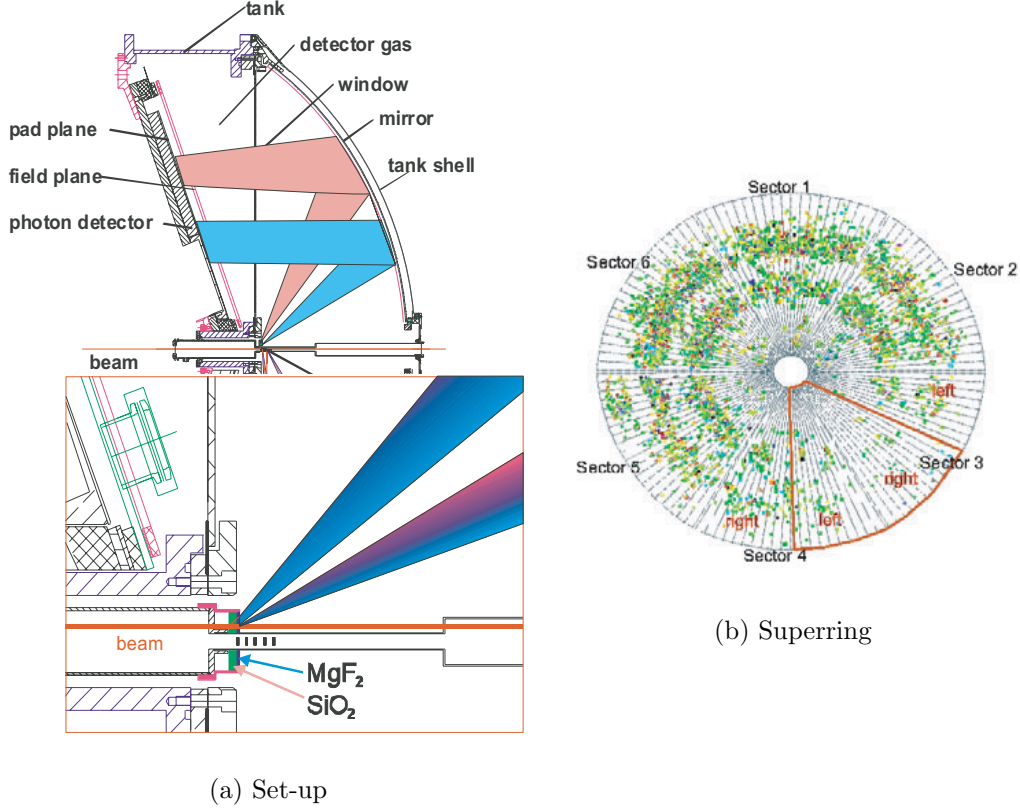
(a) Set-up

(b) Superring

Figure 4.3: *(a) OEM set-up. The two solid radiator SiO_2 and MgF_2 are places around the beam pipe and the beam is deviated to hit them. (b) 50 OEM events accumulated: the superrings structures at $\theta = 50°$ and $\theta = 70°$ as well as the shadow of the beampipe (lower right sector) are visible.*

Electronic noise is also included, assuming that it is properly described by a Gauss distribution, for those pads whose charge is above the 3σ cut applied in the electronic in the calibration runs. To get a good agreement between simulated and experimental data, where the noise might changed during the data taking, the Gauss distribution is allowed to become broader than what has been measured in the pedestal runs.

4.3   The Tof(ino) Reconstruction

The Tof Raw container (HTofRaw) contains the hardware information from the TDCs and the ADCs; in a first step this information is calibrated

to fill the Cal container (HTofCal) exactly as it is done in the MDC with a linear function which is proper of the internal structure of the digital converters. The Hit level (HTofHit) is then filled with time information calculated from equation (2.11), subtracted of the start time coming from the calibration of the Start container (HStartHit), position information calculated from equation (2.12), and angular information derived from a look-up table. Path correction using the amplitude information is also applied.

It can happen that slow particles strongly bent by the magnetic field hit several consecutive scintillator rods, leading to a significant combinatorial background when combining them with tracks. These hits are characterized, apart from being in consecutive rods, by a similar x position in the rod and a similar time of flight. These hits are removed (not from the container but from the possible combinations) by a cluster finder algorithm [133].

Tofino is read-out only from one side and the time of flight can therefore not be calculated as for Tof; only the Cal level (HTofinoCal) can be filled, calibrating the TDC information and subtracting the start time. The granularity of Tofino is also significantly low; when two or more particles hit the same scintillator rod, only the time of the first one arrived is properly calculated and interference effects strongly influence the time of flight of the others.

4.4   The Pre-Shower Reconstruction

The Raw data level (HShowerRaw) of the Shower [134] contains values of measured charge on pads in ADC channels and position of fired pads in detector coordinate system (rows and columns) of given detector module (pre, post1- or post2). Raw data are transformed with a calibrator to Cal level (HShowerCal). Values of measured charge in ADC channels are recalculated to values of generated charge in pC via a slope and an offset, unique for each pad and determined when the detector is operated in a calibration mode.

In the next step of analysis, which fills the Hit data level (HShowerHit), local maxima are searched in the 8 neighboring pads for each detector module. The position of the found maxima is then stored in detector and lab coordinates (spheric and cartesian), together with some additional associated variables like the value of charge in local max, 3 sums and variances of charge distribution around the local maximum (the sum of the 9 pads, as well as the sum of the 25 pads normalized to 9) in the 3 modules and cluster size (number of fired pads above thresholds around the local maximum).

Since Tofino is mounted to the Shower detector, a further correlation between Shower and Tofino hits is made and fills an additional data container (HShowerHitTof): it basically consists of a full copy of the Shower hit container with

the additional Tofino information (time of flight, drift time, deposited charge and of course position).

4.5   The Mdc Reconstruction

The Mdc Raw container (HMdcRaw) contains the hardware information from the TDC; this is calibrated in a first step to fill the first calibrated container (HMdcCal1), simply translating TDC values in drift time with a linear function, where the gain (slope) is determined from the internal calibration procedure of the TDC, and the offset corresponds to the time of the fastest particle traversing the cell close to the wire.
A second calibration [132] procedure fills the second calibrated container (HMdcCal2): the distance from the impact point to the wire is calculated from the drift time and the drift velocity, taken as constant in first approximation, in a second step recalculated taking into account the angle of the incoming particle and the distance from the sense wire.
The Hit level (HMdcHit) is filled by the tracking process [104]. Two tracking procedure have been developed for HADES: the so-called Dubna and Santiago tracking.
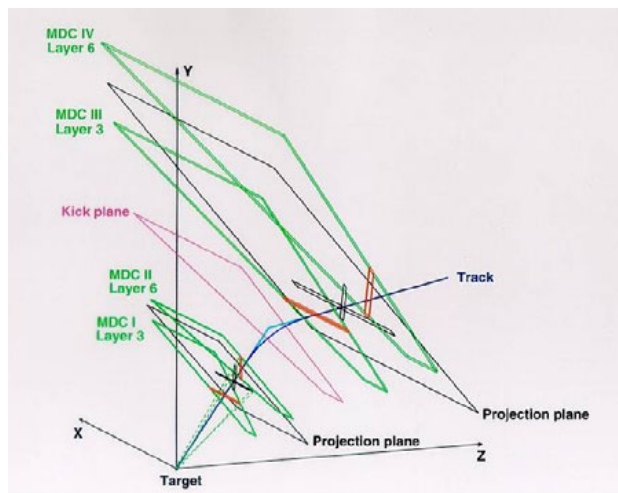
Figure 4.4: *Geometrical representation of the projection planes used by the Dubna tracking.*

The Dubna tracking determines the cluster of fired cells of one or two neighboring modules in a projection plane, shown in Figure 4.4 determined
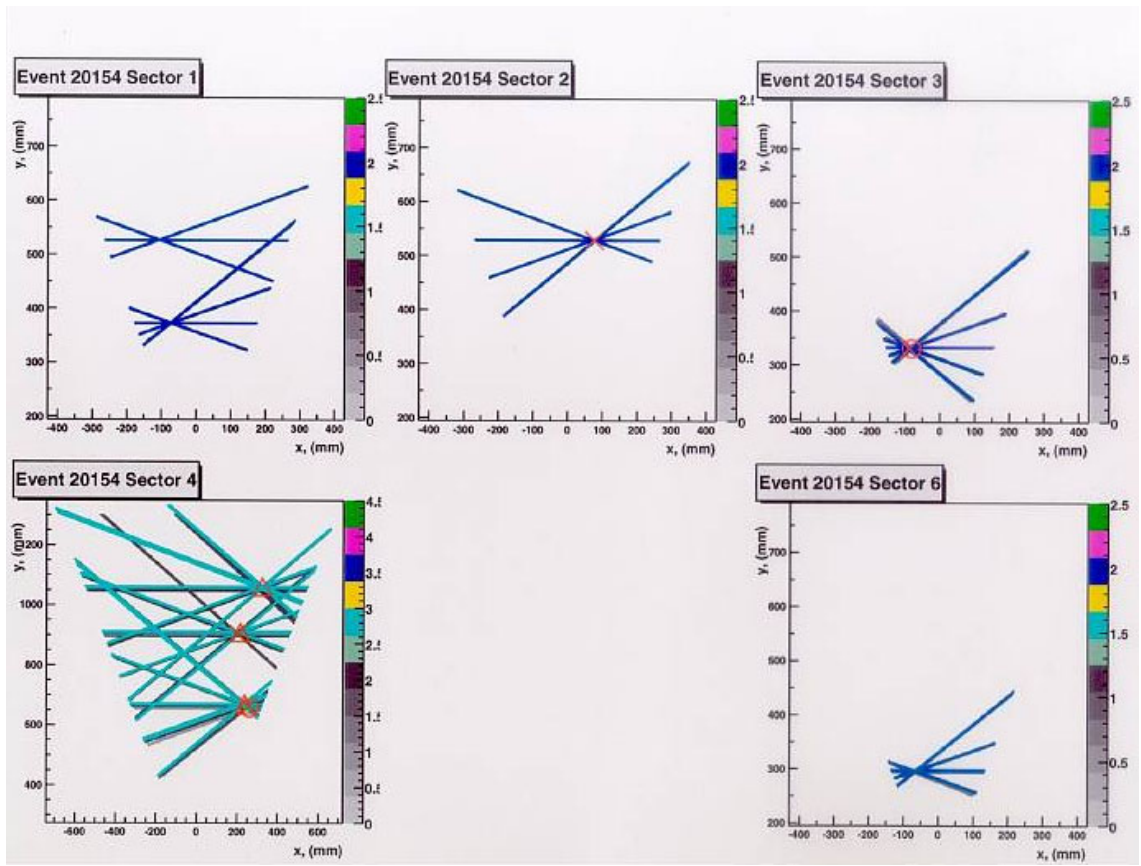
Figure 4.5: *Event display of MDCs. The different wires are visible in the picture.*

by the target for the two inner modules, by the kickplane for the two outer ones. Finally the hit is determined from the minimization of a complex functional

$$\mathcal{L} = \sum_i (t_i - f_i(x_V, y_V, z_V, x_P, y_P, v_p))^2 * w_i \qquad (4.1)$$

which depends on the drift time measured by the TDC (t_i), the vertex co-ordinates (x_V, y_V, z_V) and the track coordinates (x_P, y_P) in the projection plane, and the velocity of the particle (v_p). In a fitting procedure a χ^2 is calculated; tracks which cannot be fitted (typically tracks which do not have a vertex in the target or close pairs) are store with negative χ^2.

The Santiago tracking uses as input the distance of the track from the wire, converted into an impact coordinate. As Figure 4.6 shows, impact coordinates in different layers are combined while an area is scanned around each
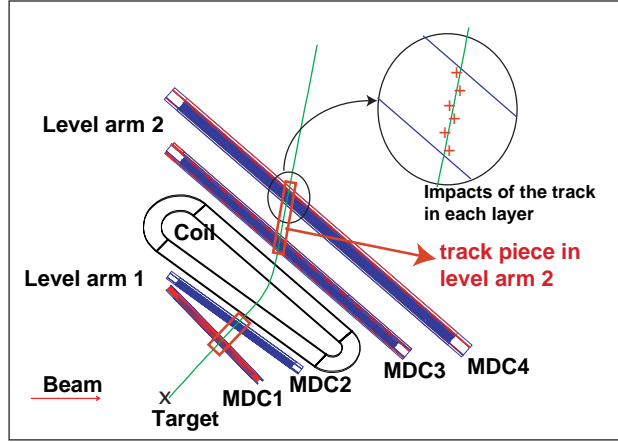
Figure 4.6: *Schematic representation of the Santiago tracking.*

crossing point and a χ^2 is calculated. A minimum χ^2 is required for a hit, and the best among neighboring candidates which share impacts is selected based on the χ^2. Impossible combinations are discarded, and a test is performed for the inner MDC to point to the target area. The algorithm works iteratively and for any number of layers. A fitting procedure is applied, providing a slope correction, until the iterative approximation converges. From two hits in successive modules, before or after the magnetic field, a segment is built (HMdcSeg) as the best approximation of a straight line.

4.6 The Vertex Reconstruction

For the complete understanding of the event, especially in typical HADES scenarios where thin segmented targets[1] are used in order to minimize reabsorption and scattering of leptons in the target, while keeping a reasonable interaction rate, a fundamental information is the point of the space where the collision between projectile and target nuclei happened.
This information, necessary to know if the interaction has happened in a physical target and therefore suppress or estimate secondary vertices, as well as for constrains in the tracks fitting, or even very helpful for alignment purposes, is derived in a procedure of vertex reconstruction, where *vertex* is exactly meant as the geometrical point where the interaction took place.
The approach to reconstruct the vertex, assuming a point-like interaction zone, consists in minimizing the 3D distance of tracks to a given point, the

---

[1]even of different materials to perform several experiments in parallel

point of closest approach to all primary tracks in the event, with a Least Squares Method. All the N straight lines reconstructed by the inner MDCs[2] are represented in the form

$$\vec{x_i} = \vec{r_i} + \hat{a_i}t, \text{ for i=1...N} \tag{4.2}$$

The distance of this line to a vertex point in space $\vec{r_V}$ is given by

$$d_i = \mid (\vec{r_i} - \vec{r_V}) \times \hat{a_i} \mid \tag{4.3}$$

Summing up to all the lines and normalizing by the error

$$Q^2 = \sum_{i=0}^{N} \frac{d_i^2}{\sigma_i^2} = \sum_{i=0}^{N} \frac{\mid (\vec{r_i} - \vec{r_V}) \times \hat{a_i} \mid^2}{\sigma_i^2} \tag{4.4}$$

The vertex is now reconstructed as the vector $\vec{r_V}$ which minimize Q^2. Corrections to account for the dependency of σ_i on the vertex itself are introduced. Outliers are treated introducing Tukey's bi-squared weights into the standard Least Squares Method [127].

4.7 The Momentum Reconstruction

Different methods have been developed for the momentum reconstruction, which reflect the historical development of the hardware installation and the different needs of the detector in different configurations. To measure the momentum of a track, its deflection due to the magnetic field has to be measured, therefore a direction (i.e. at least two points) before and after the magnetic field have to be determined.

The magnetic field is provided by the superconducting toroidal magnet ILSE, placed in between the two inner and the two outer MDCs. The generated field bends the tracks, in first approximation, only in polar direction. However the inhomogeneity of the field causes a non-neglectable deflection in azimuthal direction as well. The direction before the field is therefore provided by MDC1 and MDC2, while the direction after the field can be provided by MDC3, MDC4 and META.

4.7.1 The Kickplane

When the inner chambers MDC1 and MDC2 are installed, but not the outer MDC3 and MDC4, only the information from META (i.e. only a point

---

[2]and even outer MDCs in case the magnetic field is off

in the space) is available and a kickplane approach has to be used [127].

The kickplane approach is based on the assumption that the deflection can be approximated with an abrupt change of the trajectories on a given surface (the so called *kickplane*) and that the momentum kick suffered by the particle does not depend on the initial momentum of the particle itself, but just on its path integral in the magnetic field. Once the kickplane is parameterized and the cross point of the particle with it is determined, the momentum[3] is then calculated as a function of the momentum kick P_T and the kick angle θ

$$P = \frac{P_T}{2sin(\theta/2)} \tag{4.5}$$

Figure 4.7 shows the concept of this approach. The resolution of this method
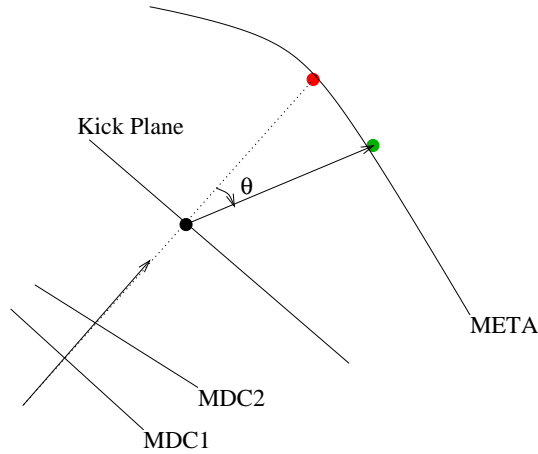
Figure 4.7: *Schematic view of the kickplane approach: a particle in the magnetic field is abruptly deflected on a hyper-surface, namely the kickplane, by a kick which depends only upon its path integral in the magnetic field.*

is entirely dominated by the polar resolution of META, a few centimeter (3-4.5 cm), leading to a $\frac{\Delta P}{P} \approx 10\%$. The main problem which arises from the lack of the outer tracking detectors is anyway the difficulties of resolving the combinatorial within several hits in META, since each combination of a hit in the kickplane and a hit in META is considered a track candidate. A filter is then applied by calculating the x coordinate for any track in Tof or Shower based on the calculated momentum and P_{T_ϕ} and comparing with the

---

[3]Since deflection occurs both in polar and azimuthal direction, both the polar and the azimuthal kicks $P_{T_\xi} = 2P * sin(\xi/2)$ $P_{T_\phi} = 2P * sin(\phi/2)$ have to be determined with simulations for each point in the kickplane.

measured one $x_{measured}$ with its resolution σ_x

$$x_{PULL} = \frac{x_{calculated} - x_{measured}}{\sigma_x} \tag{4.6}$$

after having filtered out all the unique combinations. Of course this method can be extended in case of MDC3 installed, where the hit point of META is substituted with better resolution by a hit point in MDC3.

4.7.2 The Reference Trajectories

This method [127] consists in reconstructing the momentum of a track with a Least Squares Method which uses as track model a complete parameterization with a 5-component vector $\vec{p} = (1/p, \rho, z, \theta, \phi)$. $1/p$ is the inverse of the momentum, used instead of the momentum since the statistical errors are randomly distributed over the track deflection, which is proportional to the inverse momentum, ρ is the distance of closest approach between the track and the beam axis, z is the coordinate of the closest approach, θ the polar angle and ϕ the azimuthal angle with respect to the z axis. Being $\vec{x_m}$ the 8-components vector of the (x, y) measurements in the 4 MDCs, there is a function $F : P \rightarrow X$ which maps the space of the track P into the space of the measurement X, such that $\vec{x} = F(\vec{p})$. Now if $\vec{x_m}$ is measured with its statistical error $\vec{x_m} = x_0 \pm \sigma_x$, being W the error covariance matrix, the best estimation for $\vec{p}$ is obtained with the minimization of the functional

$$Q^2 = (F(p) - x_m)^T W (F(p) - x_m). \tag{4.7}$$

Being F non-linear, it is linearized with a first order approximation of a Taylor expansion around any given point $\vec{p_0}$, and for all those point F is tabulated, such that in 1 or 2 iterations the minimization algorithm converges. The grid for the evaluation of F is chosen according to the HADES acceptance and the requirements of 1% momentum resolution.

4.7.3 The Spline Fit

To determine the momentum of a particle when one or two MDCs are installed after the magnetic field, the cubic spline fit algorithm [135] has been implemented; this method in general is not faster than the reference trajectories method, however it is more accurate in cases when the planes where the trajectories lay are not always the same or not parallel.
The input data are the hit coordinates of all the available MDCs on which a cubic[4] spline interpolation is performed to calculate (dy/dz) and finally to

---

[4]The assumption of a cubic order polynomial results in some systematical error on θ and ϕ ad therefore momentum, eliminated with correction parameters

determine equally distance points in the field region.

Since the tracks are mainly bent in polar direction, i.e. in the (XZ) plane, in a first stage the coordinates are rotated such that in the new coordinate the z direction coincide with the direction of the track, and the (dx/dz) is neglectable. A cubic spline is then assumed for the track's second derivative and its double integral is expected to be a good representation of the track. The momentum derives from the minimization of this function.

4.8 The Particle Identification

The Particle IDentification (PID) code [136] is used to identify hadrons (p, $\pi^{\pm}$, $K^{\pm}$, d) and leptons ($e^{\pm}$) with a probabilistic approach based on probability density function (pdf) for a given particle to belong to a given species. This is achieved by applying the Bayes theorem to a set of independent HADES observables and by using likelihood ratios to identify the reconstructed tracks. In a first step tracks identified by the kickplane are correlated with RICH rings by the HPidTrackFiller within a narrow angular window between the angle of the RICH and the angle of the MDC inner segment and track candidates (HPidTrackCandidate) are created independently of whether a ring is correlated or not (hadrons).

In a second step the HPidReconstructor calls several algorithms to compute the Bayesian probability of a track with observables $\vec{x} = (x_k)$ and momentum p to be of the particle type h, based on probability density function $f_k(x_k|p,h)$. The Likelihood is finally calculated assuming that the momentum is part of the hypothesis: the probability density is then a function of the measurable quantity x_k for the fixed hypothesis (p,h).

This results in a matrix for each track candidate where each algorithm returns the probability to be of each type of particle. The Bayes' theorem is then applied to take into account the relative abundance of different particle species and the probability that a track with observables $\vec{x}$ is of particle type h results normalized to 1. The Confidence Level (CL) is defined as

$$CL = 1 - 2 * \int_{-0}^{x_{obs}} pdf(x)dx \qquad (4.8)$$

and represents, assuming a pdf symmetric around the maximum, the probability for $pdf(x)$ to be closer to maximum than $pdf(x_{obs})$. A cut on CL ($CL < A$) gives a cut efficiency $Eff = A$.

This or any user-defined cut can be applied in the HPidParticleFiller to fill in HPidParticle with resulted decision on the particle ID and further physical

quantities. For the dilepton analysis a HPidDileptonFiller fills the HPid-Dilepton with the result of combined leptons. The algorithms currently used for hadron analysis analyze the β distribution as a function of the reconstructed momentum and energy loss distribution in the TOF detector also as a function of momentum.

The energy loss of a track in the TOF wall is given by

$$\epsilon = \frac{\Delta E}{L} \tag{4.9}$$

where L is the length of the track in the TOF wall and ΔE is the energy deposited in the TOF scintillator rod, proportional to the amplitude of the ADC signals

$$\Delta E \approx \frac{z^2}{\beta^2} \approx a_{hit} \approx \sqrt{a_R \cdot a_L} \tag{4.10}$$

The momentum of a particle of mass M is given by

$$p = M \cdot \beta \cdot \frac{1}{\sqrt{1 - \beta^2}} \tag{4.11}$$

Therefore measuring the momentum of a given track and its β, via the time of flight measurement and the path length, the particle can be identified by its mass.

4.9 The Trigger Software

For the trigger it is meaningless to speak about data levels, since the "analysis" is all done in the IPUs and the MU, and only a data level corresponding to the Hit goes to the data stream. Nevertheless software has been developed to check the proper functionality of the trigger hardware and optimize the algorithms and the performance with different conditions.

The MU subevent consist out of 4 subsubevents: one for each IPU, which contain rings found by the RichIPU, time of flight of particles detected by the TofIPU, local maxima determined by the ShowerIPU, one for the MU itself which contains leptons and dileptons. For each of the IPUs the analysis performed by the hardware is emulated in a dedicated task, taking the input data from the Raw categories of the respective detectors and compared at the level of the single hit. The MU lepton and dilepton emulation takes input from the IPUs containers (HMatchURich, HMatchUTof, HMatchUShower), performs the same algorithm as the hardware using the same look-up tables and fills a container (HMUEMULeptons) which can be directly compared to

the one coming from the hardware data stream (HMULeptons). The MU emulations can also run taking input from the IPUs emulations [5] and are therefore fully independent of the existence of the trigger electronic.

All these emulations can of course run as well with simulated data, where input are taken from the CalSim level of each detector; in this case the purpose is to estimate the performance of the trigger algorithms in terms of reduction and efficiency on the basis of a well known input.

---

[5]This is typically not the case when the purpose is to check the proper functionality of the hardware since, in order to minimize the error, each algorithm is emulated and tested separately.

Chapter 5

The Lepton Analysis

POINTLESS QUEST

A needle in the haystack
may be difficult to find.
Your chance of ever finding one
is small.
Especially with haystacks
of the ordinary kind
which don´t have any needles in
at all.

(Piet Hein - Grooks IV)

One of the main goals of the HADES detector is the investigation of dileptons produced in the decay of light vector mesons. A prerequisite for any deeper analysis of the dileptons or investigations on the LVL2 performance is a reliable identification of single leptons. In the present chapter the analysis steps and selection criteria are presented, which were used for the single lepton analysis of the HADES data collected in the November 2001 and 2002 beam times.

5.1   November 2001 data

In November 2001, the C+C reaction was measured with two different beam energies of 1 and 2 AGeV respectively, a beam intensity of $(1-2)\cdot 10^6$/s and a duty cycle of 9.5s / 5s, i.e. the extraction time for a spill is 9.5s. The Carbon target used was a cylinder with a diameter of 8 mm and a length of 5 mm, and a density of 2.15 g/cm^3: this leads to an interaction probability

of about 5%. The LVL1 condition which required an overall multiplicity in Tof and Tofino of at least 4 charged particles mainly selects non peripheral collisions corresponding to about 70% of the geometrical cross section. The detector set-up consisted of the Start, the Rich and the META detector completed, and 11 modules of MDC I-II (one MDC I was not operational). MDC III and IV were not installed.

In the runs with 2 AGeV, a magnetic field of 0.5 T (corresponding to a current of I=2497A), was used and a total of about 43.6 million events was analyzed.

Simulations were performed, with the event generator UrQMD 1.2 and Hgeant 3.13 and an overall amount of about 20M events were generated and analyzed. Typically in UrQMD there are 12 protons, 12 neutrons, 1 π^+, 1 π^-, 1 π^0, 0.02 η per event.

As it will be shown later, the main contribution of background di-leptons present in the HADES spectrometer arises from Dalitz decays of abundantly produced π^0 and external conversion of high energy photons in the target and in the RICH radiator gas. These pairs are characterized by small opening angles $(1 - 15°)$. The currently achieved resolution of RICH $(\sim 2 - 3°)$ and inner MDC $(\sim 0.5°)$ does not always allow to separate the Cherenkov rings and the tracks coming from such close pairs.

If not properly identified and rejected, such leptons increase the combinatorial background and screen the physics signal of interest. With the standard magnetic field of 0.5 T, used to optimize the momentum reconstruction, the low momentum partner of a close pairs is normally lost due to the strong deflection in the magnetic field. If such a pair is not resolved in the inner MDCs, only the high momentum lepton is properly identified and it thus increases the combinatorial background.

A dedicated experiment was therefore performed with a reduced magnetic field (0.07 T achieved with I =400A) and a reduced beam energy (1 AGeV): this set-up allows the reconstruction of non-resolved (pairs which form only one ring in RICH and one track in MDC) and semi-resolved (pairs with one ring in RICH but two tracks in MDC) close pairs, since even the low momentum lepton can reach the outer Pre-Shower or TOF detectors. An overall amount of approximately 8.5M events has been collected and analyzed.

5.1.1 Ring-Track Correlation

After all the detectors are properly calibrated and the hit level is reconstructed for all the detectors, the momentum is calculated with the kickplane method (the event reconstruction is described in Chapter 4). The reconstructed tracks, shown in Figure 5.1, are dominated by hadrons: protons and

pions. The black curves drawn in the figure correspond to the formula

$$p = m \cdot \beta \cdot \frac{1}{\sqrt{1 - \beta^2}}; \tag{5.1}$$

where m is the mass of protons and pions respectively.
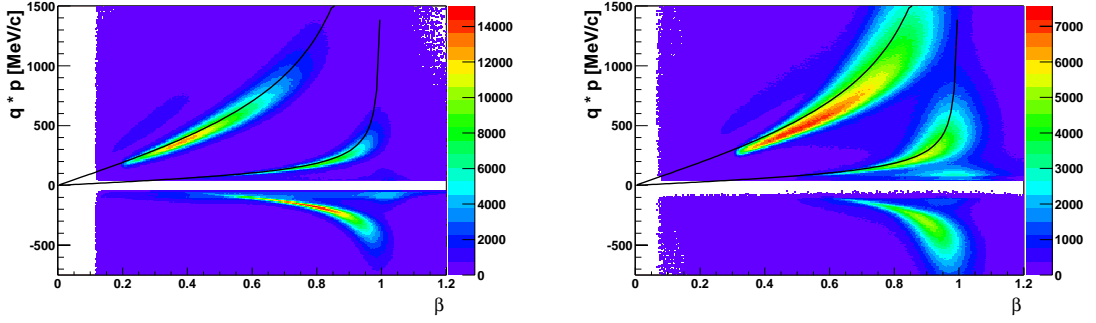
(a) Tof   (b) Tofino+Shower system

Figure 5.1: *Momentum multiplied by the charge plotted versus β calculated respectively in a) Tof and b) Tofino. Pions and protons dominate the spectrum.*

The most significant lepton selection criterion is the correlation of the reconstructed tracks with the Rich detector. To find a proper correlation window between Rich rings and the inner part of Kick Tracks a preliminary correlation is performed on any track with any ring (sector-wise). No condition is put on the ring quality. In fact, requiring a high ring quality, puts a strong bias on "good" rings. This kind of rings has obviously more pads fired, and therefore the position resolution of the ring center is better. There are still many rings with very few pads (5 or even 4) on the ring circumference: in this case the resolution of the center is worst and might be out of the window determined with a preliminary cut on high ring quality.

The same linear distance (i.e. resolution of a detector) dX spans smaller $\delta\phi$ for larger polar angles θ. To keep the solid angle constant,

$$d\Omega = dY \cdot \frac{dX}{R^2} = (R \cdot \delta\theta) \cdot \frac{(R \cdot \delta\phi \cdot \sin\theta)}{R^2} = \delta\theta \cdot \delta\phi \cdot \sin\theta \tag{5.2}$$

the $\delta\phi$ distribution should be corrected with the factor $\sin\theta$.

Figure 5.2 show the $\delta\theta$ and the $(\delta\phi * \sin\theta)$ distribution:

(a) $\delta\phi \cdot \sin\theta$ (b) $\delta\theta$
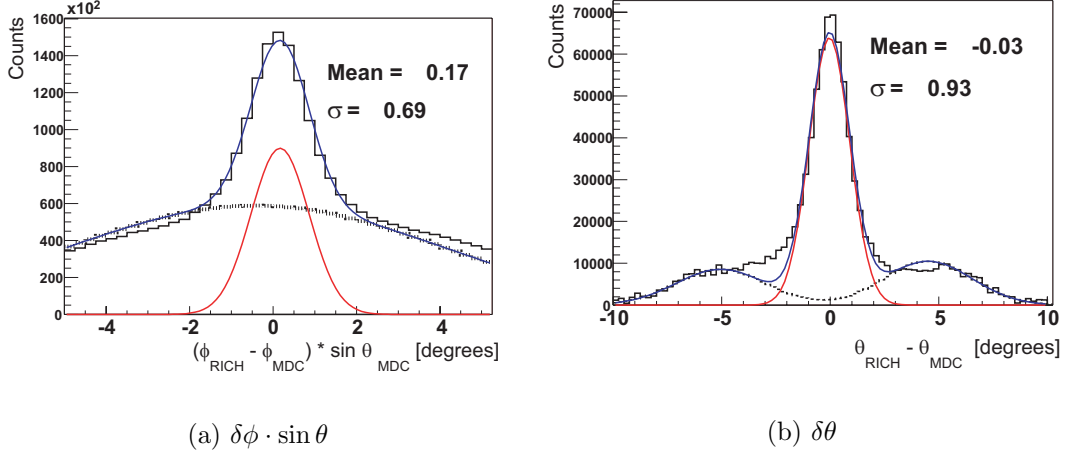
Figure 5.2: *Angular correlation between Rich and the innermost segment of a track. In a) $(\phi_{RICH} - \phi_{TRACK}) \cdot \sin\theta_{Rich}$, in b) $\phi_{RICH} - \phi_{TRACK}$. The background fit is shown by the dotted curves.*

- $\delta\theta$: center: $-0.035° \pm 0.001$, $\sigma : 0.9° \pm 0.001$

- $(\delta\phi * \sin\theta)$: center: $0.17° \pm 0.0009$, $\sigma : 0.69° \pm 0.0007$

Similar results are obtained for simulated data and November 2002 data. Methods for the fit, as well as results for simulations and November 2002 are discussed in Appendix C.

It should be noted that a separate $\delta\theta$, $(\delta\phi * \sin\theta)$ cut would result in a squared cut, which would leave a inhomogeneous background, as Figure 5.3 shows: the straight lines represent a separate cut on $\delta\theta$ and $(\delta\phi * \sin\theta)$ distributions which leaves a inhomogeneous background, which is cut away by a more appropriate elliptical cut, defined by the function

$$\xi^2 = \left(\frac{\delta\theta}{\sigma_{\delta\theta}}\right)^2 + \left(\frac{\delta\phi \cdot \sin\theta}{\sigma_{\delta\phi \cdot \sin\theta}}\right)^2 \tag{5.3}$$

Figure 5.3 a) shows the two cuts on the $(\delta\theta \, , \, \delta\phi \cdot \sin\theta)$ distribution. In the figure the straight lines mark the squared cuts, the two ellipses mark the cuts on a ξ^2 distribution which would correspond respectively to a 2σ and 3σ cut. Figure 5.3 b) shows the ξ^2 distribution, where the straight line indicates the cut at $\xi^2 = 6$, so 99% of the signal is inside this cut.

(a) $\delta\phi \cdot \sin\theta$ vs $\delta\theta$
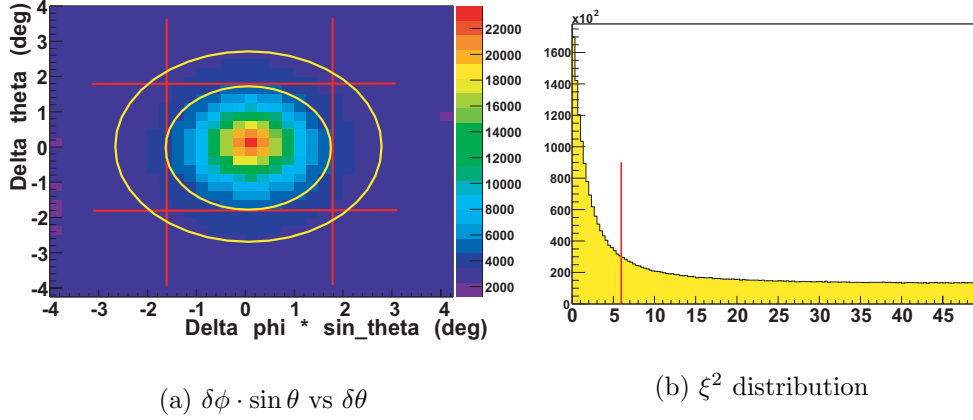
(b) ξ^2 distribution

Figure 5.3: *Angular correlation between Rich and the innermost segment of a track. The straight lines represent the squared cut, the ellipse corresponds the ξ^2 cut. The ξ^2 distribution in shown in b) where the cut is marked in red.*

5.1.2 Time of Flight Cut

For the particle candidates which are left after this cut, the correlation between β measured in Tof or Tofino respectively and the momentum calculated with the kickplane method is shown in Figure 5.4. According to the

(a) Tof system

(b) Tofino/Shower system
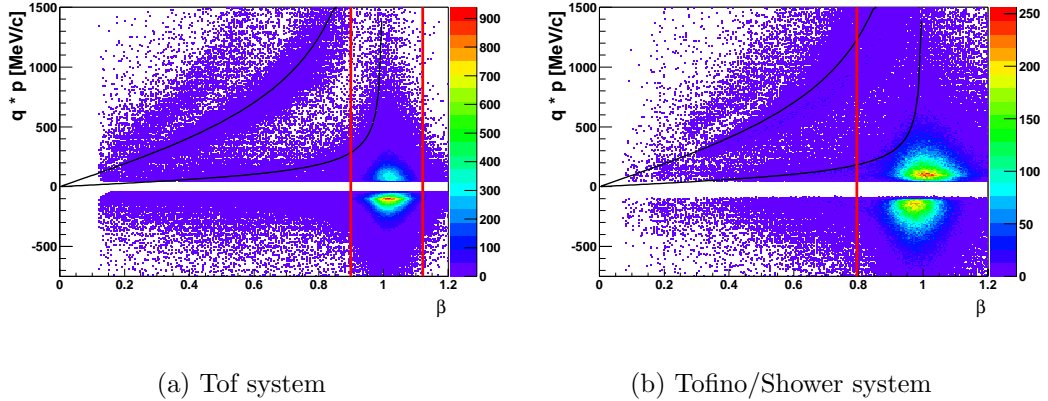
Figure 5.4: *β calculated respectively in a) Tof and b) Tofino as a function of the momentum. The pion and proton contamination is marked with the theoretical curve of Equation 5.1.*

theoretical curves of Equation 5.1 shown in the figure, a contamination of pions, and even protons might still be present. This is due to the correlation

of misidentified rings with hadron tracks. A 3σ cut on the β distributions, shown by the straight lines, and justified by the time resolution shown in Figure 5.5, respectively for Tofino-Shower and TOF system, is then applied.

- Tof: $0.899 < \beta < 1.121$

- Tofino: $\beta > 0.795$

Only a lower cut on the β distribution, i.e. an upper cut on time of flight, has been chosen for Tofino, to account for double hits in the same cell. Similar results are obtained for simulated data as well as for November 2002 data.

(a) Tof system

(b) Tofino/Shower system
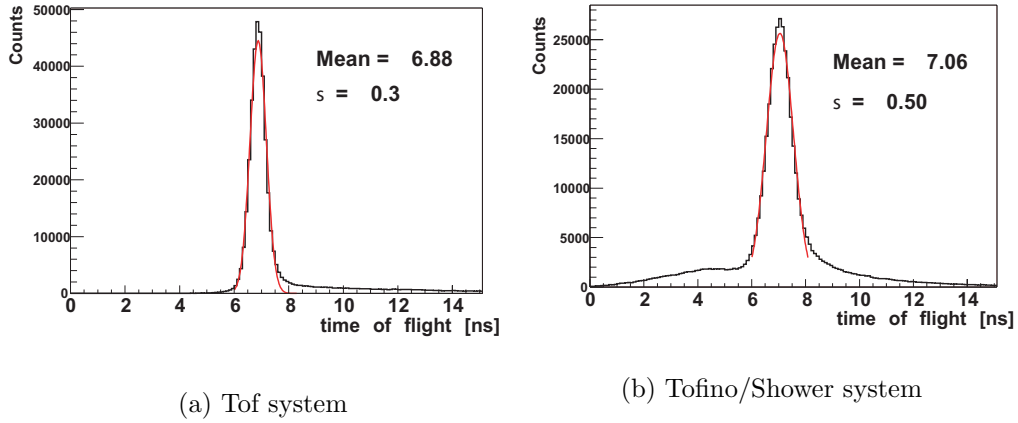
Figure 5.5: *Time of flight distributions for a) Tof and b) Tofino.*

5.1.3   Ring Quality cut

It is now possible to apply some cuts on quality parameters of the offline Ring Recognition Algorithm, namely

- average charge (i.e. Total Charge cumulated in the 13x13 fiducial area / number of pads fired in the 13x13 confidential area) > 4

- pattern matrix > 200

- number of pads (fired in the 13x13 fiducial area) > 5

Figure 5.6 shows the distribution of these quantities for all the rings which have passed all the cuts above (χ^2 ring-track correlation and time of flight).

(a) average charge   (b) pattern matrix   (c) number of pads
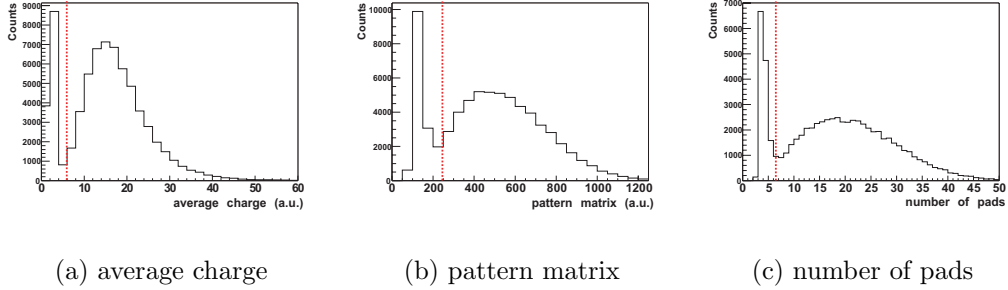
Figure 5.6: *Quality parameters of the Rich ring finder. a) Average Charge, b) Pattern Matrix c) Number of pads. The cuts are marked by the straight dashed lines and clearly cut away a fake signature (peak at low ring quality).*

The dashed lines correspond to the applied cuts. These cuts allow to remove a good fraction of misidentified rings whose signature is represented by a correlated peak at low ring quality is visible both in experimental and simulated data, while discarding only a minor part of rings correlated with Kicktrack which in simulation correspond to Hgeant leptons [102]. Similar results are obtained for simulated data as well as for the November 2002 data.

5.1.4 Shower Condition
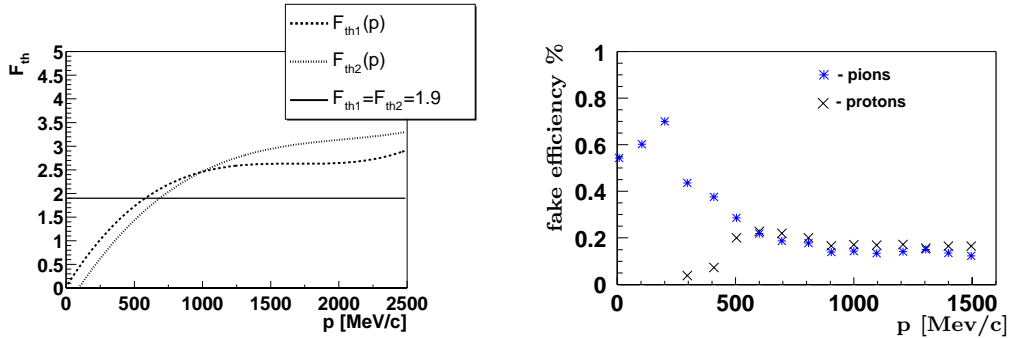
Figure 5.7: *Left:* $F_{th1}(p)$ *(dashed line) and* $F_{th2}(p)$ *(dotted line) charge factors as function of momentum. The constant charge threshold in case of* $F_{th1} = F_{th2} = 1.9$ *(solid line) is also shown. Right: The Pre-Shower electron/hadron misidentification (fakes) for the momentum dependent algorithm (Eq. 9.1) as a function of momentum for protons and pions [137].*

To allow an electron-hadron discrimination in the region of small polar

angles, i.e. the region covered by the Pre-Shower detector, the ratio between the integrated charge deposited in the second and third layer with respect to the first has been compared to different threshold values, shown in Figure 5.7, in two different electron identification criteria which have been tested in simulations [137]:

- constant thresholds $F_{th1} = F_{th2}$ (Equation 9.1): they are optimized to get the best ratio between reconstructed and misidentified electrons: electrons reconstruction efficiency is on average 80% over the full momentum range while fake electrons are about 10%;

- momentum dependent thresholds $F_{th1}(p)$, $F_{th2}(p)$: they are optimized to maintain a constant electron recognition efficiency of about 80% over the full momentum range.

However, with the additional cut on time of flight in the Tofino detector, the Pre-Shower condition based on momentum-dependent thresholds is capable to reject more than 90% of the misidentified electrons keeping the efficiency around 80%.
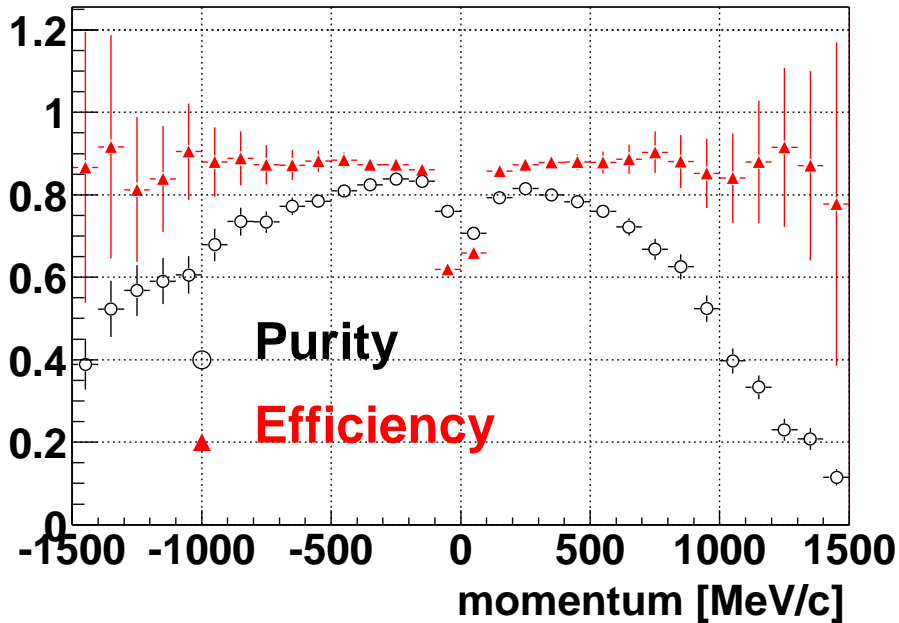
Figure 5.8: *Efficiency and purity of the single lepton signal as a function of the momentum multiplied by the charge of the particle.*

All together the cuts presented applied on a sample of simulated data, provide an efficiency of 77% and a purity of 78% for the single lepton signal. Figure 5.8 shows the efficiency and the purity of the lepton signal as a function of the momentum multiplied by the charge of the particle. The efficiency is constant over the full momentum range, except for very low momenta particles (below 100 MeV/c), which are strongly deflected and eventually curled by the magnetic field. The purity shows a strong drop for positive particles with high momenta: the contamination, shown in Figure in this region is mainly created by protons for which, according to the Bethe-Bloch formula, the energy loss increases in the successive layers of the pre-Shower detector. However each of the single hadronic contamination is lower than 1% over
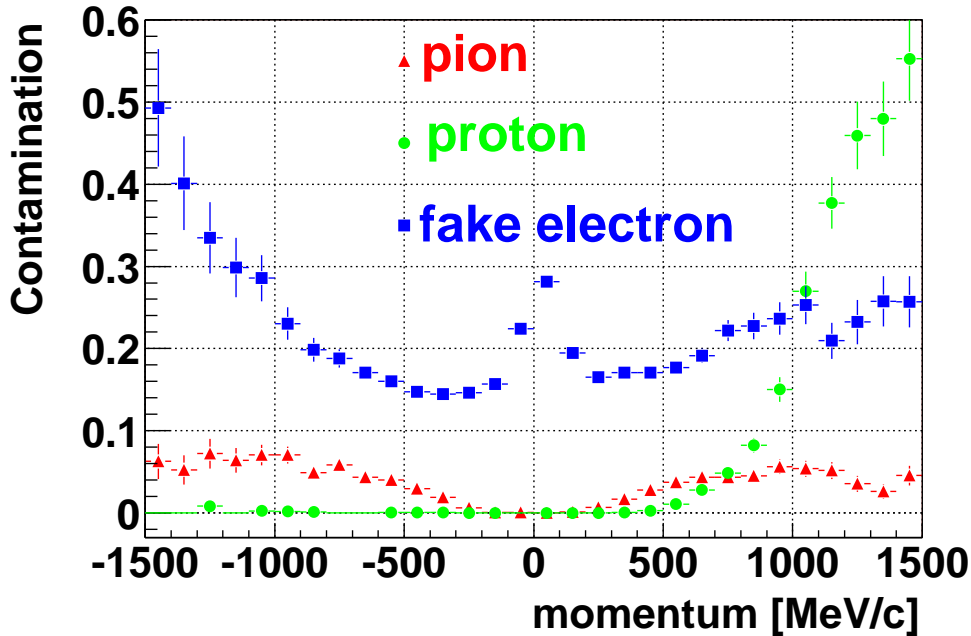
Figure 5.9: *Different contribution of the single lepton signal contamination: pion, proton and fakes, i.e. lepton reconstructed by the analysis which do not correspond to any common track in RICH, MDC, and META in HGeant.*

the full momentum range. The dominant contribution ($\sim$ 19%) arises from *traclets*, i.e. leptons properly correlated in RICH and MDCs which are correlated to the wrong hit in META by the Kickplane combinatorics.

Since these combinations have a leptonic time of flight, it is very diffcult to remove them with a kinematical cut, since they enter the same kinematical region as the real leptons, as shown by Figure 5.10. In the figure β is plotted as a function of the momentum after all the lepton cuts have been applied.

The pion contamination is marked with the theoretical curve of Equation 5.1. The distribution is broader for experimental data (left) due to the worse resolution. Simulated data with a purity of 78% is shown in the center. On the right panel simulated data is shown where the identity of the particle, fully reconstructed in all the spectrometer components (RICH, MDCs and META) is required to be leptonic (electron or positron). The Figure shows
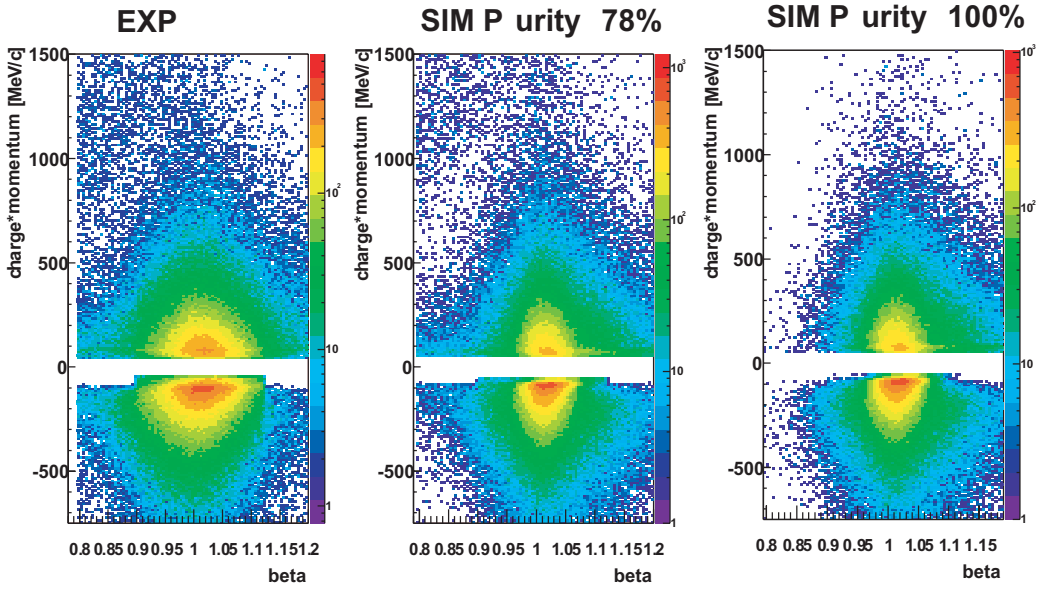
Figure 5.10: *β as a function of the momentum after all the lepton cuts have been applied for experimental data (left), simulated data (center) and simulated data where the identity of the particle is required to be leptonic (right). The pion contamination is marked with the theoretical curve of Equation 5.1.*

that no further kinematical cut is possible to eliminate the pion contamination without a significant lepton efficiency loss, and is not even necessary since the overall hadronic contamination amount to less than 2%.

5.1.5 Results

The criteria described above define the *lepton* candidate sample. The sign of the lepton is determined by the deflection in the magnetic field. The same analysis criteria have been applied to simulated data. A comparison between simulated and experimental data will be presented in the following plots. The event normalization, done for events which contain at least one reconstructed track[1], takes into account the difference between the π^0 multiplicities experimentally measured and the ones calculated by the theoretical model used for the present simulations (see Appendix B): the simulation yield is therefore scaled down by a factor 0.68 for 2 AGeV and 0.64 for 1 AGeV.
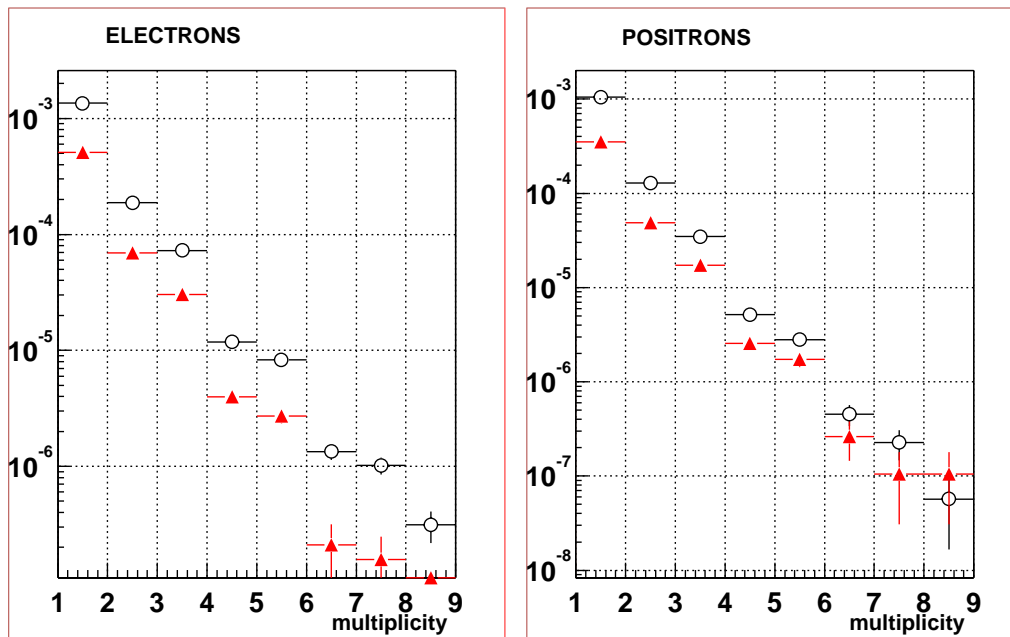
Figure 5.11: *Multiplicity for electrons (*left*) and positrons (*right*) in experimental and simulated C+C reactions at 2AGeV. Simulated events are represented by the solid curve, experimental events are shown by the dashed curve.*

---

[1]In simulations the LVL1 condition is emulated, so the event sample should be fully equivalent to the experimental one. However the normalization to events with at least one track is preferred because it takes into account experimental effects which create a positive LVL1 decision even for events without any track (like particles not coming from the target, noise, ...).

Figure 5.11 shows separately the multiplicity for electrons and positrons in experimental and simulated data for the reactions at 2 AGeV. Electrons are more abundant than positrons due to the acceptance of the magnetic field. The simulated yield is slightly higher than the experimental one, especially for electrons.

Figure 5.12 shows the azimuthal emission angle distribution of lepton candi-

(a) electrons   (b) positrons
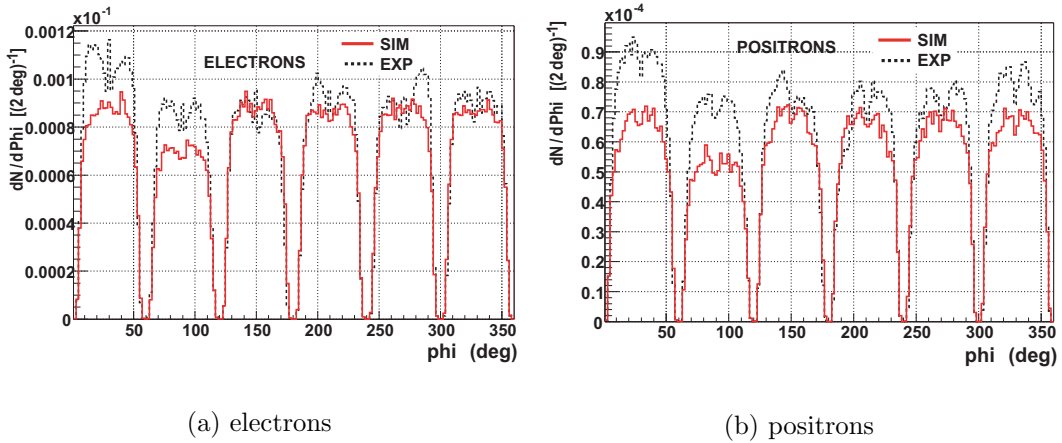
Figure 5.12: *Azimuthal distribution of a) electron and b) positron candidates for simulated (solid curve) and experimental (dashed curve) data.*

dates separately for electrons and positrons. The separation of the sectors is visible as reduced acceptance at the borders. The distributions are isotropic over all the sectors, while sector 1 ($60° < \phi < 120°$) has a lower yield because only one of the first pair of MDCs was operational therefore reducing the tracking efficiency.

The distribution inside the sector shows some differences between the experimental and simulated data, most likely due to the non ideal set-up of the magnet coils which produces a inhomogeneous azimuthal deflection visible in experimental and not in simulated data. In addition the non-ideal beam position, as well as a non-constant Rich efficiency can also effect the distribution.

Figure 5.13 show the polar emission angle distribution of lepton candidates separately for electrons and positrons. Electrons are bent by the magnetic field towards larger polar angles, positrons towards smaller polar angles. Electrons emitted at large polar angle are bent out of the acceptance, therefore their yield at large polar angle is suppressed. on the other hand positrons emitted at small polar angle have preferably a high momentum,

(a) electrons
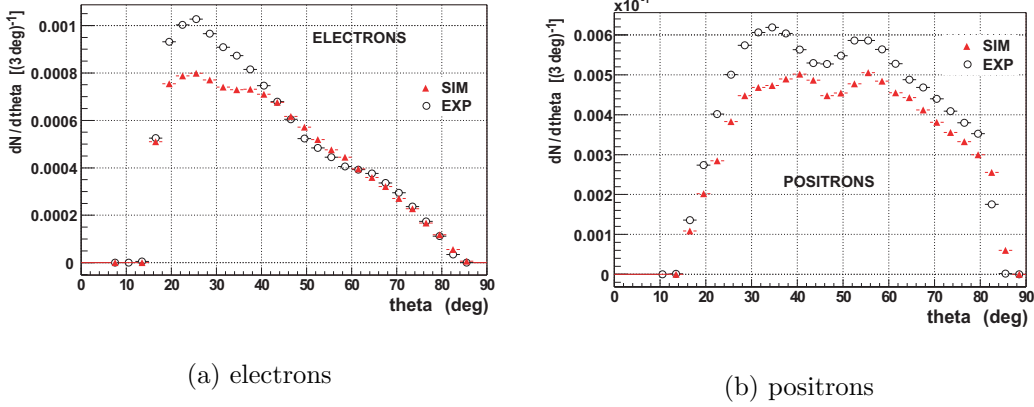
(b) positrons

Figure 5.13: *Polar angle distribution of a) electron and b) positron candidates for simulated (full triangles) and experimental (empty circles) data.*

therefore they are less bent and their yield at small polar angle is still high. This explains the differences between Figure 5.13 (a) and (b). The drop around $\theta = 45°$ in Figures 5.13 is due to the non ideal set-up of the two systems Tofino+Shower and Tof: in the reality the detectors do overlap and this leads to effects like multiple scattering or double hit counting which are not yet properly corrected. In this region the discrepancies between experimental and simulated distributions are more pronounced.

To understand the additional differences between simulated and experimental data, electrons and positron candidates have been separately analyzed for momenta lower and higher than 400 MeV/c and for the different systems (Tof or Tofino+Shower). The polar angular distribution for the mentioned cases are shown in Figure 5.14 for electrons and 5.15 for positrons.

The distributions in the Tof system at high momenta (lower left figure) are suppressed by a factor 10 both for electrons and positrons for kinematical reasons; therefore the discrepancies between simulations and experiments in this case are neglectable. In the distributions in the Tofino+Shower system at high momenta (upper left figure) and in the Tof system at low momenta (lower right figure) simulation and experiment are in good agreement both for electrons and positrons. The main discrepancies arise from the distribution in the Tofino+Shower system at low momenta (upper right figure). In this case the experimental yield overcomes the simulated one especially at smaller emission angles.

As Figure 5.7 shows, the Pre-Shower condition leaves a strong contamination of pions with momenta lower than 400 MeV/c. This contamination is cor-
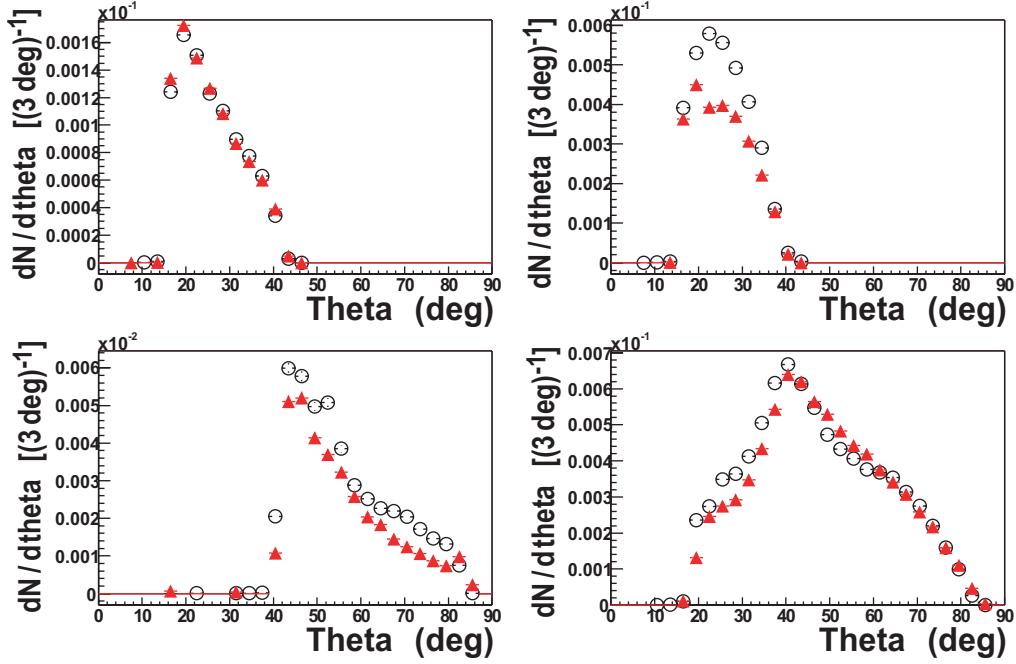
Figure 5.14: *Polar angle distribution of electron candidates for simulated (full triangles) and experimental (empty circles) data. The upper figures are for the Tofino+Shower system, the lower for the Tof system. The left figures are for momenta higher than 400 MeV/c, the right one for momenta lower than 400 MeV/c.*

related to the abundance of misidentified rings higher in experiment than in simulations especially at small polar angle: this can be see in Figure 5.4 (b) where the pion contamination might still be present (See theoretical curve) even after correlating tracks with rings. As the Figure 5.4 (b) shows even the time of flight cut in the Tofino detector does not completely eliminate the contamination, in contrast to the Tof detector where the time resolution allows more restrictive cuts. The high purity in simulations (See Figure 5.8 and 5.9) is basically achieved with the ring condition (See Figure 5.4); together with the comparison between different ring finder algorithms (See Figure 8.18), this shows how sensitive the lepton sample can react even to minor differences in the ring pattern between experimental and simulated data. This might explain the yield discrepancies which amount to about 20% and can therefore be attributed to an additional contamination in experiment. Additional investigations are needed, which would allow more restrictive cut, as for example a more narrow correlation window between the rings and the
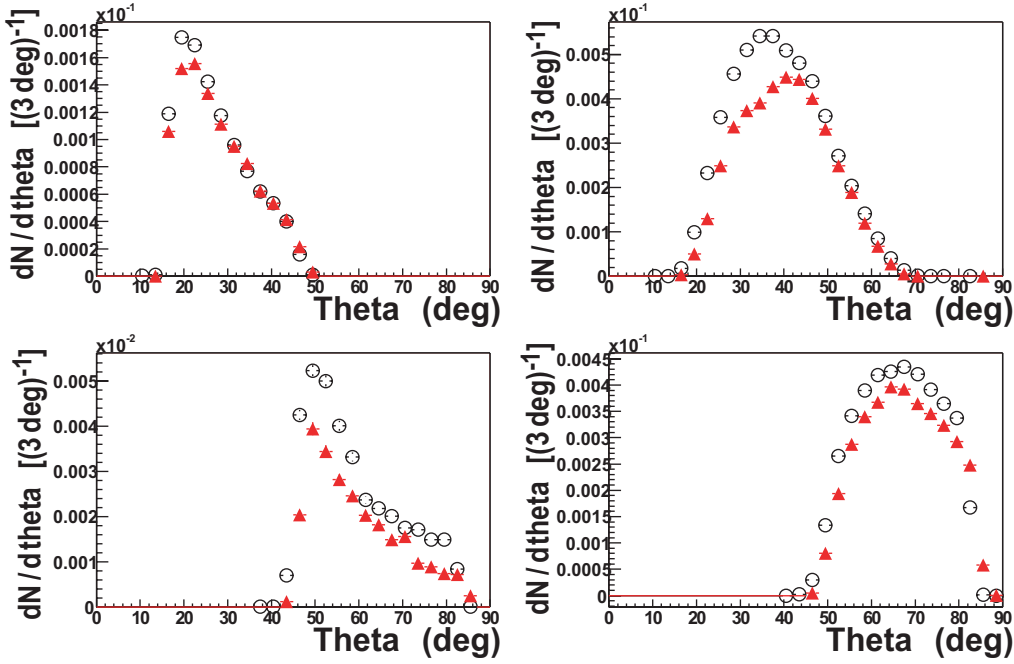
Figure 5.15: *Polar angle distribution of positron candidates for simulated (full triangles) and experimental (empty circles) data. The upper figures are for the Tofino+Shower system, the lower for the Tof system. The left figures are for momenta higher than 400 MeV/c, the right one for momenta lower than 400 MeV/c*

tracks (currently a 3σ cut is used).

Figure 5.16 shows the emission angle (polar and azimuthal) of lepton candidates for experimental (left) and simulated (right) data: the higher yield for smaller polar angles is due to the Lorentz boost of particles which are preferably emitted at very forward angles. The azimuthal acceptance is reduced at the sector borders due to the mechanical support structures. The tracking problems due to the presence of only one MDC before the magnetic field in sector 1 ($60° < \phi < 120°$) are visible both in simulated and experimental data.

The relativistic quantity which describes the motion parallel to the beam direction is the *rapidity y*. Taking z as beam direction, the rapidity is defined as

$$y = \frac{1}{2} \ln \frac{E + p_z}{E - p_z} = \tanh^{-1}(v_z) \tag{5.4}$$
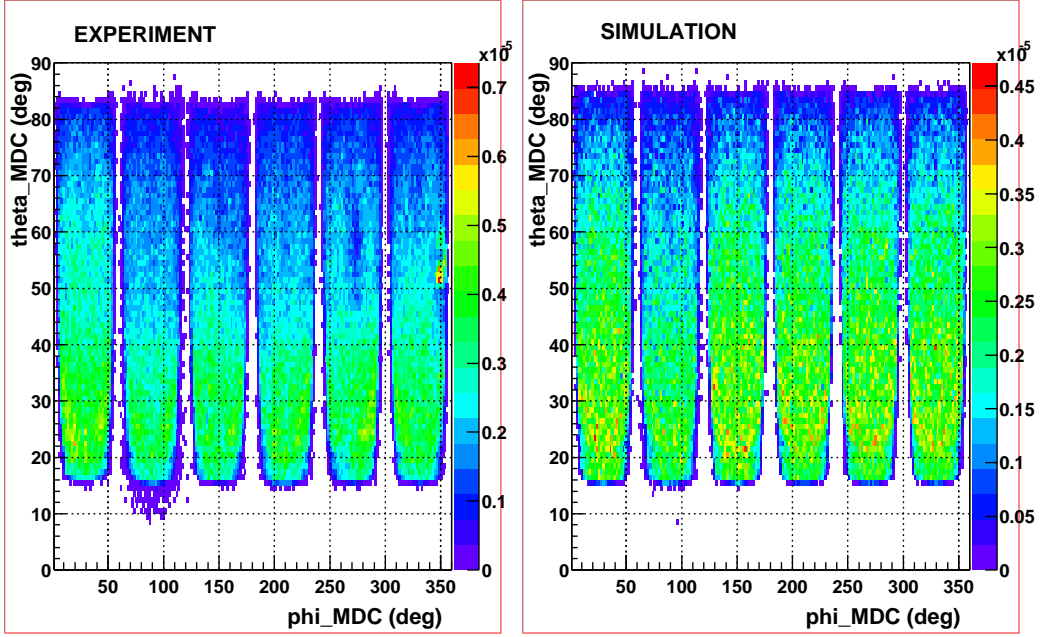
Figure 5.16: *Polar versus Azimuthal distribution of lepton candidates for experimental (left) and simulated (right) data.*

where $v_z = p_z/E$ is the velocity along the beam axis. The *pseudorapidity* is a handy variable to approximate the rapidity in the limit $m \ll p$. It is an angular variable defined by

$$
\begin{aligned}
\eta &= -\ln\left[\tan\left(\frac{\theta}{2}\right)\right] \\
\theta &= 2\tan^{-1}(e^{-\eta})
\end{aligned}
\tag{5.5}
$$

where θ is the angle between the particle being considered and the undeflected beam. The pseudorapidity is the same as the rapidity y if one sets $\beta = 1$, so it is a good approximation for the rapidity when the particle is relativistic. Table 5.1 shows the relation between θ and η for some round values:

$\theta[°]$	90	45	40.4	15.4	15	10	5.7	2.1
η	0	0.88	1	2	2.03	2.44	3	4

Table 5.1: *Relation between θ and η for some values.*

(a) electrons   (b) positrons
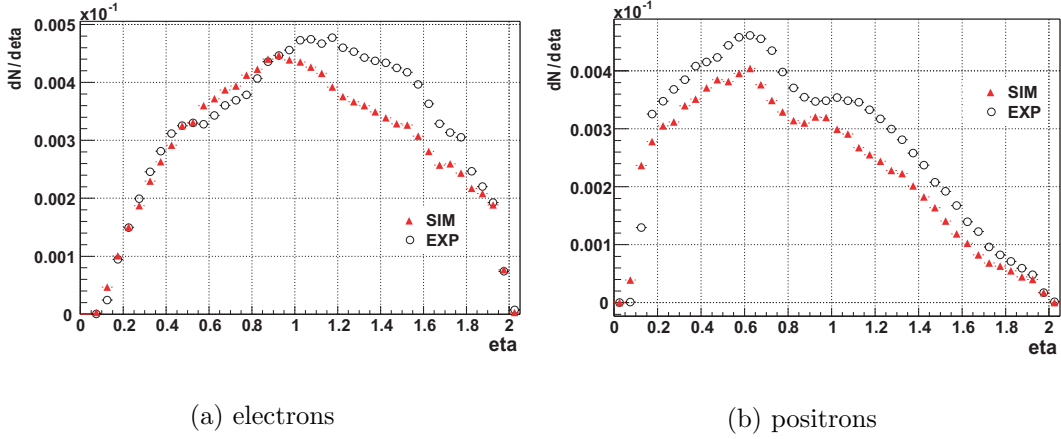
Figure 5.17: *Pseudorapidity distribution of a) electron and b) positron candidates for simulated (full triangles) and experimental (empty circles) data.*

Figure 5.17 shows the pseudorapidity distribution of lepton candidates separately for electrons and positrons. The drop around 0.8 in the integral η distribution in Figure 5.17 in the experimental curve corresponds to the drop at $\theta = 45°$ due to the border effect between the two systems, Tofino+Shower and Tof. The discrepancies between the experimental and the simulated curve reflect the discrepancies in the polar angle distribution.

The momentum is determined by the deflection in the magnetic field: since the magnetic field is toroidal, the deflection is mainly in the polar direction ($\theta_{MDC} - \theta_{META}$), which is positive -i.e. towards larger polar angles- for positrons, negative for electrons, while a deflection occurs even in azimuthal direction ($\phi_{MDC} - \phi_{META}$) due to the inhomogeneity of the field, especially at the borders of the sectors. Figure 5.18 shows the polar and azimuthal deflection for experimental and simulated data. A good agreement between simulation and experiment is reached.

The momentum of electron and positron candidates separately for System 0 (Tofino+Shower) and for System 1 (Tof) is shown in Figure 5.19 for experimental and simulated data. The shape of experimental and simulated data are in a reasonable agreement. The integral higher electron yield is justified with the magnetic acceptance of the spectrometer. In System 0 instead positrons are more abundant than electrons since they are bended towards smaller polar angle. The opposite is true for System 1 where electrons are more abundant.
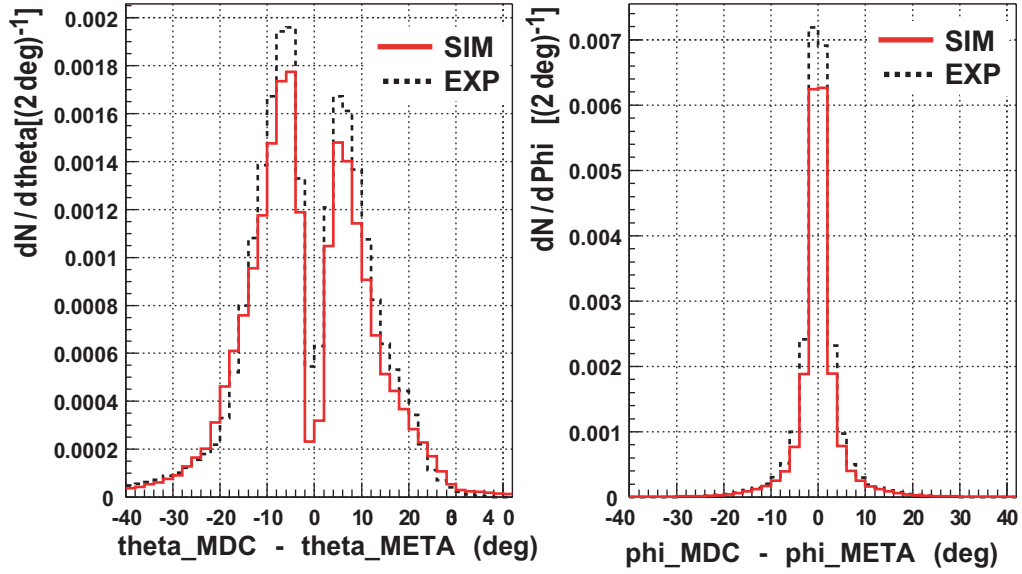
Figure 5.18: *Polar and azimuthal deflection of lepton candidates for simulated (solid curve) and experimental (dashed curve) data.*
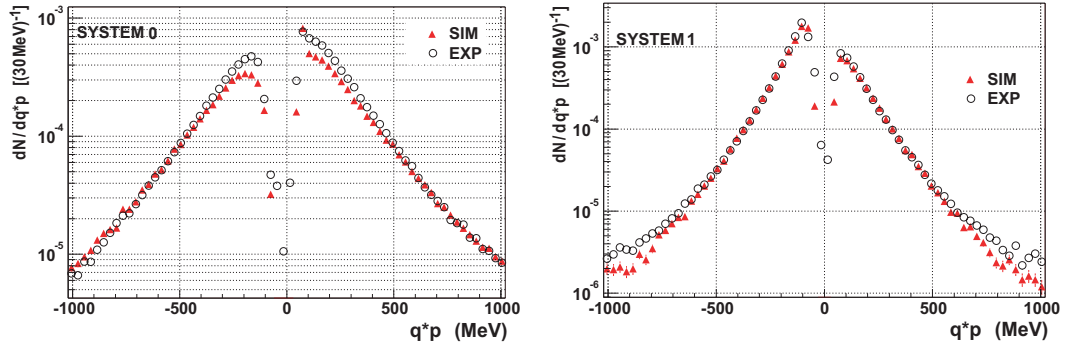
(a) Tofino+Shower   (b) Tof

Figure 5.19: *Momentum (multiplied by the charge) distribution for particles detected in System 0 (left) and System 1 (right) for simulated (full triangles) and experimental (empty circles) data.*

Another important quantity to characterize the kinematics of the reaction is the *tranverse momentum p_T* of an emitted particle, i.e. the component of
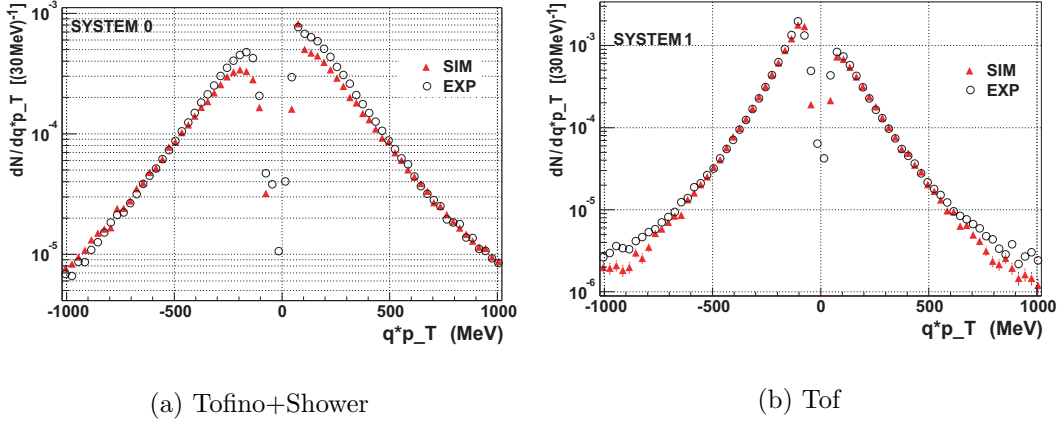
(a) Tofino+Shower

(b) Tof

Figure 5.20: *Tranverse momentum distribution for particles detected in System 0 (left) and System 1 (right) for simulated (full triangles) and experimental (empty circles) data.*

momentum in the transverse $X - Y$ plane, which is defined as

$$p_T = \sqrt{p_x^2 + p_y^2} = p \cdot \sin \theta \tag{5.6}$$

Figure 5.20 shows the tranverse momentum of electron and positron candidates separately for System 0 (Tofino+Shower) and for System 1 (Tof): the asymmetric acceptance of electrons and positrons is still visible.

Both the the momentum (Figure 5.19) and the transverse momentum (Figure 5.20) distribution show a good agreement between simulated and experimental data: as already observed the discrepancies are concentrated in the region of low momenta particles in the Tofino+Shower system.

Finally Figure 5.21 shows the momentum multiplied by the sign of the particle plotted versus the polar (left) and azimuthal (right) deflection for experimental data: the polar deflection is proportional to the inverse of the momentum, and its sign corresponds to the sign of the particle, while the azimuthal deflection depends upon the position in the sector and it is therefore symmetric with respect to positive and negative values. Similar distribution can be obtained for simulated data.

Figure 5.22 shows the dependency of the azimuthal deflection on the azimuthal position on the sector separately for electron and positron candidates in experimental data. The shape of the distribution reflects the phase-space acceptance of the detector. More detailed discussions concerning the az-
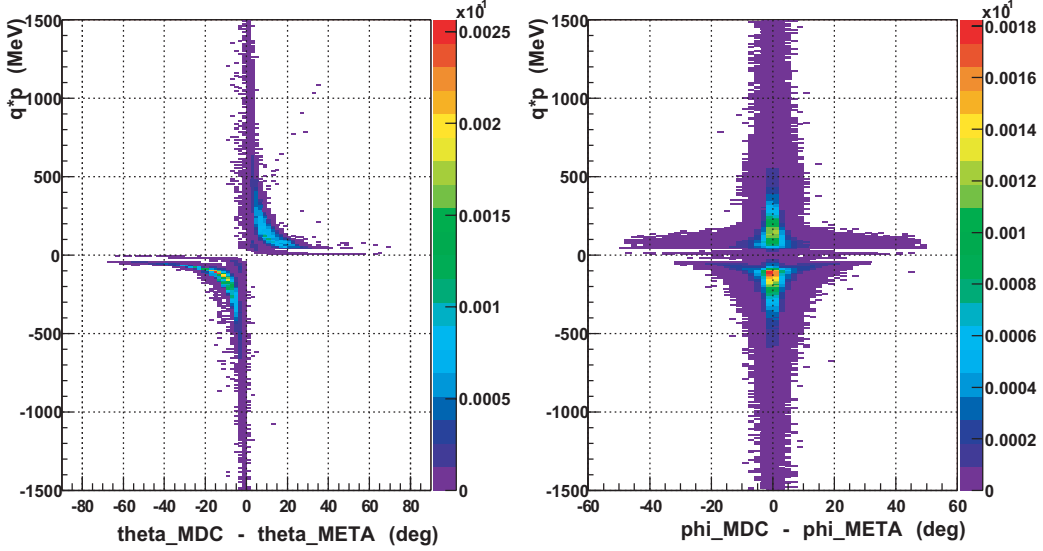
Figure 5.21: *Momentum (multiplied by the charge) plotted as a function of the polar (left) and the azimuthal (right) deflection suffered by the particle. The polar deflection is proportional to the inverse of the momentum. The azimuthal deflection depends on the position in the sector and it is symmetric with respect to positive and negative values. Distributions are obtained for experimental data. Simulated data show a similar behavior.*

imuthal deflection will be presented in Section 9.2 where they affect the choice of the cut for the Matching Unit window.

Tables 5.2 and 5.3 show the amount of reconstructed electron and positron candidates integrally and separately for System 0 (Tofino+Shower) and System 1 (Tof) in experimental and simulated data.

A comparison of the yields in experimental and simulated data is provided by Tables 5.4 and 5.5. Results are shown with the obtained yield in simulated data, and with the yield multiplied by a factor $F = 0.64$ for 1AGeV and $F = 0.68$ for 2AGeV resulting from the difference between the π^0 multiplicities experimentally measured and the ones calculated by the theoretical model used (see Appendix B).

The Tables show a reasonable agreement (within a few percent discrepancy) of the yields when the normalization factor is used.
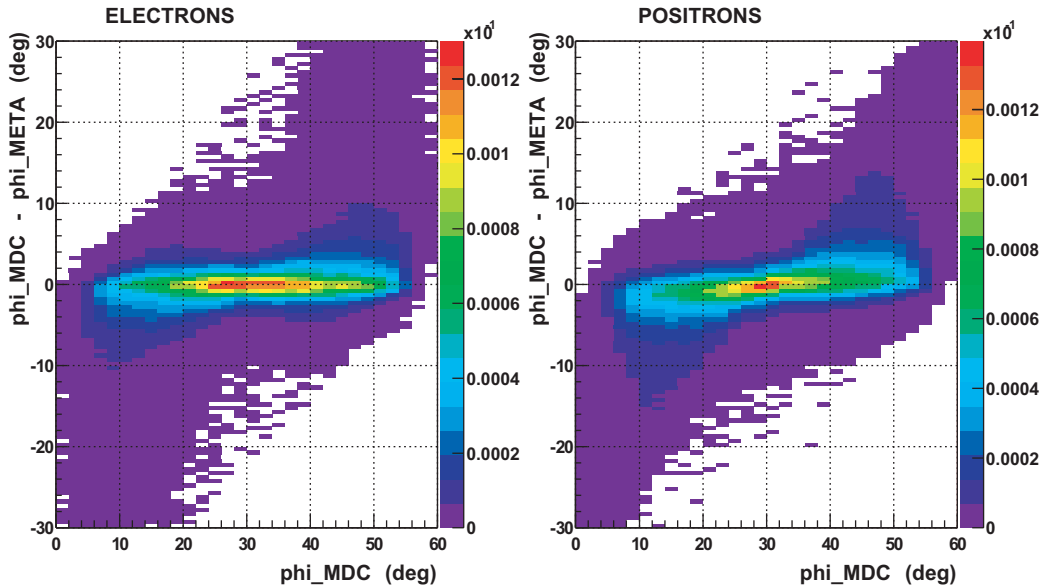
Figure 5.22: *Azimuthal deflection plotted as a function of the azimuthal position of the particle when entering the magnetic field. Distribution for electrons (left) and positrons (right) are obtained with experimental data. Simulated data show a similar behavior.*

	EXP			SIM		
	SYS0	SYS1	ALL	SYS0	SYS1	ALL
e^+	12700	23141	35841	20024	36205	56229
e^-	15973	17498	33471	23544	26871	50415
ALL	28673	40639	69312	43568	63076	106644

Table 5.2: *Reconstructed electron and positron candidates in System 0 (Tofino+Shower) and System 1 (Tof) for C+C at 1 AGeV in experimental (left) and simulated (right) data -* **NOV01 C+C 1 AGeV**.

	EXP			SIM		
	SYS0	SYS1	ALL	SYS0	SYS1	ALL
e^+	153209	300903	454112	68778	155547	224325
e^-	224298	157992	382290	100384	75339	175723
ALL	377507	458895	836402	169162	230886	400048

Table 5.3: *Reconstructed electron and positron candidates in System 0 (Tofino+Shower) and System 1 (Tof) for C+C at 2 AGeV in experimental (left) and simulated (right) data -* **NOV01 C+C 2AGeV**.

	SYS0	SYS1	ALL	SYS0		SYS1		ALL	
	EXP	EXP	EXP	SIM	SIM*F	SIM	SIM*F	SIM	SIM*F
$e^+[10^{-3}]$	2.1	3.8	5.8	3.5	**2.2**	6.4	**4.1**	9.9	**6.3**
$e^-[10^{-3}]$	2.6	2.8	5.4	4.1	**2.6**	4.7	**3.0**	8.9	**5.7**
ALL $[10^{-3}]$	4.6	6.6	11.3	7.7	**4.9**	11.1	**7.1**	18.8	**12.0**

Table 5.4: *Reconstructed electron and positron candidates per event (*$[10^{-3}]$*) in System 0 (Tofino+Shower) and System 1 (Tof) for C+C at* **1 AGeV** *-* **NOV01 EXP-SIM**.

	SYS0	SYS1	ALL	SYS0		SYS1		ALL	
	EXP	EXP	EXP	SIM	SIM*F	SIM	SIM*F	SIM	SIM*F
$e^+[10^{-3}]$	4.3	8.2	12.5	5.4	**4.1**	12.3	**9.4**	17.7	**13.6**
$e^-[10^{-3}]$	6.3	4.2	10.5	8.0	**6.1**	5.9	**4.5**	13.9	**10.7**
ALL $[10^{-3}]$	10.5	12.4	22.9	13.3	**10.3**	18.2	**14.0**	31.6	**24.3**

Table 5.5: *Reconstructed electron and positron candidates per event (*$[10^{-3}]$*) in System 0 (Tofino+Shower) and System 1 (Tof) for C+C at* **2 AGeV** *-* **NOV01 EXP-SIM**.

5.2 November 2002 data

In November 2002 the C+C reaction was measure again at the two different beam energies used in November 2001 (1 and 2 AGeV), with a beam intensity of $1 - 2 \cdot 10^6$/s. A segmented Carbon target, consisting out of two

(a) Z vs ρ

(b) Z vs θ
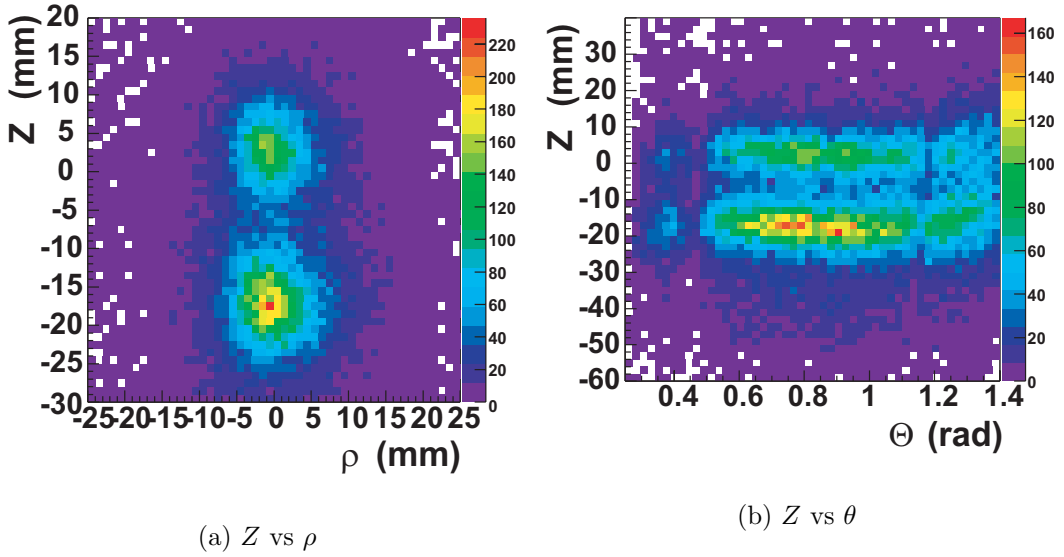
Figure 5.23: *Target reconstruction after MDC fitting. Z follows the beam line direction and θ and ρ are the track polar angle and minimum distance to the Z axis respectively.*

pieces with a diameter of 3 mm and a length of 3 mm, and a density of 2.15 g/cm^3 was used at a distance of 2 cm ($\pm$ 1 cm from nominal target position): this gives a clear signature in the vertex reconstruction, as Figure 5.23 shows. In the figure the tracks are reconstructed using MDCsI and II in sector 0, for the data collected without magnetic field. Figure 5.23 a) show the Z coordinate of the reconstructed track as a function of the minimum distance to the Z axis, Figure 5.23 a) show the Z coordinate of the reconstructed track as a function of the polar coordinate θ. The two targets are clearly visible. The detector set-up consisted of the Start, the Rich and the META detector completed, and 18 MDCs: planes I and II are complete and fully operational, in addition 4 MDCs of plane III and 2 MDCs of plane IV are installed. A problem occurred however in some of the readout mother boards which caused efficiency drops in a preliminary analysis where the problem is not taken into account.
Two LVL1 conditions on the (Tof + Tofino) multiplicity were used, with

different downscaling factors:

- Multiplicity (Tof + Tofino) $\geq$ 2: about 15% of the events

- Multiplicity (Tof + Tofino) $\geq$ 4: about 85% of the events

The LVL2 was fully operational and the trigger condition was set to at least 1 lepton candidate, defined by an azimuthal correlation of $\Delta\phi < 8° + \dfrac{\phi_{Rich}}{4}$ between a hit in Rich IPU and a hit in Tof or Shower IPU (see Chapter 9 for details).

An overall number of 242M events[2] were collected, out of which approximately 56%, i.e. about 135M, LVL1 events are downscaled and 44%, i.e. about 107M, LVL2 events.

In the runs with 2 AGeV a magnetic field of 0.5 T corresponding to a current of I=2497A, was used and a total of about 217M events was collected. In the runs with 1AGeV a reduced magnetic field (0.08 T achieved with I=500A) was used and approximately 6M events has been collected. Some events, approximately 19M, have been collected without magnetic field for alignment purposes.

In the framework of the present thesis only a preliminary analysis was performed, only half the statistics available with the runs at 2AGeV with full magnetic field were calibrated and further analyzed. Those events have been filtered with an offline LVL3, requiring at least 1 correlation between a ring found by the Rich IPU and an MDC hit in the first or the second plane. This filter reduces the events by a factor 5, so that finally approximately 18.5M LVL3 events have been analyzed and will be presented. A fraction of the full statistics, resulting in about 15M events, has not been filtered with LVL3 for normalization purposes: results for the comparison between LVL1, LVL2 and LVL3 will be shown in Chapter 9.

Despite of the possibility to use higher resolution tracking methods[3], the low resolution kickplane was used for the present analysis.

The same analysis criteria used in the November 2001 beamtime have been used for the present analysis, resulting in the same cutting values applied for the spatial correlation between Rich ring and Kick tracks, the time of flight cut, the ring quality parameters and the Pre-Shower condition. This is fully understandable since physics quantities (time of flight, spacial correlation) do not change in a different run; algorithm-dependent quantities (ring quality

---

[2]These numbers are the upper limits at the current time. No event selection (e.g. files with missing detectors HVs) or quality control has been applied yet.

[3]The other methods (Reference Trajectories and Spline Fit) which provide higher tracking resolution were still under development

parameters) were carefully checked.

The yield has been normalized to the number of LVL1 events and scaled by the enhancement factor LVL1-LVL3 calculated in Chapter 9 and presented in Table 9.2. Therefore in the following only the resulting lepton spectra will be shown emphasizing the difference with respect to November 2001 and the problems still present in this preliminary analysis.
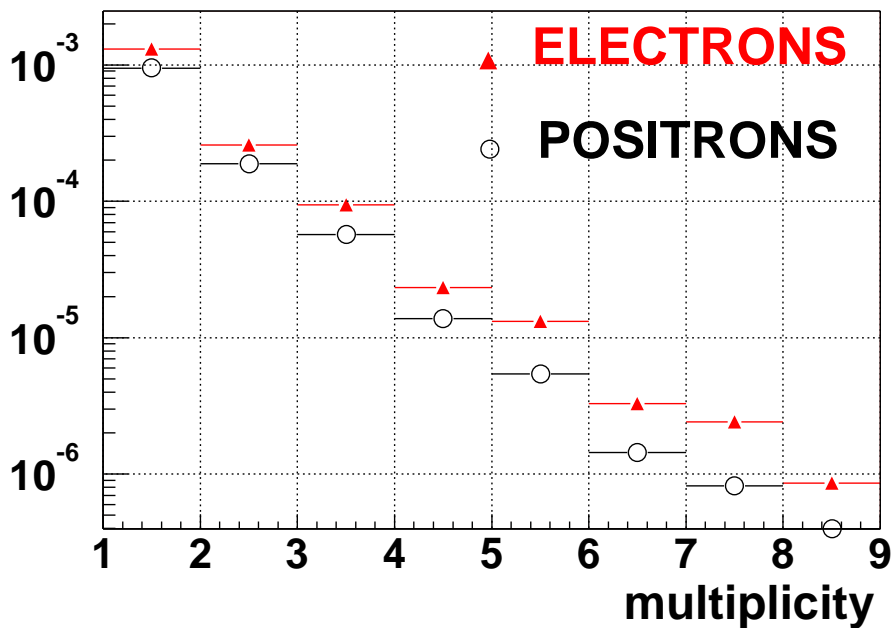
Figure 5.24: *Multiplicity for electrons and positrons in System 0 (Tofino+Shower) and System 1 (Tof) in C+C reactions at 2AGeV.*

Figure 5.24 shows separately the multiplicity for electrons and positrons in System 0 (Tofino+Shower) and System 1 (Tof) for the reactions at 2 AGeV. Electrons are more abundant than positrons due to the acceptance of the magnetic field.

Figure 5.25 shows the azimuthal emission angle distribution of lepton candidates: separately for electrons and positrons and for all the leptons. The separation of the sector is visible as reduced acceptance at the borders. The yield differences between the different sectors are most likely due to the preliminary calibration of the tracking detector, and the problem of the missing mother boards not taken into account which reduces the efficiency of the tracking (the localization of this problems is more visible in Figure 5.27). No

(a) electrons   (b) positrons
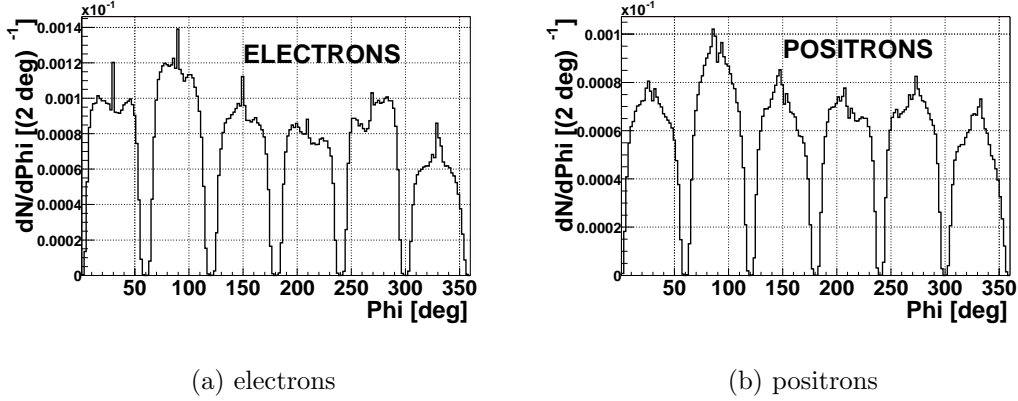
Figure 5.25: *Azimuthal distribution of a) electron and b) positron candidates.*

explanation has been found yet for the spikes sometimes present in the center
of the sectors.

(a) electrons   (b) positrons
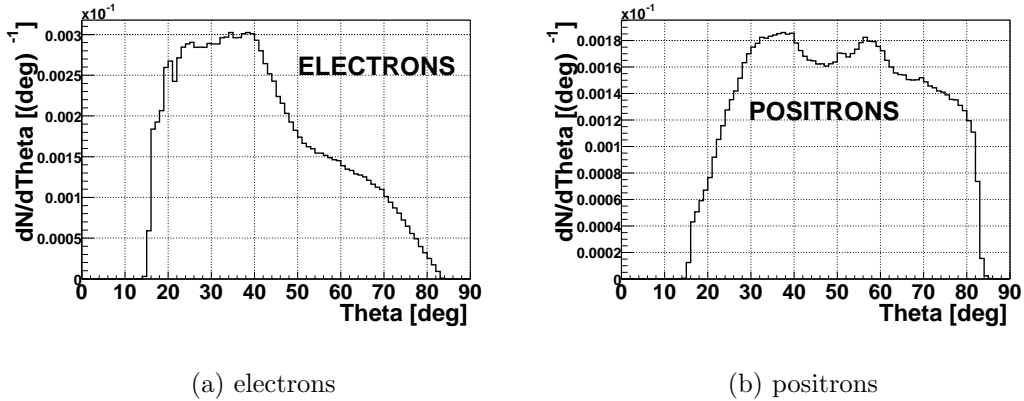
Figure 5.26: *Polar distribution of a) electron and b) positron candidates.*

Figure 5.26 shows the polar emission angle distribution of lepton candi-
dates: separately for electrons and positrons and for all the leptons. The
efficiency drop around $\theta = 45°$ is still present, due to the border/overlap
between the Tofino+Shower and the Tof system and additional structures
in the spectra indicate problems in the detector calibration. In general the
shape of the distributions is consistent with the one observed in November
2001 while a stronger contamination is due to the fact that the analysis is still
preliminary, calibration and alignment not refined and corrected, simulations

non performed yet.
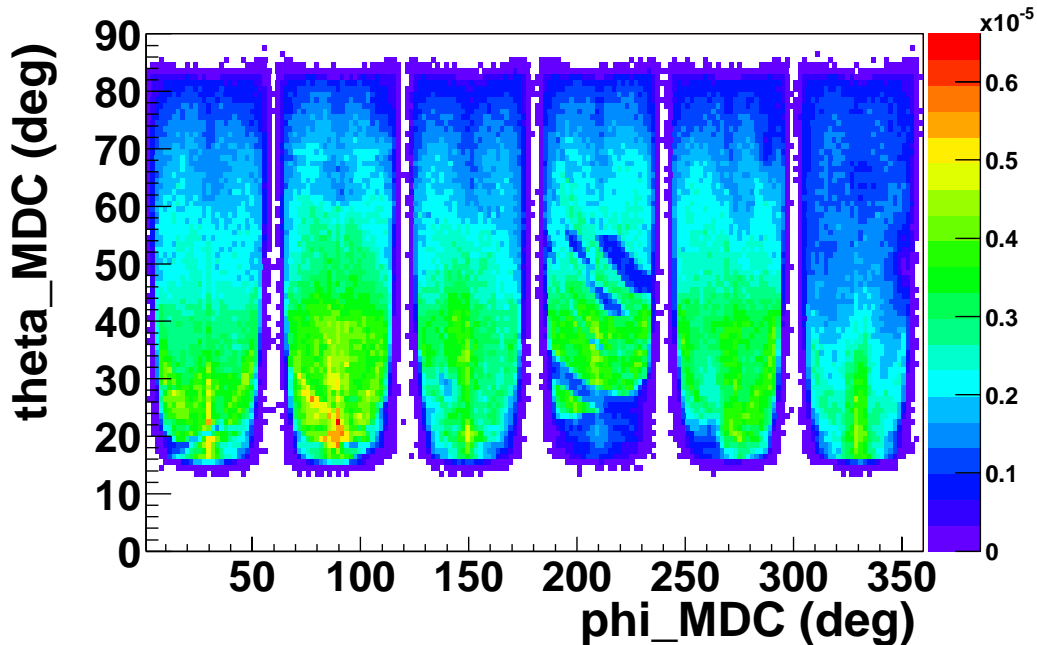
Figure 5.27: *Polar versus Azimuthal distribution of lepton candidates for experimental (left) and simulated (right) data.*

Figure 5.27 shows the polar distribution as a function of the azimuthal distribution: a higher yield in the small polar angles region is due to the Lorentz boost of particles which are preferably emitted at very forward angles. The problem of the tracking efficiency due to the missing motherboards is visible especially in sector 3 ($60° < \phi < 120°$).

Figure 5.28 shows the pseudorapidity distribution of lepton candidates. The drop around $\eta = 0.8$, corresponding to the polar angle $\theta = 45°$ of the border between Tofino+Shower and Tof is still present.

Figure 5.29 shows the polar and azimuthal deflection for experimental and simulated data. The shape of the distribution is very similar to the one obtained in November 2001.

The momentum (Figures 5.30) and transverse momentum (Figures 5.31) distributions, separated for System 0 (Tofino+Shower) and System 1 (Tof)

(a) electrons
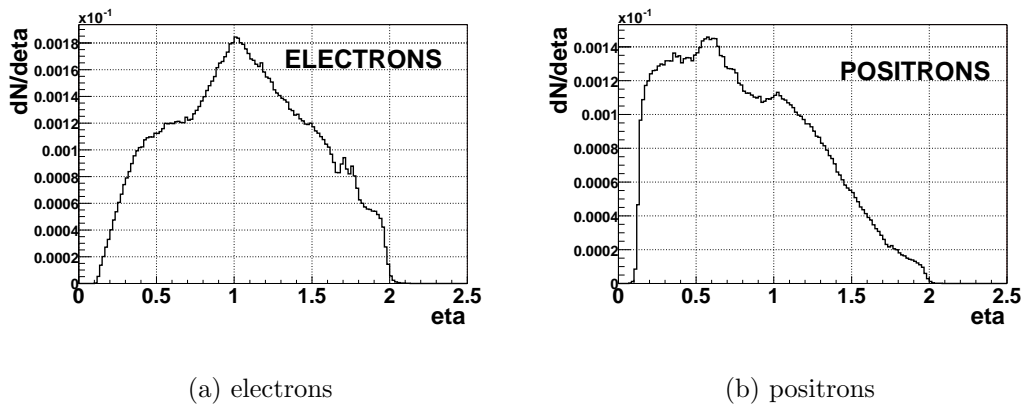
(b) positrons

Figure 5.28: *Pseudorapidity distribution of a) electron and b) positron candidates.*
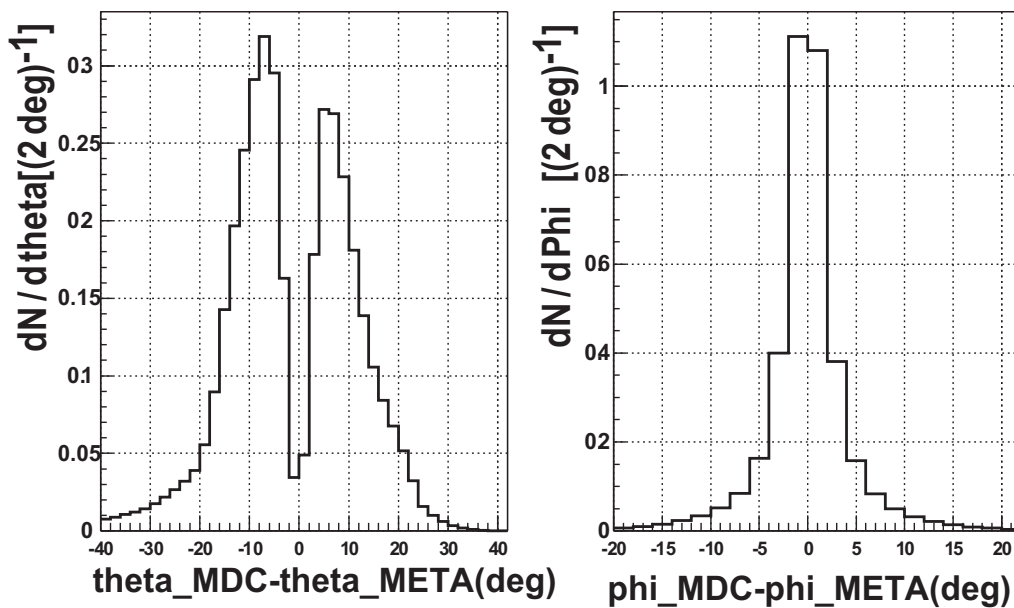
Figure 5.29: *Polar and azimuthal deflection of lepton candidates for simulated (solid curve) and experimental (dashed curve) data.*

present the same shape as November 2001: the differential abundance of electrons and positrons yield due to the magnetic acceptance of the spectrometer.

(a) Tofino+Shower

(b) Tof
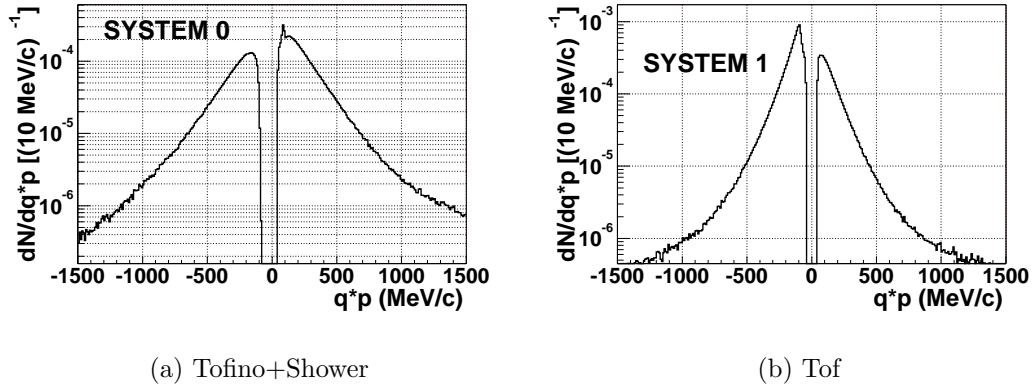
Figure 5.30: *Momentum (multiplied by the charge) distribution for particles detected in System 0 (left) and System 1 (right).*

(a) Tofino+Shower

(b) Tof
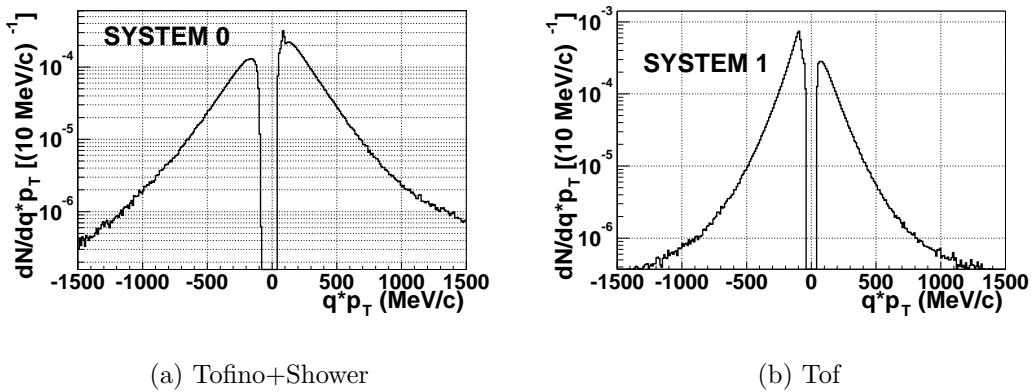
Figure 5.31: *Tranverse momentum distribution for particles detected in System 0 (left) and System 1 (right).*

Finally Figure 5.32 shows the momentum multiplied by the sign of the particle plotted versus the polar (left) and azimuthal (right) deflection for experimental data. Some artefact from badly reconstructed tracks are visible in the right upper corner of the left figure, most likely due to the kickplane which tries all the possible combinations of MDC inner segments with outer META hits.
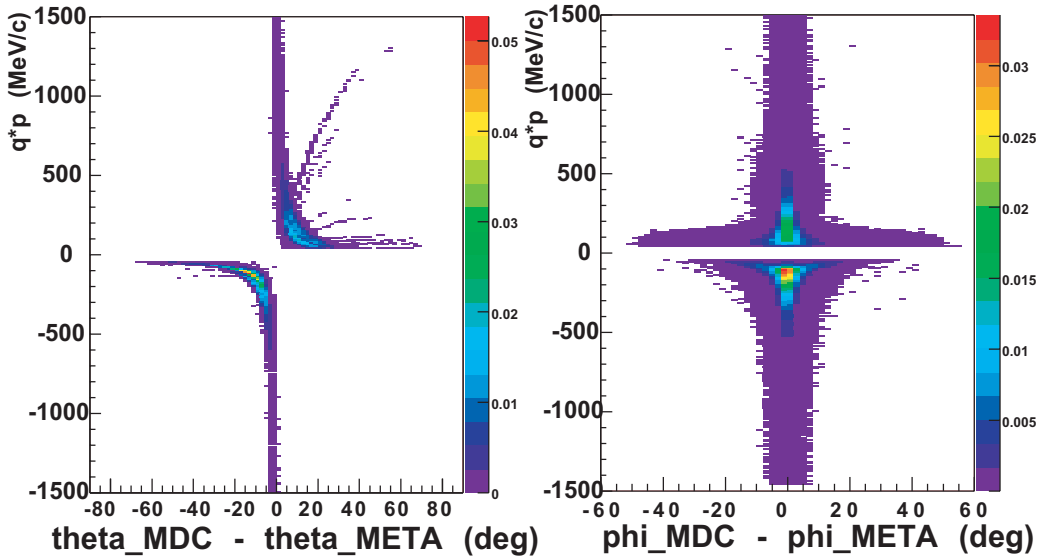
Figure 5.32: *Momentum (multiplied by the charge) plotted as a function of the polar (left) and the azimuthal (right) deflection suffered by the particle. The polar deflection is proportional to the inverse of the momentum. The azimuthal deflection depends on the position in the sector and it is symmetric with respect to positive and negative values.*

Figure 5.33 shows the dependency of the azimuthal deflection on the azimuthal position on the sector separately for electron and positron candidates in experimental data. The shape of the distribution reflects the phase-space of the detector.

Table 5.6 shows the amount of reconstructed electron and positron candidates integrally and separately for System 0 (Tofino+Shower) and System 1 (Tof).

A slight increase of the yield with respect to November 2001 measurement can be explained with the more refined calibration and analysis performed for November 2001 data which allows to select a cleaner lepton sample.
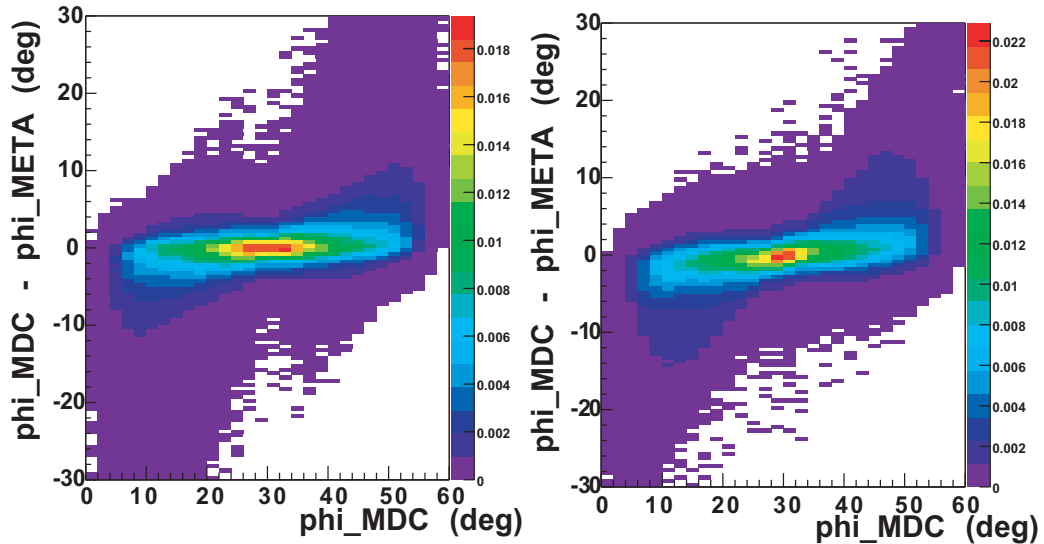
Figure 5.33: *Azimuthal deflection plotted as a function of the azimuthal position of the particle when entering the magnetic field. Distribution are obtained for electrons (left) and positrons (right).*

	2 AGeV		
	SYS0	SYS1	ALL
e^+	763319	2215081	2978400
e^-	1364585	1097816	2462401
ALL	2127904	3312897	5440801

Table 5.6: *Reconstructed electron and positron candidates in System 0 (Tofino+Shower) and System 1 (Tof) for C+C at 2 AGeV -* **NOV02 EXP***.*

Table 5.7 shows the amount of reconstructed electron and positron candidates per event ($[10^{-2}]$) integrally and separately for System 0 (Tofino+Shower) and System 1 (Tof). The absolute yield has been normalized by the number of LVL1 (minimum bias) events by a correction with the enhancement factor LVL1-LVL3 calculated in Chapter 9 and presented in Table 9.2. The absolute yield is in a good agreement with the one obtained in November 2001 shown in Table 5.5.

	2 AGeV		
	SYS0	SYS1	ALL
$e^+[10^{-3}]$	4.3	9.6	13.9
$e^-[10^{-3}]$	6.8	4.9	11.7
ALL $[10^{-3}]$	11.3	14.5	25.7

Table 5.7: *Reconstructed electron and positron candidates per event ($[10^{-2}]$) in System 0 (Tofino+Shower) and System 1 (Tof) for C+C at 2 AGeV. The absolute yield has been normalized by the number of LVL1 (minimum bias) events by a correction with the enhancement factor LVL1-LVL3 calculated in Chapter 9 and presented in Table 9.2. -* **NOV02 EXP**.

Chapter 6

The dilepton analysis

CONSOLATION GROOK

Losing one glove
is certainly painful,
but nothing
compared to the pain
of losing one,
throwing away the other,
and finding
the first one again.

(Piet Hein - Grooks)

The analysis of leptons pairs is the second step after having established a single lepton sample in order to address the physics goals of the HADES experiment. Moreover it is important for the purpose of the LVL2 to define a dilepton signal and estimate the bias of the different trigger condition on it.

The main sources of dileptons in a C+C reaction at 2AGeV are:

- external conversion of γ (79.4%)

  (mainly from $\pi^0 \to \gamma\gamma$)

- Dalitz decays of light mesons:

  - $\pi^0 \to \gamma e^+ e^-$ (20%)
  - $\eta \to \gamma e^+ e^-$ (0.04%)

- other sources (0.56%) including Δ-Dalitz, pn bremsstrahlung and the dilepton decay channels of the vector mesons.

6.1 November 2001 data

The abundance of vector mesons in a collision and therefore also of lepton pairs which constitute the signal of interest of HADES is increasing with the energy per participating nucleon [142] and in the order 10^{-6}. The relative abundance of vector mesons on the other hand also changes with the available energy, as for example the measurements of the ratio of the exclusive total cross section for the $p + p \rightarrow p + p + \phi$ and $p + p \rightarrow p + p + \omega$ [143] shows. An efficient electron identification (See Chapter 5) has to cope with the problem of hadron misidentification.

A severe problem is the relative abundance of dileptons coming from external γ conversion. Photons convert in the target and the RICH radiator gas, as well as other detector or beam line material close to the target position and although the material is optimized to minimize the conversion ($x/X_0 = 2\%$ in the target and the Rich radiator), the photon conversion together with π^0 Dalitz decays still exceed the number of high mass pairs by a factor of $\sim 10^3$. Conversion of γ rays from pion two-body decays ($\pi^0 \rightarrow \gamma\gamma$) and π^0 Dalitz decays from multi-pion production channels lead to additional electrons and positrons. The combinations of these leptons leads to a broad combinatorial background in the reconstructed dilepton invariant mass spectrum. This background contribution can be removed if the pairs from conversion and π^0 Dalitz decays are identified and both particles are removed from the lepton ensemble. The characteristic feature of these pairs is a very small opening angle. Their detection requires good two-track resolution in the RICH and in the inner tracking detectors in which the trajectories of the oppositely charged tracks are not yet separated by the action of the magnetic field. Furthermore, accidental assignments of high momentum pion tracks to nearby centers of ring candidates from low momentum electrons also add to the combinatorial background.

Due to the low statistics collected and the low tracking-momentum resolution achieved in the November 2001 runs, the main focus of the present analysis is dedicated to the signal coming from π^0 Dalitz decay, which provides important information of the low-mass region of the invariant mass spectrum, as well as useful comparison with simulation models.

Looking for the π^0 Dalitz signal the problem of photon conversion is more difficult to handle since it is more difficult to disentangle conversion pairs from π^0 low-mass pairs than from vector mesons high-mass pairs. In order to assure the best possible signal-to-background ratio, the γ conversion pairs would have to be recognized and taken out of the combinatorics, i.e. not combined with any other lepton.

The optimization of the cuts is therefore done more on the lepton correlations, since kinematical cuts, as for instance on the single-electron p_T spectra, strongly reduce the signal from π^0 Dalitz as well.

6.1.1 Dilepton cuts

Pairing is done by creating all possible combinations of electrons and positrons from the same event. Like-sign combinations are later on used to extract the desired correlated unlike-sign pairs from the reconstructed single tracks in a statistical procedure (See Section 6.1.2).
Cuts are applied either discarding only a given combination of leptons, i.e. *on the pair*. Alternatively cuts are used which not only affect the pair but also the the single leptons constituting this pair *on the pair and on the leptons*, i.e. if the pairs does not fulfill the required condition, the pair is not taken into account and also the leptons are discarded from the sample and therefore not allowed to be any longer combined with other leptons. This because the cuts which will be later on explained are considered good hints for close pairs from γ conversion.
An imperfect recognition of close pairs generates leads to single tracks, if the partner is lost because of the acceptance, or the bending of the magnetic field[1], or is not properly reconstructed or is incorrectly assigned. Such single track will contribute to the pairing and create combinatorial background. Events with two or more partially reconstructed low-mass pairs are particularly dangerous, since the resulting combinatorial pairs might have large opening angle and therefore contribute to the high-mass region. To reduce the background as much as possible, an effective rejection of γ conversion pairs is needed.

As described in Chapter 5, a lepton is characterized by the correlation between a Rich ring and a Kicktrack, where a Kicktrack is itself the correlation between a Mdc segment and a Meta hit. Therefore it is required that the two leptons which are combined into a dilepton make use of distinct objects, i.e. the tracks are fully separated.
Two leptonic tracks correlated to the same ring detected in the Rich detector are in fact a clear signature of a close pair where the partners are so close that the rings overlap, but the resolution of MDCs is sufficient to distinguish them (Figure 6.1 a). The offline ring finder in fact has a veto distance of 4 pads (i.e. $\sim 4°$) which does not allow to reconstruct two close leptons.
The case when the two leptons use the same Mdc segment is a subset of the

---

[1] Because of the magnetic field the low-momentum partner of the pair is bended out.
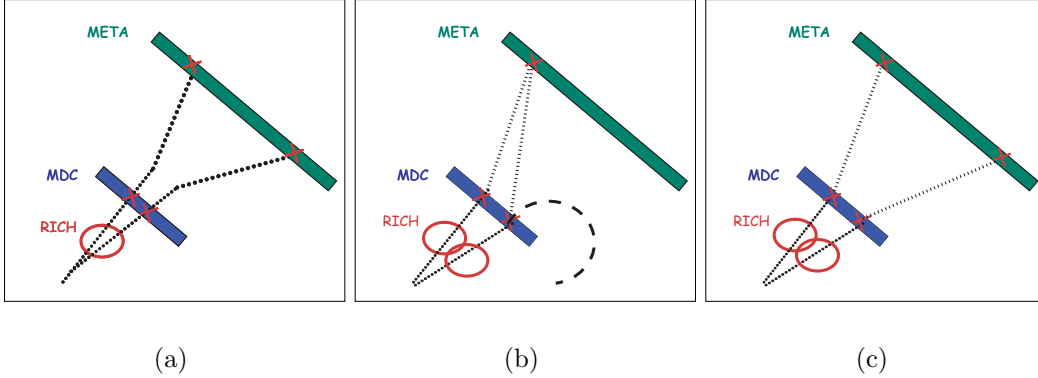
Figure 6.1: *Signature of close pairs which originate most likely from γ conversion. In (a) the two leptons share the same RICH ring, in (b) they share the same META hit, in (c) the opening angle of the pair is very small.*

more general case where the pair has a small opening angle which will be discussed later. In its geometrical acceptance Meta has a particle detection efficiency higher than 99%, therefore it is unlikely that it is responsible of a lepton loss. When two leptons use the same Meta hit, the signal most likely comes also from a close pair where the partner with low momentum, after leaving a signal in the inner detectors (Rich and inner MDCs) is completely deflected in the magnetic field and, due to the absence of Mdc 3 and 4 it is combined by the kickplane with the Meta hit of the partner. This most likely artificially generates a like-sign pair (Figure 6.1 b). Figure 6.2 shows the opening angle distribution for the case when the leptons share the same Rich hit (a) and the case when they share the same Meta hit (b): the small opening angle is a clear signature of pairs coming from external γ conversion and are therefore rejected. In Figure 6.2 the agreement of the shape of simulated and experimental data is quite good even if a deviation occurs at larger values.

The yield normalization is again done with the number of events which contain at least one fully reconstructed track and the simulation yield is scaled by the normalization factor obtained by comparing the π^0 multiplicity measured and calculated by the event generator used. The experimental yield overcomes the simulated one: this can be interpreted as indication of the fact that these miscorrelations happen more frequently in experimental than in simulated events, due to a different background situation.

The average opening angle for leptons generated by an external γ conversion is $0.5°$, while for π^0 Dalitz decay is $13°$. When two leptons produce two sep-

(a) same Rich
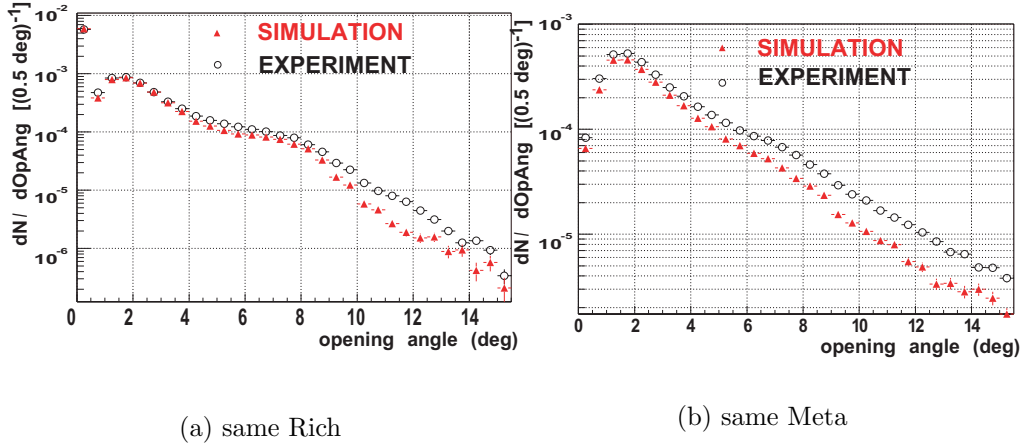
(b) same Meta

Figure 6.2: *Opening angle distribution for lepton pairs which share the same Rich hit (a) or the same Meta hit (b). The small opening angle is a clear signature for external γ conversion. The distributions are shown for experimental (empty circles) and simulated (full triangles) data.*

arated rings in Rich, two segments in MDCs, two hits in the Meta detector, yet they have a small opening angle (Figure 6.1 c), cuts can be applied on the opening angle, and the chosen value influence the efficiency and the purity of the signal. As Figure 6.3 (a) shows, for opening angles larger than $\sim 8°$ the

(a) opening angle
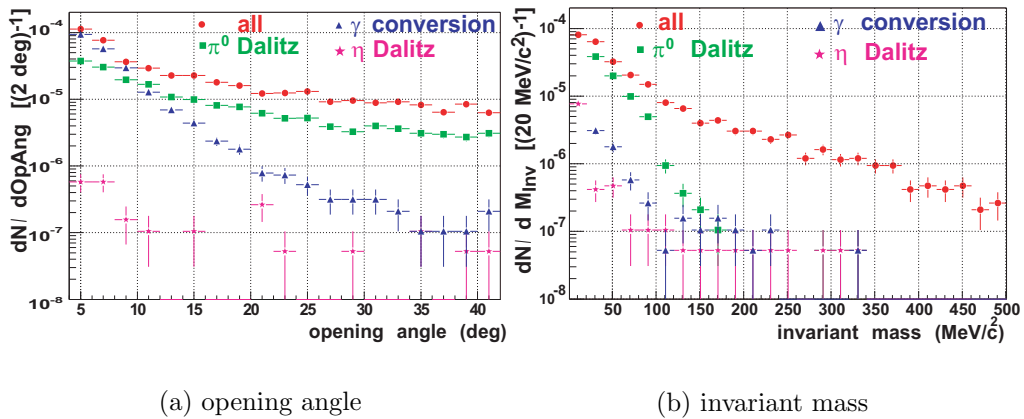
(b) invariant mass

Figure 6.3: *Contribution of the different dilepton sources (π^0 Dalitz decay, η Dalitz decay, and external γ conversion) as a function of the opening angle (a) and the invariant mass (b) -* **NOV01 SIM**.

π^0 contribution is dominant with respect to the one due to conversion which

is completely over at 15°. The figure shows the contributions of the different dilepton sources in the simulated data as a function of the opening angle (a) and the invariant mass (b). The contribution at large opening angles and large invariant mass originates from the combinatorial background. An opening angle cut has been put first at 4°, later at 8° in order to reduce the contribution from γ conversion and hence the background originating from the combination of these leptons with others.

Figure 6.4 shows respectively, as a function of the opening angle for $e^- e^-$, $e^+ e^+$, $e^+ e^-$, the reduction obtained with the different cuts:

- Cut 1: Same Rich or Same Meta: leptons which share the same Rich Hit, i.e. which are characterized using a correlation with the same Rich hit, or which share the same Meta hit are removed from the sample;

- Cut 2: opening angle: leptons whose opening angle is smaller than 4° are removed from the sample;

- Cut 3: the same as Cut 2 with 8°.

Especially Cut 1 significantly reduces the number of pairs, while the following cuts leave the distributions basically unchanged at large opening angles. The reduction obtained with Cut 1 is stronger for like-sign than for un-like sign pair, as documented in Table 6.1. This indicates that non distinct tracks which are eliminated with such a cut, are uncorrelated and arising from artefacts of analysis algorithms (no double hit resolution in Rich, missing outer MDCs).
Investigations indicate that the amount of pairs where the two leptons use the same ring overcomes by almost a factor 10 the amount of pairs which share the same META hit, as the relative yield of Figures 6.2 (a) and (b) indicates.
The agreement of the shape of experimental (left) and simulated (right) spectra is rather good. The simulated yield overcomes the experimental one: the agreement varies between 83% and 62%.
As Table 6.1 shows, the agreement between simulations and experiment is lost mainly with Cut 1, which is dominated by the rejection of pairs created using the same ring pattern most ilkley because of the different background condition in experimental and simulated data which create the non distinct tracks removed by this cut. In particular it is very difficult to perfectly model in simulation the pattern response of the RICH detector, where the exact pad multiplicity, the smearing of the ring shape for optical distortion or for the approximation of the focal plane, or the noise condition are extremely crucial
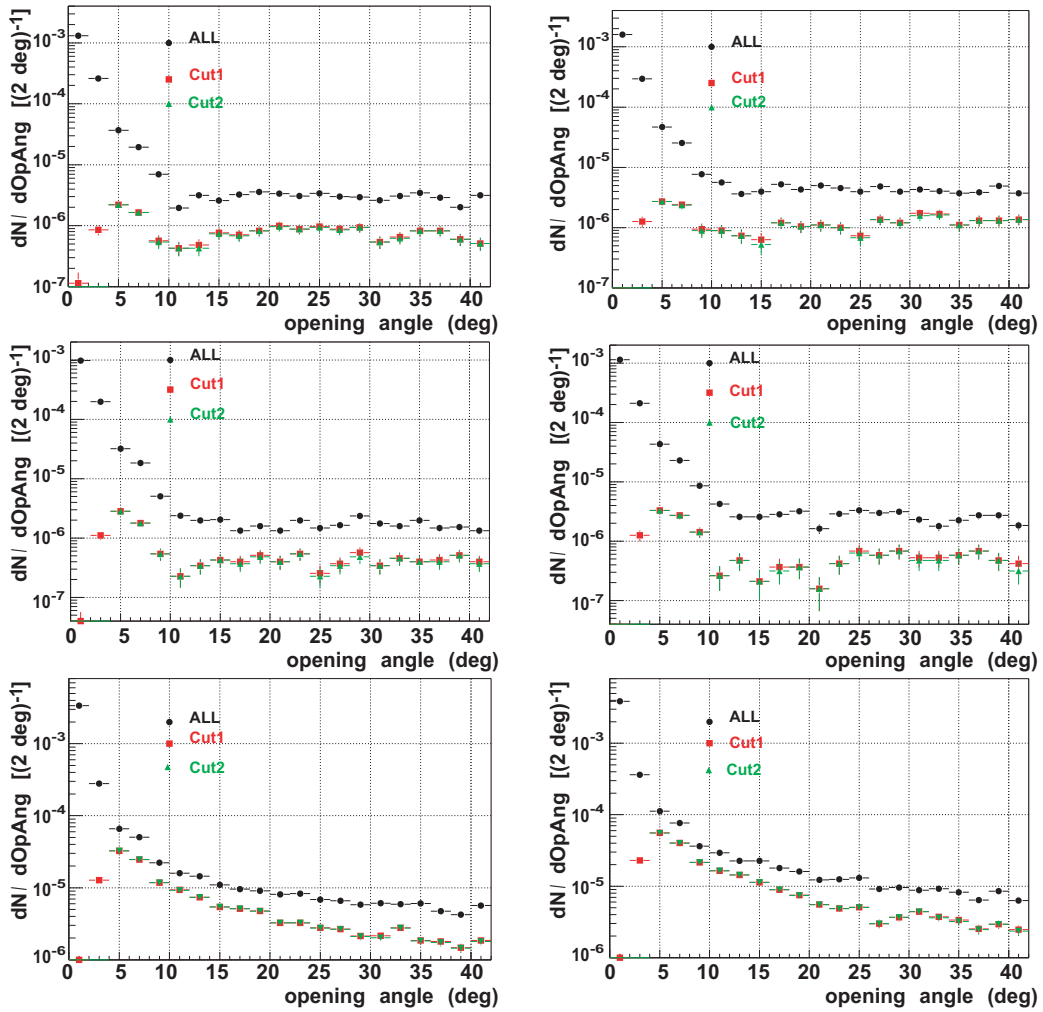
Figure 6.4: *Opening angle distribution for e^-e^- (top), e^+e^+ (center), and e^+e^- (bottom) pairs plotted for different conditions for experimental (left) and simulated (right) data.*

N. of Cut	EXP			SIM			EXP/SIM
	e^+e^+	e^-e^-	e^+e^-	e^+e^+	e^-e^-	e^+e^-	e^+e^-
none $[10^{-3}]$	1.3	1.7	4.0	1.5	2.1	4.8	83%
1 $[10^{-5}]$	2.4	3.1	17.1	2.9	4.7	28.2	61%
2 $[10^{-5}]$	2.3	2.9	15.7	2.7	4.5	25.7	61%
3 $[10^{-5}]$	1.7	2.4	9.7	2.0	3.7	15.7	62%

Table 6.1: *Overall amount of e^-e^-, e^+e^+, and e^+e^- pairs per event as a function of the different cuts compared for experimental and simulated data* **NOV 01**.

for the reconstruction of the hit.

The higher multiplicity of negative (e^-e^-) with respect to positive (e^+e^+) like-sign pairs reflects the higher multiplicity of electrons with respect to positrons and the higher pair acceptance for (e^-e^-) pairs (See Appendix D). The stronger disagreement between simulated and experimental data in the electron-electron pairs reflects the already discussed (See Chapter 5) disagreement for single electron tracks. Table 6.1 summarizes the overall amount of e^-e^-, e^+e^+, and e^+e^- pairs normalized to the number of collected events as a function of the different cuts.

It is interesting to notice that the experiment to simulation ratio is inverted for the dilepton with respect to the lepton sample. In lepton spectra (See Chapter 5) the experimental yield overcomes the simulated one. This means that events with 1 lepton multiplicity are more frequent in experimental than in real data. This can be explained with a lower reconstruction efficiency in experiment which causes a lepton loss, and a higher background in experiment which causes contamination of the lepton sample with misidentified tracks.

Like and unlike-sign pairs distributions are compared in Figure 6.5. The figure shows for experimental (a) and simulated (b) data the opening angle distribution after Cut 1 and Cut 2 have been applied, for e^-e^-, e^+e^+, and e^+e^- pairs together. A comparison between the e^-e^- and e^+e^+ distribution indicates a good agreement at small opening angles, and a higher e^-e^- yield at large angles. The like-sign enhancement at small opening angles is an artefact of the Kickplane algorithm which does not use information from MDC III and IV and therefore produces all the possible combinations between MDC segments and META hits, often resulting in two additional like-sign pairs whenever a unlike-sign pair is detected. Figure 6.6 explains

(a) EXP (b) SIM
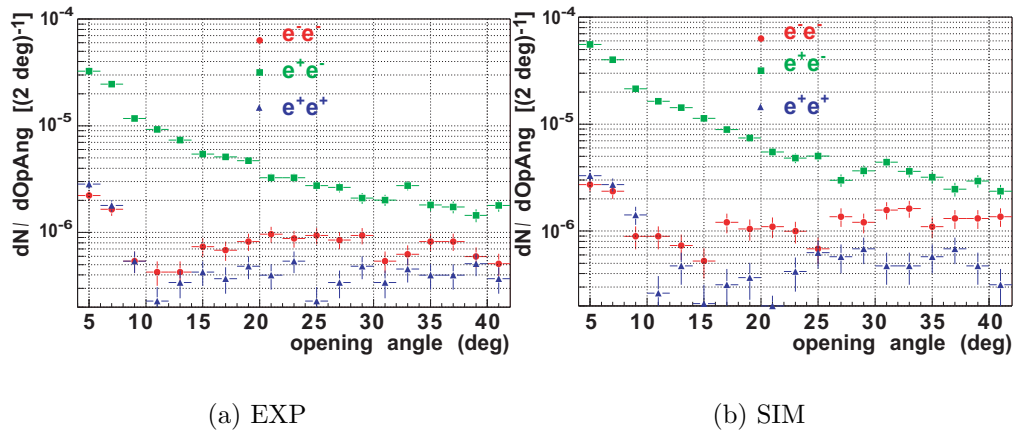
Figure 6.5: *Opening angle distribution for e^-e^-, e^+e^+, and e^+e^- pairs plotted after Cut 1 and Cut 2 have been applied for experimental (a) and simulated (b) data.*
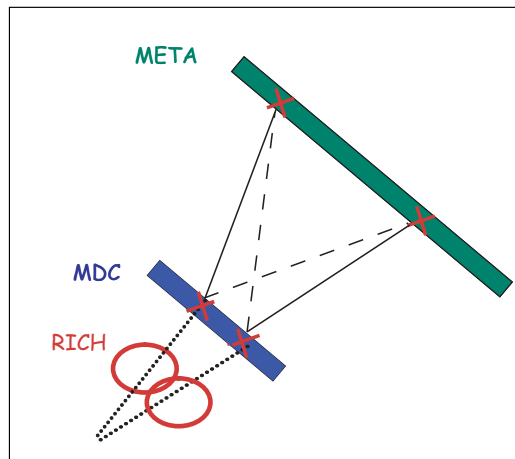
Figure 6.6: *Schematic explanation of the kickplane combinatorics. For a real unlike-sign close pair, since no signature in the outer MDC is available, the combinatorics creates two artificial like-sign pairs (dashed lines).*

this combinatorics.

While on one hand this can be considered a limitation for the estimation of the combinatorial background with the *same-event* technique, on the other hand an enhancement at small opening angles due to kickplane artefacts are visible in the unlike-sign pair distribution as well, and the same-event

technique is therefore preferred for the background subtraction (See Section 6.1.2).

The higher e^-e^- yield at large angles is due to the geometrical acceptance of the spectrometer and is discussed in Appendix D. The invariant mass is determined from the sum of the four-momentum squares as

$$m_{pair} = \sqrt{\mathbf{P}_{\mu e^+}^2 + \mathbf{P}_{\mu e^-}^2} \qquad (6.1)$$

Since the rest mass of the electrons is small, the relativistic limit $E \approx |\,p\,|$ holds, allowing to determine the invariant mass only from the three momenta of the tracks and their opening angle $\omega_{e^+e^-}$

$$m_{pair} = \sqrt{2 \cdot p_{e^+} p_{e^-} (1 - \cos \omega_{e^+e^-})} \qquad (6.2)$$

Figure 6.7 shows respectively, as a function of the invariant mass for e^-e^- (top), e^+e^+ (center), e^+e^- (bottom), the reduction obtained with the different cuts. The shape of the distributions obtained with experimental (left) and simulated (right) data is in a good agreement.

Figure 6.8 shows for experimental (a) and simulated (b) data the invariant distribution after Cut 1 and Cut 2 have been applied, for e^-e^-, e^+e^+, and e^+e^- pairs together.

From the figures it is possible to see that the cuts reduce most of the like-sign pairs with small invariant mass, i.e. with corresponding small opening angle. The cuts are applied *on the pair and on the leptons*, i.e. the leptons are discarded from the sample if the pairs do not fulfill the required condition; the impact of this condition is clearly visible on the like-sign distribution where a reduction is observed even for pairs with large invariant mass. The differences between e^-e^- and e^+e^+ reflect the difference in the opening angle distribution. Low invariant mass (i.e. low opening angle) pairs are artefact of the Kickplane, for higher invariant mass the e^-e^- yield is higher than the e^+e^+ because of the geometrical acceptance. The agreement between the shape of the distributions obtained with experimental and simulated data is good.

Figure 6.9 and 6.10 show the transverse momentum and pseudorapidity distribution for different conditions applied in experimental (a) and simulated (b) data. The different cuts do not change the shape of the distributions, but simply scale them therefore do not introduce any physical bias.

Figure 6.11 shows a comparison of the distribution of transverse momentum (a) and pseudorapidity (b) of the unlike-sign pairs after Cut 1 and Cut 2 have been applied for experimental and simulated data. The agreement be-
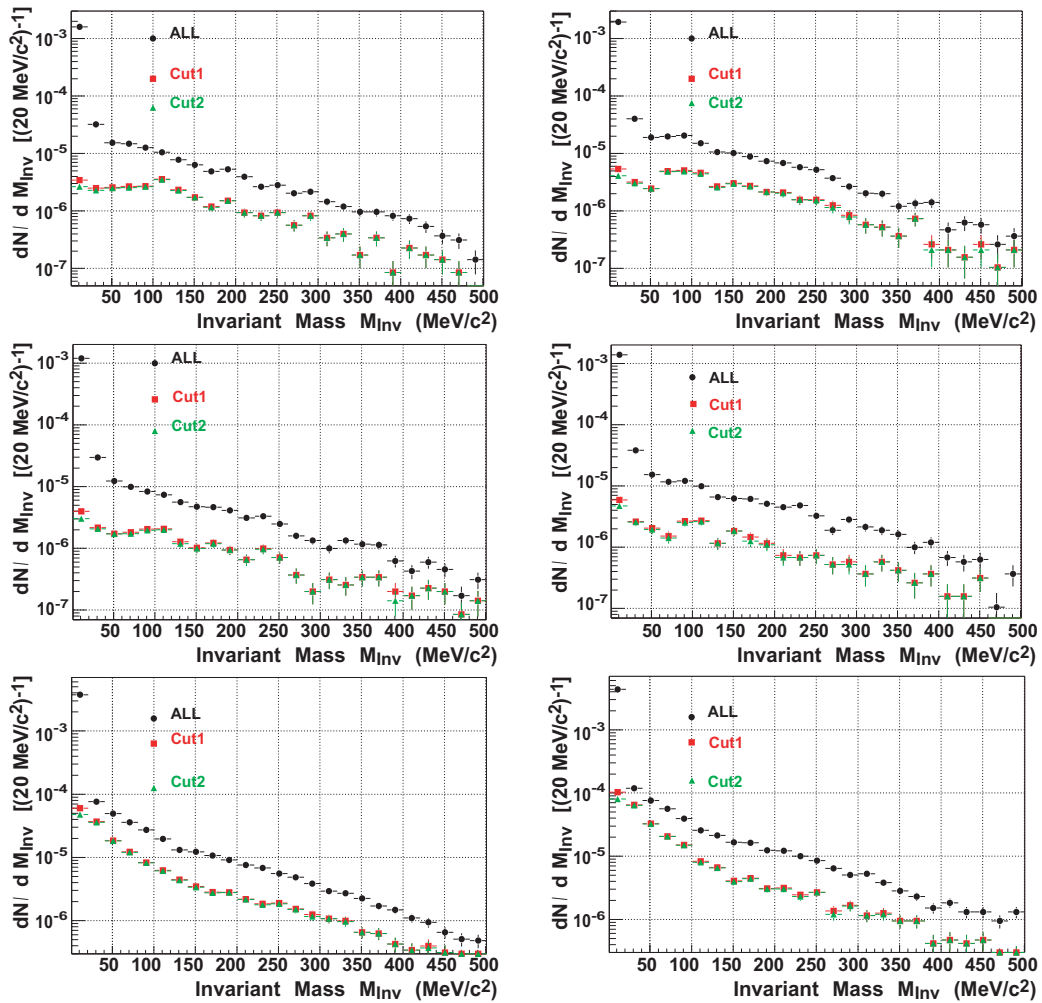
Figure 6.7: *Invariant mass distribution for $e^- e^-$ (top), $e^+ e^+$ (center), and $e^+ e^-$ (bottom) pairs plotted for different conditions for experimental (left) and simulated (right) data.*

(a) EXP   (b) SIM
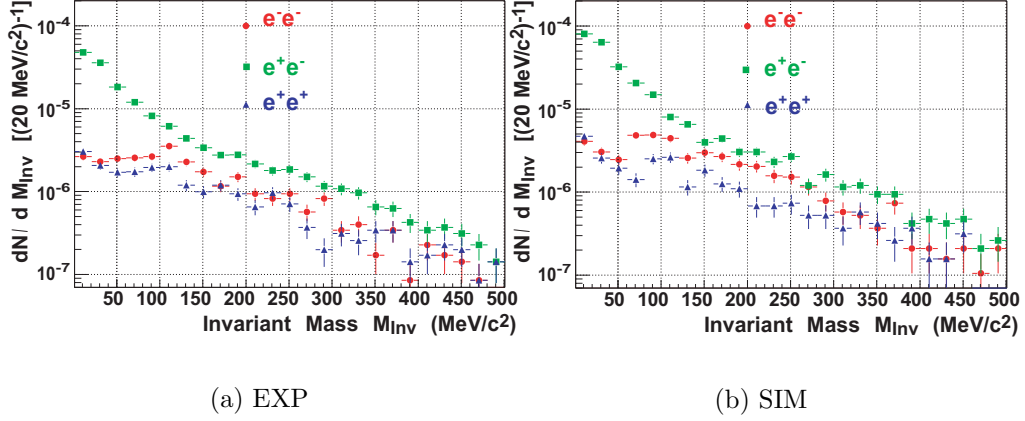
Figure 6.8: *Invariant distribution for e^-e^-, e^+e^+, and e^+e^- pairs plotted after Cut 1 and Cut 2 have been applied for experimental (a) and simulated (b) data.*

(a) EXP   (b) SIM
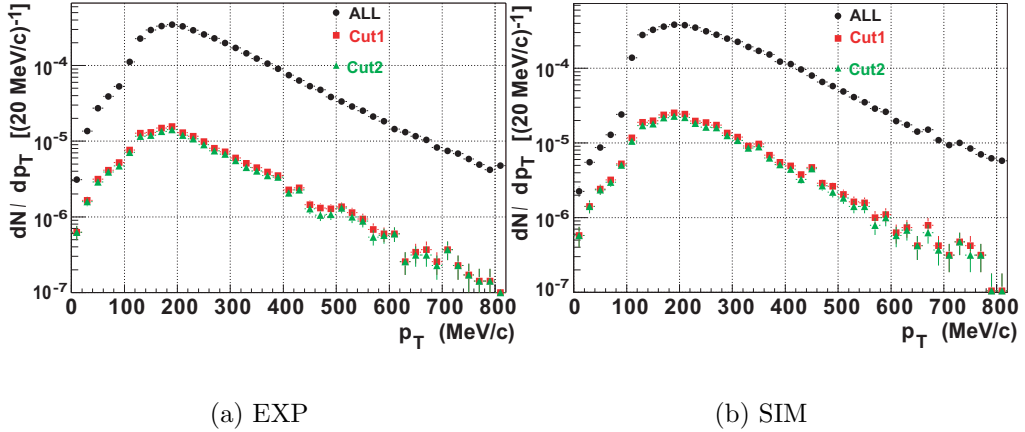
Figure 6.9: *Transverse momentum distribution for e^+e^- pairs plotted for different conditions for experimental (a) and simulated (b) data.*

tween simulated and experimental data is quite reasonable, in the tranverse momentum distribution. The pseudorapidity distribution is peaked at lower values (i.e. mid-rapidity) in simulations, while in experiment is more spread over the full range, presents a step around 0.85 and reaches agreement with simulated data only for values higher than 1.5, where the statistics is however poor. Although not fully understood, this discrepancy might be traced back to the discrepancies for the single leptons, since it is already visible in the

(a) EXP   (b) SIM
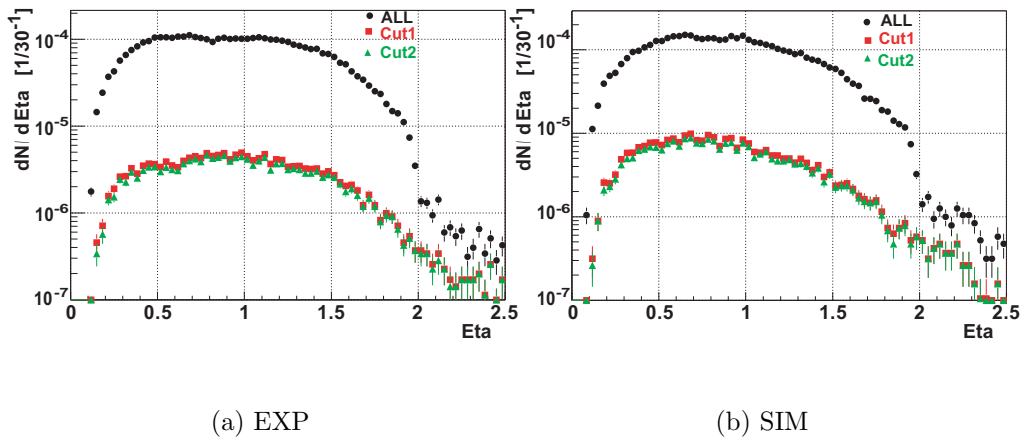
Figure 6.10: *Pseudorapidity distribution for e^+e^- pairs plotted for different conditions for experimental (a) and simulated (b) data.*

(a) p_T

(b) η
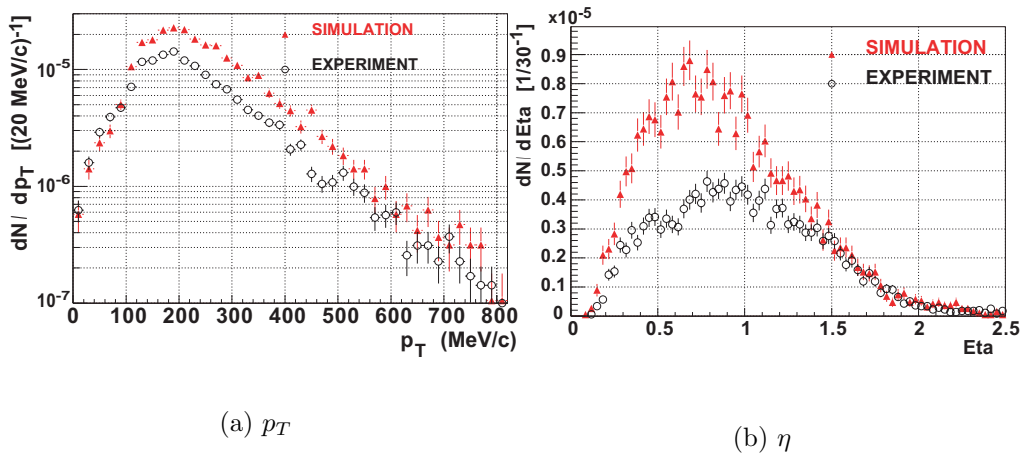
Figure 6.11: *Tranverse momentum (a) and Pseudorapidity (b) distribution of e^+e^- pairs plotted after Cut 1 and Cut 2 have been applied for experimental (empty circles) and simulated (full triangles) data.*

original shape of the dilepton distribution (See Figure 6.10 the first curve) and become more pronounced in the mid-rapidity region where the particle multiplicity is higher.

6.1.2 Combinatorial background

It has already been recalled that the dominant sources of dilepton pairs are γ conversion and π^0 Dalitz decay. These decays lead to the production of unlike-sign pairs (electron-positron). Since leptons pairing is done by creating all the possible combinations of negative N_- and positive tracks N_+, combinatorial background arises over the full invariant mass range from the the combinations of tracks which do not belong together. Even after rejecting all the combinations and all the leptons which carry a significant signature of γ conversion origin, the problem of extracting the desired correlated unlike-sign pair S_{+-}^{corr} is still unresolved. Therefore a statistical procedure has to be used to determine the combinatorial background, i.e. a distribution of *uncorrelated* pairs N_{+-}^{uncorr}, which subtracted from the unlike-sign sample N_{+-}^{total} after a proper normalization, gives the real physics signal S_{+-}^{corr}:

$$S_{+-}^{corr} = N_{+-}^{total} - N_{+-}^{uncorr} \qquad (6.3)$$

Two techniques are known and commonly employed for the definition of the combinatorial background: the like-sign technique and the mixed-event technique. The first methods is based on the fact that the same-event combinatorial like-sign background is a good approximation for the combinatorial unlike-sign background, in the absence of correlated like-sign pairs from physics origin, providing that acceptance and efficiency for electrons and positrons are tha same. In the mixed-event technique unlike-sign tracks from different events, therefore uncorrelated, are combined to yield the combinatorial like-sign background.

Like-sign technique

The multiplicity k of electrons N_- and positrons N_+ produced in a collisions can be described based on the average multiplicity of electrons $\overline{N_-}$ or positrons $\overline{N_+}$ by a Poisson probability distribution

$$P(N_\pm = k) = \frac{\overline{N_\pm}^k}{k!} e^{-\overline{N_\pm}} \qquad (6.4)$$

The probability B to observe $n_\pm$ tracks out of $N_\pm$ initial particles is binomially distributed

$$B(n_\pm = k) = \frac{N_\pm}{k!(N_\pm - k)!}(\epsilon_\pm)^k (1 - \epsilon_\pm)^{N_\pm - k} \qquad (6.5)$$

The probability to observe a lepton track ϵ is a product of the detector acceptance and efficiency and the reconstruction efficiency; the magnetic field of HADES produces an asymmetry in the e^+ and e^- acceptance, while the

reconstruction efficiency is fully symmetric; however the purity is strongly affected by the different background in the positive and negative particle spectra.

From Equation 6.5, the average number of reconstructed tracks is expressed as

$$\overline{n_+} = \epsilon_+ N_+, \ \overline{(n_+)^2} = \epsilon_+(1 - \epsilon_+)N_+\epsilon_+^2 N_+^2 \qquad (6.6)$$
$$\overline{n_-} = \epsilon_- N_-, \ \overline{(n_-)^2} = \epsilon_-(1 - \epsilon_-)N_-\epsilon_-^2 N_-^2$$

In first-order approximation, the mean number of pairs per event with N_+ positrons and N_- electrons is given by

$$\overline{n_{++}} \ = \ \kappa_{++} \sum_{k=0}^{N_+} \frac{k(k-1)}{2} B(n_+ = k) = \frac{1}{2}\kappa_{++}\epsilon_+^2 N_+(N_+ - 1) \qquad (6.7)$$

$$\overline{n_{--}} \ = \ \kappa_{--} \sum_{k=0}^{N_-} \frac{k(k-1)}{2} B(n_- = k) = \frac{1}{2}\kappa_{--}\epsilon_-^2 N_-(N_- - 1)$$

$$\overline{n_{+-}} \ = \ \kappa_{+-} \sum_{k=0}^{N_+} \sum_{l=0}^{N_-} kB(n_+ = k)lB(n_- = l) = \kappa_{+-}\epsilon_+\epsilon_- N_+ N_-$$

The factor κ denotes two-tracks efficiency introduced by physics correlation, detector or reconstruction.

From Equation 6.7, the number of pairs, averaged over all events is:

$$\langle n_{++} \rangle \ = \ \sum_{N_+=0}^{\infty} \overline{n_{++}}P(N_+) \qquad (6.8)$$

$$= \ \frac{1}{2}\kappa_{++}\epsilon_+^2 \sum_{N_+=0}^{\infty} N_+(N_+ - 1)P(N_+)$$

$$= \ \frac{1}{2}\kappa_{++}\epsilon_+^2 (\overline{N_+})^2$$

$$\langle n_{--} \rangle \ = \ \sum_{N_-=0}^{\infty} \overline{n_{--}}P(N_-) = \frac{1}{2}\kappa_{--}\epsilon_-^2 (\overline{N_-})^2 \qquad (6.9)$$

$$\langle n_{+-} \rangle \ = \ \sum_{N_+=0}^{\infty} \sum_{N_-=0}^{\infty} \overline{n_{+-}}P(N_+)P(N_-) = \kappa_{+-}\epsilon_+\epsilon_- \overline{N_+ N_-} \qquad (6.10)$$

Equation 6.10 represents the unknown unlike-sign combinatorial background. A comparison of $\langle n_{++} \rangle$ and $\langle n_{--} \rangle$ with $\langle n_{+-} \rangle$, shows that the geo-

metric mean of like-sign background is a good approximation for the unlike-sign combinatorial background

$$\underbrace{\langle n_{+-} \rangle}_{\text{UN-LIKE SIGN BG}} \equiv \underbrace{2\sqrt{\langle n_{++} \rangle \langle n_{--} \rangle}}_{\text{LIKE SIGN BG}}$$

$$\kappa_{+-}\epsilon_+\epsilon_-\overline{N_+ N_-} \equiv \sqrt{\kappa_{++}\kappa_{--}}\,\epsilon_+\epsilon_-\overline{N_+ N_-} \tag{6.11}$$

providing that

$$\kappa_{+-} = \sqrt{\kappa_{++}\kappa_{--}} \tag{6.12}$$

i.e. the two-track efficiency κ is pair-charge independent. In case of HADES this is not fully true, as will be shown in Appendix D, therefore a factor $K = \dfrac{\kappa_{+-}}{\sqrt{\kappa_{++}\kappa_{--}}}$ is introduced in the combinatorial background. However a charge asymmetry of the single track reconstruction probability ϵ does not affect the results.

The necessary assumption to use this technique is that the like-sign pair are uncorrelated, i.e. are not produced by the same process. This assumption can be considered true as the *correlated* like-sign pair production requires higher-order processes, the strongest of those, $\pi^0 \rightarrow e^+e^+e^-e^-$ which is however charge symmetric, is suppressed by a factor ~ 380 relative to the π^0 Dalitz decay.

This technique, widely used by the CERES experiment [68], is used by HADES as well, especially because the like-sign combinatorial background allows to reproduce the enhancement at small opening angles resulting from the kickplane combinatorics.

Mixed-event technique

The mixed-event technique computes the combinatorial background by pairing un-like sign tracks from different events; this strategy leads to inherently uncorrelated pairs. Modifying the Equation 6.7, the mean number of mixed unlike-sign pairs from two randomly chosen events A and B with initial multiplicity $N_\pm^A$ and $N_\pm^B$ is

$$\overline{n_{+-}^{mix}} = \sum_{k=0}^{N_+^A}\sum_{l=0}^{N_-^B} kB(n_+^A = k)lB(n_-^B = l) + \sum_{k=0}^{N_-^A}\sum_{l=0}^{N_+^B} kB(n_-^A = k)lB(n+^B = l) \tag{6.13}$$

where each track of event A is combined with all the tracks of event B with opposite charge. Averaging over many pairs of events

$$\langle n_{+-}^{mix} \rangle^{AB} = \sum_{i=1}^{\infty} \sum_{k=1}^{\infty} \overline{n_{+-}^{mix}} P^A(i) P^B(k)$$

$$\epsilon_+^A \epsilon_-^B \overline{N_+^A N_-^B} + \epsilon_-^A \epsilon_+^B \overline{N_-^A N_+^B} \tag{6.14}$$

Finally the mixed unlike-sign distribution has to be normalized with the number of mixed-events pairs N_{mix}

$$\langle n_{+-}^{mix} \rangle = \frac{N_{exp}}{N_{mix}} \langle n_{+-}^{mix} \rangle^{AB} = \overline{\epsilon_- \epsilon_+}\, \overline{N_- N_+} \tag{6.15}$$

where N_{exp} is the total number of fully analyzed events, including those with lepton multiplicity 0 and lepton multiplicity 1 which do contribute to the mixing procedure.

Comparing Equation 6.10 and 6.15, it can be shown that the mixed event technique provides a good approximation of the "real" combinatorial background

$$\langle n_{+-}^{mix} \rangle \equiv \langle n_{+-} \rangle$$

$$\overline{\epsilon_- \epsilon_+}\, \overline{N_- N_+} \equiv \kappa_{+-} \epsilon_- \epsilon_+ \overline{N_- N_+} \tag{6.16}$$

if the conditions

$$\epsilon_- \epsilon_+ = \overline{\epsilon_- \epsilon_+} \tag{6.17}$$

$$\kappa_{+-} = 1 \tag{6.18}$$

are fulfilled.

The condition 6.18 can be experimentally approximated by mixing events with similar properties (particle multiplicity, lepton multiplicity) and averaging over all the event classes. The condition 6.18 corresponds to an perfect two-tracks resolution and is therefore approximately fulfilled for large opening angle pairs, surely not for small opening angle pairs. Since the HADES focus in this first experimental runs is quite on the continuum low-mass dilepton spectra, and for the reasons mentioned above (See Like-sign technique), the technique selected for the computation of the combinatorial background is the like-sign one and the N_{+-}^{uncorr} of Equation 6.3 is provided by 6.10.

Figure 6.12 shows the total N_{+-}^{total} invariant mass spectrum together with the combinatorial background N_{+-}^{uncorr} calculated with the like-sign technique

as geometrical mean of the N_{++} and N_{--} distribution and with the two-track efficiency factor $K = 0.995$ (See Appendix D) for experimental (a) and simulated (b) data. The figure shows that the contribution at high invariant mass are merely unphysical since they are well reproduced by the background. The expected most dominant sources of the dilepton signal are π^0 and, to a much smaller extent, η Dalitz decays up to 150 MeV/c^2.

(a) EXP   (b) SIM
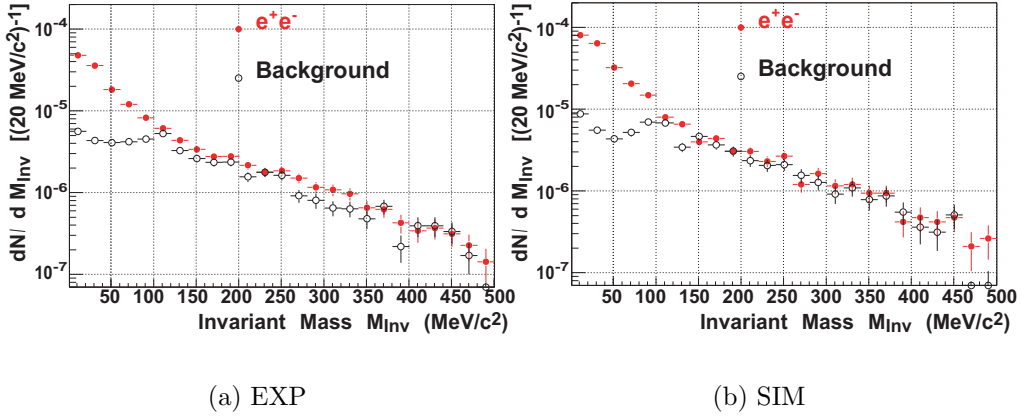
Figure 6.12: *Invariant mass distribution of all e^+e^- pairs (N_{+-}^{total}) and combinatorial background (N_{+-}^{uncorr}) calculated with the like-sign technique for experimental (empty circles) (a) and simulated (full triangles) (b) data.*

Finally the combinatorial background N_{+-}^{uncorr} is subtracted from the total yield of unlike-sign N_{+-}^{total} pairs and the resulting signal S_{+-}^{corr} is shown in Figure 6.13 in a comparison between simulated and experimental data. In the low mass region (π^0 Dalitz) simulations overestimate data by factor $\sim 2 - 3$ while in higher mass region the agreement between simulations and data significantly improves. While discrepancies are still present in the single lepton yields, the efficiency for close tracks reconstruction requires further investigations. Moreover the normalization factor applied in simulations which takes into account an overestimation by 20-30% of pion production in UrQMD with respect to the one measured by TAPS, comes from an extrapolation to the full rapidity interval assuming a homogeneous distribution. The shape of the π^0 Dalitz decay can be recognized in the low-mass region, while the lack of statistics does not allow any conclusions for the higher mass range.

The signal obtained in the simulated data is now compared to the contributions of the different dilepton sources in Figure 6.14. The combinatorial background is a good estimation to suppress the uncorrelated yield at large opening angle (See Figure 6.3 (b)). Even after the background subtraction
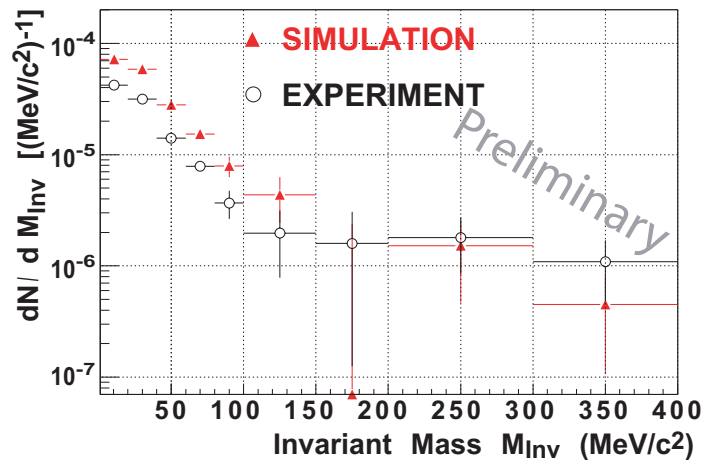
Figure 6.13: *Invariant mass distribution of all e^+e^- pairs (N_{+-}^{total}) after subtraction of the combinatorial background (N_{+-}^{uncorr}) calculated with the like-sign technique for experimental(empty circles) and simulated (full triangles) data. The variable bin size takes into account the reduced statistics at higher invariant mass.*

the signal still exceeds the sum of the different contribution and improvements, such as the correction for efficiency and acceptance, are still needed.
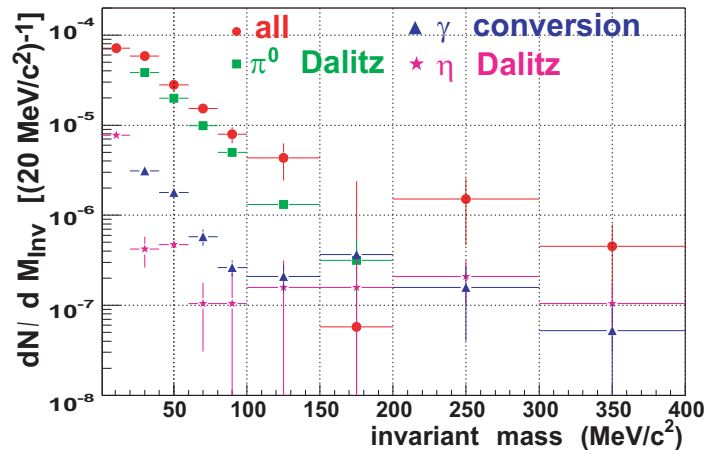
Figure 6.14: *Contribution of the different dilepton sources (π^0 Dalitz decay, η Dalitz decay, and external γ conversion) as a function the invariant mass compared to the distribution of all e^+e^- pairs (N_{+-}^{total}) after subtraction of the combinatorial background -* **NOV01 SIM**.

6.2   November 2002 data

The main focus of November 2002 runs is to explore the low-mass continuum region of the invariant mass spectrum with higher statistics available than in November 2001, and better resolution due to the higher number of MDCs installed. With more severe cuts on opening angle it is also possible to investigate other contribution than the π^0 Dalitz, like for instance the η Dalitz decay.
However the preliminary analysis presented in the framework of this thesis, the low-resolution tracking (kickplane method) still employed, half of the collected statistics not analyzed, the preliminary calibration and alignment, the still missed analysis of the empty-target events, the still missed simulations with the new improved detector set-up, do not allow to draw any quantitative conclusion at this point.
The same cuts tuned with the analysis of November 2001 data have been applied on dileptons. More emphasis will be put on the opening angle cut at 8° which allows to explore the region above π^0. Figure 6.15 shows, as a function of the opening angle for e^-e^- (a), e^+e^+ (b), e^+e^- (c), the reduction obtained with the different cuts:
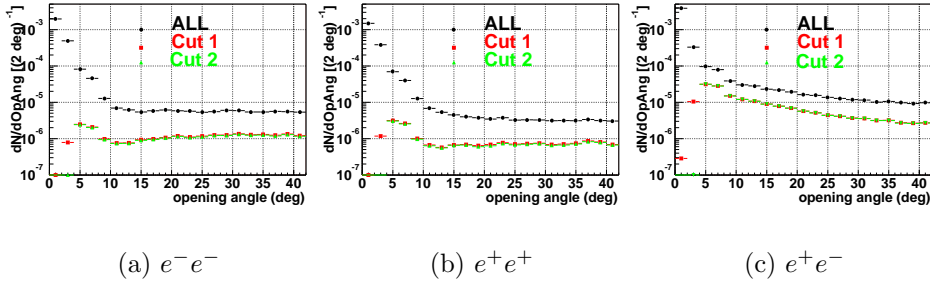
(a) e^-e^- (b) e^+e^+ (c) e^+e^-

Figure 6.15: *Opening angle distribution for e^-e^- (a), e^+e^+ (b), e^+e^- (c) pairs plotted for different conditions.*

Even in this case the most significant reduction is carried by Cut 1, especially for the like-sign pairs. Moreover the cut suppresses the like-sign pairs stronger the unlike-sign ones, like in the data set of November 2001.
In Table 6.2 the overall amount of e^-e^-, e^+e^+, and e^+e^- pairs normalized by the number of collected events is summarized as a function of the different cuts.
 The multiplicities in the Table have been scaled by the enhancement factor calculated for dilepton contents due to LVL2 and LVL3 with respect to LVL1 events calculated in Chapter 9 and presented in Table 9.2. On average the

N. of Cut	e^+e^+	e^-e^-	e^+e^-
all $[10^{-3}]$	2.1	2.8	4.9
1 $[10^{-5}]$	4.1	4.8	22.3
2 $[10^{-5}]$	3.8	4.5	20.9
3 $[10^{-5}]$	2.9	3.8	13.2

Table 6.2: *Overall amount of e^-e^-, e^+e^+, and e^+e^- pairs per event as a function of the different cuts* **NOV 02 - EXP**.

yield is higher than in November 2001 data set. This can be traced back to a higher yield in the single lepton tracks and can be also explained with the preliminary character of the November 2002 analysis which leaves more room for lepton misidentification and signal impurity.

Figure 6.16 shows the opening angle distribution together for e^-e^-, e^+e^+, and e^+e^- pairs after Cut 1 and Cut 2 (a) or after Cut 1 and Cut 3 (b) have been applied. The strong opening angle cut (8°) removes the artefacts of the kickplane combinatorics, while the higher statistics collected in November 2002 runs allows to explore larger opening angle pairs.
Again the difference between e^-e^- and e^+e^+ distribution is explained by the geometrical acceptance at larger opening angles while a good agreement is obtained at low opening angles (visible especially in Figure 6.16 (a)) thanks to the kickplane artefacts.

(a) CUT 2   (b) CUT 3
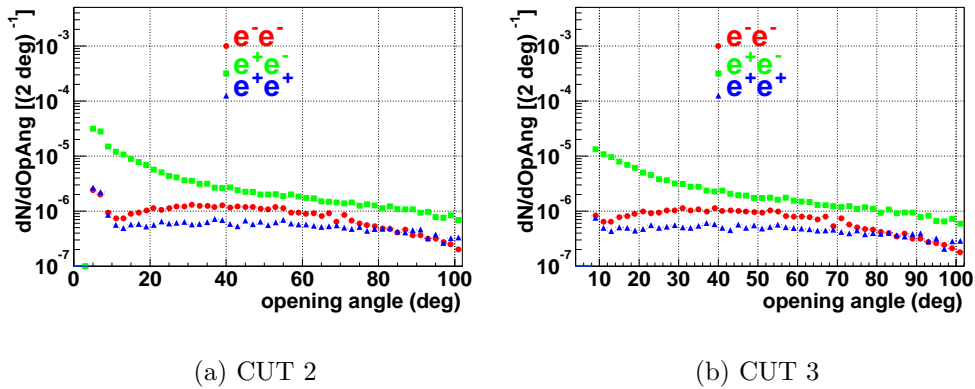
Figure 6.16: *Opening angle distribution for e^-e^-, e^+e^+, and e^+e^- pairs plotted after Cut 1 and Cut 2 (a) or after Cut 1 and Cut 3 (b) have been applied.*

Figure 6.17 shows respectively, as a function of the invariant mass for

e^-e^- (a), e^+e^+ (b), e^+e^- (c), the reduction obtained with the different cuts. Figure 6.18 shows the invariant mass distribution together for e^-e^-, e^+e^+,
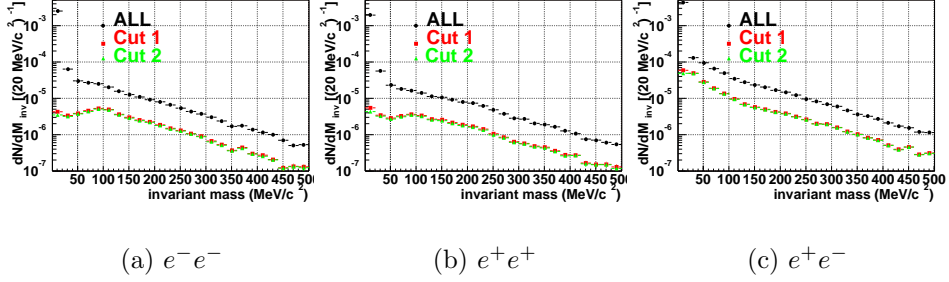
(a) e^-e^- (b) e^+e^+ (c) e^+e^-

Figure 6.17: *Invariant mass distribution for e^-e^- (a), e^+e^+ (b), e^+e^- (c) pairs plotted for different conditions.*

and e^+e^- pairs after Cut 1 and Cut 2 (a) or after Cut 1 and Cut 3 (b) have been applied. As also shown in Figure 6.16, the stronger opening angle cut (8°) removes all the artificial enhancements at small invariant mass, together, since the cut also removes the single-leptons from the lepton sample, with a significant part of the combinatorial background. Even in this case, it is possible to see that the higher statistics collected in November 2002 runs allows to explore larger invariant mass pairs.

(a) CUT 2   (b) CUT 3
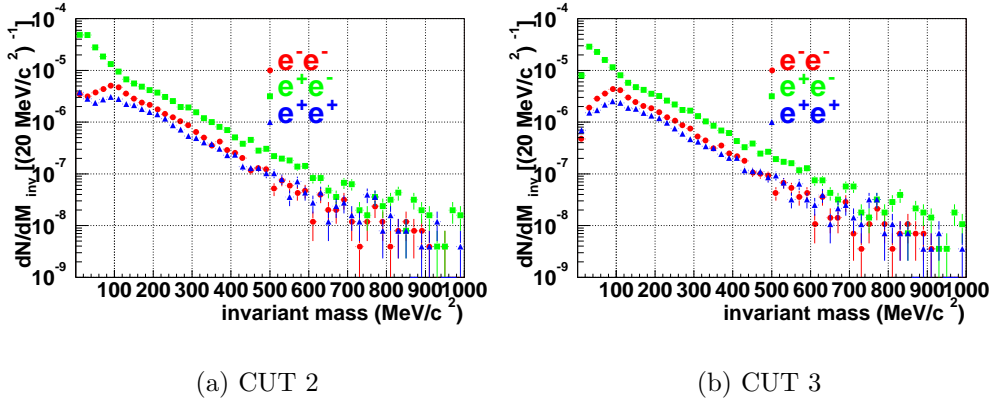
Figure 6.18: *Invariant mass distribution for e^-e^-, e^+e^+, and e^+e^- pairs plotted after Cut 1 and Cut 2 (a) or after Cut 1 and Cut 3 (b) have been applied.*

Figure 6.19 shows the distribution of transverse momentum (a) and pseu-

dorapidity (b) of the unlike-sign pairs after Cut 1 and Cut 2 or Cut 1 and Cut 3 have been applied. The stronger opening angle cut (Cut 3) does not change the shape of the transverse momentum, while for the pseudorapidity a stronger suppression in the mid rapidity region occurs. This is most likely connected to the higher particle multiplicity, and the suppression obtained with Cut 3. The shape of the distributions does not change significantly with
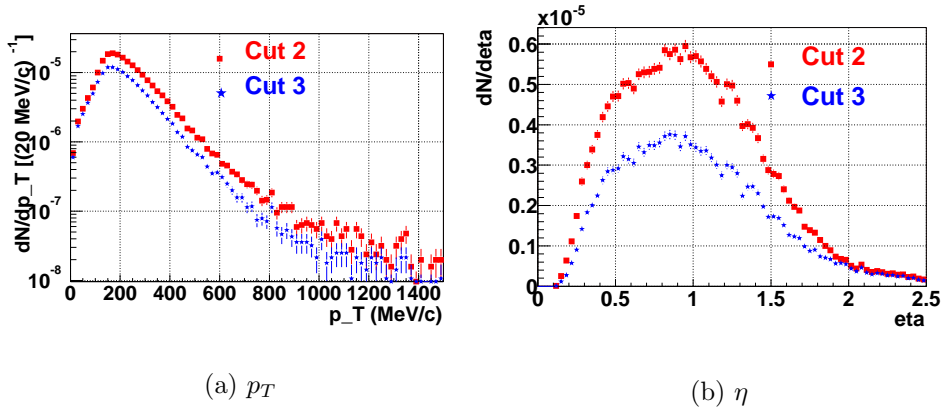
(a) p_T (b) η

Figure 6.19: *Tranverse momentum (a) and Pseudorapidity (b) distribution of e^+e^- pairs plotted after Cut 1 and Cut 2 or after Cut 1 and Cut 3 have been applied* **NOV 02 - EXP**.

the two cuts (Cut 2 and Cut 3), i.e. with 4° or 8° opening angle cut and the dominant part of the transverse momentum spectrum is still the one below 200 MeV/c, i.e. the kinematics region of Dalitz decays. The shape of all the distributions are in good agreement with the ones obtained in November 2001. Therefore even in this case the region of mid-rapidity presents a drop with respect to the yield in simulated data.

The combinatorial background has been estimated as in November 2001 with the like-sign technique with the two-track efficiency factor $K = 0.995$. Figure 6.20 shows the total N_{+-}^{total} invariant mass spectrum together with the combinatorial background N_{+-}^{uncorr} for the different opening angle cuts Cut 2, i.e. 4° (a) or Cut 3, i.e. 8° (b).

The combinatorial background N_{+-}^{uncorr} is finally subtracted from the total yield of unlike-sign N_{+-}^{total} pairs and the resulting signal S_{+-}^{corr} is shown. Figure 6.21 shows a comparison between the signal resulting after the 4° and the 8° opening angle cut. The shape of the π^0 Dalitz decay can be recognized in the low-mass region, in the intermediate region the η contribution can be distinguished. The larger opening angle cut (8°) reduces the yield only in

(a) CUT 2

(b) CUT 3
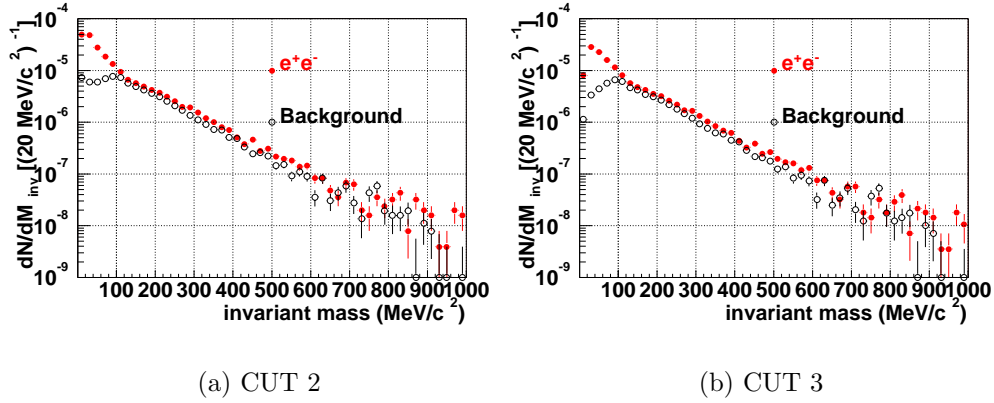
Figure 6.20: *Invariant mass distribution of all e^+e^- pairs (N_{+-}^{total}) and combinatorial background (N_{+-}^{uncorr}) calculated with the like-sign technique for opening angle cut at 4° (a) or 8° (b).*
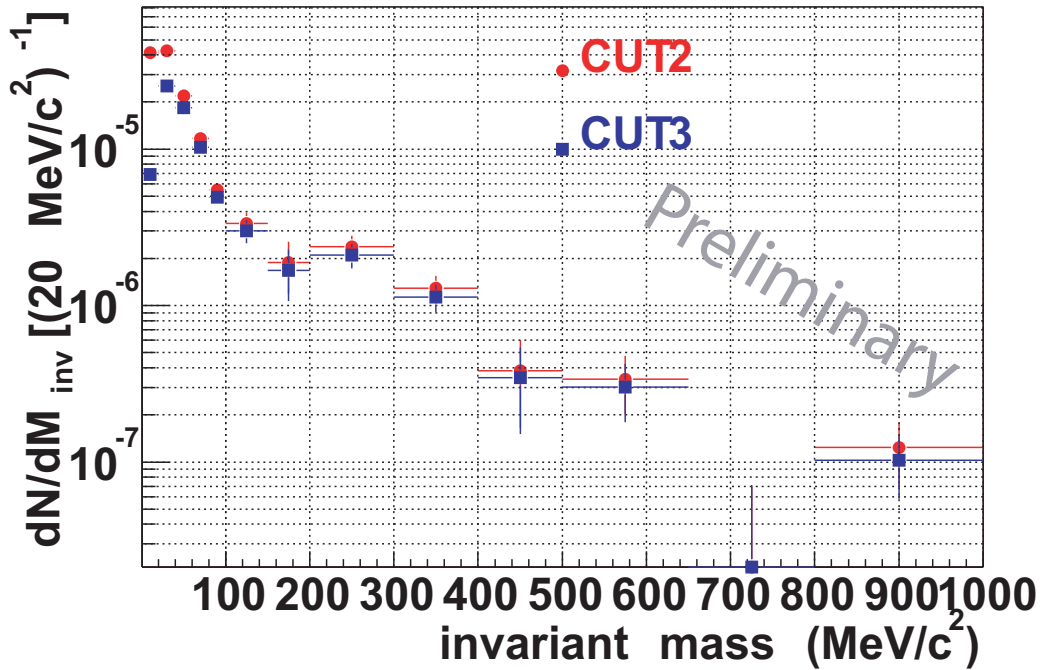
Figure 6.21: *Invariant mass distribution of all e^+e^- pairs (N_{+-}^{total}) subtracted by the combinatorial background (N_{+-}^{uncorr}) calculated with the like-sign technique for 4° and 8° opening angle cut. A variable bin size has been chosen to take into account the reduced statistics at higher invariant mass.*

the first two bins.

As useful comparison, the signal resulting after the background subtraction is plotted together for November 2001 and November 2002 data in Figure 6.22.

(a) CUT 2

(b) CUT 3
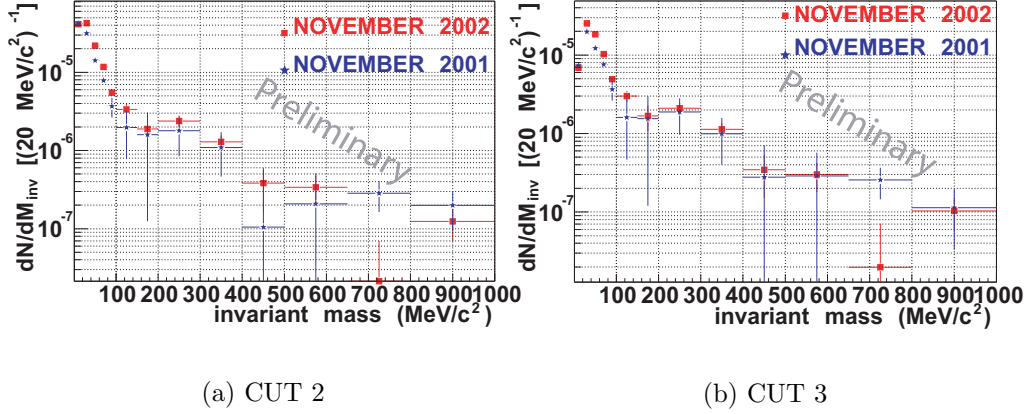
Figure 6.22: *Invariant mass distribution of all e^+e^- pairs (N_{+-}^{total}) subtracted by the combinatorial background (N_{+-}^{uncorr}) calculated with the like-sign technique for November 2001 and November 2002 data after Cut 1 and Cut 2 (a) or after Cut 1 and Cut 3 (b) have been applied. A variable bin size has been chosen to take into account the reduced statistics at higher invariant mass.*

Both the spectra have been normalized with the number of collected LVL1. For the November 2002 the enhancement factor of the LVL2-LVL3 trigger (calculated in Chapter 9) has been used for the normalization. Figure 6.22 shows the signal separately for cut 2 and Cut 3. Cut 3 provides a stronger suppression, emphasizing the distinction between the π^0 Dalitz region and the rest of the spectrum. The agreement between the two data sample is quite good. The higher statistics collected in November 2002, also thanks to the background event rejection of the trigger, clearly visible from the much smaller error bars, allows investigations over a wider invariant mass range. Moreover the impact of the trigger, which will be discussed later in Chapter 9, results in a strong dilepton enhancement.

6.3 Systematic Error

In the previous sections the dilepton pairs spectra were described in terms of the quantities invariant mass, transverse momentum, pseudorapidity and opening angle. Since these quantities are derived from observables of the

experiment, an estimation of the systematical errors for the relevant observables and the influence of these errors on the derived quantities has to be made.

The required experimental observables are mainly the momentum of the electron and positrons and their respective angular coordinates (i.e. polar and azimuthal angle). The angular position of a particle is determined by the track finder algorithm. This algorithm introduces an average error of 0.19 mrad for the polar angle and 1 mrad for the azimuthal angle [127].
Additionally the determination of the particle's original emission angle is affected by multiple scattering mainly in the RICH detector. This energy dependent contribution leads to an uncertainty of approximately 5.5 mrad for each angular coordinate in case of an electron of 0.5 GeV/c [102].
The error in the reconstructed momentum increases with momentum. With the kick plane method it varies between 4% and 10% in the relevant momentum range and it leads to higher deviations for smaller momenta.

These errors propagated in the variables which describe the dilepton signal amount to about 10% on the average transverse momentum, about 2% on the rapidity over the full range, and an error on the invariant mass varying between 5% in the region of 100 MeV/c^2 and 10% in the region of 400 MeV/c^2 [102].

Statistical errors, shown through the discussion, are far below the systematic errors. The data sample of November 2002 brings a significant improvement in this sense.

Part III

PERFORMANCE OF THE HADES DILEPTON TRIGGER

In this part the HADES second level trigger (LVL2) is characterized in terms of performance of the single electronic circuit boards as well as lepton and dilepton efficiency and event reduction of the full system. The reference system for this analysis are simulated lepton and dilepton distribution as well as the experimental lepton and dilepton signal deduced and described in Part II. These studies of the LVL2 have been mainly developed along two main directions:

- the performance of the single components: the purpose of this analysis is to monitor of the proper functionality of the individual hardware components;

- the performance of the full system: here the goal is to understand qualitatively and quantitatively the efficiency, the background suppression and the potential bias introduced by the LVL2 on the physics properties, by varying the parameters used in the system.

All the LVL2 boards have been emulated in software. This allows to check the functionality of the single electronic boards, test and optimize the LVL2 algorithms and emulate the functionality of the full LVL2 system even when it is not operational with both real and simulated data.
Tests of the functionality of all the single boards are presented in Chapter 7, showing the expected behavior with less than 1% discrepancy. The event reduction rate achieved with the LVL2 are also discussed.

Chapter 8 is fully dedicated to the study of the Rich IPU performance, since the ring recognition algorithm is the most selective component of the LVL2 and it is the only one which significantly differ from the one used offline. The efficiency has been studied with simulations of events consisting of one electron and with simulated electrons embedded in a realistic environment of simulated events. Furthermore overlapping and non-overlapping rings (close and open pairs) have been studied and the LVL2 finally has been compared to the offline ring finder. Since both the online and the offline ring finder algorithms are dominated by misidentified rings, the comparison is performed on the basis of lepton candidates.

Chapter 9 deals with the performance of the full system. The efficiency of the Shower condition applied in the corresponding IPU, and the influence of the Matching Unit are analyzed. The performance of the full LVL2 is estimated with the analysis of data collected in November 2002, when the LVL2 was operational and a significant fraction of non-triggered events was collected.

Chapter 7

Hardware Performance of the Second Level Trigger

Anyone who has never made a mistake has never tried anything new.

(Albert Einstein)

The Second Level Trigger (LVL2) has been designed and built by the HADES-Giessen group, brought into operation fully integrated with the rest of the HADES data acquisition system, and finally used for the first time as event selector in the November 2002 run with a C+C reaction at 2AGeV. The LVL2 has been designed to run at the event rate of 10^5 Hz[1], that means to deliver a trigger (i.e. a decision for the event: to accept it or discard it) on average every 10 μs. However, by splitting the full algorithm in several smaller processes, each of which can be processed in the required time of 10 μs, and pipelining the data into the next step, the trigger algorithm can take more than 10 μs to process a single event at the expenses of a delay. This introduces a delay (*latency*) between LVL1 and LVL2, which is fixed to a maximum of 200 μs since the buffer memories allow to store a maximum of 20 events.

In the November 2002 run, when all the components of the LVL2 were operational and the trigger condition was ≥ 1 lepton within the matching window $\Delta\phi < 8° \pm \frac{\phi_{RICH}}{4}$, very conservative condition on Tof (20 ns), Shower IPU operated only with a local maximum search, ring and veto thresholds set to 8 and 3 for the Rich IPU, respectively a rate of 7 kHz in the LVL1 and 1.1

---

[1]10^5 Hz is the conceptual design goal, the lower rate achievable by the LVL2 hardware is mainly determined by the current version of the Matching Unit hardware with limited processing resources; in addition other limiting factors are different DAQ components and the interaction of the single components with their BUSYs (LVL1, LVL2, internal).

kHz in LVL2 were achieved, with an event reduction[2] of ≈ 12.

7.1   Hardware Performance

The studies of the hardware performance, i.e. the analysis of the behavior of the single boards, has been of quite importance during the phase when the LVL2 was finally brought into operation. This was the way errors and faults both in the hardware itself and the in implementation of the algorithms in the hardware could be detected and corrected [138].

All the components of the LVL2 have been *emulated*[3] in software, taking
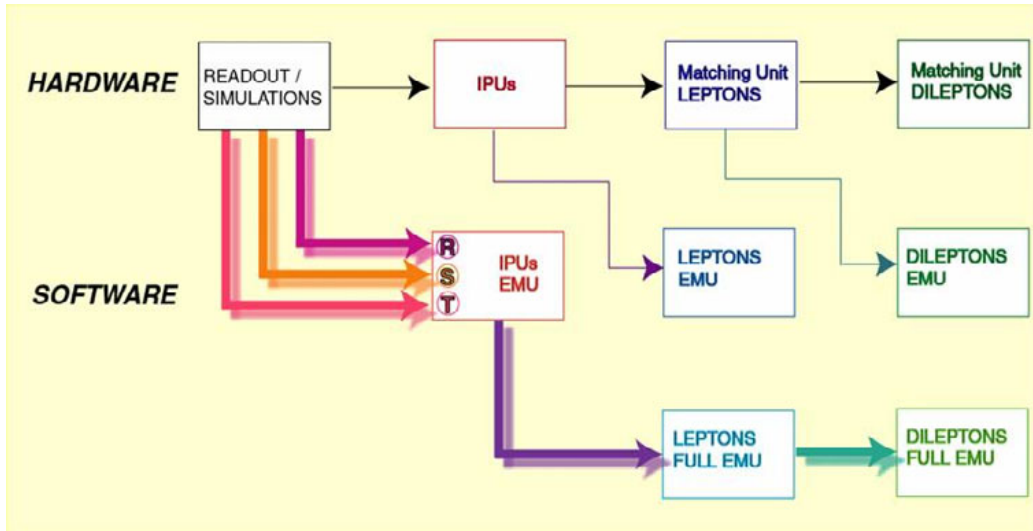
Figure 7.1: *Schematic view of the trigger emulation software. The path of the data in the hardware is at the top of the figure. The first Emulation level always takes input data from the immediately previous step. The full Emulation is meant to be fully independent on the trigger boards and to run even when the trigger is not operational or with simulated events.*

as input exactly the same data as the board which is emulated; all the processing steps the LVL2 is splitted into are individually emulated, in order to be able to identify where a discrepancy is. Figure 7.1 shows a schematic view of the LVL2 emulation software, which will be technically described in

---

[2]$\frac{7}{1.1} < 12$ because of the downscaled events.

[3]the difference between *simulation* and *emulation* has to be stressed here: the emulation does *exactly* what the hardware does, exactly with the same rounding, cutoff, characteristics of the hardware.

Appendix E.
The first Emulation level always takes input data from the immediately previous step, for instance the Rich IPU Emulation takes input from `HRichRaw` and produces the output `HRichHitIPU` which contains exactly the same objects as `HMatchURich`, i.e. the output container of the Rich IPU board. This is the same for all the IPUs. The MU lepton Emulation takes input from the IPUs containers (`HMatchURich`, `HMatchUShower`, `HMatchUTof`) and produces `HMUEMULeptons`, which contains exactly the same objects as `HMULeptons`, i.e. the output container of the MU. The same is true for the dilepton emulation. In case the trigger is not operational, or to reproduce the response of the trigger with simulated data, the full Emulation runs the lepton and dilepton matching algorithm, not based on the IPU boards containers but on the IPU Emulation containers which have been filled with the Emulation process taking data from the read-out (`Raw` or `CalSim` containers).

Hardware and software-emulation results can be compared on the hit level with a 1:1 correspondence; this means that one hit from a sample is compared with only one hit from the other sample, the closest possible in the other sample, to see whether the hit is found, if it is found exactly in the same position, or if it is not found at all. This allows to establish a percentage of *discrepancies*, which are a quality parameter of the functionality of the hardware[4].

7.1.1   Rich IPU

With respect to the other boards, the Rich IPU presents a higher complexity, because the final results delivered as lepton signature is not expressed in the original coordinate space (i.e. the pads), but on a derived parameter space (i.e. the ring centers).
The emulation of the Rich IPU takes as input data from the raw container of the Rich (`HRichRaw`), i.e. position in detector coordinates (row and columns) of the fired pads after a pedestal-comparison[5].
  One of the first problems which creates potential uncertainties in this reconstruction, especially if compared with the other IPUs, is that the Rich IPU does not have included the Read-Out functionality, but instead gets the information about the fired pads from a Read-Out Controller, which sends them as well to the Event Builder, and therefore to the data stream, from

---

[4]except for the case of the Rich IPU where it is not possible to check the information on the pad pattern which is transferred to the IPU board.

[5]the difference between pedestal-comparison and the more standard expression pedestal-subtraction has already been explained in 4.2
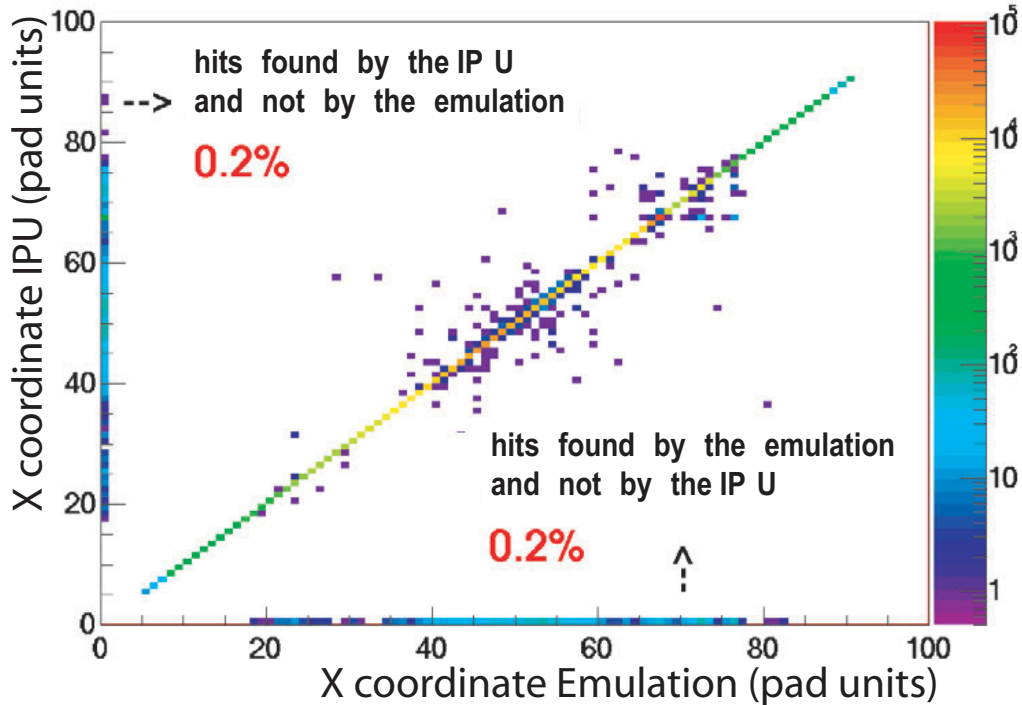
Figure 7.2: *X pad location for ring centers found by the hardware Rich IPU (vertical axis) plotted versus the location found by the software Emulation of the Rich IPU. The diagonal line corresponds to rings found in the same position by the hardware and the emulation. The entries at the axis correspond to rings found by the IPU and not by the Emulation or vice versa.*

where the `HRichRaw` container is filled. Minor problems have been observed in the transfer of the information about fired pads to the IPU and to the Read-Out, which sometimes is not identical. Moreover, since the ring recognition algorithm evaluates only a few pads inside the full ring mask, and since this evaluation is not done simply counting the pads but evaluating groups of pads, the proper reconstruction of the single pad in the correct position is of crucial importance for the ring recognition. In addition isolated or localized hardware problems may occur in different scenarios.

This could justify the few discrepancies (some few per mill) which are left when comparing hardware with software-emulation. Figure 7.2 shows the comparison between the X coordinate of the centers of the ring found by the IPU and by its emulation: a spatial resolution of 1 pad is obtained with less than 0.4% discrepancies.

7.1.2 Shower IPU

The emulation of the Shower IPU takes as input data from the raw container of the Shower (`HShowerRaw`), since the pedestal-suppression is already performed during the Read-Out. With respect to the Rich IPU, it presents the big advantage that the read-out functionality is fully integrated in the board, so the input information does not need to be splitted in different boards and sent to two different buffers with the risk to introduce discrepancies.

Figure 7.3 shows the comparison between the X coordinate of the local maxima found by the IPU and by its emulation: a spatial resolution of 1 pad is obtained with no discrepancies.
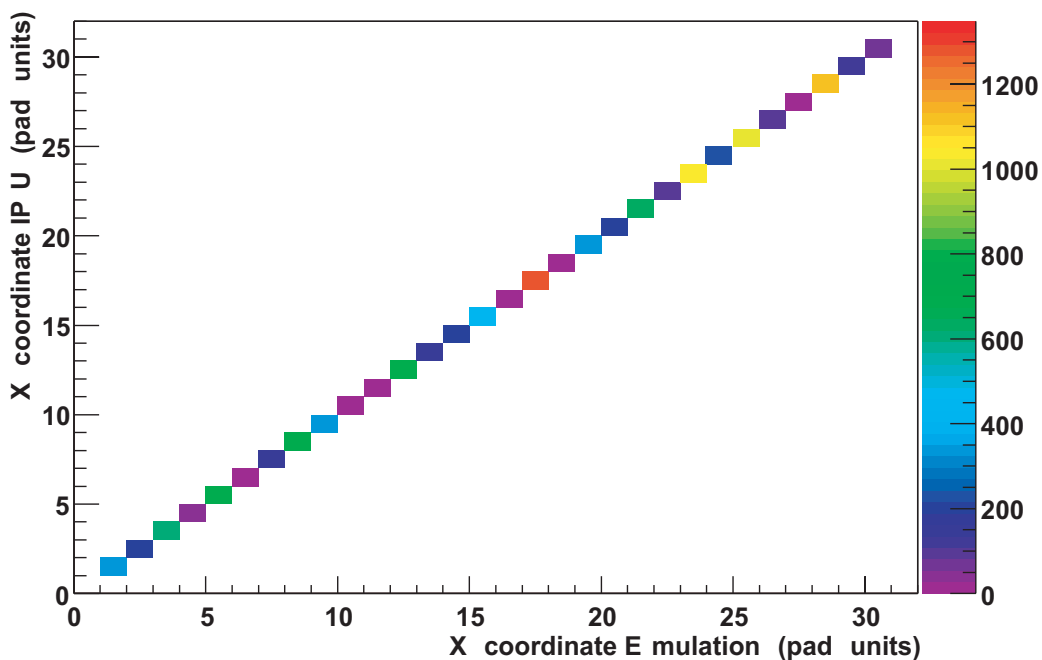
Figure 7.3: *X pad location for hits found by the hardware Shower IPU (vertical axis) plotted versus the location found by the software Emulation of the Shower IPU. The diagonal line corresponds to rings found in the same position by the hardware and the emulation. The entries at the axis correspond to rings found by the IPU and not by the Emulation or vice versa.*

7.1.3   Tof IPU

The Tof IPU algorithm is exactly the same as the one performed offline: calibration of the digital converters, calculation of the time-of-flight and the impact position, walk correction, mapping to angular lab coordinates. The emulation of the Tof IPU therefore coincides with the offline reconstruction, providing that the calibration is the same, and that the start-time, unavailable in the IPU, is re-summed to the offline calculated time.

Since the Start detector is not included in the LVL2, and therefore the start

(a) Time IPU vs Time Emulation

(b) ϕ IPU - ϕ Emulation
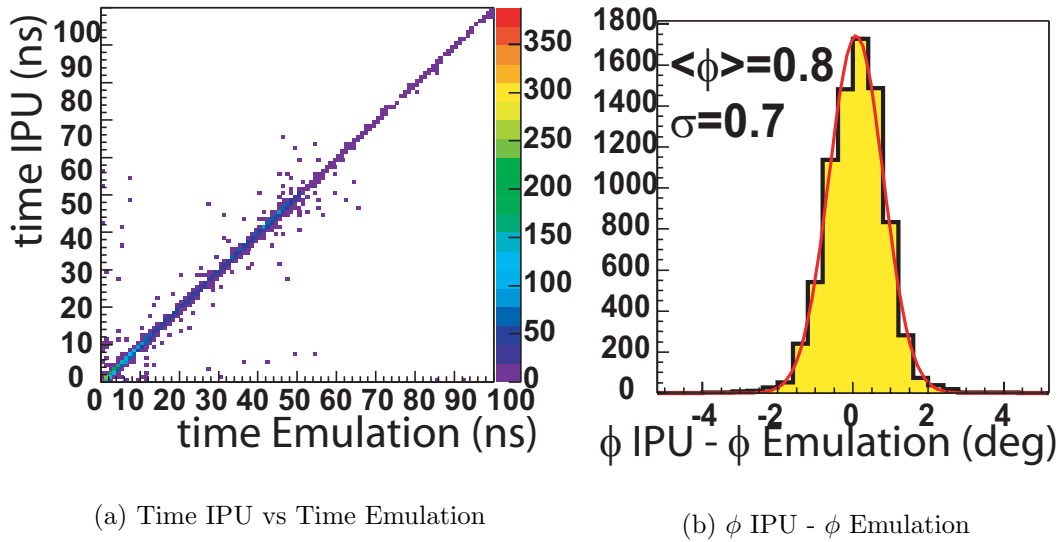
Figure 7.4: *Correlation between Tof IPU and its software emulation. The limitations in resolution reflects the use of different rounding in the hardware and in the software. Figure a) shows the time correlation. Figure b) shows the difference between the azimuthal coordinate calculated by the IPU and by the Emulation. The resolution satisfies the matching requirements.*

time cannot be subtracted, it is necessary to take into account an unknown but estimable offset time when selecting the hits as lepton signatures. Therefore the efficiency merely depends on the calibration precision.
Figure 7.4 shows the time and the azimuthal correlation between Tof IPU and its software Emulation (without Start correction). The Discrepancies are mainly due to border effects[6]. The resolution (due to different rounding and look-up tables used by Offline) fulfills the matching requirements.

---

[6]When a hit is detected out of the detector acceptance, it is cut away. At the borders this leads to some few discrepancies.

7.1.4 Matching Unit

The Matching Unit (MU) emulation performs the two steps of the MU algorithm, namely the lepton and the dilepton selection. The lepton selection takes as input data from the different IPUs, while the dilepton selection uses the MU lepton information, i.e. in both cases part of the MU data stream itself. While the dilepton trigger has been implemented but not fully tested and really employed in a real experiment, the lepton selection is fully tested and gives 100% correlation with the emulation results.

The reduction capability of the matching algorithm depends uniquely on the
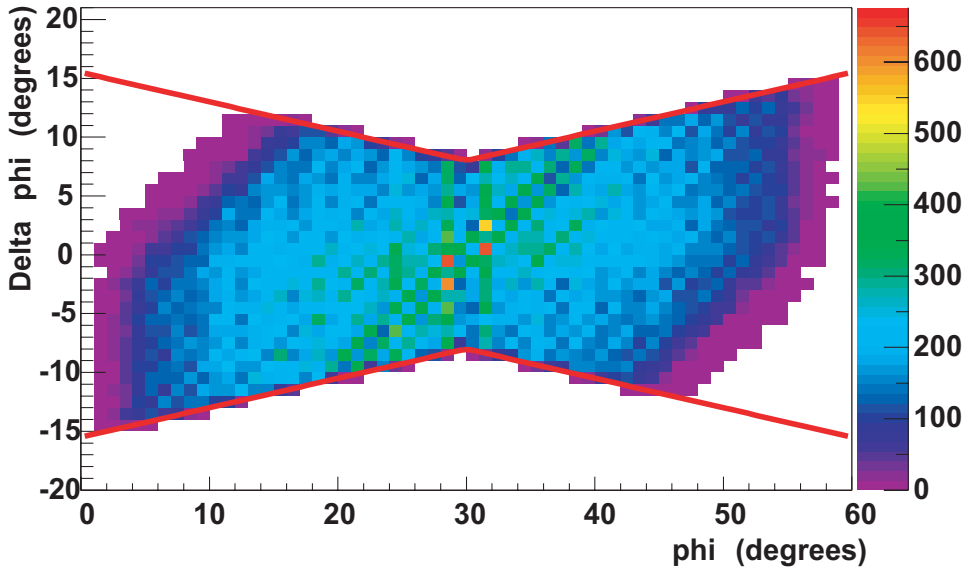
Figure 7.5: $\Delta\phi(\phi_{\mathrm{RICH}} - \phi_{\mathrm{META}})$ *as a function of* ϕ_{RICH} *of all the leptons found by the Matching Unit. All the hits are inside the azimuthally variable matching window, marked in red.*

width of the correlation window. Any cut on the θ polar window would result in a momentum cut, and therefore has not been employed so far, when the focus of the investigation was on the low and middle-mass part of the dilepton spectrum. A big improvement on the ϕ azimuthal matching window, which is also affected, though in a second order, by the magnetic field deflection, occurred with the implementation of ϕ-dependency of the ϕ window itself. This means that the ϕ window, small in the center of the sector where the field is homogeneous and therefore no deflection occurs, is allowed to become broader at the border of the sector where the inhomogeneity increase, with

a linear function

$$\phi_{cut} = \phi_0 + slope \cdot \phi \qquad (7.1)$$

Figure 7.5 shows such a window.

The efficiency of such angular cuts obviously depends also on the detector alignment which can never be calculated and taken into account in the online analysis and therefore the matching window has to be large enough to account for such a correction later on.

The momentum resolution, however relevant only in case of a cut on the invariant mass, not yet performed, is limited by the low resolution of META which is in this case used to extrapolate the position after the magnetic field.

7.2   Event Reduction

Since the electromagnetic decay of the vector mesons $\rho, \omega, \phi \rightarrow e^+ e^-$ is on the order of $10^{-5} - 10^{-6}$, the LVL2 is built to enhance the signal-to-background ratio, that means reduce the events where no such a signature occurs, therefore enhancing the fraction of events with such a signature. The requirements are the capability to reduce background events up to a rate which is writable to tape and does not saturate the read-out capability of all the detectors, without introducing a strong physical bias on the signal of interest. The studies of the performance of the full system consists in optimizing simultaneously (i.e. with the same trigger conditions) the efficiency and the event reduction [139, 140].

The event reduction depends on the reaction and the energy and the quality (focus, halo, ...) of the incoming beam. However the major fraction of triggered events are still events which do not contain any leptons, i.e. the LVL2 is fake-dominated. This is unavoidable with an online analysis and accepted as long as the necessary event reduction is achieved.

Nevertheless, because the LVL2 is fake-dominated, a significant change in the event reduction is expected also depending upon the general conditions of the experimental set-up. This mainly involves effects which can occur in the Rich detector, since the other detectors involved in the trigger are in general no affected by problems like noise, high beam intensity or mis-focused beam, misidentification of particles. This kind of problems, typically arising in the Rich detector, can also have dramatic consequences even in the timing performance of the full system: the MU in fact, starts the lepton search only when at least one ring is detected by the Rich IPU, otherwise the event is immediately discarded. The MU therefore counts on a given reduction achieved already by the Rich IPU, which allows the system to perform at the

full speed; in case such a reduction is not achieved, the MU algorithm would limit the rate capability and therefore the feasibility of experiments where rare signals are searched.

One Ring

Veto Threshold	Ring Threshold 6	7	8	9
1	0.213	0.110	0.051	0.026
2	0.282	0.173	0.094	0.052
3	0.303	0.209	0.132	0.084
4	0.316	0.233	0.166	0.116
5	0.319	0.239	0.177	0.130

One Ring

Veto Threshold	Ring Threshold 6	7	8	9
1	0.240	0.134	0.062	0.032
2	0.298	0.196	0.112	0.064
3	0.311	0.221	0.146	0.095
4	0.318	0.238	0.174	0.125
5	0.319	0.240	0.181	0.136

Two Rings

Veto Threshold	Ring Threshold 6	7	8	9
1	0.095	0.034	0.010	0.002
2	0.186	0.086	0.032	0.011
3	0.225	0.135	0.064	0.028
4	0.252	0.173	0.104	0.055
5	0.259	0.186	0.125	0.076

Two Rings

Veto Threshold	Ring Threshold 6	7	8	9
1	0.125	0.050	0.015	0.004
2	0.213	0.112	0.044	0.016
3	0.241	0.155	0.083	0.038
4	0.259	0.184	0.119	0.068
5	0.261	0.192	0.135	0.086

Table 7.1: *Fraction of accepted events for different ring and veto thresholds. Required were at least one ring and two rings respectively. Values calculated from experimental data (C+C at 2 AGeV -* **November 2001** *beamtime - Rich IPU* **Emulation** *(left)* **Variation** *(right))*

Table 7.1 and Table 7.2 show the fraction of events positively triggered as a function of the Rich IPU thresholds in the same C+C reaction at 2AGeV, but performed in two different runs: November 2001 and November 2002. Event reduction is shown for trigger condition set to one or two rings, i.e. the trigger is positive when the event contains at least 1 or 2 rings respectively. The event reduction is being studied for two different versions of the ring recognition algorithm (see Section 8.1) and are denoted with the name *Emulation* for the version implemented in the hardware in the beamtime November 2001 and November 2002, *Variation* for the version implemented only in the Beamtime January 2004.
Comparing respectively the two Tables in 7.1 (left and right) and the two Tables in 7.2 (left and right) shows that the variation introduced in the Rich

One Ring

	Ring Threshold			
	6	7	8	9
Veto Threshold 1	0.258	0.138	0.059	0.027
2	0.331	0.210	0.108	0.057
3	0.365	0.252	0.150	0.088
4	0.392	0.293	0.201	0.130
5	0.398	0.305	0.218	0.152

One Ring

	Ring Threshold			
	6	7	8	9
Veto Threshold 1	0.288	0.165	0.075	0.037
2	0.355	0.238	0.129	0.073
3	0.382	0.272	0.168	0.102
4	0.398	0.303	0.213	0.144
5	0.399	0.308	0.224	0.159

Two Rings

	Ring Threshold			
	6	7	8	9
Veto Threshold 1	0.123	0.043	0.011	0.002
2	0.208	0.099	0.036	0.011
3	0.256	0.144	0.066	0.027
4	0.304	0.202	0.112	0.053
5	0.318	0.225	0.142	0.077

Two Rings

	Ring Threshold			
	6	7	8	9
Veto Threshold 1	0.156	0.061	0.019	0.005
2	0.239	0.125	0.052	0.017
3	0.280	0.170	0.083	0.037
4	0.317	0.220	0.131	0.067
5	0.322	0.235	0.154	0.088

Table 7.2: *Fraction of accepted events for different ring and veto thresholds. Required were at least one ring and two rings respectively. Values calculated from experimental data (C+C at 2 AGeV -* **November 2002** *beamtime - Rich IPU* **Emulation** *(left)* **Variation** *(right))*

IPU algorithm with local maximum performed only on those pads which do fulfill the thresholds condition (see 8.1) does not significantly effect the event reduction.

The tables show how the same algorithm with the same thresholds performed on the same reaction can deliver very different results, depending upon the experimental conditions; in this case the reasons of these strong differences is not in the noise suppression or in the quality of the pedestals[7]. In November 2002 the Rich IPU achieves a lower reduction because of events where high current discharges most likely arising from bad beam quality hit directly the photon pad plane, firing several pads out of which the IPU reconstructs a ring.

Table 7.3 shows the fraction of events positively triggered as a function of the Rich IPU thresholds in the same C+C reaction at 1AGeV, performed in November 2001. Again the reduction is shown for trigger condition set to

---

[7]the number of average pads per event is 150 in November 2001 and 50 in November 2002

one or two rings. The energy dependency results in a factor ~ 2.

One Ring

	Ring Threshold			
	6	7	8	9
Veto Threshold 1	0.197	0.093	0.028	0.013
2	0.250	0.134	0.049	0.025
3	0.269	0.156	0.068	0.038
4	0.285	0.182	0.096	0.060
5	0.288	0.188	0.106	0.071

One Ring

	Ring Threshold			
	6	7	8	9
Veto Threshold 1	0.214	0.106	0.035	0.017
2	0.263	0.148	0.060	0.031
3	0.278	0.168	0.079	0.045
4	0.287	0.187	0.104	0.067
5	0.289	0.191	0.110	0.075

Two Rings

	Ring Threshold			
	6	7	8	9
Veto Threshold 1	0.067	0.020	0.004	0.001
2	0.111	0.044	0.014	0.005
3	0.138	0.067	0.027	0.010
4	0.166	0.099	0.050	0.023
5	0.174	0.113	0.066	0.034

Two Rings

	Ring Threshold			
	6	7	8	9
Veto Threshold 1	0.084	0.028	0.007	0.002
2	0.128	0.056	0.020	0.007
3	0.153	0.080	0.036	0.015
4	0.174	0.111	0.061	0.029
5	0.177	0.119	0.074	0.041

Table 7.3: *Fraction of accepted events for different ring and veto thresholds. Required were at least one ring and two rings respectively. Values calculated from experimental data (C+C at* **1 AGeV** *-* **November 2002** *beamtime - Rich IPU* **Emulation** *(left)* **Variation** *(right))*

However it should also be remarked that the employ of higher thresholds with the purpose of reducing the high number of misidentified rings would also result in a relative increase of γ conversions signal. The online ring recognition algorithm in fact, as well as the offline one, is not capable establish a clear criterion for distinguishing between rings which correspond to a single leptons (*singles*) and rings which are correlated with two close tracks (*doubles*), despite of the fact that these two ring samples clearly have different characteristics, as Figure 7.6 shows.

Because of the conservative time-of-flight cut (20 ns), the local maximum search in the Shower IPU without the charge increase condition (which causes a lepton signature for any kind of particle hit), and the broad matching window, the miscorrelation between misidentified rings with a hit originated by another particle is likely and the event reduction is therefore lower.
For the reasons mentioned above, not a single value but rather a range of

values is quoted in Table. 7.4 as result for the event reduction with different trigger condition: 1/2 rings, 1/2 leptons. For the standard thresholds (8/4) a reduction factor around 10 is achieved, values up to 30 (9/2) are possible at the expense of an efficiency loss (see Table 8.1). Requiring two rings the factor can be increased to 15-25 for standard thresholds (8/4 and 8/3). In the most relaxed threshold situation (6/5) still a factor of 5 can be achieved. The factors for two rings are influenced by a large tail in the distribution of the number of rings per event caused by a small fraction of events with high pad occupancies due to shifting detector pedestals. Ring thresholds below six are not feasible since more than 80 percent of the events contain a sufficient number of random pads on a ring circumference to fulfill this condition.

The reduction achieved with 2 rings is not too different from the reduction achieved with 1 lepton, therefore this latter one is generally preferred because the first condition would have an efficiency $\epsilon_{RichIPU}^2$, while the second $\epsilon_{RichIPU} \cdot \epsilon_{matching}$, and $\epsilon_{matching}$ is higher than $\epsilon_{RichIPU}$.

Unless an invariant mass cut is applied, the dilepton condition would not lead to a stronger reduction with respect to the 2 leptons conditions, since like-sign pairs cannot be discarded, because they are used for the estimation of the combinatorial background.

(a) 13x13

(b) ring circumpherence
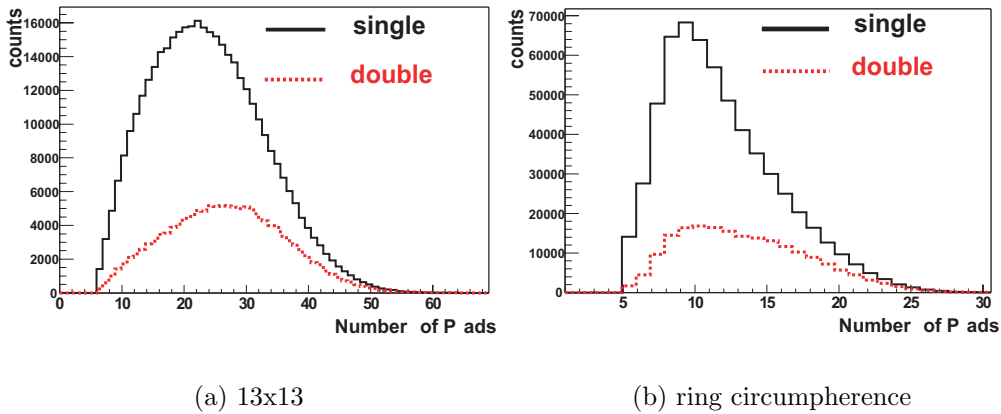
Figure 7.6: *Multiplicity of fired pads lying in the full 13x13 ring mask (a) or in the ring circumference (b). Rings correlated with one track are shown in the solid curve. Rings correlated with two close tracks in the dashed one.*

Trigger Condition	Event Reduction
1 ring	9 - 15%
2 rings	5 - 8%
1 lepton	4 - 7%
2 leptons	3 - 4%
1 dilepton	???

Table 7.4: *Fraction of accepted events for different trigger conditions, measured and estimated for experimental data of C+C reactions at 2 AGeV in November 2001 and November 2002 beamtime.*

Chapter 8

Performance of the Online Ring Recognition

Love is a burnin' thing,
An' it makes a firy ring.
Brought from wild desire
I fell into a ring of fire.

I fell into a burnin' ring of fire.
I went down, down, down, and the
flames went higher.
And it burns, burns, burns, that ring
of fire, that ring of fire.

(Johnny Cash - The ring of fire)

In the framework of the present thesis, much attention has been dedicated to the studies of the efficiency of the online ring recognition, because it is the most selective algorithm of the LVL2 and because it is the only one among the LVL2 algorithms which significantly differs from the algorithm used in the offline analysis.

The first problem which arises is the problem of the reference to use. No unambiguous result exist for dilepton production in heavy ion reactions measured by HADES, and on the other hand heavy ion reactions offer no kinematical constrain on which to base the studies of the efficiency of a new system, being it an algorithm or a detector.
Simulations involve the employ of event generators whose yields and distributions are not fully established, and the study of the efficiency of an analysis algorithm as the LVL2 also requires the simulation of the detectors response

(the so called *digitization*), which are models based on assumptions, extrapolations, whose error are not always well known.

A reliable reference system would consist in a well known, already measured, kinematically constrained reaction such as elementary reactions like $p + p, \pi + p$. The focus of HADES attention is currently directed towards these measurements.

Nevertheless a comparison between the results of the LVL2 *online* analysis and the analysis performed *offline* gives important information about the relative performance of the LVL2, although it does not provide a value for the absolute efficiency of the LVL2. In this context, to emphasize that these studies are just a *relative* comparison, also the reciprocal behavior has been studied, i.e. not only the relative efficiency of the LVL2 with respect to the offline analysis but also vice versa the relative efficiency of the offline analysis with respect to the LVL2.

In the context of a comparison between online and offline analysis, it is useful to remind which are the main differences between these two approaches, a part for the natural fact that the first occurs online with strict time constrains while the second can make use of more time, more information and the possibility to be refined and corrected. Therefore the offline algorithm should deliver a more selective information about the rings, with more discrimination capabilities.

8.1   Variations of the RICH IPU Algorithm

Different variations of the algorithm have been tested in order to optimize the performance of the algorithm, concerning the grouping of the pads, the thresholds cut and the local maximum condition. The different pad grouping have been already summarized in Figure 3.4 [122].

Concerning the thresholds cut, two possible variations have been tested:

- thresholds are independently applied on the ring and the veto region values;

- thresholds are applied on a combination of the ring and veto region values.

The main consequence is that the first variation does not allow rings with too many pads in the veto region to be selected as lepton candidates even if they have a high ring quality, i.e. it discard smeared rings, rings with high noise contribution and close pairs more than the second variation.

Concerning the local maximum, the tested variations are:

- local maximum is applied on all the possible ring centers, i.e. on all the pads, using the ring region value as quality parameter;

- local maximum is applied only on those ring which fulfill independently the thresholds on the search mask, i.e. ring and veto quality, and the ring region value is used as quality parameter;

- local maximum is applied only on those ring which fulfill the combined condition on the search mask thresholds, and the ring region value is used as quality parameter.

The first one, originally implemented in hardware since it allows the search mask and the local maximum process to run in parallel, with a smaller latency and less consumption of resources, show a significant drop of efficiency due to the fact that two neighboring candidates for the same lepton can be simultaneously discarded, one by the condition on the veto (not evaluated in the local maximum) and one by the local maximum itself.

In the following the name ***Emulation*** will be used for the version implemented in the hardware in the beamtime November 2001 and November 2002, where thresholds are independently applied on the ring and the veto region values and local maximum is applied on all the possible ring centers, i.e. on all the pads, using the ring region value as quality parameter; while the name ***Variation*** will be used for the version implemented only in the Beamtime January 2004 where thresholds are independently applied on the ring and the veto region values and local maximum is applied only on those ring which fulfill independently the thresholds on the search mask, i.e. ring and veto quality, and the ring region value is used as quality parameter.

8.2   Efficiency with Simulations

Full simulations of the HADES detector including an emulation of the hardware ring recognition algorithm were done for different scenarios, in particular to analyze the response of the online ring recognition algorithm to single electrons and to electron pairs. The electronic noise is simulated in a realistic way (see Section 4.2.1), the contribution from direct hits is not included in the simulations. Two sets of optical parameters have been used to process the simulations: one corresponding to the single photon efficiency obtained from the parameter in Figure 2.4, one with the reduced photon efficiency measured in November 2002 [102].
The efficiency has been studied for the two versions of the online ring recognition algorithm, and varying the thresholds of the algorithm.

8.2.1 Efficiency for single leptons

The efficiency for single electrons is studied with electrons emitted from the target and the same electrons embedded in the background coming from a C+C reaction at 2 AGeV simulated with UrQMD (see Appendix B). A realistic contribution from electronic noise (1%) is included in both cases.
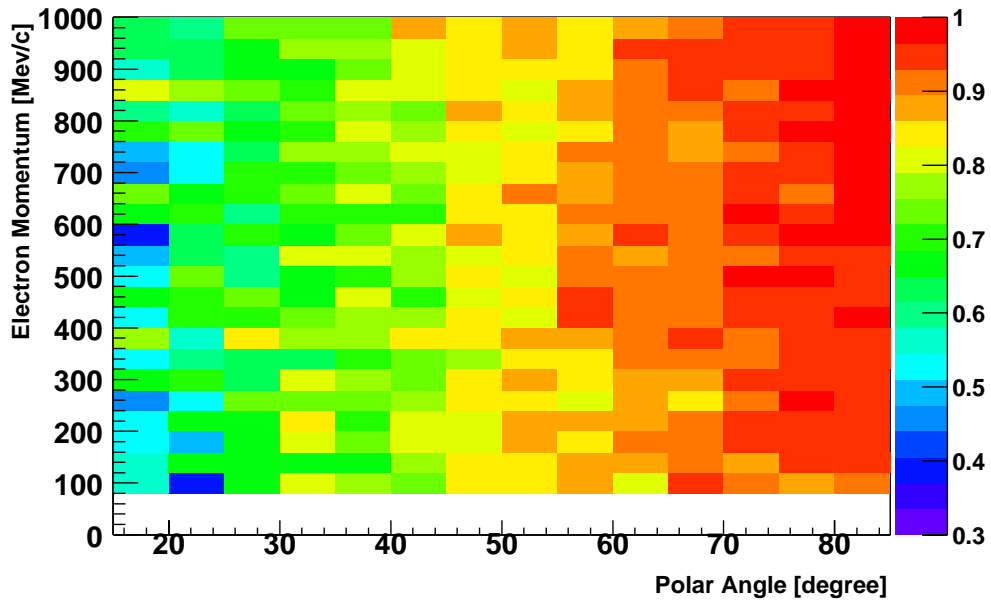
Figure 8.1: *Ring recognition efficiency of the online algorithm (8,4) as a function of electron momentum and polar angle. Results are shown for a white single electron distribution ($15° < \theta < 85°$, $100 < p < 1000$ MeV/c) in a C+C background at 2 AGeV* **Emulation**.

The ring recognition efficiency for the C+C case as a function of electron momentum and polar angle is shown in Figure 8.1.
The efficiency is constant over the full relevant momentum range from 100 to 1000 MeV. A strong drop in efficiency from values close to 1 down to 0.7 is visible towards smaller polar angles. This arises from:

- the deteriorated photon statistics due to decreasing radiator path length towards smaller polar angles, and

- the increasing number of incomplete rings due to the frames of the detector segments.

The efficiency matrix was calculated with the standard threshold values - used in most hardware tests and optimized with Au+Au simulations at 1 AGeV [122] - for the ring recognition algorithm (ring region: 8, veto region: 4). The integrated efficiencies for different threshold combinations are shown in Table 8.1 and 8.2.

	Ring Threshold			
	6	7	8	9
5	0.936301	0.904647	0.855079	0.787475
4	0.930785	0.899302	0.849661	0.782033
3	0.91148	0.879997	0.830429	0.763216
2	0.855347	0.823962	0.775736	0.710206
1	0.661493	0.634183	0.592595	0.539171

Table 8.1: *Ring recognition efficiency for simulated rings as a function of algorithm thresholds in the ring and veto region. Values calculated from simulated data (single electron embedded in C+C background at 2 AGeV) with normal Rich efficiency* **Emulation***.*

	Ring Threshold			
	6	7	8	9
5	0.938351	0.906819	0.857275	0.789574
4	0.937814	0.906258	0.856592	0.788793
3	0.93574	0.904012	0.853981	0.785425
2	0.923415	0.890492	0.839972	0.769854
1	0.823522	0.634183	0.768121	0.69549

Table 8.2: *Ring recognition efficiency for simulated rings as a function of algorithm thresholds in the ring and veto region. Values calculated from simulated data (single electron embedded in C+C background at 2 AGeV) with normal Rich efficiency -* **Variation***.*

Efficiencies as a function of the pad multiplicity on the ring circumference are shown in Figure 8.2 for the case of single electrons embedded in a C+C background. The multiplicity of pads on the ring circumference around the center of the *simulated* ring is used to provide a common reference also for undetected rings and for rings detected on different positions for different

(a) pads
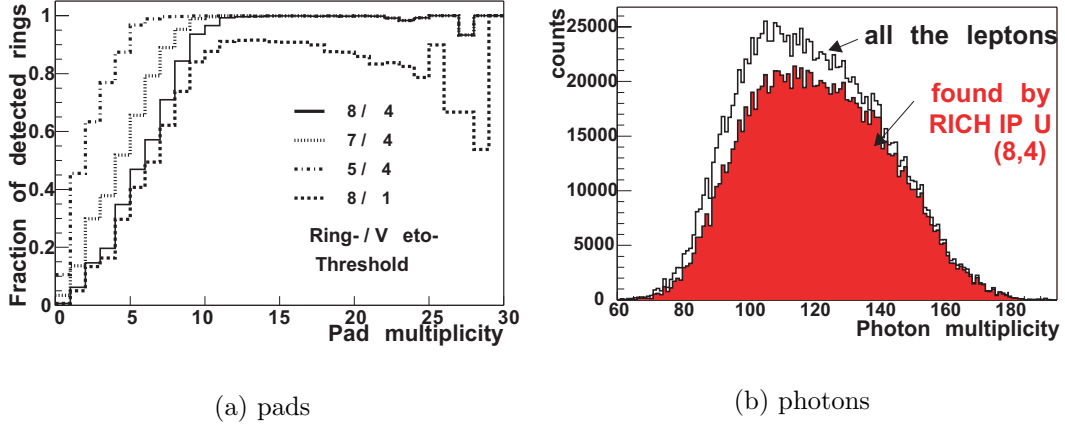
(b) photons

Figure 8.2: *In (a): Fraction of simulated electrons detected by the online algorithm as a function of the pad multiplicity around the real ring center. Distributions are shown for different threshold values. In (b): Photon multiplicity distribution for all the simulated electrons, and for those which are found by the online algorithm (8,4)* - **Variation**.

threshold values. With the standard threshold values (solid line) an efficiency loss is only visible at smaller multiplicities. This efficiency loss improves with lower thresholds in the ring region (dotted and dashed-dotted line) without showing a saturation behavior. Efficiencies at multiplicities below the threshold cutoff are due to rings detected with a sufficiently high multiplicity on a position different from the simulated center because of the extension of pad clusters.

The high efficiency at higher pad multiplicities indicates that the veto condition does not discard events. The effect of the veto condition only becomes visible with the severe condition of less than one valid group in the veto region (dashed line), which is due to the random noise in the simulation and not due to contributions from the ring itself in its veto region.

8.2.2 Efficiency for lepton pairs

Different scenarios have been tested for lepton pairs. The signal of interest of HADES are open pairs coming from direct decay of ρ, ω and ϕ mesons; in this case the ring are fully separated. The *dilepton* efficiency therefore simply results from the single lepton efficiency folded with the proper phase-space. Simulations have been performed with a thermal generator of ω mesons decaying into e^+e^- pairs. Figure 8.3 shows the single lepton and the pair

(a) single   (b) pair
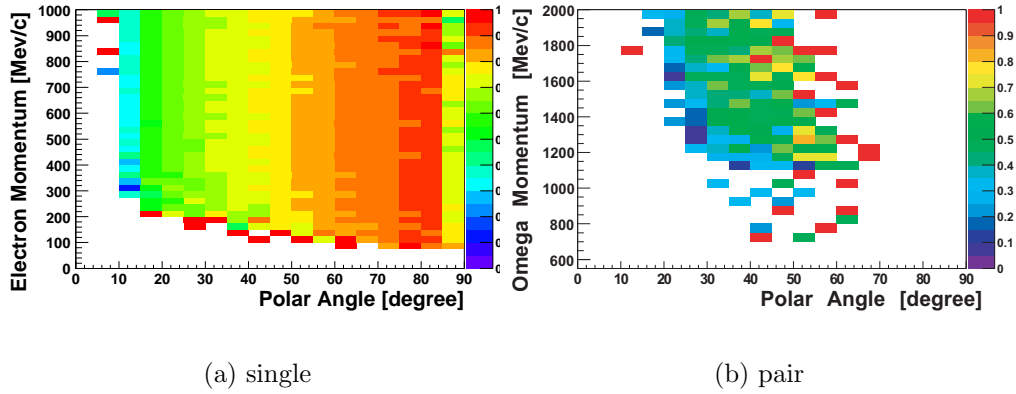
Figure 8.3: *Ring recognition efficiency of the online algorithm as a function of electron momentum and polar angle. Results are shown for a single electrons and electron pairs emitted from an isotropic thermal source of ω mesons -* **Emulation***.*

efficiency as a function of momentum and polar angle. The relatively low value for the pair efficiency is due to the angular correlation between the two leptons originating from the ω meson decay which typically enter opposite regions of the efficiency, and when one is lost in the low efficiency region then the ull pair is missed.

However the most abundant lepton pairs coming from γ conversion or π^0 Dalitz have small opening angle and therefore the rings are close to each other or even overlap. To investigate the performance of the algorithm under these conditions, a set of simulations was performed where two leptons per event were emitted from the target at varying opening angles, in different regions of the detector:

- $20° < \theta < 35°$

- $35° < \theta < 50°$

- $50° < \theta < 65°$

- $65° < \theta < 80°$.

Figure8.4 shows the single lepton identification efficiency for the two versions of the online algorithm, as a function of the opening angle. At large polar angle the radiator length is longer, and therefore more Cherenkov photons are produced and on average more pads fired, leading to a larger efficiency. But in the region where the two rings overlap, a higher number of pads fired
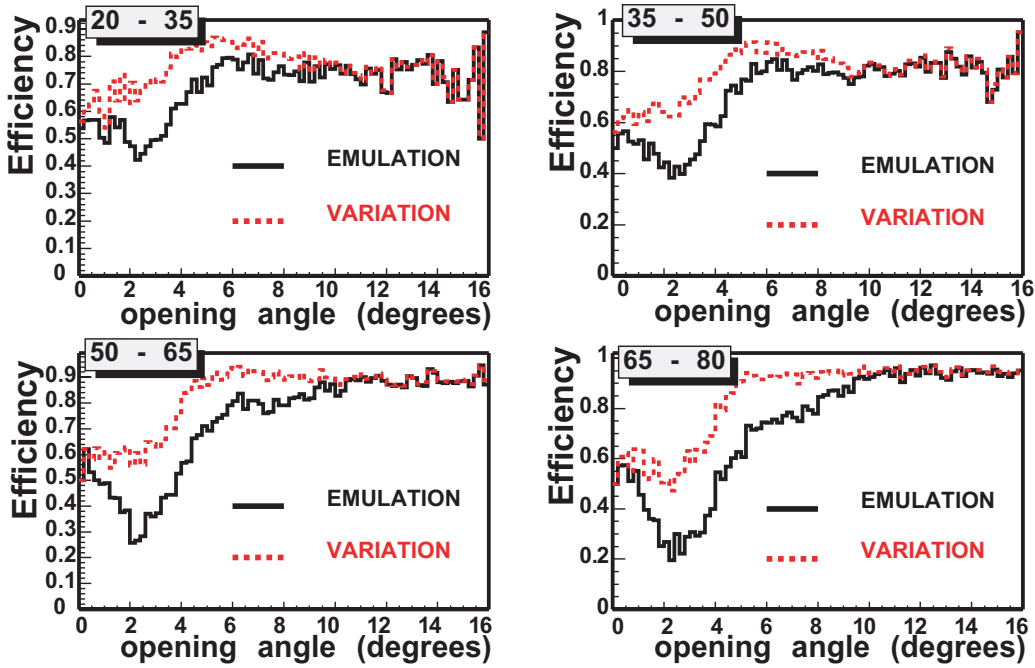
Figure 8.4: *Single lepton identification efficiency as a function of the opening angle for different polar angle regions, for the two versions of the online algorithm: the full line for* **Emulation***, the dashed line for* **Variation***.*

leads to a destructive interference and causes a drop of the efficiency. The **Variation** version is more efficient for small opening angle pairs because the local maximum discrimination is performed uniquely on the ring candidates which have fulfilled the thresholds condition and can no longer be discarded.

Table 8.3 summarizes the efficiency of the online ring recognition algorithm in different scenarios: with single electrons, embedded electrons, close and open electron pairs. The two different versions of the algorithm have been considered, with the typical thresholds $(ring, veto) = (8, 4)$. In addition the two sets of optical parameters corresponding to different photon efficiency have been studied.

8.3   Relative Efficiency Online-Offline

The only analysis which can be done with experimental data, without an absolute reference system, is a comparison between the rings found with the two different ring finders: the online and the offline one. Due to the

Source		(8,4) EMULATION		(8,4) VARIATION	
		single e	pair	single e	pair
single e	High Eff	85.0%	-	85.6%	-
	Low Eff	73.1%	-	76.9%	-
embedded e	High Eff	84.9%	-	85.6%	-
	Low Eff	72.9%	-	76.7%	-
pairs 20-35	High Eff	68.1%	47.7%	77.8%	59.1%
	Low Eff	57.9%	34.7%	62.5%	41.0%
pairs 35-50	High Eff	73.2%	55.6%	81.6%	66.8%
	Low Eff	61.9%	38.8%	66.4%	45.0%
pairs 50-65	High Eff	75.5%	60.8%	85.6%	74.2%
	Low Eff	69.1%	48.5%	74.7%	56.3%
pairs 65-80	High Eff	77.7%	66.0%	88.7%	80.3%
	Low Eff	75.8%	59.0%	82.3%	68.0%
pairs ω	High Eff	77.2%	45.3%	77.6%	45.6%
	Low Eff	64.2%	30.4%	64.3%	30.6%

Table 8.3: *Efficiency of the online ring recognition algorithm in different scenarios: single electrons, embedded electrons, close and open electron pairs. The two different versions of the algorithm have been considered, with the typical thresholds (8,4). In addition the two sets of optical parameters corresponding to different photon efficiency have been studied. For electron pairs the efficiency of the single electron as been calculated as well as the pair efficiency.*

low photon statistics, and especially due to the background situation, both the online and the offline ring finder algorithms produce a large number of misidentified rings (*fake* rings), which do not correspond to any real lepton. Since the online and the offline ring recognition algorithm do not necessarily find the same fake rings, it does not make sense to compare directly these two samples.

Real rings are selected by requiring a correlation between rings and lepton signatures coming from other detectors, i.e a full lepton analysis as the one described in Chapter 5 is performed using independent ring information either from the online or from offline ring recognition.

8.3.1 Difference between Online-Offline Ring Recognition Algorithm

The online ring recognition algorithm is much simpler than the offline, mainly because of time, implementation and resources constraints. The main differences between the two algorithms are

- implementation

  - online: hardware
  - offline: software

- timing performance

  - online: up to 100000 events/second[1]
  - offline: 25 events/second

- analyzed area

  - online: 32 pads in the ring region + 48 pads in the veto region
  - offline: $13 \times 13 = 169$ pads (all the pads in the ring mask)

- charge information

  - online: ignored
  - offline: considered

- number of algorithms

  - online: 1
  - offline: 2 + 4 additional tests + preprocessing (unpacker, calibration, cleaning, labeling)

The two algorithms have been compared with respect to the most significant properties of ring finder algorithms; in addition the online ring finder has been characterized with different sets of simulations.

---

[1]with an average occupancy of 6.7% equally distributed among the two readout controllers which together cover the full area of a Rich sector, higher than the one achieved with C+C reactions so far treated

8.3.2 Efficiency in Nov01 Exp

In November 2001 the LVL2 was not used as a trigger source; however most of its components were operational, and among those the Rich IPU which was extensively tested with standard thresholds (8,4) which were later set to more restrictive values in order not to overload the MU. With the help of the Rich IPU Emulation it is possible to estimate the relative performance of online and offline ring finder algorithms, for different thresholds and different variation of the online algorithm.

Efficiency of ONLINE with respect to OFFLINE

Figure 8.5 shows the fraction of offline lepton candidates also found by the Rich IPU with the thresholds (8,4): in fig a) for the algorithm currently implemented in hardware, in fig b) for the variation which performs the local maximum only on those candidates which pass the thresholds selection. Both versions of the ring finder are homogeneous over the detector area and similar for all the sectors. The integral efficiency increases from 68% to 79% with the new variation.

This set (8,4) and different thresholds (8,3) are presented separately for

(a) **Emulation**   (b) **Variation**
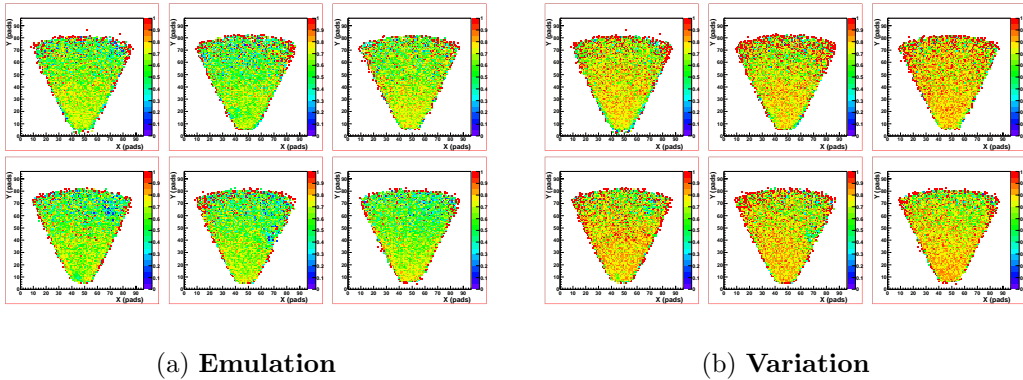
Figure 8.5: *Fraction of offline lepton candidates also found by the Rich IPU with the thresholds (8,4) as a function of the position in the different sectors: in fig a) for the algorithm currently implemented in hardware, in fig b) for the variation which performs the local maximum only on those candidates which pass the thresholds selection -* **NOV01 EXP***.*

the runs at 1 and 2 AGeV in Table. 8.9 for different tracks multiplicities. The reduced efficiency in the runs at 1 AGeV is due to the field set-up with reduced intensity, which discard less close pairs of those kind which leaves a

signature in the inner MDCs; those one typically produce overlapping rings which are more easily discarded by the different veto mechanisms of the two algorithms.
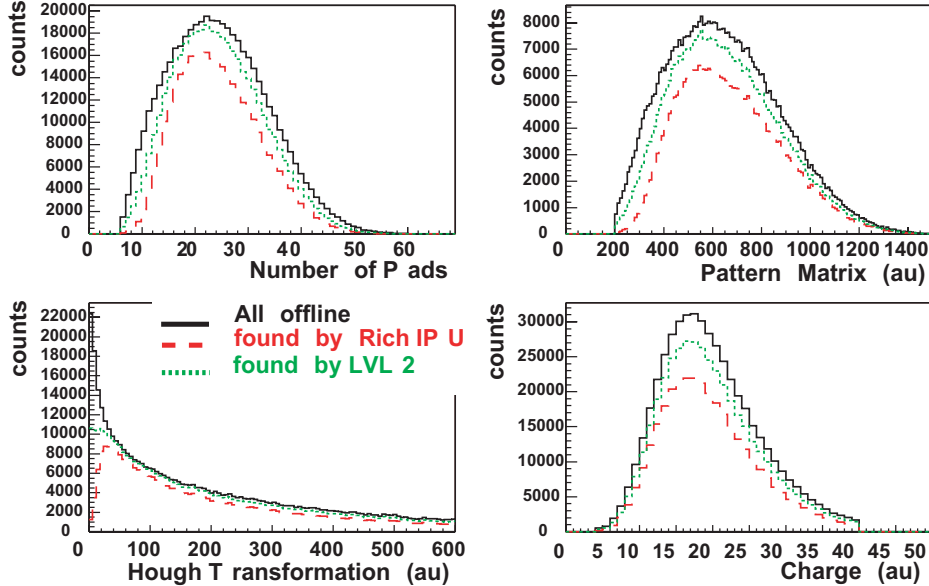
Figure 8.6: *Distributions of several quality parameters of the offline ring finder (from upper left to lower right: Number of pads in the 13x13 matrix, Pattern Matrix, Hough Transformation, Average Charge per fired pad) for offline lepton candidates (black), the fraction of those also found by the RichIPU with the thresholds (8,4) (red) and the fraction of those in events positively triggered (green) for the hardware emulation -* **NOV01 EXP Emulation**.

Figures 8.6 and 8.7 show the fraction of offline lepton candidates also found by the RichIPU as a function of some meaningful parameters of the offline ring finder respectively for the algorithm currently implemented in hardware and for the variation of the algorithm. The fraction of lepton candidates in positively triggered events is slightly higher than the fraction of lepton candidates found by the Rich IPU: or in other words the efficiency of the LVL2 is slightly higher than the efficiency of the Rich IPU. In the best case, when the variation of the Rich IPU is used with (8,4) thresholds the LVL2 efficiency reaches the value of 92%.
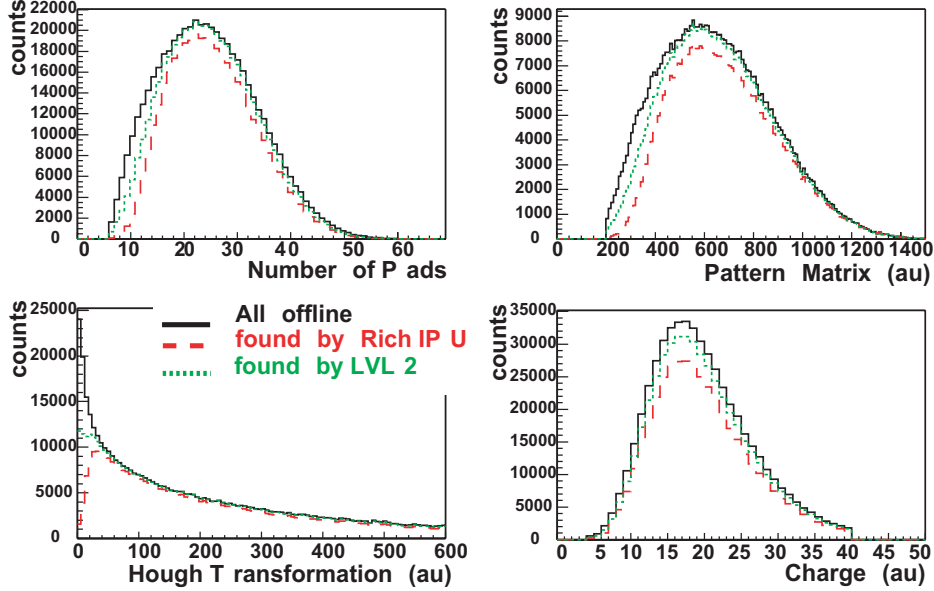
Figure 8.7: *Distributions of several quality parameters of the offline ring finder (from upper left to lower right: Number of pads in the 13x13 matrix, Pattern Matrix, Hough Transformation, Average Charge per fired pad) for offline lepton candidates (black), the fraction of those also found by the RichIPU with the thresholds (8,4) (red) and the fraction of those in events positively triggered (green) for the variation of the hardware emulation -* **NOV01 EXP Variation**.

	(Ring,Veto) Thresholds							
	(8,4) EMU		(8,4) VAR		(8,3) EMU		(8,3) VAR	
multiplicity	1AGeV	2AGeV	1AGeV	2AGeV	1AGeV	2AGeV	1AGeV	2AGeV
All	61.6%	68.2%	74.9%	79.9%	48.3%	55.6%	63.4%	69.8%
1 track/ring	62.6%	67.9%	74.7%	79.1%	49.9%	55.8%	64.2%	69.3%
>= 2 tracks/ring	59.3%	68.9%	75.2%	82.5%	44.8%	55.2%	61.7%	71.3%

Table 8.4: *Relative efficiency of online ring finder with respect to offline lepton candidates for C+C reactions at 1 and 2 AGeV with different thresholds and variations of the ring finder algorithms -* **NOV01 EXP**.

Efficiency of OFFLINE with respect to ONLINE

The relative efficiency of the offline ring finder with respect to lepton candidates selected with the Rich IPU is about 52%. This value, significantly lower than the relative efficiency of the online ring finder with respect to offline lepton candidates, is explained with the fact that the online algorithm has a higher fraction of misidentified rings. These rings might be correlated to non leptonic tracks and therefore are not matched by offline rings.

Figures 8.8 and 8.9 shows dependency on some hardware effects. Sector 0
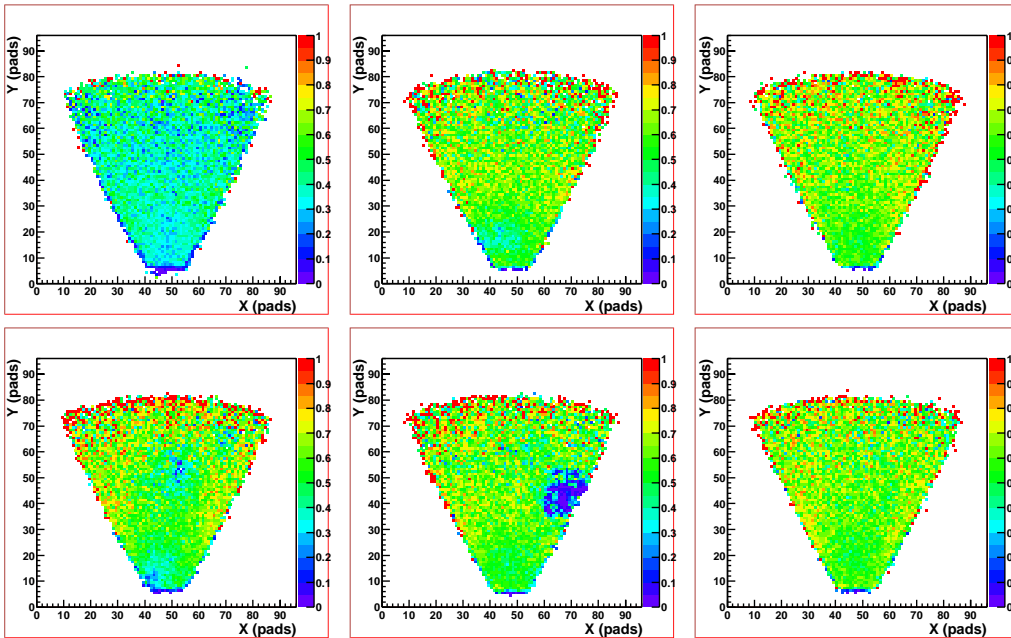
Figure 8.8: *Fraction of online lepton candidates also found by the Rich -* **NOV01 EXP***.*

has a higher level of noise in the fired pads, which leads to more rings found by the online algorithm, which is more sensitive to noise than the offline; these rings, typically fakes, are not reconstructed by the offline. Sector 4 has an area which typically shows many pads firing due to an unrecoverable manufacturing problem of the pad plane: even in this case the effect is that more fake rings are found by the online and not by the offline. Conditions for different track multiplicities are reported in Table 8.5.
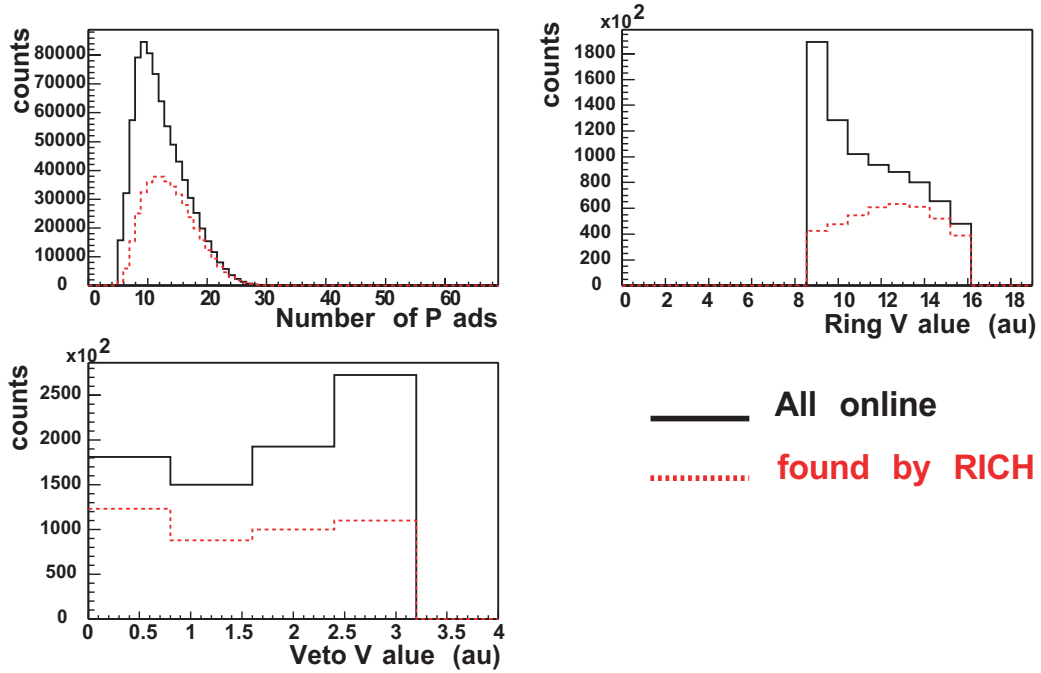
Figure 8.9: *Distributions of several quality parameters of the online ring finder from upper left to lower right: Number of pads in the ring region, ring value, veto value -* **NOV01 EXP**.

multiplicity	1AGev	2AGeV
All	51.7%	52.9%
1 track/ring	49.6%	50.1%
>= 2 tracks/ring	56.4%	60.7%

Table 8.5: *Relative efficiency of offline ring finder with respect to online lepton candidates for C+C reactions at 1 and 2 AGeV -* **NOV01 EXP**.

8.3.3 Efficiency in Nov01 Sim

In simulations the relative efficiency of online and offline ring finder algorithm is significantly better. The reason is to be found in the difference in the original distributions between experimental and simulated data and will be studied in the next paragraph.

Efficiency of ONLINE with respect to OFFLINE

Figure 8.10 shows the fraction of offline lepton candidates also found by the Rich IPU with the thresholds (8,4); with simulated data the difference in efficiency between the standard Rich IPU emulation and the variation is very small and significant only in the reactions at 1 AGeV or with (8,3) thresholds. It was already mentioned that this set-up enhances the contribution of close pairs, which are more sensitive to the two variations. The (8,3) thresholds are more restrictive on the veto region and even in this case the difference between the two variations of the algorithm become important.
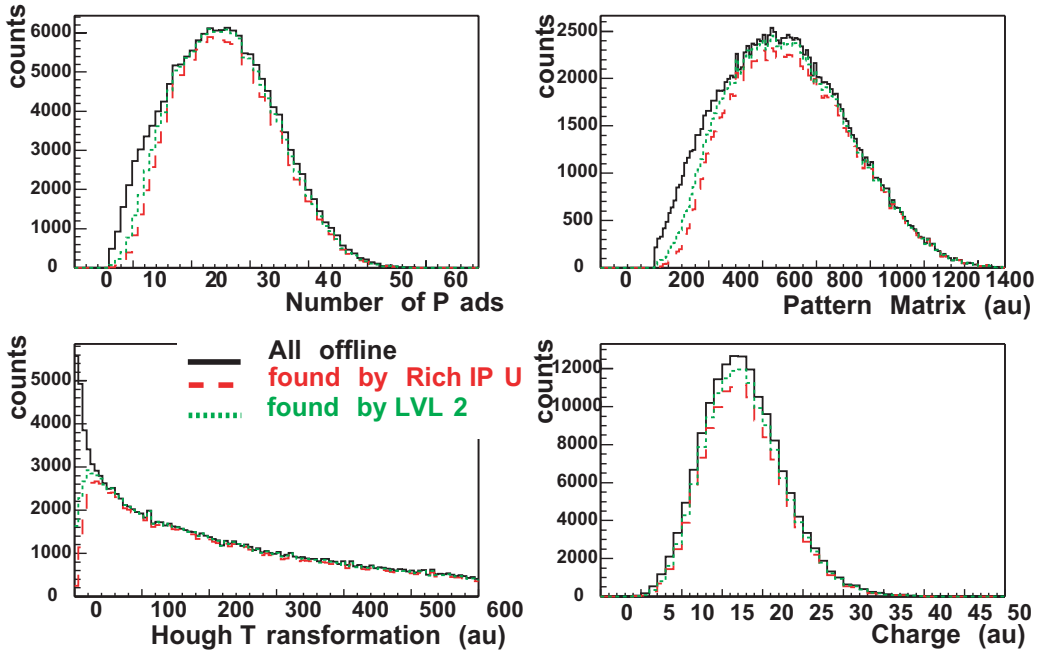
Figure 8.10: *Relative efficiency of online ring finder with respect to offline lepton candidates. Distributions of several quality parameters of the offline ring finder (from upper left to lower right: Number of pads in the 13x13 matrix, Pattern Matrix, Hough Transformation, Average Charge per fired pad) for offline lepton candidates (black), the fraction of those also found by the RichIPU with the thresholds (8,4) (red) and the fraction of those in events positively triggered (green) -* **NOV01 SIM**.

With (8,4) thresholds the efficiency is about 85% for 2 AGeV, and goes from 69% to 81% in 1 AGeV. With (8,3) thresholds the efficiency is lower and goes from 65% to 79% for 2 AGeV, and from 57 to 73% in 1 AGeV. Results

for different experimental conditions and track multiplicities are reported in Table 8.6. The absolute values are higher than in experimental data.

	(Ring,Veto) Thresholds							
	(8,4) EMU		(8,4) VAR		(8,3) EMU		(8,3) VAR	
multiplicity	1AGeV	2AGeV	1AGeV	2AGeV	1AGeV	2AGeV	1AGeV	2AGeV
All	69.5%	85.8%	81.6%	85.8%	57.6%	65.6%	72.7%	79.2%
1 track/ring	70.3%	84.9%	81.4%	85.0%	58.8%	65.4%	73.0%	78.3%
>= 2 tracks/ring	67.7%	88.3%	82.1%	88.3%	54.7%	66.1%	71.8%	81.6%

Table 8.6: *Relative efficiency of online ring finder with respect to offline lepton candidates for C+C reactions at 1 and 2 AGeV with different thresholds and variations of the ring finder algorithms -* **NOV01 SIM***.*

Efficiency of OFFLINE with respect to ONLINE

The relative efficiency of the offline ring finder with respect to online lepton candidates is about 70% in 2AGeV and 63% in 1 AGeV. It is homogenous over the full pad plane for all the sectors as Figure 8.11 shows. Table 8.7 reports the results for the relative efficiency of offline ring finder with respect to online lepton candidates. Even in this case the values are higher than in experimental data.

multiplicity	1AGev	2AGeV
All	63.3%	70.2%
1 track/ring	62.2%	68.8%
>= 2 tracks/ring	66.0%	74.2%

Table 8.7: *Relative efficiency of offline ring finder with respect to online lepton candidates for C+C reactions at 1 and 2 AGeV -* **NOV01 SIM***.*
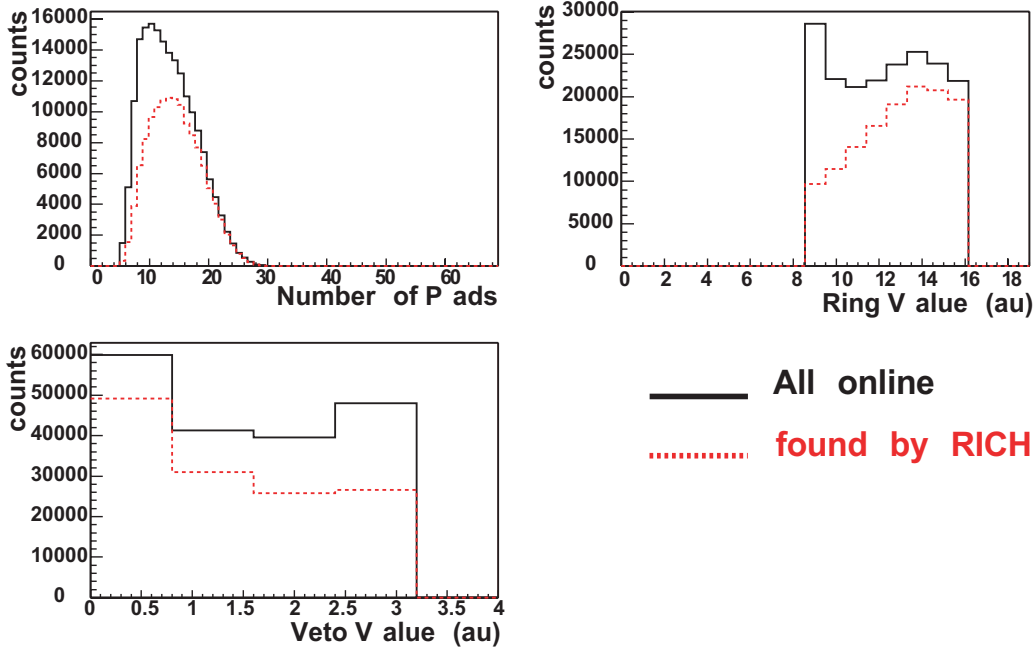
Figure 8.11: *Relative efficiency of offline ring finder with respect to online lepton candidates. Distributions of several quality parameters of the online ring finder(from upper left to lower right: Number of pads in the ring region, ring value, veto value -* **NOV01 SIM**.

8.3.4   Simulation - Experiment comparison

Comparing experimental and simulated distributions is very important in order to understand the differences between the relative online-offline efficiency in simulated and experimental events. Figure 8.12 shows some quality parameters of the offline ring finder for experimental and simulated ring which have been used to build a "lepton candidate" (i.e. fake rings are mostly excluded). The quality values of the algorithm (Pattern Matrix and Hough Transformation) do not depend on the deposited charge and for them the agreement is quite good. The disagreement in the average charge distribution could be due to some problems in reproducing in simulations the experimental voltage settings or to the noise distribution.

The difference between simulated and experimental rings can be understood especially in the framework of the coupling of photons within one or more pad, and all the related problem (cross-talk, optical distortion, etc...) which contribute to the final effect: the overall number of pads fired in the complete 13×13 confidential area of a ring are compatible in simulations

(a) hough transformation   (b) pattern matrix   (c) average charge
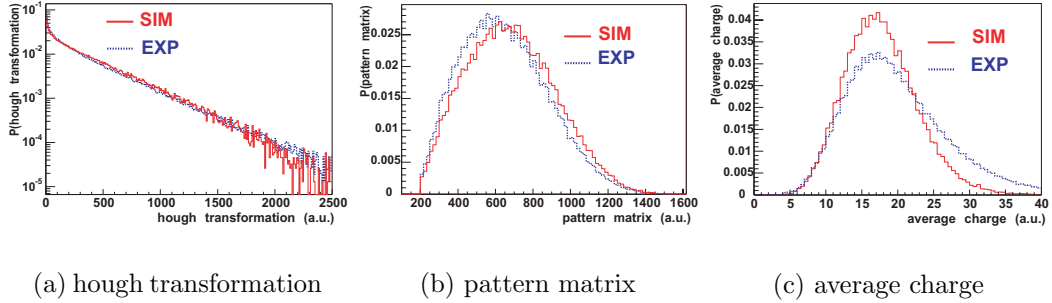
Figure 8.12: *Quality parameters of the offline Rich ring finder algorithm, respectively a) Hough Transformation, b) Pattern Matrix, c) Average Charge for experimental (dashed blue line) and simulated (full red line) data -* **NOV01**.

(a) pads in 13×13 confidential area

(b) pads in IPU ring region
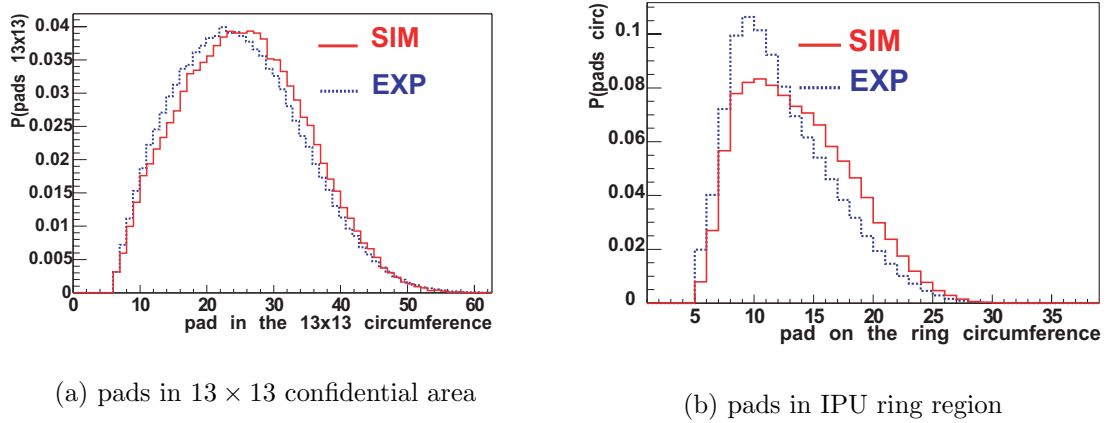
Figure 8.13: *Distribution of pads a) in 13×13 confidential area evaluated with different weight by the offline ring finder, b) in the 32-pads ring region evaluated by the online ring finder for experimental (dashed blue line) and simulated (full red line) data -* **NOV01**.

and experiment, whereas the differential number of pads fired in the different region which characterize the ring area (and which are more relevant for the online than for the offline analysis) still present significant discrepancies. Figure 8.13 shows the distribution of pads in the 13×13 ring mask evaluated by the offline ring finder and the distribution of pads in the 32-pads ring region evaluated by the online ring finder.

Figure 8.14 shows the distribution of pads in the ring circumference evaluated by the IPU, and the ring and veto value, quality parameters of the

(a) ring region
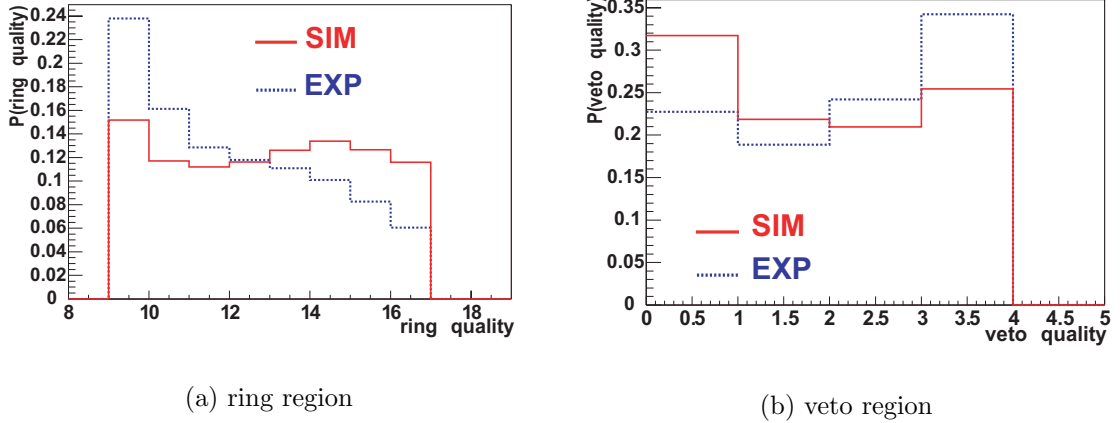
(b) veto region

Figure 8.14: *Distribution of quality parameters of the online ring finder a) ring region, b) veto region for experimental (dashed blue line) and simulated (full red line) data -* **NOV01**.

online algorithm. From the picture is then clear why more lepton candidates are found in simulations: the overall number of pads is compatible, but in simulations there are more pads on the ring and less pads on the veto region.

Table 8.8 shows some of the relevant properties of rings found in experimental and simulated data at different polar angles. Some are properties of the Offline ring finder (Hough Transformation, Pattern Matrix, Charge, N.of Pads (13x13)), some are properties of the Online ring finder (N.of Pads (ring mask), Ring Value, Veto Value). All the quantities of the Offline ring finder show a smooth increase for larger polar angle, due to the increase of the radiator path length, even if simulation show a more linear behavior, especially in the angular range $30° < \theta < 50°$.

The quantities of the Online ring finder show a more constant behavior due to the more discretizeness of the quantities, even if a slight increase is observed for the Ring and the Veto Value[2]. The remarkable thing is however in the different behavior of the Number of Pads reconstructed in the full 13x13 or in the ring mask. While the first one significantly increase at large polar angle, the second one is more constant around 13 pads. This might indicate an increased smearing of the ring pattern at large polar angle.

---

[2]the increase in the Veto Value is of course an obstacle for an ideal ring recognition.

Ring Property	SIM	EXP
$20° < \theta < 30°$		
Hough Transformation	255.8	257.7
Pattern Matrix	650.1	631.7
Charge	416.4	488.9
N.of Pads (13x13)	23.24	23.22
N.of Pads (ring mask)	12.38	11.70
Ring Value	12.04	11.47
Veto Value	1.303	1.662
$30° < \theta < 40°$		
Hough Transformation	279.6	284.0
Pattern Matrix	666.3	646.2
Charge	429.7	508.9
N.of Pads (13x13)	23.92	23.91
N.of Pads (ring mask)	12.75	12.05
Ring Value	12.29	11.69
Veto Value	1.326	1.628
$40° < \theta < 50°$		
Hough Transformation	310.6	264.1
Pattern Matrix	678.9	626.8
Charge	448.6	477.1
N.of Pads (13x13)	24.71	23.33
N.of Pads (ring mask)	13.05	11.30
Ring Value	12.46	11.42
Veto Value	1.402	1.704
$50° < \theta < 60°$		
Hough Transformation	356.1	301.9
Pattern Matrix	701.8	638.0
Charge	479.1	490.8
N.of Pads (13x13)	26.01	24.37
N.of Pads (ring mask)	13.6	11.65
Ring Value	12.69	11.57
Veto Value	1.489	1.789
$60° < \theta < 70°$		
Hough Transformation	401.0	372.6
Pattern Matrix	721.9	683.4
Charge	512.6	525.0
N.of Pads (13x13)	27.26	26.69
N.of Pads (ring mask)	14.1	12.86
Ring Value	12.88	12.05
Veto Value	1.516	1.773
$70° < \theta < 80°$		
Hough Transformation	446.1	464.9
Pattern Matrix	739.5	731.4
Charge	555.1	559.3
N.of Pads (13x13)	28.57	29.07
N.of Pads (ring mask)	14.56	13.86
Ring Value	13.02	12.43
Veto Value	1.542	1.769

Table 8.8: *Properties of rings found in experimental and simulated data at different polar angles. Some are properties of the Offline ring finder (Hough Transformation, Pattern Matrix, Charge, N.of Pads (13x13)), some are properties of the Online ring finder (N.of Pads (ring mask), Ring Value, Veto Value)* - **NOV01 SIM-EXP**.

8.3.5   Efficiency in Nov02 Exp

To estimate the relative efficiency of the ring recognition algorithm in the experiments performed in November 2002, only LVL1 events can be analyzed, since the LVL2 are biased by the Rich IPU algorithm itself. In addition the different performance of the Rich detector in November 2002 should also be kept in mind: a deteriorated photon detection efficiency, as measured with the *OEM* experiments [102], a lower level of noise due to an improved pedestal calibration, but problems with the beam focusing resulting in strong discharges directly on the pad plane.

Efficiency of ONLINE with respect to OFFLINE

Like in November 2001, both the hardware emulation and the variation versions of the ring finder are homogeneous over the detector area and similar for all the sectors. The integral efficiency increases from 57% to 70% with the new variation. With a more relaxed veto condition (8,4) the integral efficiency was estimated to increase to values of 68% with the hardware algorithm and to 77% with the variation. Conditions for different track mul-

	(Ring,Veto) Thresholds			
multiplicity	(8,4) EMU	(8,4) VAR	(8,3) EMU	(8,3) VAR
All	68.2%	77.6%	57.5%	70.5%
1 track/ring	67.9%	76.9%	57.6%	70.0%
>= 2 tracks/ring	69.1%	79.9%	57.0%	72.0%

Table 8.9: *Relative efficiency of online ring finder with respect to offline lepton candidates for C+C reactions at 1 and 2 AGeV with different thresholds and variations of the ring finder algorithms -* **NOV02 EXP**.

tiplicities are reported in Table 8.9. These values are in a good agreement with the ones estimated in November 2001.
Figures 8.15 show the fraction of offline lepton candidates also found by the RichIPU as a function of some meaningful parameters of the offline ring finder in the upper figure for the algorithm currently implemented in hardware, in the lower figure for the new variation. The veto threshold 3 is rather restrictive, especially with the experimental conditions of November 2002, and leads to a significant efficiency loss also for high quality rings.
The new variation improves the efficiency especially for high quality rings.
Again the fraction of lepton candidates in positively triggered events is slightly
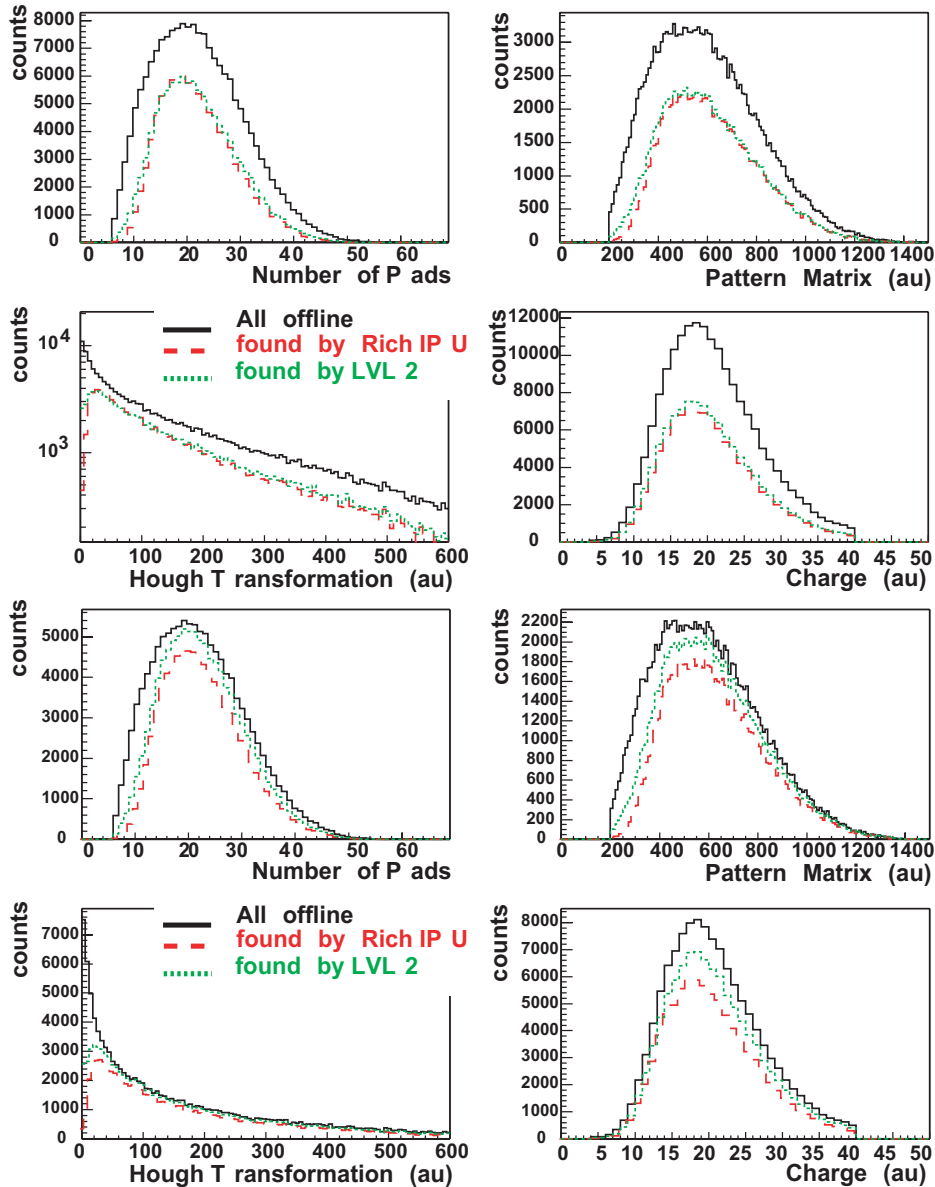
Figure 8.15: *Distributions of several quality parameters of the offline ring finder (from upper left to lower right: Number of pads in the 13x13 matrix, Pattern Matrix, Hough Transformation, Average Charge per fired pad) for offline lepton candidates (black), the fraction of those also found by the RichIPU with the thresholds used in November 2002 (red) and the fraction of those in events positively triggered (green) for the hardware emulation -* **NOV02 EXP Emulation** *(up)* **Variation** *(down) .*

higher than the fraction of lepton candidates found by the Rich IPU. The dependency of the LVL2 efficiency on the Rich IPU efficiency will be explained later.

Efficiency of OFFLINE with respect to ONLINE

The relative efficiency of the offline ring finder with respect to lepton candidates selected with the Rich IPU is about 53% and homogeneously distributed around the detector area, as Figure 8.16 a) shows. Conditions for different track multiplicities are reported in Table 8.10.
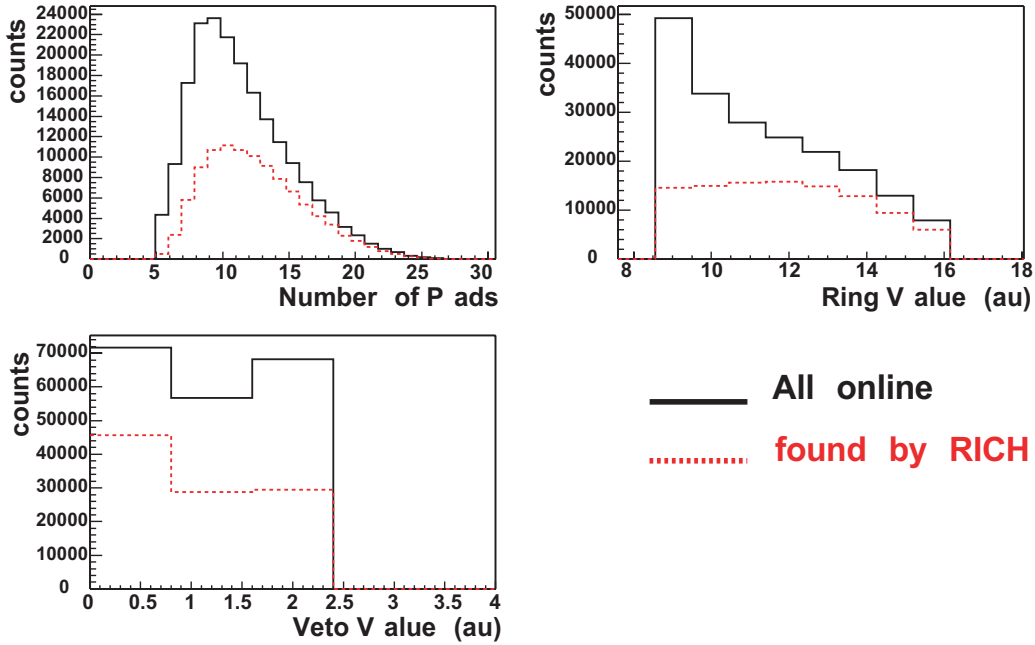
Figure 8.16: *Relative efficiency of offline ring finder with respect to online lepton candidates. In a) fraction of online lepton candidates also found by the Rich; in b) distributions of several quality parameters of the online ring finder(from upper left to lower right: Number of pads in the ring region, ring value, veto value -* **NOV02 EXP***.*

Figure 8.16 b) shows the fraction of online lepton candidates also found by the Rich as a function of some meaningful parameters of the online ring finder: in this case the pads are counted only on the ring region of the Rich IPU mask. The efficiency drop is significant especially in the region of low ring quality.
To conclude, the online algorithm shows an efficiency between 60% and 80%

multiplicity	
All	52.9%
1 track/ring	53.1%
>= 2 tracks/ring	52.1%

Table 8.10: *Relative efficiency of offline ring finder with respect to online lepton candidates for C+C reactions at 1 and 2 AGeV -* **NOV02 EXP**.

with respect to the offline lepton candidates for the C+C reactions at 2 AGeV, a slightly less for the reactions at 1 AGeV. The efficiency depends on the thresholds and can be significantly improved with the new variation of the RichIPU algorithm without any loss in the reduction capabilities.

The online lepton candidates however still contain a significant fraction of misidentifies rings which justify the lower efficiency of the offline algorithm. Simulations show better agreement between the two algorithms because, despite of the good reconstruction of the global ring properties, the differential distribution of pads in the different regions of the ring mask has still some discrepancies most likely due to optical distortion and smearing of the ring, hardly reproducible in simulations.

The online ring finder is therefore considered as a good particle identification algorithm to be used alone and in a combination with the offline ring finder. Figure 8.17 shows the single lepton efficiency calculated for electrons originated from the target in a simulated C+C reaction at 2 AGeV. The efficiency is calculated for the online and the offline algorithm separately and for a combination with a logical AND or a logical OR. In all the cases the efficiency is constant over the full momentum range (b), while it increases with the number of originally produced photons (a). For the online algorithm (IPU) a slight drop at large number of photons is observed as a consequence of the veto region.

Figure 8.18 shows the single lepton purity for the online and the offline algorithm separately and for a combination with a logical AND or a logical OR. In all the cases the purity increases for increasing polar angle (a) as a consequence of the increased ladiator path length which makes the ring reconstruction easier, while it drops with increasing momentum (b), especially for the online algorithm (IPU). The online algorithm, being more simple, originates a higher number of misidentified rings which are then combined with high momentum hadrons which have a reasonable lepton signature in the other detectors (Tof and Pre-Shower).

(a) Number of Photons
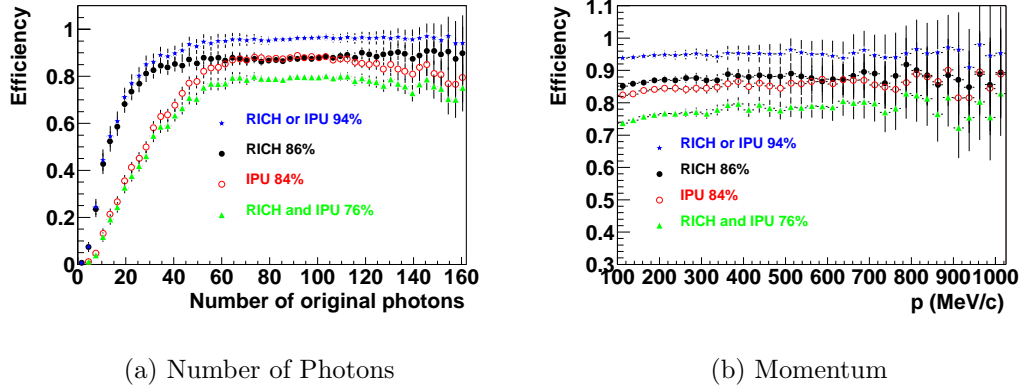
(b) Momentum

Figure 8.17: *Single lepton efficiency as a function of the number of originally produced photons (a) and the momentum (b) for the online algorithm (IPU), the offline one (RICH), for a combination with a logical AND (RICH and IPU) or a logical OR (RICH or IPU).*

(a) Polar Angle
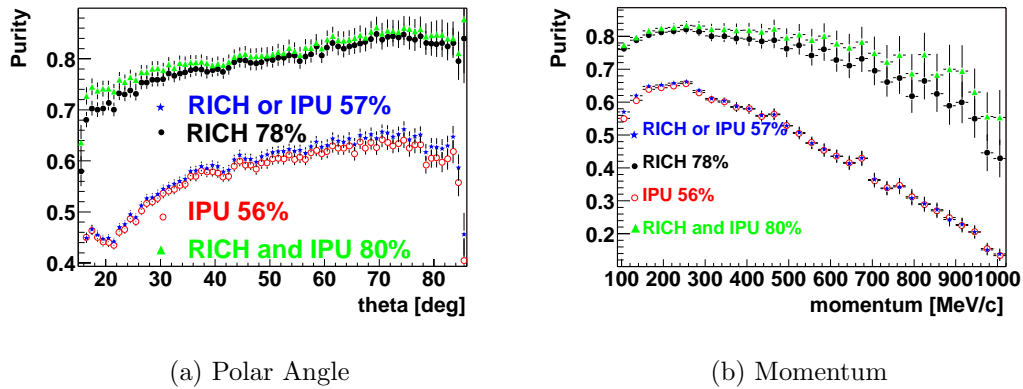
(b) Momentum

Figure 8.18: *Single lepton purity as a function of the polar emission angle (a) and the momentum (b) for the online algorithm (IPU), the offline one (RICH), for a combination with a logical AND (RICH and IPU) or a logical OR (RICH or IPU).*

Chapter 9

Performance of the Second Level Trigger

We wish to find the truth, no matter where it lies.
But to find the truth we need imagination and skepticism both.
We will not be afraid to speculate, but we will be careful
to distinguish speculation from fact.

(Carl Sagan)

Since the operation of the trigger occurs online and discarded events are not recoverable[1], the studies of the efficiency of the LVL2 and all its components is of great importance in order to extrapolate, correct and renormalize the physics results measured when the trigger is in operation.

The efficiency of the LVL2 is a very complex topic because of the several algorithms the LVL2 is comprised of and because of the reference used. Since the signal of interest of the HADES detector are e^+e^- pairs, and the LVL2 is designed for the reconstruction of such a signature, the natural choice would be to define the efficiency of the trigger as the fraction of e^+e^- pairs reconstructed with the LVL2 analysis. The *dilepton* efficiency therefore simply results from the single lepton efficiency folded with the proper phase-space. ($\epsilon_{pair} = \epsilon_{single}^2$); but the *event* efficiency of the trigger, which is the proper relevant quantity for the LVL2, since the trigger selects *events*, not *leptons*

---

[1]a fraction of non-triggered events, so called *downscaled* events is however always recorded, in order to be able to monitor the behavior of the trigger and normalize the final results.

is clearly higher[2] ($\epsilon_{pair} = 2\epsilon_{single} - \epsilon_{single}^2$) since the event is triggered even if only one lepton is found.

9.1   Efficiency of the Shower Algorithm

The shower recognition algorithm can be separated in a step where local maxima are determined and a step where a charge increase is calculated, the so called cluster search.

Concerning the local maxima search, the only difference between the IPU
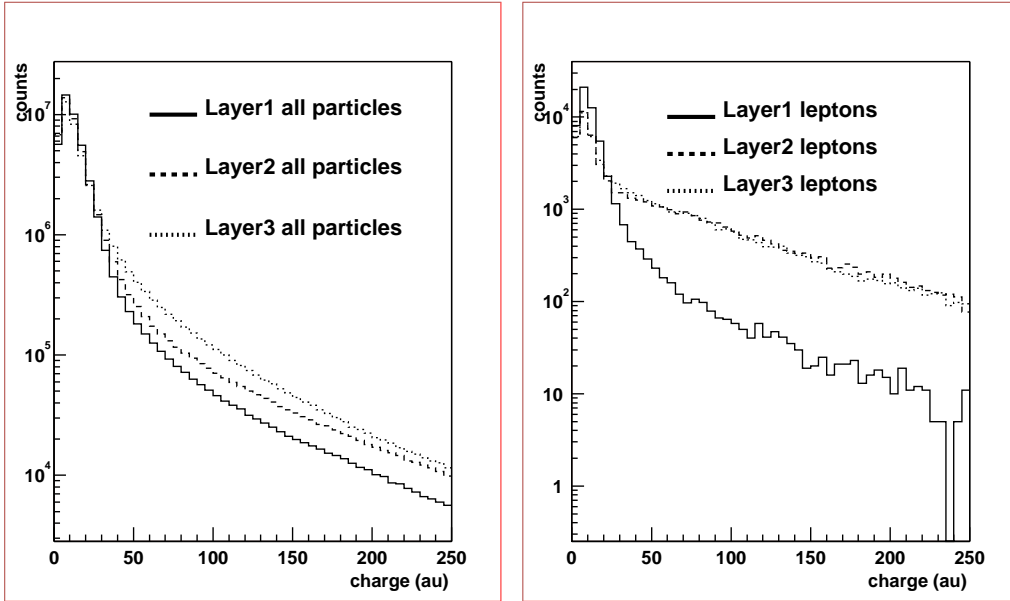
Figure 9.1: *Distributions of charge collected in the three detector planes for all the particles (left figure) and the lepton candidates (right figure). Lepton candidates have a clear increase of the charge collected in the successive layers with respect to the first, due to the development of the electromagnetic shower.*

algorithm and the one implemented in the offline analysis, is that the offline search for a maximum in the 8 neighboring pads, while the IPU uses only the 4 neighboring pads (even if later the charge sum is calculated on the full 3×3 pads area), therefore allowing a even higher close hit discrimination

---

[2] $\epsilon_{pair} = 1 - (1 - \epsilon_{single})^2 = 1 - (1 - 2\epsilon_{single} + \epsilon_{single}^2) = 1 - 1 + 2\epsilon_{single} - \epsilon_{single}^2 = 2\epsilon_{single} - \epsilon_{single}^2$

than the offline algorithm[3]. The main difference arises for the cluster search, where the efficiency of the IPU algorithm drops to about 30% for leptons with $p < 400$ MeV/c[4]. The performance of the Shower IPU have been studied with experimental data from C+C reaction at 2AGeV, collected during the November 2001 beamtime [141]. Tracks have been reconstructed and for the present analysis only those with p > 400 MeV/c have been considered; for p < 400 MeV/c the Pre-Shower detector efficiency drops: in this momentum range lepton identification is done via time of flight.

The charge distributions collected by the first, the second and the third de-
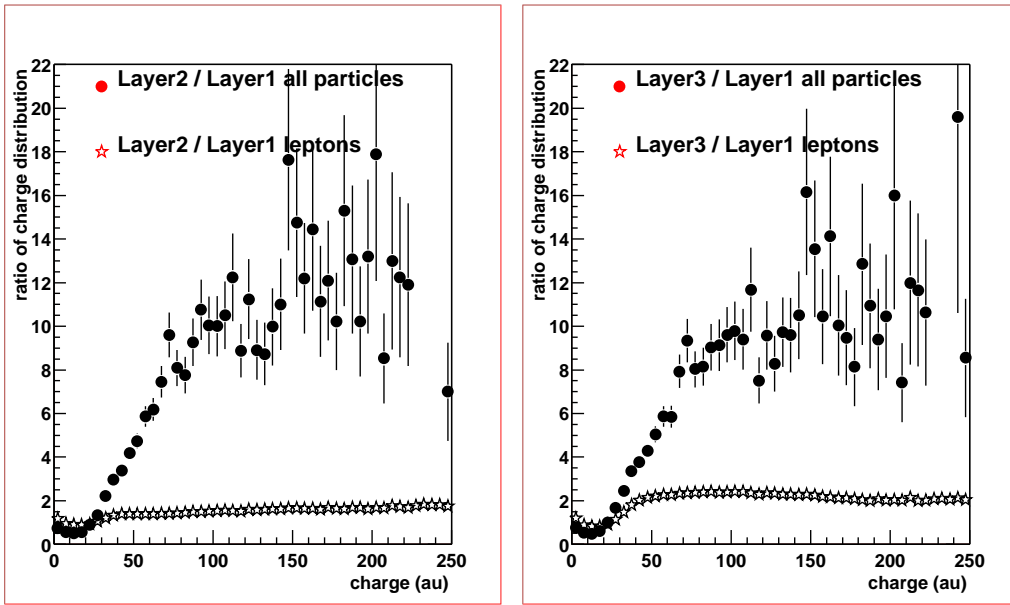
Figure 9.2: *Ratio of the charge distributions in the second (left figure) and third (right figure) detector plane with respect to the first plane. The full circles represents the ratios for lepton candidates (correlated to rings in the RICH detector with a leptonic time of flight). The empty stars represents all the particles, dominated by hadrons.*

tector layer are shown in Figure 9.1 for all the particles (left figure) and for lepton candidates (right figure), which are defined by a correlation to rings in the RICH detector within a narrow angular window and by a leptonic time of flight. The ratio of these distributions in Figure 9.2 qualitatively shows

---

[3]at a distance of 2m and with the spacial resolution achieved by the Shower pads, the close hit probability is anyway very low.

[4]which are however out of the signal of interest of HADES.

the different behavior of leptons and hadrons: leptons develop an electro-
magnetic shower and therefore produce an increase of charge in successive
layers, hadrons do not.

Figure 9.3 illustrates the selection criterion of the system for lepton/hadron
discrimination. The ratio of the charge collected in the second (Q_S^{L2}) or the
third layer (Q_S^{L3}) with respect to the first one (Q_S^{L1}) correspond to the Pre-
Shower condition (3.3) with the minimum bias threshold $Q^{Thres} = 0$.

The figure shows the probability distribution function of the maximum ratio
between the second/third and the first layer for hadrons and lepton can-
didates. A clear enhancement at higher ratios for the lepton candidates
is observed, giving credits to the Pre-Shower condition (3.3) as good lep-
ton/hadron discrimination. From the figure an efficiency of about 75% can
be estimated whereas a still high hadron contamination is present for the
selected thresholds (typically 1.9).
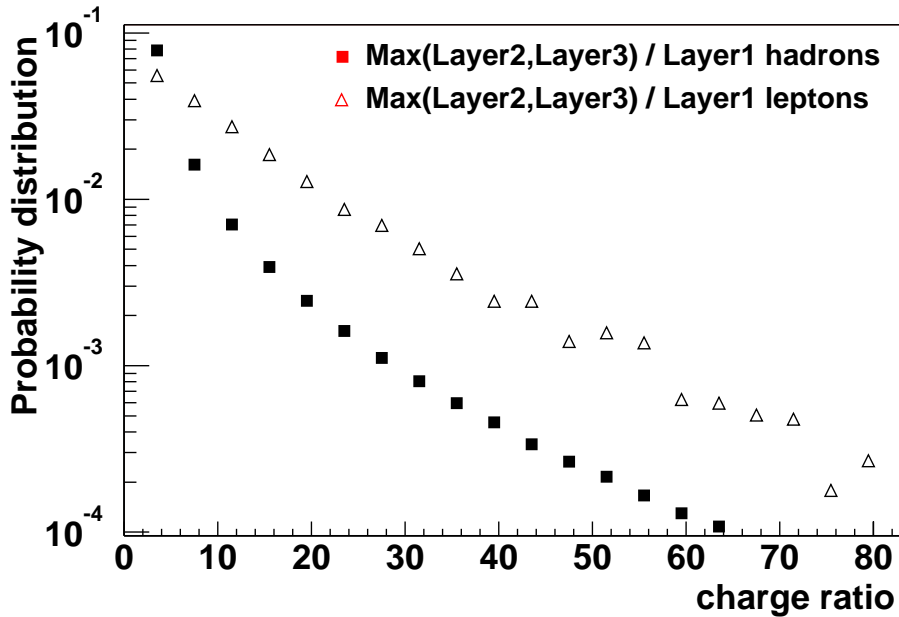
Figure 9.3: *Probability distribution function of the maximum ratio between
the second/third layer and the first one for hadron (full squares) and lepton
candidates (empty triangles). Leptons are scaled down by a factor 1000.*

Among all the reconstructed tracks with momentum larger than 400 MeV/p,
around 0.09% have a correlation with a good lepton candidate selected by
the RICH; if the sample of tracks is preliminary filtered with a Pre-Shower

condition

$$\frac{Q_S^{L2}}{Q_S^{L1}} > F_{th1} \text{ or } \frac{Q_S^{L3}}{Q_S^{L1}} > F_{th2} \tag{9.1}$$
$$\text{with } F_{th1} = F_{th2} = 1.9$$

the percentage of correlation with the RICH increases to 0.17%; the tracks which do not fulfill the Pre-Shower condition have a ring content of 0.04%. The Pre-Shower is therefore enhancing the leptonic signal, or reducing the hadronic background of a factor 4.

In order to reconstruct all the leptons, even the ones with p < 400 MeV/c however important for the reconstruction of the low-mass part of the dilepton spectrum (i.e. π^0 Dalitz, important normalization factor), the offline algorithm has been modified with the implementation of a momentum-dependent threshold, which allows to keep the efficiency constant to about 80% in the full momentum range.

9.2 Influence of the Matching Unit

The influence of the MU window has been studied. A window in polar angle clearly puts a bias on the momentum of the leptons. But a deflection occurs even in azimuthal angle due to the inhomogeneity of the magnetic field.

In particular the ϕ kick takes place when the particle enters or leaves the field region. and has opposite sign when leaving as compared to entering. When entering or leaving the field, the ϕ kick has opposite sign for positive and negative charges (at the same angles). The effects when entering and leaving the field do not cancel (even in first order) and the net effect is always some focusing towards the middle of the sector for both polarities.

This effect is due to:

- 5° difference in the coil entrance and exit angle with respect to the beam axis. This most likely explains the slight rotation of the distribution in Figure 9.4 (a) (linear in ϕ);

- bending of the trajectory while the particle passes the field region. This results in a further difference between entrance and exit angle (with respect to the coil). This explains most likely the ears in the distribution in Figure 9.4 (a) which should depend on $\Delta\theta$ [144].

Figure 9.4 shows the azimuthal deflection of lepton candidates as a function of the azimuthal emission angle for tracks respectively with momenta

lower (a) and higher (b) than 400 MeV/c. The MU window used in November 2002 experiment is marked. Particles with relatively high momenta are

(a) p < 400 MeV/c   (b) p > 400 MeV/c
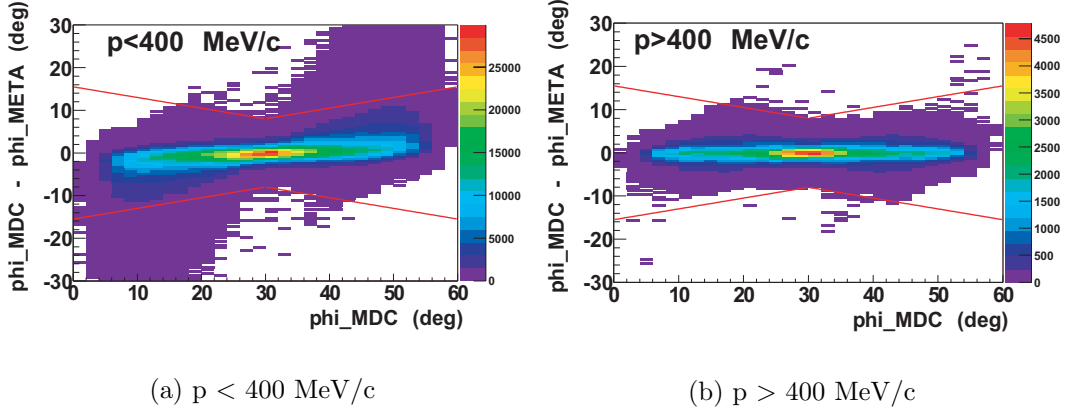
Figure 9.4: *Azimuthal deflection of lepton candidates as a function of the azimuthal emission angle for tracks respectively with momenta lower (a) and higher (b) than 400 MeV/c. The MU window used in November 2002 experiment is marked.*

not affected by the MU window, while low momenta particles are inhomogeneously cut by the window.

The dependency of the ϕ kick on the ϕ emission angle and the polar emission angle has been studied. In the middle of the sector ($15° < \phi < 45°$) the azimuthal deflection is rather weak, while it becomes stronger at the borders ($\phi < 15°$ or $\phi > 45°$). Investigations on the dependency on the polar deflection are being carried in order to linearize and reduce the MU window without efficiency loss, which would allow higher reduction factor, needed for heavier systems than C+C.

9.3   Efficiency of the LVL2

The LVL2 efficiency is rather dominated by the Rich IPU efficiency[5], especially if estimated with respect to the offline analysis. In principle the efficiency of the LVL2 for the single lepton has to be lower than the Rich IPU efficiency, since lepton candidate has to pass additional filters to be selected, even if the Shower and Tof condition, as well as the matching window do not significantly cut the lepton signal, being very conservative in these runs.

---

[5]and, as natural consequence, on the RICH detector efficiency

However, since the LVL2 selects *events* and not *leptons*, it turns out that the *event efficiency* is the more meaningful quality to characterize the trigger. In this sense it is important to stress that the LVL2 is not designed to efficiently reconstruct lepton signatures, but instead to significantly reduce the number of events without such signatures, therefore enhancing the signal/background ratio. Infact the lepton misidentification dominant in the LVL2 leads to an efficiency increase. To be noticed also that real leptons are generally sources of fake rings which accompain a real ring: they are mainly produced at a distance of approximately 1 ring-diameter from the center of the real ring and arise from combining a couple of fired pads from a real ring with some additional noise outside of the real ring. Table 9.1 shows the comparison between the *leptons* efficiency of the Rich IPU and the *events* of the full LVL2.

| | (Ring,Veto) Thresholds | | | | | | | |
| | (8,4) EMU | | (8,4) VAR | | (8,3) EMU | | (8,3) VAR | |
multiplicity	1AGeV	2AGeV	1AGeV	2AGeV	1AGeV	2AGeV	1AGeV	2AGeV
	November 01 EXP							
Rich IPU	61.6%	68.2%	74.9%	79.9%	48.3%	55.6%	63.4%	69.8%
LVL2	78.1%	85.7%	87.8%	92.0%	63.4%	73.8%	77.5%	84.4%
	November 01 SIM							
Rich IPU	69.5%	85.8%	81.6%	85.8%	57.6%	65.6%	72.7%	79.2%
LVL2	81.5%	92.3%	90.3%	92.4%	69.2%	75.9%	82.7%	87.3%
	November 02 EXP							
Rich IPU	-	68.2%	-	77.6%	-	57.5%	-	70.5%
LVL2	-	83.6%	-	89.3%	-	61.6%	-	83.4%

Table 9.1: *Comparison between the lepton efficiency of the Rich IPU and the event efficiency of the LVL2 for C+C reactions at 1 and 2 AGeV with different thresholds and variations of the ring finder algorithms (respectively November 2001 beamtime, November 2001 simulations, November 2002 beamtime).*

9.3.1 Efficiency in Nov02 Exp

In November 2002 an experiment with C+C reaction at 2AGeV was performed, with the LVL2 fully operational. An overall number of 242M events were collected, out of which approximately 56%, i.e. about 135M, LVL1 events - so called *downscaled* - and 44%, i.e. about 106M, LVL2 events.

The thresholds used in the Rich IPU were 8 for the ring region and 3 for the veto region; a 20 ns cut was used in the Tof IPU, while the Shower IPU used only the local maximum search. The matching window implemented in the Matching Unit was $\Delta\phi < 8° + \frac{\phi_{Rich}}{4}$, and the trigger condition was ≥ 1 lepton.

The downscaled events, i.e. LVL1, consist on a given fraction[6] of the primary LVL1 rate which is recorded independently of the Matching Unit decision[7]. To save computational time and optimize the rate, the Matching Unit could avoid any operation when such an event occurs, however for debugging purpose in this run the Matching Unit was operational also in the downscaled events and its decision was recorded[8].

To estimate the relative bias of the LVL2 (and LVL3) trigger on the LVL1 data sample, the lepton and dilepton analysis (See Chapter 5 and 6) was performed on LVL1, LVL2 and LVL3 events and the shape of some meaningful distribution was compared.

Figure 9.5 and 9.6 show respectively the azimuthal and polar emission angle distribution of lepton candidates, separately for electrons and positrons and for the Tof and Tofino-Shower system: the overlap of the three distributions is rather good, except for the LVL3 distribution in sector 4, most likely due to a Rich efficiency artificially reduced with the employ of high pedestal thresholds, to reduce some noisy area of the detector. The azimuthal region between 180° and 240°, corresponding to sector 3, has a lower yield due to some hardware problems (missing motherboards) in the MDCs which significantly reduce the efficiency of the tracking.

Figure 9.7 shows the polar and azimuthal deflection of lepton candidates: the deflections are shown for LVL1, LVL2 and LVL3 with the notation mentioned above and show a perfect agreement. Figure 9.8 shows the polar and azimuthal deflection are shown as a function of the reconstructed momentum for LVL1 (left) and LVL2 (right). The polar deflection is proportional to the inverse momentum and some artefact from badly reconstructed tracks is visible in the right upper corner, while the azimuthal deflection show a strong correlation with low momenta particles. Figure 9.9 shows the relative bias of LVL2 and LVL3 on the LVL1 data sample for the lepton candidates: the contribution from LVL3 is completely dominated by the LVL2 bias, which is completely neglectable in all the phase-space except for in the region of high

---

[6]EventHeader.downscaling=10 in this run

[7]EventHeader.downscalingFlag=1

[8]EventHeader.triggerdecision; it is 0 for negative trigger decisions, 1 for positive trigger decisions, 2 when the decision is positive but the MU stopped the analysis due to a high number of hit to match.
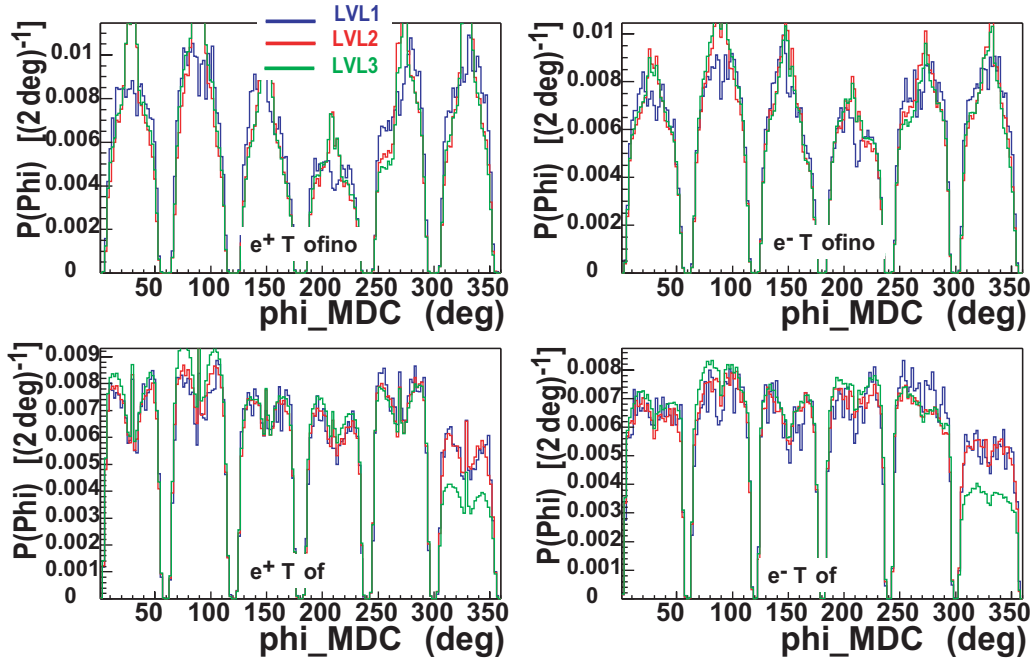
Figure 9.5: *Azimuthal emission angle distribution of leptons, from upper left to lower right: e^+ in Tofino/Shower, e^- in Tofino/Shower, e^+ in Tof, e^- in Tof; blue: LVL1, red: LVL2, green: LVL3.*

pseudorapidity, to indicate a significant contribution from the short radiator path length of the Rich detector.

No bias is produced by the LVL2 and LVL3 filter on the dilepton signal, as Figures 9.10 and 9.11 shows for like and unlike sign lepton pairs, up to some few percent statistical error due to the low dilepton contents in the LVL1 events so far analyzed.

The integral lepton/dilepton efficiency of the LVL2 can be given as the fraction of lepton/dilepton candidates in LVL1 events with a positive trigger decision: a 62% efficiency was estimated for leptons and a 84% efficiency was estimated for dileptons with opening angle larger than 4°, and 92% for dileptons with opening angle larger than 8°. The relative efficiency of LVL2 with respect to LVL1 can be estimated as well as the ratio between the number of leptons/dileptons found in LVL2 events and the number of leptons/dileptons found in LVL1 events multiplied by the downscaling factor - 1[9]. Even in this case an efficiency of 62% is found for leptons and an efficiency of 84% for

---

[9]If the downscaling factor is 10, it means that one out of 10 events is taken without the MU takes a decision. The other 9 events are subject to the MU decision,
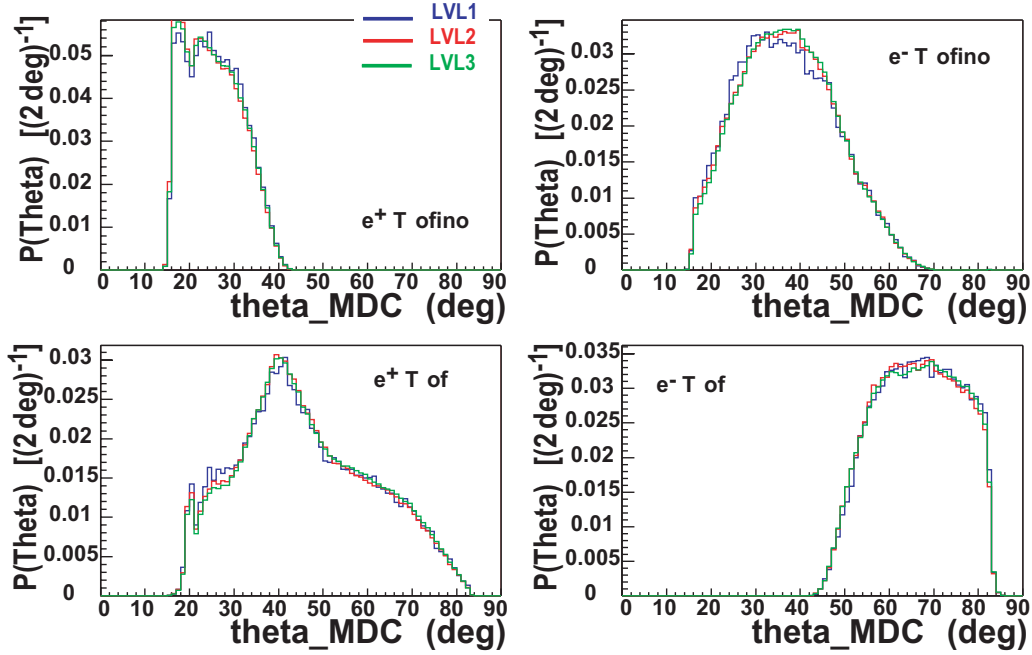
Figure 9.6: *Polar emission angle distribution of leptons, from upper left to lower right: e^+ in Tofino/Shower, e^- in Tofino/Shower, e^+ in Tof, e^- in Tof; blue: LVL1, red: LVL2, green: LVL3.*

dileptons.

The lepton efficiency increases to 83% in case the variation of the Rich IPU algorithm was used and with the more relaxed thresholds (8,4) in the Rich IPU even higher to almost 90%. The dilepton efficiency increases consequently.

Table 9.2 shows the multiplicity of leptons per event, separately for electrons and positrons in System 0 (Tofino/Shower) and System 1 (Tof) for the LVL1, LVL2 and LVL3 events, as well as the multiplicity of dileptons, separately for e^+e^+, e^-e^-, and e^+e^-, depending upon the different cuts used in Chapter 6. The relative enhancement gained at the different steps of the trigger in terms of lepton and dilepton yield is then estimated in the lower part of the table.

In the LVL2 events an enhancement by a factor 7.5 is found in the lepton yield, and by a factor 11 in the open pairs dilepton yield with respect to the LVL1 events. The LVL3 carries a further enhancement by an average 1.6 to achieve at the end an enhancement by a factor 13 is found in the lepton yield, and by a factor 17 in the open pairs dilepton yield of LVL3 events with respect to the LVL1 events.
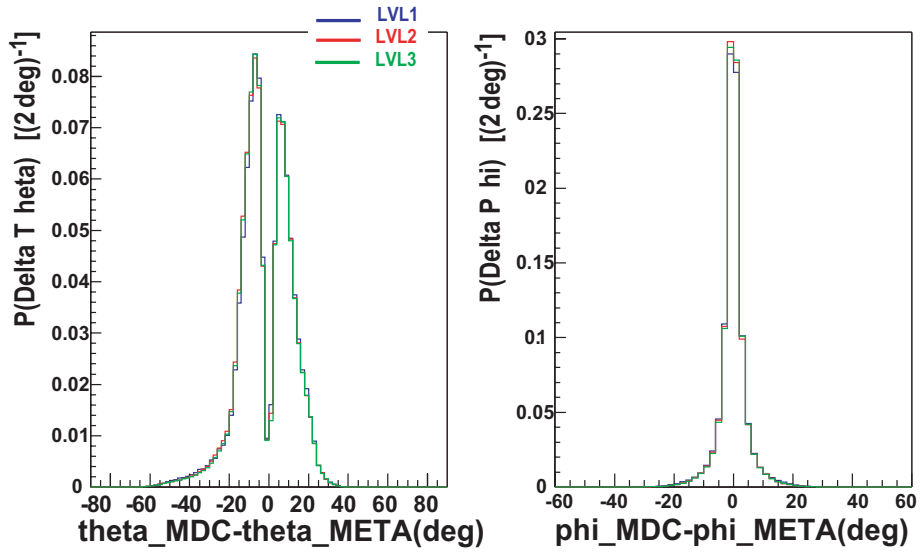
Figure 9.7: *Deflection of leptons in the magnetic field; on the right: polar and on the left: azimuthal deflection; in the polar deflection the opposite contribution of e^+ and e^- is visible; blue: LVL1, red: LVL2, green: LVL3.*
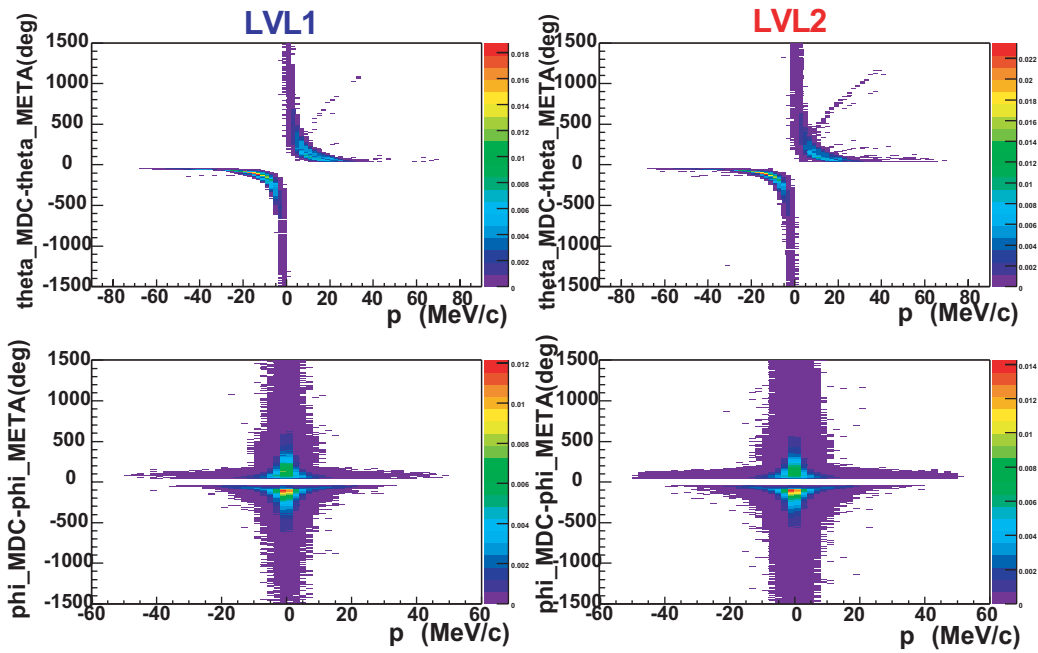
Figure 9.8: *Polar and azimuthal deflection as a function of p for LVL1 (right) and LVL2 (left).*
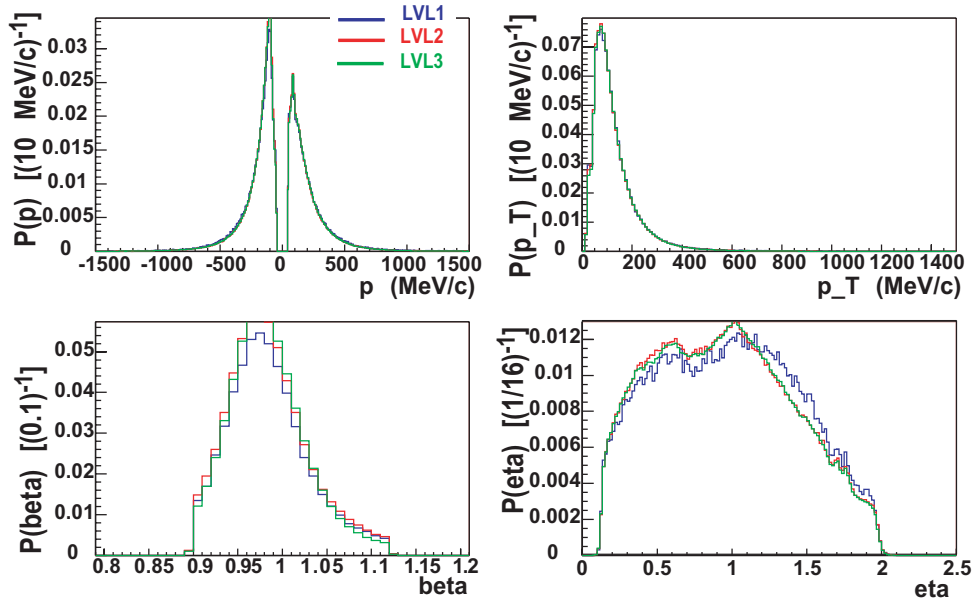
Figure 9.9: *Different distribution of leptons, from upper right to lower left:*
$p \cdot q$, p_T, β, η; *blue: LVL1, red: LVL2, green: LVL3.*

Thanks to the achieved enhancement, a much higher statistics is available in the November 2002 runs with respect to November 2001, as Figure 9.12 shows. In the figure the dilepton invariant mass spectrum is shown after the subtraction of the combinatoiral background, calculated with the like-sign method. Both distributions are normalized to the number of LVL1 and LVL3 events. The higher statistics achieved thanks to the LVL2 allows investigations of dielectron production over a wider invariant mass range.

9.4   Systematic Error

The performance of the online ring recognition and the LVL2 have been described in terms of their efficiency and the reduction capability. The fake probability is not a relevant quantity since the trigger is not designed to select the physical signal, but to reject the background events. The trigger is therefore expected to be entirely dominated by misidentified signal (leptons or dileptons) but this is unrelevant as long as the required event reduction is achieved.

The efficiency was mainly estimated taking as a reference the resulting lepton and dilepton spectra determined by the offline analysis. In this case the
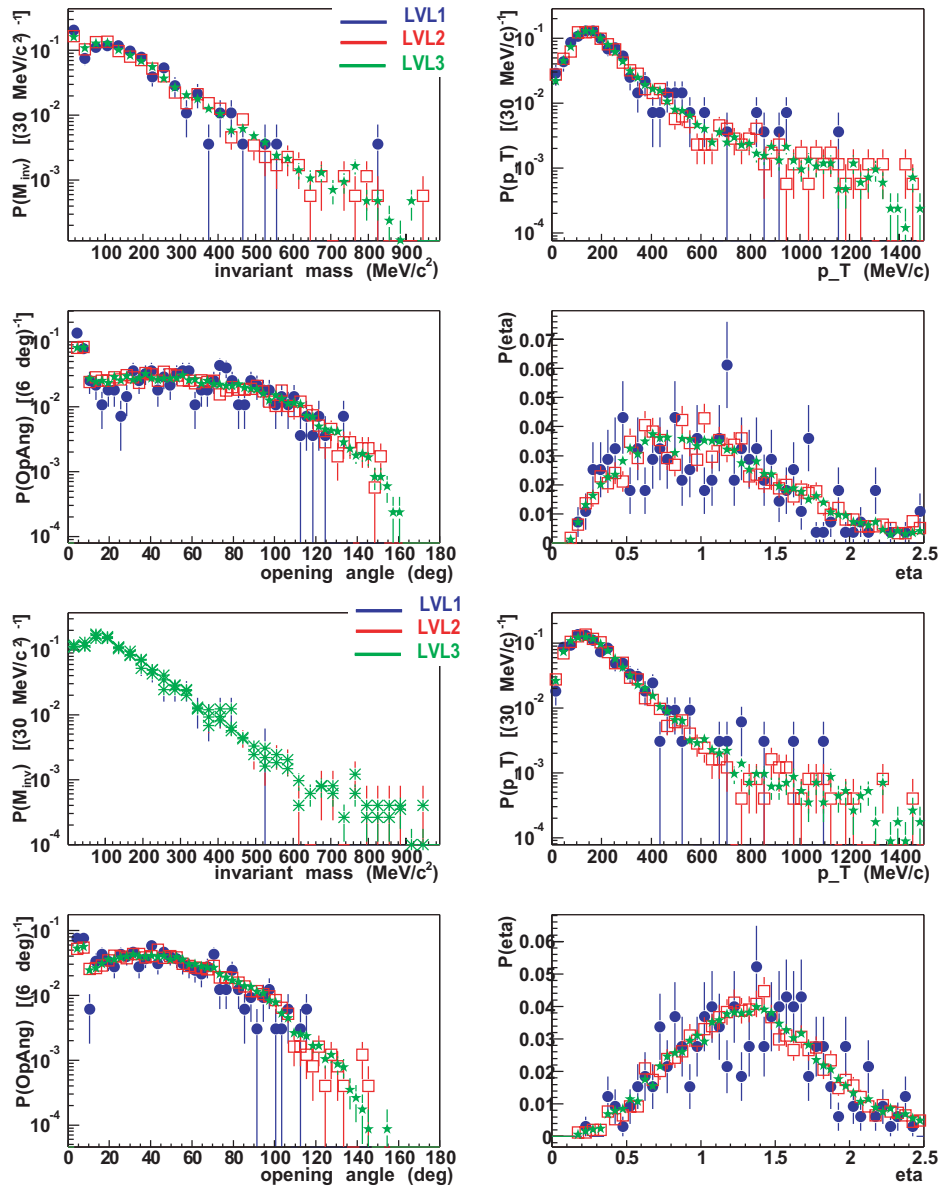
Figure 9.10: *Different distribution of positive like-sign dileptons, from upper right to lower left: invariant mass, transverse momentum, opening angle, pseudorapidity; blue: LVL1, red: LVL2, green: LVL3. e^+e^+ (up), e^-e^- (down) .*
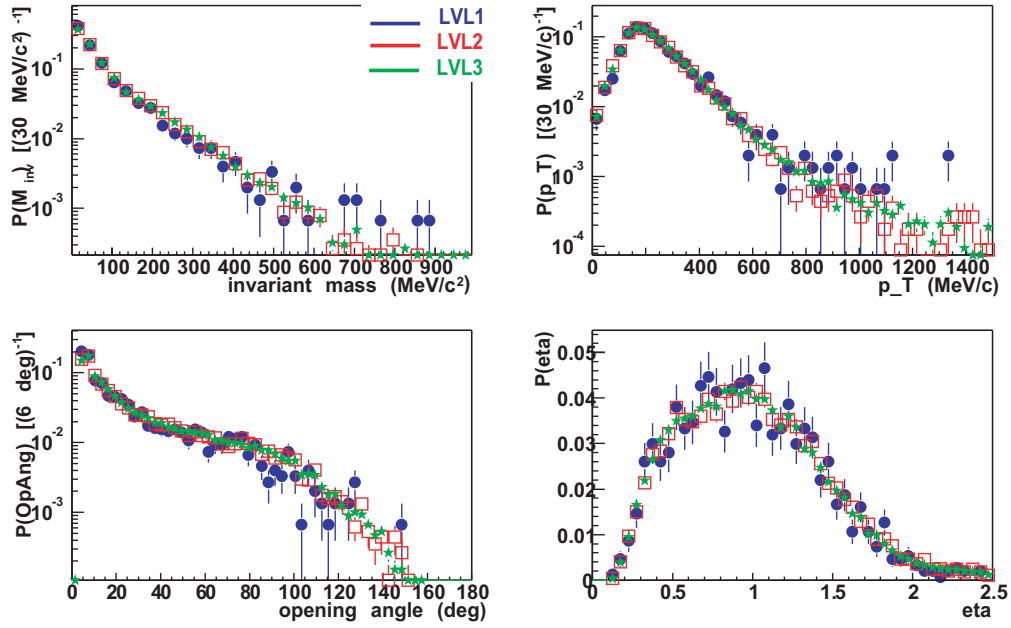
Figure 9.11: *Different distribution of unlike-sign dileptons (e^+e^-), from upper right to lower left: invariant mass, transverse momentum, opening angle, pseudorapidity; blue: LVL1, red: LVL2, green: LVL3.*

systematic error is described in 6.3.

The statistical error is also well below the systematic error. The bias of the LVL2 and LVL3 was estimated based on the available analyzed statistics of LVL1, LVL2 and LVL3 events. The statistical error in the dilepton spectra (Figures 9.10 and 9.11) due to the low dilepton contents in the LVL1 events is limited to the region of high invariant mass and large opening angle.

MULTIPLICITY	LVL1			LVL2			LVL3		
Leptons	SYS0	SYS1	ALL	SYS0	SYS1	ALL	SYS0	SYS1	ALL
$e^-[10^{-3}]$	4.4	9.6	13.9	26	80	106	47	136	184
$e^+[10^{-3}]$	6.9	4.9	11.8	47	40	87	84	68	152
All $[10^{-3}]$	11.3	14.5	25.8	73	119	193	131	204	335
DiLeptons	e^+e^+	e^-e^-	e^+e^-	e^+e^+	e^-e^-	e^+e^-	e^+e^+	e^-e^-	e^+e^-
All $[10^{-3}]$	2.1	2.8	4.9	16	22	39	23	32	59
Cut1 $[10^{-5}]$	4.1	4.8	22.3	34	47	226	55	73	345
Cut2 $[10^{-5}]$	3.8	4.5	20.9	32	46	211	52	70	327
Cut3 $[10^{-5}]$	2.9	3.8	13.2	26	39	146	42	61	229
ENHANCEMENT	LVL1-LVL2			LVL2-LVL3			LVL1-LVL3		
Leptons	SYS0	SYS1	ALL	SYS0	SYS1	ALL	SYS0	SYS1	ALL
e^-	5.9	8.3	7.6	1.8	1.7	1.7	11.0	14.2	13.2
e^+	6.8	8.2	7.4	1.8	1.7	1.7	12.2	13.9	13.0
All	6.5	8.2	7.5	1.8	1.7	1.7	11.6	14.1	13.0
DiLeptons	e^+e^+	e^-e^-	e^+e^-	e^+e^+	e^-e^-	e^+e^-	e^+e^+	e^-e^-	e^+e^-
All	7.1	7.9	8.0	1.4	1.4	1.5	11.0	11.4	12.0
Cut1	8.3	9.8	10.0	1.6	1.5	1.5	13.4	15.2	15.5
Cut2	8.4	10.2	10.1	1.6	1.5	1.5	13.7	15.5	15.6
Cut3	9.0	10.3	11.1	1.6	1.6	1.6	14.5	16.0	17.3

Table 9.2: *Multiplicity and enhancement of leptons per event, separately for electrons and positrons in System 0 (Tofino/Shower) and System 1 (Tof) for the LVL1, LVL2 and LVL3 events, and dileptons, separately for e^+e^+, e^-e^-, and e^+e^- depending upon the different cuts used in Chapter 6.*
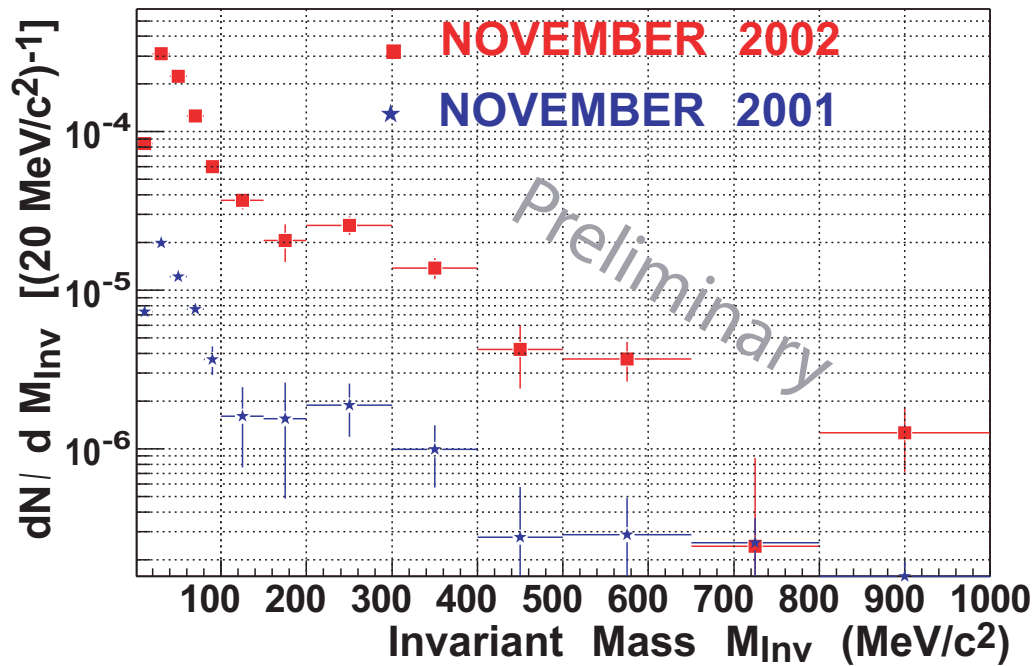
Figure 9.12: *Invariant mass distribution of all e^+e^- pairs (N^{total}_{+-}) subtracted by the combinatorial background (N^{uncorr}_{+-}) calculated with the like-sign technique for November 2001 and November 2002 data normalized to the number of LVL1 (November 2001) and LVL3 (November 2002) events. A variable bin size has been chosen to take into account the reduced statistics at higher invariant mass.*

Chapter 10

Conclusions and Outlook

TO THE READER
A compliment
with which to end a book

The reader my expectant mind projected
was, gentle reader, not a bit like you.
So if this book was less than you expected,
believe me, I've been disillusioned too.

(Piet Hein - Grooks IV)

The HADES second level trigger was operational during the last several commissioning and production beam times at GSI. In this work the performance of the trigger has been studied.

The cross check using the software implementation of the trigger algorithms has revealed a good reliability of the hardware processors which perform the trigger selection. The studies of the trigger performance have been carried out by comparing the results with the offline analysis with experimental and simulated data.

As the ring recognition is the most selective algorithm of the trigger and it is the only algorithm different from the one performed offline, its contribution has been studied in more detail.

Single electron distributions, as well as electrons embedded in a realistic environment of a C+C reaction at 2 AGeV simulated with the UrQMD event generator have been simulated with Monte Carlo methods in the spectrometer response. The quantum efficiency of the Rich CsI photocathode has been taken into account for different scenarios modeled after dedicated measurements performed with two different solid radiators (SiO_2 and MgF_2).

Different variations of the online ring recognition algorithm have been stud-

ied. An overall single lepton efficiency up to 85% was derived from the simulations: above the Cherenkov threshold, no dependency on the momentum of the lepton has been found, while the efficiency increases with polar angle due to the increased radiator path length.

Simulations of close and open pairs have been performed. An efficiency drop at small opening angles is due to the interference of the two rings patterns which overlap and veto each other. The response of the ring recognition algorithm to open pairs has been studied with a thermal generator of ω mesons decaying into e^+e^- pairs. The two correlated leptons can be detected simultaneously with an efficiency up to 45%.

Lacking a calibration experiment, such as for instance $p+p \rightarrow p+p+\eta \rightarrow p+p+e^++e^-$ the online ring recognition efficiency has also been estimated by a comparison with the rings found by the offline analysis. Due to the low photon statistics, and especially due to the background situation, both the online and the offline ring finder algorithms produce a large number of misidentified rings which do not correspond to any real lepton.

Since the online and the offline ring recognition algorithm do not necessarily find the same fake rings, real rings are selected by requiring a correlation between rings and lepton signatures coming from other detectors, i.e comparing the lepton samples obtained with a full lepton analysis performed using ring information either from the online or from offline ring recognition. A lepton sample is determined by a spatial correlation between the reconstructed track and the center of the ring detected by the Rich; in addition cuts on the time of flight as well as on some ring quality parameters have been applied to refine the lepton signature, and a condition on the charge collected in the different layers of the Pre-Shower detector which allows to discriminate electrons from pions. The selected cuts provide an efficiency of 77% and a purity of 78% estimated on the basis of the simulated sample.

The lepton analysis, performed with simulated and experimental data, gives a reasonable agreement on the shape of the lepton distributions while uncertainties are still present in localized areas of the detector. The shape of the polar angle distribution for particles with low momenta and low polar angle is attributed to hadron contamination not fully suppressed by the Pre-Shower nor by the Tofino and correlated to misidentified rings more abundant in experiment than in simulations.

A dilepton sample is obtained by pairing all the lepton tracks with opposite sign. Cuts are applied to remove the combinations where the lepton tracks use the same hit information in one subdetector: the Rich, the Mdc or Meta. Since these signatures are considered good hints of a close pair origi-

nating from external γ conversion, once the pair is rejected, the two lepton tracks which have been used are not combined with any other track of the same event. The impact of two different opening angle cuts (at $4°$ and $8°$) has been studied.

The combinatorial background has been calculated with the like-sign technique and subtracted. The dilepton yield has been normalized to the number of events which contain at least one reconstructed track to take into account experimental effects which create a positive LVL1 decision even for events without any track. The yield obtained with simulated data has been scaled to take into account the difference between the π^0 multiplicities experimentally measured and the ones calculated by the UrQMD model used for the simulations.

A reasonable agreement on the shape of the dilepton distributions is obtained, except for the pseudorapidity where discrepancies are found especially in the mid-rapidity region. These discrepancies might be traced back to the single lepton discrepancies and might become stronger in the region where the particle multiplicity is higher (i.e. mid-rapidity). A yield discrepancy within 30% indicates a need for improvements in the absolute normalization. For the analysis of the data sample collected in November 2002, only the first preliminary calibration was available, while no simulations were performed with the detector set-up as in November 2002; improvements will result from more refined calibration and detector alignment, as well as from an optimization of the different cuts in comparison with simulations. A further improvement, especially needed for heavier systems, will be provided by the installation of an RPC which will replace Tofino, guaranteeing higher granularity and better time resolution.

Based on the lepton and dilepton sample the comparison between online and offline ring candidates has been performed. It has been estimated that up to 80% of the offline lepton sample would be recognized as a ring by the online ring finder, while up to 92% of the same sample would be positively triggered with the complete lepton-trigger selection. For a lepton trigger the event efficiency is larger than the lepton efficiency due to the abundance of misidentified rings that, combined with a hadron track thanks to the open matching window, originate a positive trigger decision. Moreover when more than one lepton is produced in a given event, the probability for a positive trigger is higher than the probability to reconstruct all the leptons in the event.

On the other hand only 53% of the online lepton sample is recognized as a ring by the offline ring finder. This is due to the fact that the online algorithm is more simple than the offline and therefore generates a higher number of

misidentified rings which are then combined to hadron tracks. On the other hand the asymmetry in the ring mask and the veto distance of the offline ring finder introduce a bias to close pair which is not present in the online algorithm, although the veto region also reduces the sensitivity to close pairs.

The online ring finder is therefore considered as a good particle identification algorithm to be used alone and in a combination with the offline ring finder. In a first step it is used alone as input for the third level trigger performed offline in correlation with Mdc hit pattern information. The online ring finder has also been fully integrated in the particle identification code, providing, when used in combination with the offline algorithm, an increase in the signal efficiency and purity when used in a combination with the offline algorithm.

The second level trigger was fully operational in the November 2002 beam time when the C+C reaction was measured at 2 AGeV. Some more restrictive thresholds in the online ring recognition algorithm implemented in the Rich IPU were used together with minimum bias condition in the Shower and Tof IPU; a broad matching window was used in order not to introduce any momentum cut and to compensate for the inhomogeneous magnetic field at the border of the sectors. The trigger condition was that an event must contain at least one lepton. The dilepton condition, although fully implemented and tested, was not used since it was the first experiment with the LVL2 fully operational, and no higher reduction was needed from the data acquisition point of view. An overall number of 242M events was collected, out of which approximately 56% LVL1 events are downscaled and 44% LVL2 events with an event reduction factor of 12.

Due to the more restrictive thresholds of the Rich IPU only 57% of the offline lepton sample is recognized as a ring by the online algorithm, while 62% of this sample is however in positively triggered events. Since for a single lepton trigger condition the efficiency for dileptons is higher than the efficiency for leptons, the overall LVL2 efficiency for dileptons with opening angle larger than $4°$ or $8°$ is respectively 84% and 92%.

Thanks to this combined performance of event rejection and efficiency, a lepton enhancement by a factor 7.5 has been achieved, while the enhancement of dileptons with opening angle larger than $4°$ or $8°$ is respectively by a factor 10 and 11. The shapes of the lepton and dilepton distributions obtained for LVL1 and LVL2 events are in a very good agreement, which allow to conclude that the LVL2 does not introduce any physical bias in the data.

The analysis of November 2002 data is still preliminary and therefore

room for improvement is available, while effort has still to be put in some missing aspects of the analysis, as for instance the acceptance and efficiency correction, the studies of the absolute normalization and the combinatorial background.

Especially for these last purposes, while these pages are being written, the HADES spectrometer is measuring the $p + p \rightarrow p + p + \eta$ reaction. The LVL2 trigger is operational with rather conservative conditions which are optimized for minimizing the physical bias and the efficiency loss. Due to the low background situation these conditions provide a reduction by a factor ~ 10 and allow to collect approximately the same number of LVL1 and LVL2 events. Thanks to the kinematics constrains the reaction $p + p \rightarrow p + p + \eta$ can be measured and the leptonic channel can be absolutely normalized to the well known elastic yield and to the hadronic channels, and the integral efficiency of the detector, the trigger and the reconstruction software can be determined, without heavily relying on simulations. Due to the amount of the collected LVL1 events, the LVL2 trigger single electron efficiency can be disentangled and calculated.

Appendix A

A Picture of the Collision: Participants and Spectators

The world as you see it right here, right now,
is reality,
regardless of what the scientists say it might be...
But the world as revealed by scientific discoveries
is also reality...
What you've got here, really, are two realities, one of
immediate artistic appearance
and one of underlying scientific explanation,
and they don't match and they don't fit and they don't
really have
much of anything to do with one another.

(Robert M. Pirsig -
Zen and the Art of Motorcycle Maintenance)

To study nuclear matter in dense and hot conditions, the most popular experimental tool are relativistic heavy ion reactions. The most significant reactions are those where the hot and dense conditions are met, i.e. the collisions with a small impact parameter. the *impact parameter b* is classically defined as the distance between the direction vectors of the centers of the colliding nuclei, $b = 0$ for central collisions, $b = R_P + R_T$ for peripheral collisions. At relativistic energies, the total cross section is approximated by

$$\sigma_G = \pi(R_P + R_T)^2 \tag{A.1}$$

and it is constant as a function of b^2

$$\frac{d\sigma_G}{db^2} = \pi \tag{A.2}$$

A schematic view suggests that nucleons emitted from a reaction of two colliding nuclei at relativistic energies can roughly be separated into groups called *participants* and *spectators*, depending upon the impact parameter of the reaction. The participants may receive a considerable momentum transfer, whereas the spectator nucleons do not [30]. The experimental observable is the multiplicity of charged particles observed in the detectors, which is a monotone decreasing function of the impact parameter b. To each value of multiplicity M it is possible to associate the integral of the cross section

$$S = \sum_{m=M}^{\infty} \sigma(m) \tag{A.3}$$

such that

$$\int_0^B d(b^2) \frac{d\sigma_G}{db^2} = S, \tag{A.4}$$

In this way the impact parameter

$$B^2 = \frac{S}{\pi}. \tag{A.5}$$

and the average value of b^2 for the multiplicity interval $[m_i, m_j]$ can be calculated as

$$b_{ij}^2 = \frac{B_i^2 + B_j^2}{2}. \tag{A.6}$$

Although spectator nucleons are not so relevant within the scope of the HADES experiment[1], nevertheless protons are the most abundant particles detected by the HADES detector and they are important in order to have a full description of the reaction.

A.1   Symmetric Systems: C-C

This concept has led to the implementation of spectators in PLUTO [31]. With this new feature it is possible to get a more realistic description of the behavior of participants and spectators as depicted in Figure A.1 The *reduced impact parameter* is defined as the ratio between the impact parameter and the maximum value that this quantity can assume, and therefore runs from 0 to 1. The geometrical model used in PLUTO [32] has been compared with

---

[1]projectile-like spectators are emitted at small forward angles and are not in the acceptance of the detector, target-like spectators have such a small momentum that they are curl up in the magnetic field
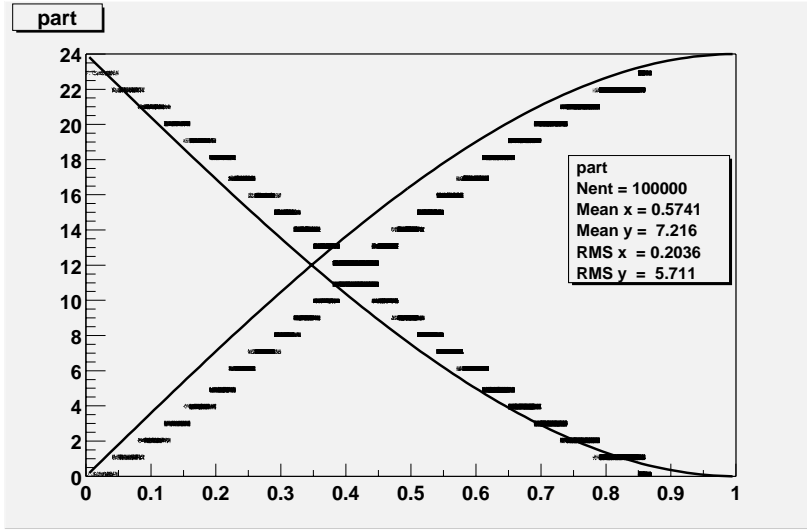
Figure A.1: *C+C participants and spectators as a function of the reduced impact parameter. Dashed lines are obtained with data generated by PLUTO, whereas the full lines have been calculated with eq. A.7.*

the so called *equal-participant model* where the number of participants is given by [33]

$$A_F(x) = \frac{1}{4}A_P(2 - 3\cos\theta_1 + \cos^3\theta_1) + \frac{1}{4}A_T(2 - 3\cos\theta_2 + \cos^3\theta_2) \quad \text{(A.7)}$$

with

$$\cos\theta_1 = (x - \frac{x_{min}}{x})\frac{R_P + R_T}{2R_P} \quad \text{(A.8)}$$

$$\cos\theta_2 = (x + \frac{x_{min}}{x})\frac{R_P + R_T}{2R_P} \quad \text{(A.9)}$$

and

$$x_{min} = \frac{R_T - R_P}{R_T + R_P} \quad \text{(A.10)}$$

A.2   Asymmetric Systems: Cr+Al

For asymmetric systems, like Cr+Al, also measure by HADES it is important to have a distinction between target-like spectators and projectile-like spectators, which has been implemented as well. The behavior of participants and spectators is once again shown in Figure A.2 for the reaction Cr+Al as a function of reduce impact parameter.
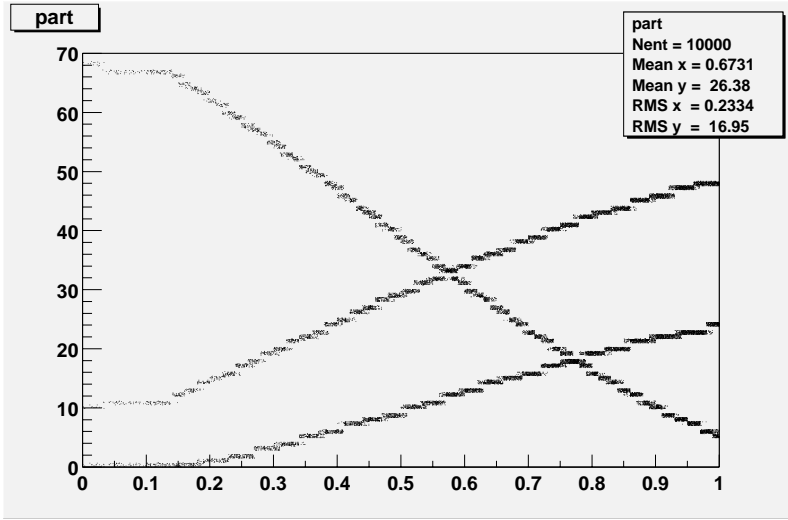
Figure A.2: *Cr+Al participants, target-like and projectile-like spectators as a function of the reduced impact parameter. Dashed lines are obtained with data generated by PLUTO.*

A.3   Kinematical Characteristics of the Model

A collision of two nuclei is considered, where the projectile nucleus has relativistic velocity, so it is Lorentz-contracted, while the target is fixed in the lab frame. After the collision, it is possible to distinguish between three different regions:

- target-like spectators, centered at rapidity $y = 0$

- participants, centered at mid-rapidity $y = y_{CM}$

- projectile-like spectators, centered at rapidity $y = y_{BEAM}$

A.3.1   Symmetric Systems: C-C

The multiplicity distribution per rapidity interval dN/dy has been calculated for events produced by QMD and PLUTO and then compared in Figure A.3 The differences between these two models can be better visualized by comparing the $p_T - y$ distributions, shown in Figure A.4 The intermediate region between the so called *low-temperature fireballs*[2] and the participant fireball itself is poorly reproduced in PLUTO. These transition

---

[2]target-like and projectile-like spectators have a temperature which is one order of magnitude lower than the fireball temperature.
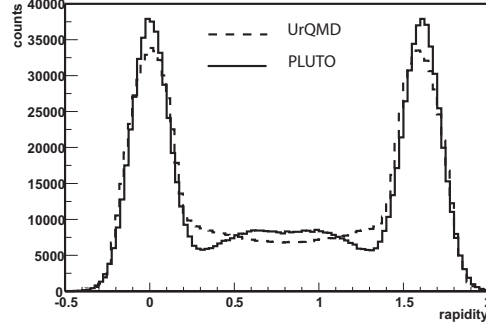
Figure A.3: *Rapidity distribution of protons. The blue line represents events calculated with PLUTO, the red one with UrQMD.*

regions are clearly visible in the calculations from QMD because a transport model follows the whole evolution of the system, but are completely missing in PLUTO which sharply cuts the three regions.

(a) PLUTO

(b) UrQMD
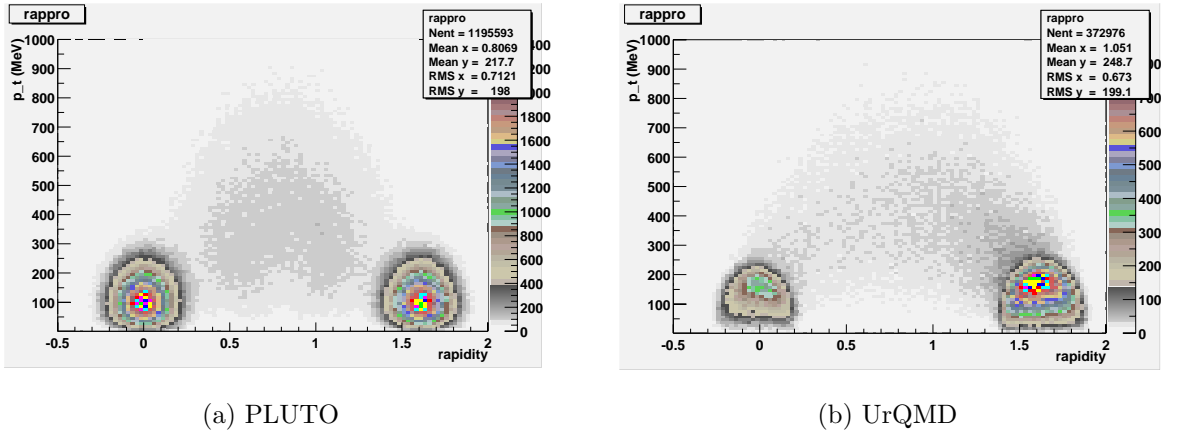
Figure A.4: *Inclusive* $p_T - y$ *distribution of protons. It is possible to see that the intermediate regions as well as the internal structure of the participants and spectators fireballs are not reproduced with PLUTO.*

The problem is confirmed again by the momentum and the angular distribution in the HADES acceptance[3] (Figure A.5). In the momentum distribution the corner where the fireballs are cut is clearly visible. It is clearly visible how the sharp distinction between the fireballs in PLUTO completely cuts away the transition region. The emission polar angle distributions also show

---

[3]i.e. $18° < \theta < 88°$ and $p > 100 MeV/c$.

(a) Momentum

(b) Polar Angle
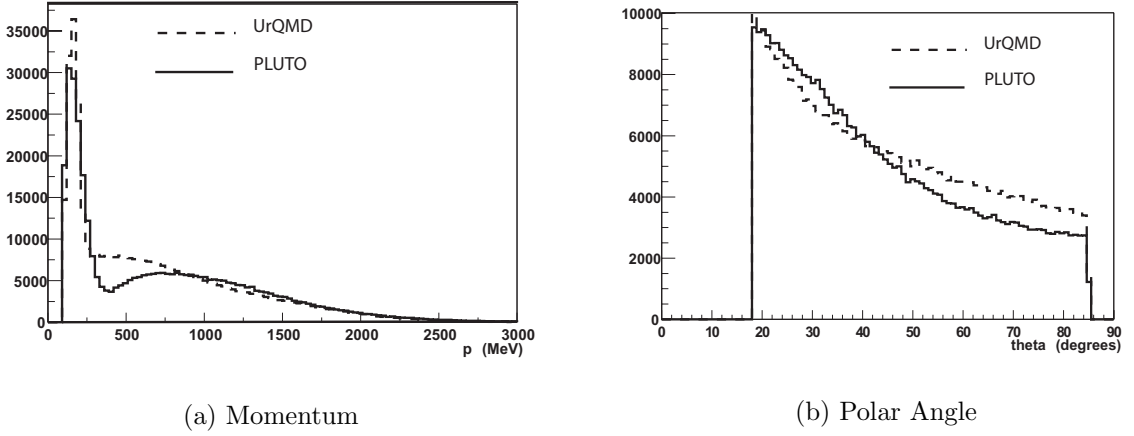
Figure A.5: *Momentum and angular distribution for protons generated with PLUTO and UrQMD within the HADES acceptance. The blue lines are obtained with PLUTO, the red ones with UrQMD events.*

a disagreement with QMD distribution where PLUTO drops more quickly at large angles, having no counts in the transition region. PLUTO distribution drops more rapidly at large angles due to the absence of counts in the transition region.

A.3.2   Asymmetric Systems: Cr+Al

For an asymmetric system the form and the magnitude of the dN/dy spectrum changes depending upon the masses of the colliding nuclei, as it is shown in Figure A.6 for QMD events. This asymmetry is not reproduced
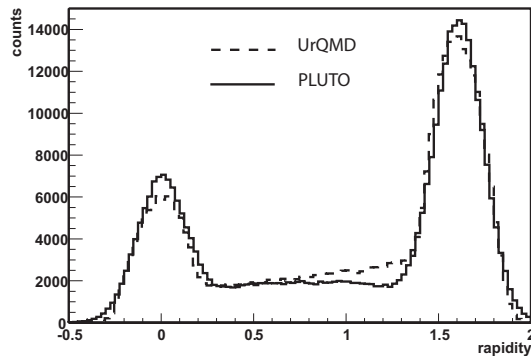
Figure A.6: *Rapidity distribution of protons. The blue line represents events calculated with PLUTO, the red one with UrQMD.*

with PLUTO.

Although the participant fireball is set at y_{CM}, the extended structure of the fireballs, and the intermediate transition region is not reproduced and does not show any shift in the $p_T - y$ distribution (Figure A.7)

(a) PLUTO   (b) UrQMD
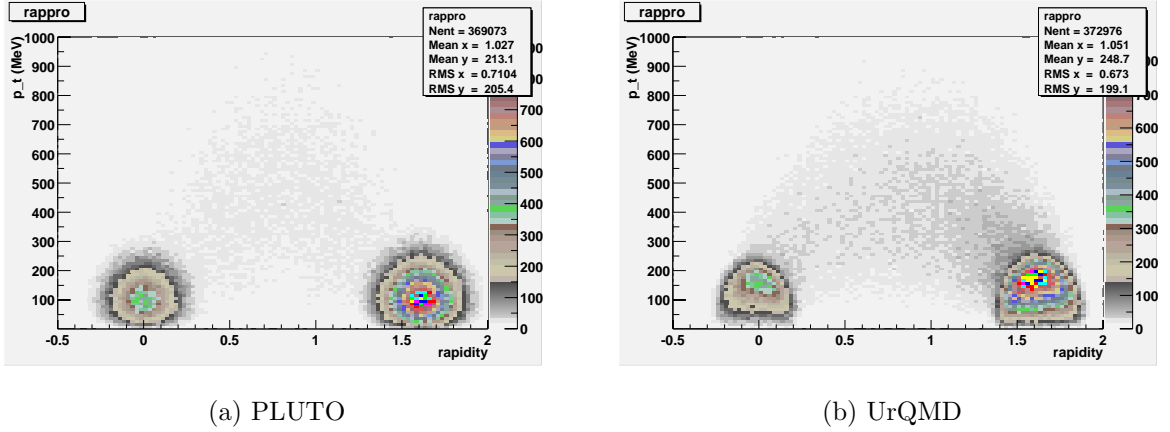
Figure A.7: *Inclusive* $p_T - y$ *distribution of protons. Once again the intermediate regions are not reproduced with PLUTO, as well as the asymmetry in the participants region and the extended structure of the fireballs.*

A.4   Methods Used in the Code Implementation

To account for target-like spectators and projectile-like spectators, the PFireball class has been modified. A flag has been introduced in the definition of the fireballöl, which can assume a value of 0 for participants, 1 for target-like spectators, or 2 for projectile-like spectators. The flag is 0 by default, and can be set to a different value in the definition of the fireball of by the function setSpectator() and can be read by the function getSpectator(). The function sampleNProd() has been modifeid to calculate the average number of target-like spectators $At - Npar(At, Ap, b)$ and the average number of projectile-like spectoators $Ap - Npar(Ap, At, b)$ where At and Ap are the mass number of the target and the projectile respectively and $Npar$ is given in the function Npar().

Finally to account for the rapidity distribution, the function setToMidrapidity(float agev), which boosts a thermal source to the correct rapidity with

agev being the energy per nucleon of the projectile (expressed in GeV/u), has been modified, such that

- $\beta_Z = 0$ for target-like spectators

- $\beta_Z = \beta_{CM} = \frac{p_{lab}}{E_{1lab}+m_2} = \sqrt{\frac{agev}{agev+2.\cdot0.9315}}$ for participants

- $\beta_Z = \beta_{BEAM} = \frac{p}{E} = \sqrt{\frac{agev\cdot2.\cdot0.9315}{agev+0.9315}}$ for projectile-like spectators

where 0.9315 GeV is the mass of a bound nucleon.

Appendix B

Theoretical Models for Ultrarelativistic Heavy Ion Collisions

> *It must be hard to be a model,*
> *because you'd want to be like*
> *the photograph of you,*
> *and you can't ever look that way.*
>
> *(Andy Warhol)*

Although the strong interaction which regulates the phenomenology of heavy ion collisions is described by the gauge theory of the Quantum Chromo Dynamics (QCD), no exact solution is derivable yet in the low momentum transfer region, i.e. when quarks are confined into hadrons. Here microscopic and macroscopic transport models attempt to describe the time evolution of the system from the initial state of the reaction up to the freeze-out of all the products of the reaction on an event by event basis, that allows for the same analysis used for experimental data.

The transport theories are generally based on the derivation and solution of the Hamiltonian equation of motion of the elementary degrees of freedom (being they quarks and gluons or baryons and mesons), deriving the solutions for an effective Lagrangians, where the interaction between nucleons is described in terms of the $\sigma - \omega$ model, by the exchange of a scalar and a vector field.

The Quantum Molecular Dynamics (QMD) model [145, 146, 147] is a N-body theory where the equations of motion, derived from a generalized variational principle for the classical 6 time-dependent phase-space parameters (q_i, p_i) which describe each nucleon, are solved numerically. The target and projec-

tile nucleons are distributed in a sphere proportional to the mean density of the nucleus and their initial momenta are stochastically chosen between 0 and the local Thomas-Fermi momentum.

Nucleons propagate by means of a Cascade model [148], where particles are emitted on straight trajectories. Interaction is governed by a Coulomb potential, which does not include any compression effects due to the presence of the nuclear medium, which are instead implemented in the Ultrarelativistic QMD (UrQMD) [149] with a non-relativistic density-dependent Skyrme-type equation of state with an additional Yukawa and Coulomb potentials.

Collisions are performed in a geometrical point-particle sense, i.e. two particles collide if the minimum relative distance of centroids of the Gaussians during their motion satisfies a requirement for the cross-section which depends on the CM energy, on the species and the quantum numbers of the colliding particles. Elementary cross-sections are fitted to available experimental data.

Particle production happens via excitation and subsequent decay of a meson or baryon resonance or, for incident beam energy higher than 10 AGeV, via string excitation and fragmentation. Several baryon and meson species are included in UrQMD and, through baryon-antibaryon and isospin symmetry, the respective antibaryon states are included as well as all isospin-projected states [150].

UrQMD is used as event generator for HADES full scale simulations to provide a basis of comparison with experimental data collected in C+C reactions at 1 and 2 AGeV. The HADES data analyzed and presented in the framework of the present thesis are focussed on low invariant mass dilepton region. Table B.1 presents a comparison between the π^0 and the η multiplicities resulted from UrQMD calculations [151] and the ones measured by the TAPS experiment [152] for different beam energies.

 UrQMD seems to reproduce the measured values with a good agreement in the rapidity interval covered by the TAPS acceptance,

$$
\begin{aligned}
\frac{\langle M \rangle_{\pi^0}^{TAPS}}{\langle M \rangle_{\pi^0}^{UrQMD}} \;&=\; 1.00 \text{ at } 0.8 \text{ AGeV} \\
&=\; 0.92 \text{ at } 1.0 \text{ AGeV} \\
&=\; 0.82 \text{ at } 2.0 \text{ AGeV}
\end{aligned}
\tag{B.1}
$$

Source	TAPS	UrQMD	TAPS	UrQMD	TAPS	UrQMD
E [AGeV]	0.8	0.8	1.04	1.00	2.0	2.0
Δy	0.42-0.74		0.42-0.74		0.8-1.08	
$\langle M \rangle_{\pi^0}[10^{-2}]$	6.0±0.4	6.0	8.0±0.5	8.7	13.7±1.7	16.7
$\langle M \rangle_{\eta}[10^{-4}]$	2.3±0.7	0.2	7.2±1.4	2.4	85±15	52.7
Δy	all		all		all	
$\langle M \rangle_{\pi^0}[10^{-2}]$	22.2±1.8	32.3	33.5±2.5	52.2	82.6±8.4	122.3
$\langle M \rangle_{\eta}[10^{-4}]$	6.9±2.5	1.5	17±5	9	294±46	225.1

Table B.1: *Comparison of mean multiplicities for π^0 and η measured by TAPS and calculated by UrQMD dor the $^{12}C + ^{12}C$ reaction at different energies. The rapidity interval Δy covered by TAPS is indicated for the different energies. The extrapolation to the full rapidity interval is done with the assumption of an isotropic angular distribution.*

while a discrepancy appears for the extrapolated full acceptance

$$
\begin{aligned}
\frac{\langle M \rangle_{\pi^0}^{TAPS}}{\langle M \rangle_{\pi^0}^{UrQMD}} &= 0.69 \text{ at } 0.8 \text{ AGeV} \\
&= 0.64 \text{ at } 1.0 \text{ AGeV} \\
&= 0.68 \text{ at } 2.0 \text{ AGeV} \quad\quad \text{(B.2)}
\end{aligned}
$$

which assumes an isotropic angular distribution of pions in CM system and neglect any collective flow effect, which could account for a 10% factor. These correction factors have been used to correct the simulated spectra presented in Chapter 5 and 6.

Appendix C

Estimation of the RICH-MDC correlation window

In the lepton analysie (See Chapter 5) the RICH rings are correlated to MDCs inner segments, in order to select tracks with a RICH lepton signature for a further analysis and discard hadron tracks as well as misidentified rings. The polar and azimuthal coordinates of the ring centers have to be matched with the polar and azimuthal coordinates of the MDCs segments witin a matching window determined by analyzing experimental data and comparing them with simulated ones.

Matching is done by creating all the possible correlations between rings found by the RICH and the inner MDCs segments which have been used to reconstruct a track.

C.1 Azimuthal correlation

Figure C.1 (a) shows the difference of the azimuthal angle measured by RICH and by MDC. As already mentioned, to keep the solid angle spanned by the correlation window constant,

$$d\Omega = dY \cdot \frac{dX}{R^2} = (R \cdot \delta\theta) \cdot \frac{(R \cdot \delta\phi \cdot \sin\theta)}{R^2} = \delta\theta \cdot \delta\phi \cdot \sin\theta \qquad (C.1)$$

the $\delta\phi$ distribution should be corrected with the factor $\sin\theta$.

The combinatorial background shows two structures visible in the origi-

(a) FIT 1   (b) FIT 2
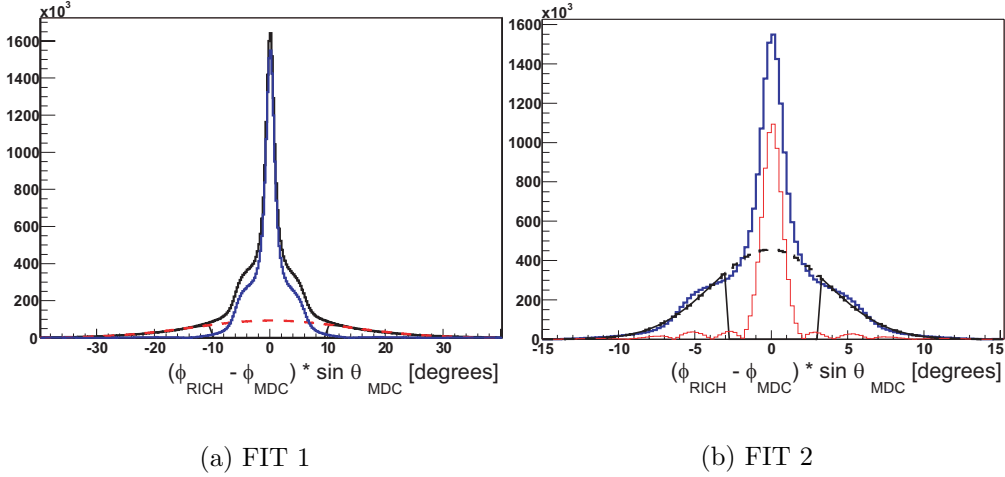
Figure C.1: *Azimuthal angle correlation between recognized rings and MDC inner segments. In (a) the combinatorial background is fitted and subtracted. The result of this first subtraction is plotted in (b) where the combinatorial background arising from fake rings accompayining the real one is fitted and subtracted.*

nal distribution, coming from different origins: the one extending over the full range is the combinatorics with all the hits multiplicity, the one concentrated in the $(-10°, +10°)$ range is originated by fake rings accompayining a real ring. These are mainly produced at a distance of approximately 1 ring-diameter from the center of the real ring. Their origin will be clear later. An iterative fitting procedure is applied. In the first step a gaussian-shaped background is fitted in the range $[(-\infty, -10)\bigcup(+10, +\infty)]$ and then subtracted. The histogram resulting from the subtraction in then plotted in Figure C.1 (b). Again a gaussian-shaped background is fitted in the range $[(-10, -3)\bigcup(+3, +10)]$ and then subtracted. The result is presented in Figure C.2 (a).

Similar results are obtained with simulated data, presented in Figure C.2 (b). The width of the distribution is more narrow since the optical distortion of the RICH mirror, which generates smearing of the ring pattern with a worst position resolution, is not included in the simulations.

(a) EXP

(b) SIM
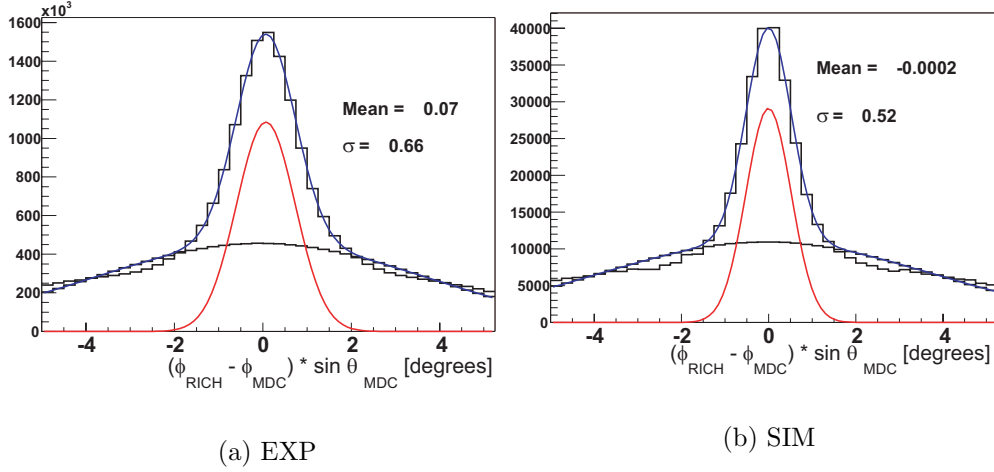
Figure C.2: *Azimuthal angle correlation between recognized rings and MDC inner segments. The results of the fitting procedure is shown for experimental (a) and simulated (b) data.*

C.2   Polar correlation

The polar angle correlation presents some additional difficoulties. The polar, as well as the azimuthal angle of the RICH result from the mapping of the single pads. The mapping table has been generated by a Monte Carlo simulation: a homogeneous distribution of electrons (with known θ and ϕ emission angle) starting from the target position is simulated; the position is then projected on a gievn pad on the pad plane and the mapping is established. Therefore the mapping assumes that the vertex of the electrons is in the target. But due to the optical properties of the mirror, any parallel track is reflected on the same position.

The MDCs cluster finder is based on a projection plane which is determined by the target position, and only after the fitting procedure the "real" angular coordinates are determined. If a track is not fitted, the angular position is determined assuming the vertex of the track in the target.

Since secondary vertices, due to bad focussing of the beam, most likely arise before and not after the target position, due to the presence of some material in the beam line, the background is not symmetric. Figure C.3 schematically shows this point.

The fitting procedure has been therefore carried with the help of simulations, where it is possible to identify the different background sources. Figure C.4 shows the difference of the polar angle measured by RICH and by MDC:
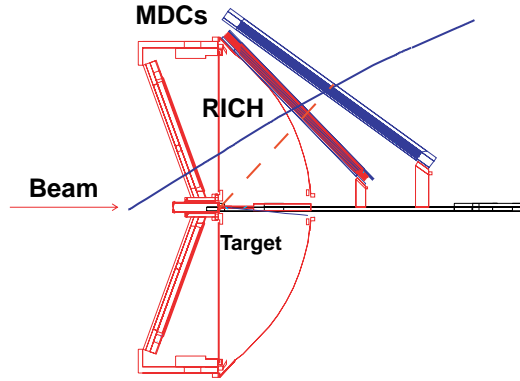
Figure C.3: *Schematic explanation of the problem arising when matching the polar angle θ measured by RICH and MDC. Tracks originating before the target (solid line) have a larger angle in MDC (dashed line), therefore the background is not homogeneous.*

all the range is shown in (a) where the contribution of the different background sources is marked. Different flags can be assigned to rings and tracks
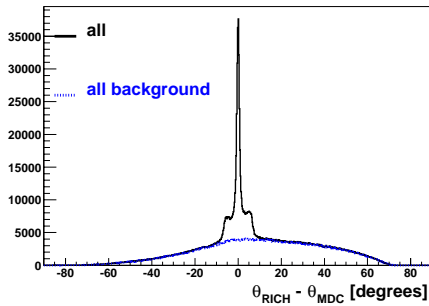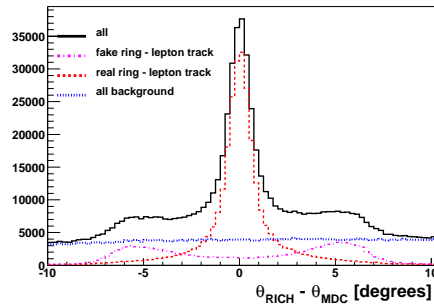
(a) $(-85°, +85°)$ (b) $(-10°, +10°)$

Figure C.4: *Polar angle correlation between recognized rings and MDC inner segments for $(-85°, +85°)$ (a) and $(-10°, +10°)$ (b). The correlation has been obtained with simulated data. The different contributions are separated.*

depending upon their origin, known from the Monte Carlo input; rings can be

- Ring 0: misidentified patterns;

- Ring 1: originated by leptons, recontructed in the proper position

(takin into account a possible deviation due to detector resolution and optical smearing).

Kickplane tracks can be originated by:

- Track 0: wrong correlation between MDC and META hits, the MDC hit has no leptonic origin;

- Track 1: wrong correlation between MDC and META hits, but the MDC hit is originated by a lepton (it is important to separate this case from the previous one, since this case most likely describes a low momentum lepton which is bended out by the magnetic field; in this case a correlation is expected in the RICH);

- Track 2: proper correlation between MDC and META hits, but of hadronic origin;

- Track 3: proper correlation between MDC and META hits, originated by a lepton.

The background marked in Figure C.4 (a) consists of the correlations between

- Ring 0 - Track 0: a fake ring with a fake track;

- Ring 0 - Track 2: a fake ring with a hadron track;

- Ring 1 - Track 0: a real ring with a fake track;

- Ring 1 - Track 2: a real ring with a hadron track.

This background is expected to be homogeneously distributed in the detector phase-space, but for the reasons mentioned above (secondary vertices *before* the target) it is not.
Figure C.4 (b) is a zoom of (a): apart from the background just described, two main contributions are distinguished: the proper signal, consisting of the correlations between

- Ring 1 - Track 1: a real ring with a wrong track correlation which has a leptonic content in MDC;

- Ring 1 - Track 3: a real ring with a lepton track.

It is interesting to observe the shape of the background costisting of the correlation between

- Ring 0 - Track 1: a fake ring with a wrong track correlation which has a leptonic content in MDC;

- Ring 0 - Track 3: a fake ring with a lepton track.

As observed in the azimuthal correlation, these correlations are originated by fake rings accompayining a real ring. These are mainly produced at a distance of approximately 1 ring-diameter from the center of the real ring. These fake rings arise from combining a couple of fired pads from a real ring with some additional noise outside of the real ring.

With the current knowledge, the experimental distribution is treated again with an iterative fitting procedure. Figure C.5 (a) shows the differ-
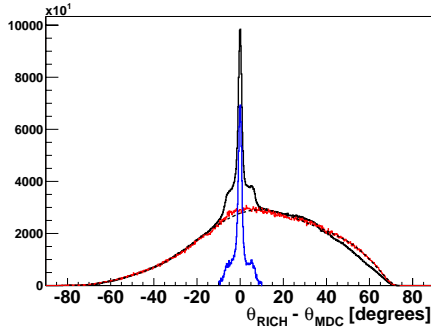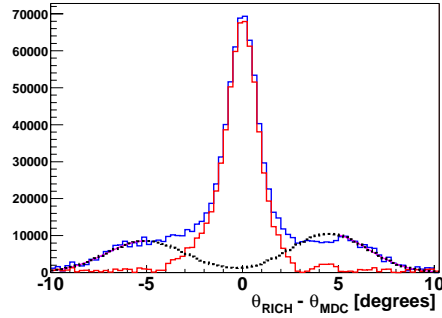
(a) FIT 1   (b) FIT 2

Figure C.5: *Polar angle correlation between recognized rings and MDC inner segments. The combinatorial background estimated from simulations is subtracted (b); the resulting histogram is plotted in (b) where the combinatorial background arising from fake rings accompayining the real one is fitted and subtracted.*

ence of the polar angle measured by RICH and by MDC: the background marked ans subtracted in the figure has been obtained from the shape of the background in the simulated data multiplied by a proper factor. However the distribution can be fitted with a 9th order polinomial, which is also plotted in the figure (dashed curve).

After having subtracted this first background, the resulting distribution is plotted in Figure C.5 (b). A second background consisting of two gaussian curves fitted in the two separate ranges $(-10, -5)$ and $(+5, +10)$ is then subtracted. This results in a gaussian-shaped signal which is plotted and fitted in Figure C.6
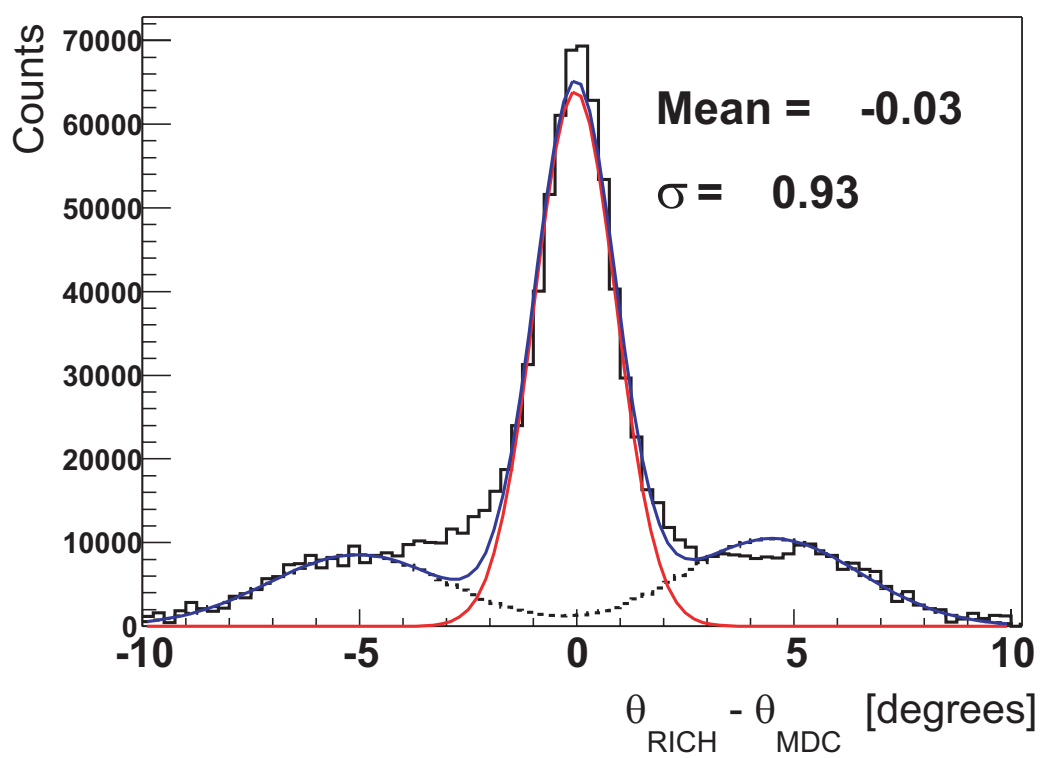
Figure C.6: *Polar angle correlation between recognized rings and MDC inner segments, resulting after the fitting procedure.*

Appendix D

Studies of two-tracks efficiency

*PUTTING TWO AND TWO
TOGETHER*

*To accumulate things
you can´t possibly use
is a burdensome
form of conceit.
Or in other words:
never have two pairs of shoes
if you haven´t got
two pairs of feet.*

(Piet Hein - Grooks IV)

In Section 6.1.2 it has been shown that the like-sign technique used for estimating the comniatorial background for the HADES dilepton spectra

$$N_{+-}^{uncorr} = 2\sqrt{\langle n_{++}\rangle\langle n_{--}\rangle} \qquad (D.1)$$

is a good approximation of the unknown unlike-sign combinatorial background, providing that

$$\kappa_{+-} = \sqrt{\kappa_{++}\kappa_{--}} \qquad (D.2)$$

i.e. the two-track efficiency κ is pair-charge independent. In case of HADES this is not fully true, therefore a factor $K = \dfrac{\kappa_{+-}}{\sqrt{\kappa_{++}\kappa_{--}}}$ has to be introduced to obtain a proper value for the combinatorial background. Since it has been shown (See Section 6.1.2) that the charge asymmetry of the single track reconstruction probability ϵ does not affect the results for the combinatorial background, only the pair acceptance is further considered.

The e^+e^-, e^+e^+, e^-e^- infact do not have the same accepatance through the HADES spectrometer due to the different bending they undergo in the magnetic field. The studies of the geometrical acceptance have been per-

(a)

(b)
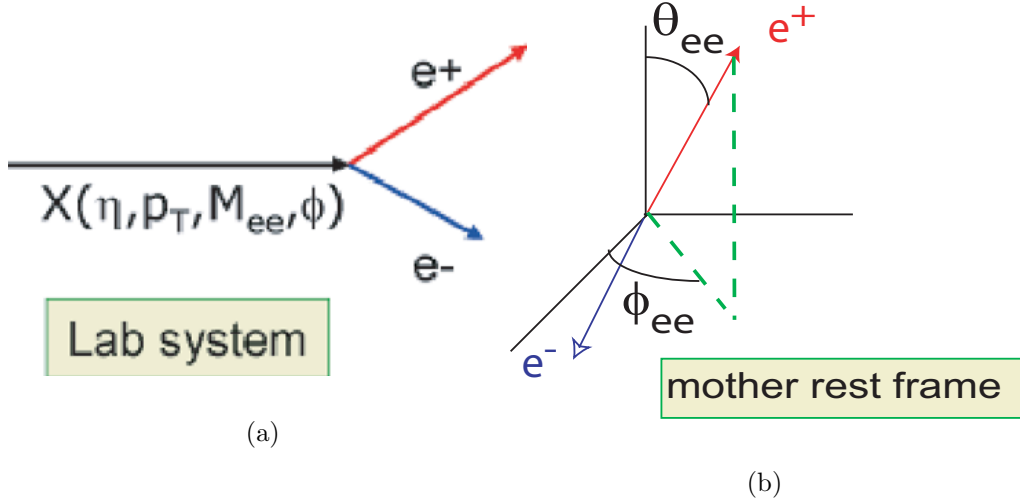
Figure D.1: *Structure of the event generator: a pair source is generated with an homogeneous isotropic distribution in η, p_T, M_{ee} and ϕ (a). The decay of the pair source into e^+e^-, e^+e^+, e^-e^- with an isotropical distribution of decay angles θ_{ee}, ϕ_{ee}, and the proper Lorentz boost, is separately analyzed.*

formed with simulated data. A "white" pairs source generator has been developped, and the isotropic decay into e^+e^-, e^+e^+, e^-e^- has been separately analyzed.

The pair source has an isotropical homogeneous distribution in pseudorapidity η, transverse momentum p_T, invariant mass M_{ee} and azimuthal coordinate ϕ, which will be later on integrated since the detector acceptance is homogeneous in ϕ, as Figure D.1 shows. A given range for η, p_T, M_{ee} and ϕ has been determined, based on the experimental data, shown in Figure D.2. The range has been therefore chosen like the following:

- η: 0-2 in 10 bins

- p_T : 0-1 GeV/c in 10 bins

- M_{ee}: 0-1 GeV/c^2 in 10 bins

- ϕ: 0-1 rad in 10 bins

(a) η (b) p_T (c) M_{ee}
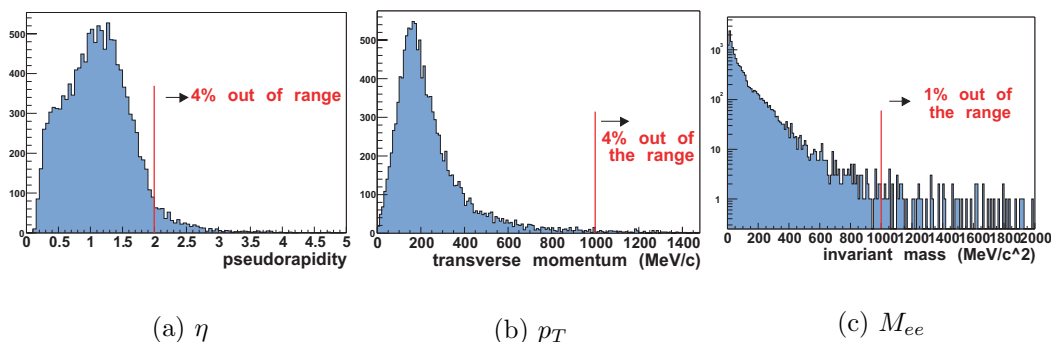
Figure D.2: *Distribution of psudorapidity (a), transverse momentum (b) and invariant mass (c) for unlike-sign pairs reconstructed with experimental data from a C+C reaction at 2AGeV.*

such that not more than 5% of the lepton candidates found in the experimental data lay out of range selected for the acceptance calculation. Figure D.3 shows the pseudorapidity (a), transverse momentum (b) and invariant mass (c) distribution of the pairs produced by the pair source generator. The

(a) η (b) p_T (c) M_{ee}
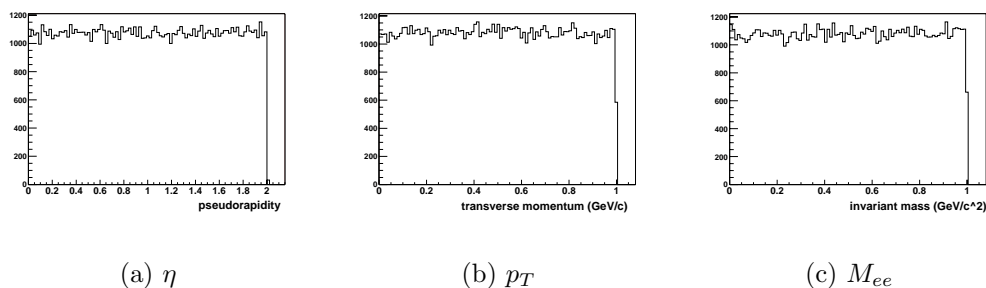
Figure D.3: *Psudorapidity (a), transverse momentum (b) and invariant mass (c) distributions of the simulated e^+e^- pairs produced by the pair source generator and used as input for the calculation of the geometrical acceptance.*

decay of the pair source into e^+e^-, e^+e^+, e^-e^- with an isotropical distribution of decay angles θ_{ee}, ϕ_{ee} in the rest frame of the pair source, and the proper Lorentz boost given by the three momentum of the pair source, is separately analyzed. The interaction of the decay products (i.e. e^+e^-, e^+e^+, e^-e^-) with the detector is studied with Monte Cralo methods (HGeant). The geometrical acceptance is defined as the fraction of produced pairs whose decay products (e^+e^-, e^+e^+, e^-e^-) crosses all the detectors (RICH, MDC, TOF/Pre-Shower). This results in a three dimensional matrix (η, p_T, M_{ee})

since the ϕ dependence is as expected flat. Figure D.4 shows the geometrical acceptance as a function of η, p_T, M_{ee} for e^+e^- (solid green curve), e^+e^+ (dashed red curve), e^-e^- (dotted blue curve), where each plot is integrated over all the other variables. The figure shows a charge asymmetry for the

(a) η

(b) p_T

(c) M_{ee}
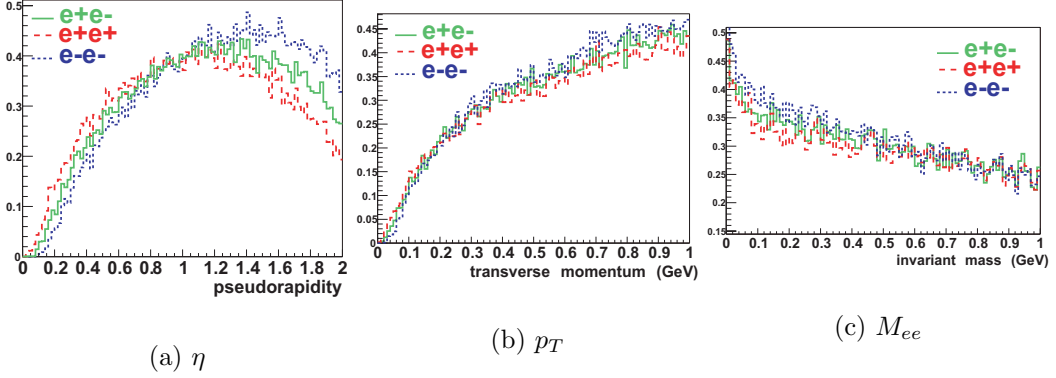
Figure D.4: *Pair acceptance as a function of psudorapidity (a), transverse momentum (b) and invariant mass (c) for e^+e^- (solid green curve), e^+e^+ (dashed red curve), e^-e^- (dotted blue curve). Each plot shows a variable and is integrated over all the other variables.*

pair acceptance, especially as a function of the pseudorapidity, which carry indeed the information about the magnetic field set-up of the spectrometer; the difference however does not overcome a 10% level. The acceptance is an increasing function of the transverse momentum, keeping low values ($< 15\%$) at low p_T and reaching around 40% at higher p_T values.

Figures D.5 D.6, D.7 show the geometrical acceptance as a function of η,

(a) e^+e^-

(b) e^+e^+

(c) e^-e^-
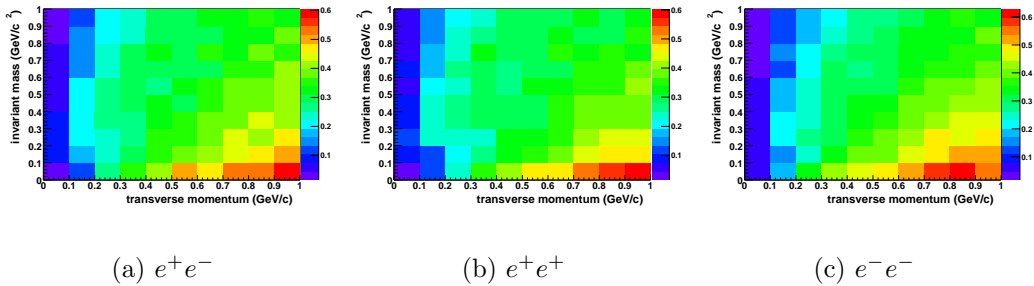
Figure D.5: *Pair acceptance as a function of transverse momentum and invariant mass for e^+e^- (a), e^+e^+ (b), e^-e^- (b).*
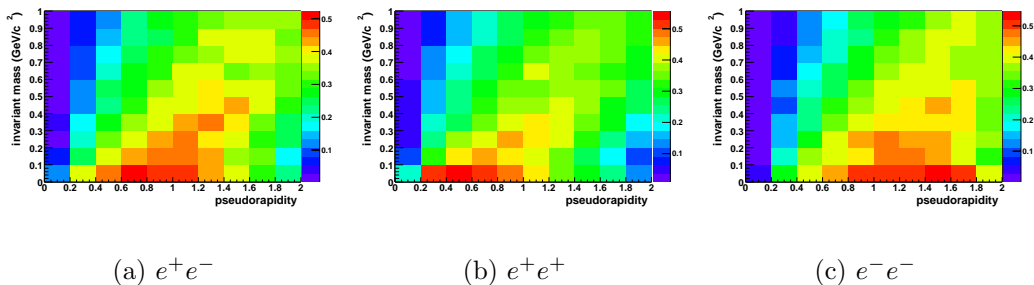
(a) e^+e^- (b) e^+e^+ (c) e^-e^-

Figure D.6: *Pair acceptance as a function of pseudorapidity and invariant mass for e^+e^- (a), e^+e^+ (b), e^-e^- (b).*
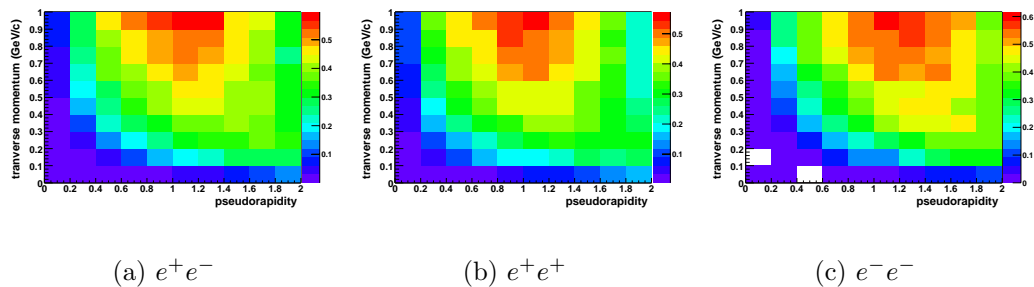
(a) e^+e^- (b) e^+e^+ (c) e^-e^-

Figure D.7: *Pair acceptance as a function of transverse momentum and pseudorapidity for e^+e^- (a), e^+e^+ (b), e^-e^- (b).*

p_T, M_{ee} for e^+e^- (a), e^+e^+ (b), e^-e^- (c). Once again, the main difference in the pair acceptance is shown by the pseudorapidity distribution.

It is possible (though not trivial) to prove that, applying the obtained acceptance matrix to the reconstructed lepton pairs, one can reconstruct the original isotropical distribution of pair source. The original distributions are recalculated, bin by bin, taking into account the 3D empty bins. Figure D.8 shows a comparison between the recalculated original invariant mass distribution and the distribution obtained by applying the acceptance matrix to the reconstructed lepton pairs.

The obtained matrices can be used to fold the e^+e^-, e^+e^+, e^-e^- spectra in the η, p_T, M_{ee} variables. This has not been done yet, since the range of the pair source generator, as well as the analyzed statistics have to be extended in order to get a reasonable description of the differential geometrical
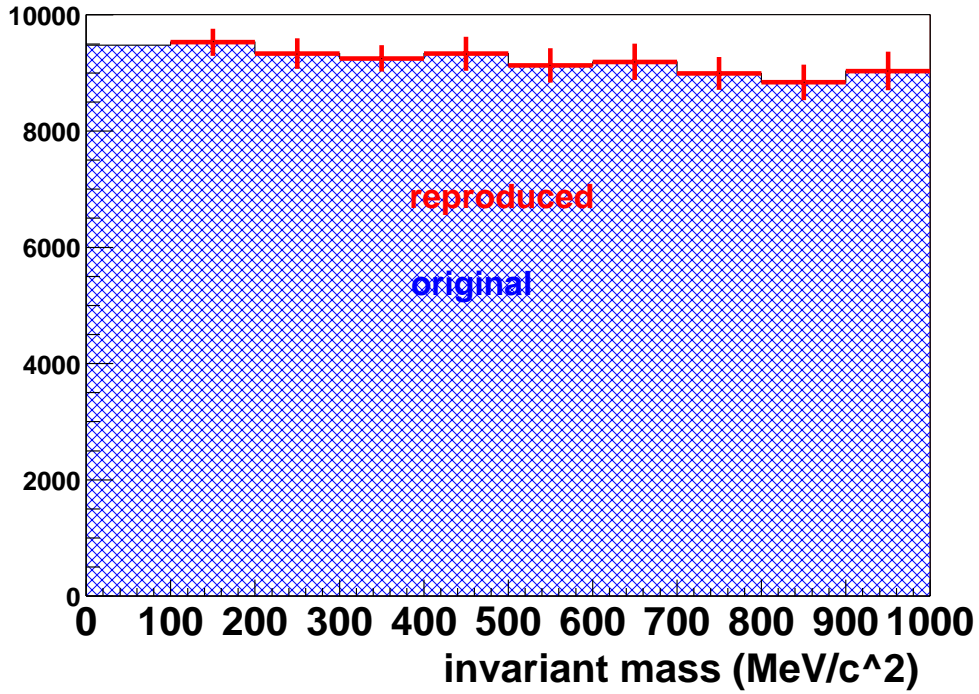
Figure D.8: *Comparison between the recalculated original invariant mass distribution and the distriution obtained by applying the acceptance matrix to the reconstructed lepton pairs.*

acceptance. However an integral correction factor

$$K = \frac{\kappa_{+-}}{\sqrt{\kappa_{++}\kappa_{--}}} = 0.995 \tag{D.3}$$

has been calculated and applied in the computation of the combinatorial background.

Appendix E

Technical Implementation of the Trigger Libraries

MURPHY'S LAWS OF COMPUTER PROGRAMMING
* Any given program, when running, is obsolete.
* Any given program costs more and takes longer.
* If a program is useful, it will have to be changed.
* If a program is useless, it will have to be documented.
* Any program will expand to fill available memory.
* The value of a program is proportional to the weight of its output.
* Program complexity grows until it exceeds the capabilities of the programmer who must maintain it.
* Any non-trivial program contains at least one bug.
* Undetectable errors are infinite in variety, in contrast to detectable errors, which by definition are limited.
* Adding manpower to a late software project makes it later.

The `trigger` and `triggerutil` libraries are fully integrated in the HY-DRA framework, mainly independently linkable and compilable, still present some dependencies which will be explained at the proper stage. The structure of the code does not always follow a logical evolution, but rather the historical development of the code and the necessity to analyze different things or compensate different effects at precise stages of the HADES trigger implementation.

E.1   Trigger Library

The trigger module contains the methods for the decodification of the MU data, to store the unpacked data, the necessary parameters with the proper tools for their implementation, I/O, and storage, the Matching Unit emulation and the definition of all the categories.

E.1.1   The Matching Unit Subevent

The decodification of the MU sub-event which collects the trigger data is performed by the Matching Unit unpacker (`HMatchUUnpacker`) and the classes which define the containers where to store the information from the data stream are `HMatchURich`, `HMatchUTof`, `HMatchUShower`, `HMULeptons`, `HMUDileptons`. The additional class `HMUData` is used for the decodification of the Matching Unit sub-event Header, which is the first task in the Matching Unit unpacking process and contains important information how to run the unpacker.

Class	Data Member	Description
HMatchURich	iRingX	x coordinate of ring center in standard detector coordinate system
	iRingY	y coordinate of ring center in standard detector coordinate system
	fColumn	x coordinate of ring center in hardware notation
	fColumnPattern	pattern which encodes the y information of several hits
	fRow	y coordinate of ring center in hardware notation
	fRowNb	Row + offset
	fSegmentId	sector in standard notation (0-5)
	fFifoNb	Fifo which has computed the ring finder
	fTheta	θ coordinate in lab coordinate system
	fPhi	ϕ coordinate in lab coordinate system
HMatchUShower	fColumn	x coordinate of hit in detector coordinate system
	fRow	y coordinate of hit in detector coordinate system
	fRowPattern	pattern which encodes the y information of several hits

	fRowOffset	row offset
	fSector	sector in standard notation (0-5)
	fTheta	θ coordinate in lab coordinate system
	fPhi	ϕ coordinate in lab coordinate system
	fBuildId	shower ipc module
HMatchUTof	fPhi	azimuthal coordinate in lab coordinate system (deg)
	fErrPhi	error on azimuthal coordinate
	fTheta	θ coordinate in lab coordinate system (deg)
	fErrTheta	error on θ coordinate
	iPhi	ϕ coordinate in lab coordinate system (0-255)
	iTheta	θ coordinate in lab coordinate system (0-255)
	sec	sector in standard notation (0-5)
	time	time of flight (ns)
	PID	identifier of the particle (=1 for leptons, =2 for other particles)
HMULeptons	iRichNr	index of Rich hit used for lepton
	iMetaNr	index of Meta hit used for lepton
	iDetBit	flag for Meta detector (=0 for Tof, =1 for Shower)
	iSector	sector in standard notation (0-5)
	fThetaRich	θ coordinate of Rich hit in lab coordinate
	fPhiRich	ϕ coordinate of Rich hit in lab coordinate
	fThetaMeta	θ coordinate of Meta hit in lab coordinate
	fPhiMeta	ϕ coordinate of Meta hit in lab coordinate
	iFlag	lepton flag (=0 for positrons, =1 for electrons)
	fMom	momentum (0-255)
HMUDiLeptons	iN1	index of 1st Lepton used for dilepton
	iN2	index of 2nd Lepton used for dilepton
	fMass	invariant mass

Since the Unpacker does not only decode the information contained in the

data stream, but add some useful information in the output categories (like for instance the angular coordinates of hits in the lab frame), parameters are needed, for the Rich and Shower mapping, which are taken from the respective detector module: `HTriggerParRichMap` and `HTriggerParShowerMap`.

E.1.2   The Matching Unit Emulation

In the trigger module there are also classes for the Matching Unit Emulation adn the classes to define the containers where to store the output. The Matching Unit Emulation can be processed either with experimental data, taking input from the IPUs (`HMatchURich`, `HMatchUTof`, `HMatchUShower`) and storing them in `HMUEMULeptons` and `HMUEMUDiLeptons`, or with simulated data, taking input from the IPUs Emulations and writing ouptut in `HMUEMULeptonsSim` and `HMUEMUDiLeptonsSim`, or with experimental data where no information about the IPUs is available, once again taking input from the IPUs Emulation and writing output in `HMUEMULeptonsExp` and `HMUEMUDiLeptonsExp`.

E.1.3   The Trigger Parameters

The `HTriggerDetector` class is responsible to build the categories and to activate the input/output of the parameters. Parameters can be stored, therefore read from or written into

- ascii files

- root files

- ORACLE database

Parameters useful for the LVL2 analysis are described in Table E.2. The Tof time of flight cut is put in the MULep parameters, since it is used only in the `muEmulationExp` or `muEmulationSim` task: in all the other cases the Tof IPU provides this information already in the data stream.
The binning of the momentum table is determined by the resolution of the detctor and makes use of the symmetry between different sectors (all the sectors feel the same field) and the symmetry inside each sector (each half sector is equal).
The context `TriggerProduction` is conventionally chosen for *the same* parameters used by the hardware for that run.
`HTriggerContFact` is the factory for the parameter containers in libTrigger, and has methods to set and create and add the parameter containers with

Class	Data Member	Description
HTriggerParMuLep	MUTheta	θ window of the matching (0-255)
	MUphioffset	offset of ϕ window (0-255)
	MUphislope	inverse slope of ϕ window
	MUfield	current of the magnetic field (ampere)
	MUtof	time of flight cut
HTriggerParMUDilep	MUcutoff	cutoff on number of dileptons
HTriggerParMomMap	Thetabins	θ binning
	Deltathetabins	$\Delta\theta$ binning
	Phibins	ϕ binning
	mumom[64][64][8]	array of momentum

Table E.2: *Container classes for the Trigger parameters.*

the different contexts to the list of containers: creating a parameter container means calling the constructor of the corresponding parameter container: for an actual context, which is not an empty string and not the default con text of this container, the name is concatinated with the context. The containers are initialized in the init of the run-time-data-base (`rtdb`), which is normally called in the Hades eventloop: it iterates over the container list and initialize all the containers. The containers are destroyed, together with the parameters which, as soon as they are created, do not belong to a task, but instead to the rtdb itself, in the Hades delete, which occurs at the end of the eventloop.

The management of the input/output of the parameters is done by the `HTriggerParAsciiFileIo`, with the proper read and write functions, and `HTriggerParRootFileIo` which initialize and fills the root containers with the proper version and context.

The `HTriggerTaskSet` defines and manages tasks. All the categories are defined in the `triggerinfodef` class. All the classes are properly linked in the `TriggerLinkDef` class.

E.2   Triggerutil Library

The triggerutil module contains all the IPUs emulation, i.e. the RichIPU emulation and the ShowerIPU emulation, and the related classes for the

implementation both in simulation and experimental data; no new categories need to be defined (they are in `triggerinfodef.h`), and therefore also the detector structure and the container factory are taken from the trigger library.

E.2.1   The Rich IPU Emulation

The Rich IPU emulation is implemented in the `HRichAnalysisIPU` class, which internally calls the `HRichRingFindIPU` (`pHardRingFind`→`Execute()`). In the `HRichAnalysisIPU` another function is also called, namely the `Data-WordCut()`, which recalculates the number of dataword which the hardware Rich IPU board would have sent to the Matching Unit. This information is very important when the Emulation has to be compared to the hardware results.

In the `Execute` of the `HRichRingFindIPU`, a preliminary labelling is performed, a process of decomposition of an image into smaller parts. In this case the areas containing groups of fired pads is specified in order to perform the ring recognition algorithm only on potential ring centers which are all the pads lying on a ring around any fired pad, weighted by the number of times they have been found. Such a procedure significantly reduces computation time because only a fraction of the whole pad plane is scanned for rings.

For this purpose the interesting region where to determine a ring has to be evaluated in the function `makeLabelPattern()`, which consists in the derivation of the label mask from the pattern search mask: the labelling mask corresponds to the ring region of the pattern search mask, where each pad is counted only once.

After that, the ring recognition is performed, splitted in the two sub-processes of `RingSearch()` and `MaxSearch()`. A pattern (`patterCoord`) with a ring region and a veto region is applied to each pad found in the labeling process (potential ring center). The ring and veto regions of the pattern consist of groups. In each group it is enough if 1 pad is fired ("logical OR") to consider the whole group fired. The groups in each region are summed up. A threshold (`fRichIPUParThr`→`getThresholds(region, sector)`) is set independently for each of the two regions.

The ring search algo is likely to identify one or more neighbouring pads as the center of a potential ring candidate. Therefore, a local maximum search over 4/ 8 directly neighbouring pads is performed to determine the center. The quality parameter for the local maximum search is only the value of the ring region (the veto region is not considered) for all the pads, even the ones which do not fulfill the threshold condition. This means that, using for instance the threhsolds (8,3) the case like in Table. E.3 would be discarded. A variation where the local maximum is performed, taking as quality parameter the ring

(9,2)	(10,3)

Table E.3: *example for the local maximum condition*

value of only those pads which do fulfill the thresholds condition has been extensively tested, giving interesting results.

The container filled with the output results is `HRichHitIPU`, which is very similar to the `HMatchURich`, except that the specific hardware information (`FifoNb`, `RowNb`, `ColPattern`,...) are missing and there are in addition some quality parameter of the algorithm:

- `iRingQuality`: is the value of the ring region

- `iVetoQuality`: is the value of the veto region

- `nPads`: is the number of pads in the ring circumference (i.e. the ring region evaluated by the Rich IPU)

The Rich IPU Emulation in Simuated Data

In simulations the analysis is performed exactly in the same way as with experimental data, but in addition the "true" information from Geant needs to be propagated to the Hit level. This hidden information consists mainly of the content of the so-called HGeantKine data structure that is filled during a run of the simulation package HGEANT.

This data structure holds the complete information about a particle that is tracked through the detector that is setup within HGEANT. In this context a track is unequivocal identified via its track number, a unique number for each particle used to identify its properties in the different data substructures. In each successive step of analysis this number has to be propagate, to be able at the end to discriminate the origin of a hit object: in case of a Rich ring to decide if it was produced from noise or from a real signal of which particles, and how many and which pads correspond to which photons, and so on... .

The HLinearCategory `HRichTrack` (basically a TClonesArray) holds objects containing the tracknumber of hits in the RICH from HGEANT. This array is sortable by e.g. the pad address. After sorting, there is a first (min index) track number and a last (max index) track number for each pad. This means that the id numbers of the particles associated to one hit (fired pad) on the RICH pad plane are stored in a row. Therefore, in order to access it later on, the first and last index in the array have to be stored between which to find the relevant numbers for a pad. Consequently, these two array indices

are stored as data members in `HRichCalSim` (`nTrack1` and `nTrack2`). One `HRichCalSim` object represents one fired pad in the RICH.

In `HRichHitIPUSim` (this object represents one recognized ring candidate) there are the following additional data members:

- `iRingPadNTrack1[256]`: contains all lower array indices from `HRich-Track` for the fired pads in the ring

- `iRingPadNTrack2[256]`: contains all upper array indices from `HRich-Track` for the fired pads in the ring

- `iRingTrack[256]`: is filled with all HGEANT track numbers between the lower and upper index

- `iRingFlag[256]`: is a flag used to distinguish between a photon and an ionizing particle track1/2/3: three HGEANT track numbers are selected from the above list (`iRingTrack`) according to their number of appearances in the list. The rest is discarded. The weight (frequency of appearance) in the list is stored in the three

- `weight1/2/3` numbers

The track numbers for the photons are those for the creator (parent particle). For charged particles (IP=ionizing particles) the track number is their own number. Therefore the variable `iRingFlag` was introduced to distinguish.

Parameters for the Rich IPU Emulation

The parameters needed for the Rich IPU emulation are descried in Table E.4

The `NPadDimensions` has a misleading name: as Table E.4 shows, it does not indicate the number of regions in the ring search mask (ring region and veto region), but instead the x and y coordinates of the pads. To distinguish between the ring and veto region, the following convention has been adopted: the fist pad in the group does not provide any indication for the pads, but instead its first coordinate indicates how many pads the group is made of (typically 3 or 4), and the second coordinate indicates if the group belongs to the ring region (0) or to the veto region (1).

The convention is to use the `RICHIPUEmulation` context strictly only for *the same* parameters which were used in the hardware for that run, and any other context (`RICHIPUconservativethr` for instance) for all the other purposes. The Rich IPU is often performed, for investigation purposes, with rather conservative thresholds, which generate a huge number of rings, mostly

Class	Data Member	Description
HRichIPUParPattern	NPadDimensions	dimensions of the pad (2 in this case: x and y)
	NGroups	number of groups in region
	NPadsinGroup	number of pads in group
	pattern[29][5][2]	pattern of the searching mask
HRichIPUParThresholds	thresholds[2][6]	thresholds for the ring and veto region for all the 6 sectors
HRichIPUParLocMax	locmax	indicates the region where local maximum has to be performed: 4 or 8 neighbouring pads
	locmaxflag	indicates whether the local maximum search has to be performed or not

Table E.4: *Container classes for the Rich IPU parameters.*

fakes. There are cases, for instance when Particle Identification is performed afterwards based also on rings from the `HRichHitIPU` container, or when the LVL2 has to be emulated, when more restrictive thresholds have to be applied. This can be done without re-running the full analysis starting from the Raw container, which most likely is not available any longer in the context of the same file, thanks to the `HRichIPURemake class`. This class takes the new parameters and filter out, for instance by the class `HLocMaxFilter`, the rings which do not fulfill the new more restrictive conditions.

E.2.2   The Shower IPU Emulation

The `HShowerCalibraterIPU` class calculates new value of measured charge from the Raw level as the Shower IPU does, by using calibrations parameters from the parameter container `HShowerCalPar`

$$\text{Charge} = \text{Charge}_{\text{RAW}} \times \text{Slope} + \text{Threshold} \qquad (\text{E.1})$$

The calculated charge is saved in the Cal level (HShowerCalIPU). The `HShower-HitFinderIPU` is the reconstructor for performing the analysis in the same way as the Shower IPU does it. The necessary parameters are:

- `m_iThr1, m_iThr2`

  : used in the same way like in the hardware

- `m_iAlgFlag`

  : defines the mask for the conditions:

    - `0x01`: look for charges above thr1
    - `0x02`: check if the pad is a local maximum from 5 pads
    - `0x04`: check if (sum1 > sum0+thr2 || sum2 > sum0+thr2) (sumX from 9 pads)
    - `0x08`: check if (sum1 > thr2 || sum2 > thr2)

In hardware the condition 0x08 works only if 0x04 is set. In this algorithm they work independently. If `iAlgFlag` is 0 then every hit which fulfills ANY condition is stored. Otherwise the hits for which ALL conditions defined in the `iAlgFlag` are fulfilled are written out.

The `HShowerCheckIPU` compares the results of the software Shower IPU emulation with the data from the MU data stream. The class makes some debug histograms and save them in the finalize() method. The location of the output is set by the setOutputFile() method. If pName is empty then the histograms are written to gFile If it is '!' then the histograms are not written anywhere, otherwise they are stored with the RECREATED file named pName.

E.3   Rich IPU Implementation in the PID Code

The Rich IPU Emulation has been fully implemented in the PID code for several reasons. The first one is that a detailed analysis of teh Rich IPU performance, with an absolute reference or withe respect to the offline analysis is not only a topic of the present work, but has to be constantly monitored an measured for the proper operation of the system and the corerct normalization of the physics results.

Another reason is that the the Rich IPU ring finder is another, independent algorithm which is performed "for free"[1]. It shows equivalent performance with respect to the offline algorithm and can therefore provide important information for the Particle Identification. Leptons can for instance be chosen if they are recognized as rings by one or the other algorithm, or by any of them or by both of them, optimizing respectively the efficiency and the purity

---

[1]i.e. it is performed online by the hardware, therefore it does not consume CPU time.

of the signal.

For this purpose in `HPidTrackFiller` the match with Rich IPU has been added: it is flagged with `bNoRichIPU`, a flag which turns off the Rich IPU matching with KickTracks. The match is performed with a χ^2

$$\chi^2 = \left(\frac{\theta_{RICH} - \theta_{TRACK}}{\sigma_{theta}} \right)^2 + \left(\frac{(\phi_{RICH} - \phi_{TRACK}) \cdot \sin \theta_{TRACK}}{\sigma_{\phi \cdot \sin \theta_{TRACK}}} \right) \quad \text{(E.2)}$$

and it is required that $\chi^2/ndf < 3$, where $ndf = 2$ is the number of degrees of freedom, σ_{theta} and $\sigma_{\phi \cdot \sin \theta_{TRACK}}$: the gaussian shape of the χ^2 distribution assures that 99.9% of the signal is inside this cut.

The match is performed such that *one and only one* Rich IPU ring is allowed to match a KickTrack, and when more than one ring is inside the matching window, the best candidate (i.e. the one with the best χ^2 is taken) and the mutiplicity of matchable rings is stored.

The results of the matching between KickTrack and Rich and/or RichIPU are stored in `HPidTrackCand`, where the index of Rich IPU categories (`nRingIPUId`) has been added, with default value of -1 in case there is no match, together with the information of how many times the IPU ring was used (`nRingIPUCount`), and how many IPU rings match a track (`nRingIPUMult`). The rest of the PID code runs as well with this implementation, the HPidReconstructor calls the PID algorithms, where in case of the Rich IPU only a dummy algorithm has been implemented, which returns a positive value in case a ring was found. No investigation on the possibility to discriminate Rich IPU rings based on their qualities have been performed, since the qualities calculated in the Rich IPU algorithm are very discrete and rough.

Appendix F

Everything You Always Wanted to Know About LVL2 But Were Afraid to Ask

> *I'm astounded by people*
> *who want to 'know' the universe*
> *when it's hard enough*
> *to find your way around Chinatown.*
>
> *(Woody Allen)*

ESTIMATIONS

Reduction

1 RICH IPU:	up to 10
1 LEPTON :	up to 20

Efficiency Simulation

Single Lepton:	up to 85%
Pair from ω meson:	up to 45%

Efficiency Relative to Offline

RICH IPU:	up to 80%
LVL2:	up to 92%

ACHIEVED IN NOV02

Reduction

1 LEPTON:	12

Efficiency Relative to Offline

Single Lepton RICH IPU:	57%
Single Lepton LVL2:	62%
Dielpton (opening angle $> 4°$) LVL2:	84%
Dielpton (opening angle $> 8°$) LVL2:	92%

Enhancement LVL1-LVL2

Lepton:	7.5
Dilepton (opening angle $> 4°$):	10
Dilepton (opening angle $> 8°$):	11

List of Tables

List of Figures

Bibliography

[1] U.Mosel, *Fields, Symmetryes, and Quarks*, McGraw Hill (1989).

[2] P.N.Bogolyobov, Ann. Inst. Henri Poincare, 8, 163 (1967).

[3] A.Chodos et al., Phys. Rev. D 9, 3471 (1974).

[4] T.DeGrand et al., Phys. Rev. D 12, 2060 (1975).

[5] K.Gottfried and V.F.Weisskopf, *Concepts of Particle Physics*, Clarendon Press (1984).

[6] T.D.Lee, *Particle Physics and Introduction to Field Theory*, Harold Academy Press (1981).

[7] G.E.Brown and M.Rho, Phys. Lett. 82 B, 177 (1979).

[8] R.Friedberg and T.D.Lee, Phys. Rev. D 15, 1694 (1977) and D 16, 1096 (1977).

[9] R.Hagedorn, Nuovo Cimento Suppl. 3, 147 (1965).

[10] C.Y.Wong, *Introduction to High Energy Heavy-Ion Collisions*.

[11] T.T.Takahashi et al., Phys. Rev. D65 114509 (2002); S. Necco and R. Sommer, Nucl. Phys. B622, 328 (2002), JLQCD Collaboration, hep-lat/0212039.

[12] Y.Sumino, *QCD potential as a "Coulomb-plus-linear" potential*, arXiv:hep-ph/0303120 v3 (2002).

[13] W.Weise, *Chiral Dynamics and Hadrons in Dense Matter*, in International School of Heavy Ion Reactions, 3rd Course, Erice, Italy, October 1993. World Scientific, Singapore (1994).

[14] K.Hagiwara et al., *Review of Particle Physics*, Phys. Rev. D 66 (2002).

[15] C.M.Ko and G.Q.Li, J. Phys. G, Nucl. Part. Phys. 22 1673-1725 (1996).

[16] V.Koch, *Introduction to chiral symmetry*, LBNL Report 38000 (1995).

[17] V.Koch, *Aspects of chiral symmetry*, International Journal of Modern Physics E, vol 6, n.2, 203-249 (1997).

[18] A.Drees et al., *Open charm contribution to dilepton spectra produced in nuclear collisions at SPS energies*, Z. Phys. C (1997).

[19] J.Wambach and R.Rapp, *Theoretical interpretation of low-mass dileptons*, Nucl. Phys. A 638 171c (1998).

[20] T.Schäfer, E.V.Shuryak, *Instanton in QCD*, hep-ph/9610451 (1996).

[21] M.Rho, Phys. Rep. 240:1-242 (1994).

[22] S.Klimt et al., *Chiral phase transitionin the SU(3) Nambu and Jona-Lasinio model*, Phys. Lett. B 249 (1990) 386.

[23] G.E.Brwon etal., Phys.Rev. Lett 66, 2720 (1991).

[24] P.Braun-Munzinger, J.Stachel, Nucl. Phys. A 638, 3c (1998).

[25] P.Braun-Munzinger et al., Phys. Lett B 465, 15 (1999).

[26] J. Cleymans and K. Redlich, Phys. Rev. Lett. 81, 5284 (1998).

[27] R. Stock, Phys. Lett. B 456, 277 (1999).

[28] P. Braun-Munzinger, Nucl. Phys. A 681, 119c (2001).

[29] Z. Fodor and S.D. Katz, hep-lat/0106002 (2002).

[30] J.D.Bjorken, *Highly relativistic nucleus-nucleus collisions: The central rapidity region*, Phys. Rev. D 27 (1983) 140.

[31] M.Kagarlis, *Pluto++: A Monte Carlo simulation tool for hadronic physics*, GSI Report (2000). http://www-hades.gsi.de/computing/pluto/html/PlutoIndex.html

[32] G.Gosset et al., *Central collisions of relativistic heavy ions*, Phys. Rev. C 16, 629-657 (1977).

[33] J.P.Bondorf and H.Niefenecker, *Nuclear electromagnetic bremsstrahlung: a new tool for studying heavy-ion reactions*, Nucl. Phys A 442, 478-503 (1985).

[34] http://www.gsi.de

[35] M.Soyeur, *Vector Mesons in the Nuclear Medium* in International School of Heavy Ion Reactions, 3rd Course, Erice, Italy, October 1993. World Scientific, Singapore (1994).

[36] L.G.Landsberg, Phys. Rep. 128, 301 (1985).

[37] F.Klingl, N.Kaiser, W.Weise, *Effective Lagrangian approach to vector mesons, their structure and decay*, Z. Phys. A 356, 193-206 (1996).

[38] M.N.Rosenbluth, Phys. Rev. 79, 615 (1950).

[39] J.J.Sakurai, *Currents and Mesons*, The University of Chicago Press (1969).

[40] R.P.Feynman, *Photon Hadron Interactions*, Benjymin, Reading (1972).

[41] R.I.Dzhelyadin et al., Phys. Lett. B 102, 296 (1981).

[42] V.P.Druzhinin et al., Preprint, INP84-93 Novosibirsk

[43] C.M.Ko, V.Koch, Q.Li, *Properties of hadrons in the nuclear medium*, Annu. Rev. Nucl. Part. Sci. 47, 505-539 (1997).

[44] Z.Aouissat, G.Chanfray, P.Schuck, J.Wambach, *Dropping σ meson mass and in medium S-wave $\pi\pi$ correlations*, nucl-th/9908076 (1996).

[45] M.Asakawa, C.M.Ko, *Medium effects on the rho meson*, Phys.Rev.C, vol 48, n° 2 (1993).

[46] R.Rapp, G.Chanfray, J.Wambach, *Low mass e^+e^- pairs propagation from in medium ρ meson propagation*, Proc. of the Int. Workshop XXV, Hirschegg '97, on 'QCD Phase Transitions', nucl-th/9701064 (1997).

[47] M.Post, S.Leupol and U.Mosel, *The ρ spectral function in a relativistic resonance model*, Nucl. Phys. A 689 (2001)753.

[48] K.Ozawa et al., *Observation of ρ/ω meson modification in nuclear matter*, Phys. Rev. Lett. 86, 5019-5022 (2001).

[49] M.Post, and U.Mosel, *Coupling of baryon resonances to the $N\omega$ channel*, Nucl. Phys. A 688 (2001) 808.

[50] F.Klingl, N.Kaiser, W.Weise, Nucl. Phys. A 624 (1997) 527.

[51] D.E.Groom et al., Particle Data Group, *Review of Particle Physics*, Eur. Phys. J. C 15, 1-878 (2000).

[52] W.S.Chung, C.M.Ko, Q.Li, *Phi production in hot dense matter*, XXXVI International Winter Meeting on nuclear physics, Bormio, 1998

[53] The HADES Collaboration, *Dilepton production in CC and $\pi^{\pm}$ Reactions*, GSI Darmstadt (2001).

[54] J.Ritman, *Measurement of the ω meson transition form factor by measuring the reaction $\pi^{+}p \rightarrow \pi^{+}p\omega$ with the HADES spectrometer*, internal report (2000).

[55] C.Ernst, S.A.Bass, S.Soff, H.Stöcker and W.Greiner, *Transport calculation of dilepton production at ultrarelativistic energies*, arXiv:nucl-th/9907118 (1999).

[56] http : //macdls.lbl.gov/DLS$_W$WW$_F$iles/DLS.html, Yegneswaran et al., *The dilepton spectrometer*, Nucl.Inst.&Meth. A290 (1990) 61-75

[57] DLS Collaboration, *Dilepton Production from p-p to Ca-Ca at the BEVALAC*, Nucl. Phys A 583 (1995) 617-622c.

[58] R.J. Porter et al., Phys. Rev. Lett. 79, p. 1229 (1997).

[59] W. Peters, M. Post, H. Lenske, S. Leupold and U. Mosel. Nucl. Phys. A 632, p. 109 (1998).

[60] W.K.Wilson et al., Phys. Rev. C 57, 1865 (1998).

[61] E.L.Bratkovskaya, W.Cassing, W.Rapp, J.Wambach, *Dilepton production and m_T scaling at BEVALAC/SIS energies*, Nucl. Phys. A 634 (1998) 168.

[62] E.L.Bratkovskaya et al., Phys. Lett. B 445, 265 (1999).

[63] E.L.Bratkovskaya et al., Nucl. Phys. A 686, 568-588 (2001).

[64] http : //www.physics.uni − heidelberg.de/physi/ceres/, P.Holl et al., *Study of electron pair production and photon production in Pb-Au collisions at the CERN SPS*, CERN-SPSLC 96-1, SPSLC/P280 (1996), P.Holl et al., *Technical Note on the NA45/CERES UpGrade*, CERN/SPSLC 96-50, SPSLC/R110 (1996).

[65] B.Lenkeit et al., *Recent results from Pb-Au collisions at 158 GeV/c per nucleon obtained with the CERES spectrometer*, Nucl. Phys. A661, 23c (1999).

[66] G.Agakichiev et al., *Enhanced production of low-mass electron pairs in 200 GeV/u S-Au collisions at the CERN SPS*, Phys. Rev. Lett. 75, 1272-1275 (1995).

[67] G.Agakichiev et al., Eur. Phys. J C4, 231 (1998).

[68] M.A.G. Hering, *Dielectron Production in Heavy Ion Collisions at 158 CeV/c per Nucleon*, PhD Thesis, Tecnical University Darmstadt (2001).

[69] H.Sako, *Development of New GENESIS*, Technical Report 03-24, CERES Collaboration (2000).

[70] Carlos Perez de los Heros, *Low-mass dielecton production in S-Au collisions at 200 GeV/n.*, PhD Thesis, Weizmann Insitute of Science, Rehovot Israel (1996).

[71] S.Damianovic, *Electron Pair Production in Pb-Au Collisions at 40 AGeV*, PhD Thesis University Heidelberg (2002).

[72] R.Rapp and J.Wambach, Adv. Nucl. Phys. 25 (2000.)

[73] Dinesh, Kumar, Srivastava and Bikash Chandra Sinha, *A second look at single photon production in S+Au collisions at 200 AGeV and implications for quark hadron phase transition*, Eur Phys. J. C12:109-112 (2000).

[74] C.M.Hung and E.V.Shuryak, *Dilepton/photon production in heavy ion collisions and the QCD phase transition*, Phys. Rev, C56:453-467 (1997).

[75] R.Baier, M.Dirks and K.Redlich, *Thermal dileptons from $\pi - \rho$ interactions in a hot pion gas*, Phys. Rev, D55:4344-4354 (1997).

[76] J.Murray, W.Bauer and K.Haglin, *Revisiting lepton pairs at the SPS*, (1998).

[77] E.L.Bratkovskaya and W.Cassing, *Dilepton production from AGS to SPS energies within a relativistic transport approach*, Nucl. Phys. A 619:413-446, (1997).

[78] M.Bleicher, A.K.Dutt-Mazumder, C.Gale, C.M.Ko and V.Koch, *Baryonic contributions to the dilepton spectra in relativistic heavy ion collisions*, (2000).

[79] G.Q.Li, C.M.Ko, G.E.Brown and H.Sorge, *Dilepton production in proton nucleus and nucleus nucleus collisions at SPS energies*, Nucl. Phys A611:539-567 (1996).

[80] G.E.Brown and M.Rho, *On the manifestation of chiral symmetry in nuclei and dense nuclear matter* (2001).

[81] R.A.Schneider and W.Weise, *Thermal dileptons from quark and hadron phases of an expanding fireball*, Eur. Phys. J A9:357-364 (2000).

[82] R.Rapp, G.Chanfray and J.Wambach, *Rho meson propagation and dilepton enhancement in hot hadronic matter*, Nucl. Phys. A617:472-495 (1997).

[83] R.Rapp and J.Wambach, *Low mass dileptons at the CERN-SPS: Evidence for chiral restoration?*, Eur. Phys. J A6:415-420 (1999).

[84] C.H.Lee, H.Yamagishi and I.Zahend, *Dilepton and photon emission rates from a hadronic gas*, III Phys. Rev. C58:2899-2906 (1998).

[85] K.Gallmeister, B.Kampfer and O.P.Pavlenko, *Is there a unique thermal source of dileptons in Pb+Au reactions (158 AGeV)?*, Phys. Lett. B473:20-24 (2000).

[86] G.E.Brown, G.Q.Li, R.Rapp, M.Rho and J.Wambach, *Medium dependence of the vector-meson mass: Dynamical and/or Brown-Rho scaling?*, Acta Phys. Polon., B29:2309-2321 (1998).

[87] W.Cassing, E.L.Bratokovskaya, Phys.Rep. 308, 65 (1999).

[88] M.Masera for the HELIOS-3 Collaboration, Nucl. Phys. A 590, 93c (1995);
A.L.S. Angelis et al., Eur. Phys. J.C.

[89] M.C.Abreu et al., (NA38 Collaboration), Phys. Lett. B 368, 230 (1996);
M.C.Abreu et al., (NA50 Collaboration), Nucl. Phys. A 610, 331 (1996).

[90] The HADES Collaboration, *A proposal for a High Accepance Di Electron Spectrometer*, GSI Darmstadt (1994).

[91] P.Salabura et al., *HADES: a high acceptance dielelctron spectrometer*, Nucl. Phys. B 44, 701 (1995).

[92] C.Garabatos et al., *The HADES dilepton spectrometer*, Nucl. Phys. B 618, 607 (1998).

[93] M.Boöhmer, *Das Auslesesystem für den Ringabbildenden Cherenkovdetektor im HADES Spektrometer*, Diploma Thesis, Physik Department der Technischen Universität München, Institut(1999).

[94] P.A.Cherenkov, *The visible glow of pure liquids under the action of gamma-rays*, Phys. Rev. Lett 52, 378 (1937).

[95] J.Litt et al., *Cherenkov counter technique in hgigh energy physics*, 1973.

[96] T.Ypsilantis et al., *Theory of ring imaging Cherenkov counters*, Nucl. Inst. and Meth. A 343, 30 (1994).

[97] J.Seguinot et al., *A historical survey of ring imaging Cherenkov counters*, Nucl. Inst. and Meth. A 343, 1 (1994).

[98] K.Zeitelhack et al., *The HADES RICH Detector*, Nucl. Inst. and Meth. A 433, 201 (1999).

[99] R.Gernhäuser et al., *Photon detector performance and radiator scintillator in the HADES RICH* Nucl. Inst. and Meth. A 371, 300 (1996).

[100] J.Friese et al., Nucl. Inst. and Meth. A 502, 241-245 (2003).

[101] R.Gernhäuser et al., Nucl. Inst. and Meth. A 438, 104 (1999).

[102] L.Fabbietti, *Study of the e^+e^- pair acceptance in the dilepton spectrometer HADES*, PhD Thesis, Physik Department der Technischen Universität München, Institut E-12 (2003).

[103] T.Bretz, *Magnetfeldeigenschaften der Spektrometer HADES*, PhD Thesis, Physik Department der Technischen Universität München, Institut(1999).

[104] J.Markert, PhD Thesis in preparation, IKF Frankfurt (2004).

[105] C.Garabatos et al., *Optimisation of low-mass drift chambers for HADES*, NIM A 412, 38 (1998).

[106] H.Bokemeyer et al., *Development of low-mass drift chambers for the HADES spectrometer*, NIM A 477, 397 (2002).

[107] H.A.Bethe, Ann. d. Phys. 5 (1930).

[108] W.Leo, *Techniques for Nuclear and Particle Physics Experiments*, Springer-Verlag (1987).

[109] A.Balanda et al., *Development of a fast pad readout system for the HADES shower detector*, Nucl. Inst. and Meth. A 417, 360 (1998).

[110] G.D.Alekseev et al., *Investigation of Self-Quenching Streamers*, Nucl. Inst. and Meth. 177, 365 (1980).

[111] M.Atac, A.V.Tollestrup, *Self-Quenching Streamers*, Nucl. Inst. and Meth. 200, 345 (1982).

[112] E.Berdermann et al., Nucl. Phys. (Proc. Suppl.) B 78, 533-539 (1999).

[113] C.Lichtblau, *Entwicklung schneller Elektronik für dal HADES-Flugzeitsystem*, Diploma Thesis, II Physikalisches Institut, Justus Liebig Universität Giessen (1999).

[114] C.Agodi et al., *The HADES time-of-flight wall*, Nucl. Inst. and Meth. A 492, 14-25 (2002).

[115] R.Bassini et al., *A 32 channel ADV(TDC) on VME Board.*, IEEE Nuclear Science Symposium, Albuquerque (NM), USA (1997).

[116] P.Fonte, *Viability analysis of a RPC TOF wall for the HADES small angles region*, HADES Collaboration Meeting XI Bratislava (2002).

[117] J.Garzon, *RPCs wall status*, HADES Collaboration Meeting XIII Catania (2003).

[118] K.Garrow, *HADES simulation of TOF and SHOWER*, (1993).

[119] J.Lehnert et al., *The trigger system for the HADES detector*, Proceeding of the X IEEE Real Time Conference, Beaune 51 (1997).

[120] M.Traxler et al., *The Second Level Trigger System for the HADES Detector*, IEEE Transactions on Nuclear Science 47/2, 376 (2000).

[121] J.Lehnert et al., *Ring Recognition in the HADES Second Level Trigger*, Nucl. Inst. and Meth. A 433, 268 (1999).

[122] J.Lehnert, *Echtzeit-Mustererkennung zum Elektronennachweis mit einem RICH-Detektor in relativistischen Shwerionenkollisionen*, PhD Thesis, II Physikalisches Institut, Justus Liebig Universität Giessen (2000).

[123] J.Lehnert et al., *Performance of the HADES Ring Recognition Hardware* Nucl. Inst. and Meth. A 502, 261 (2003).

[124] E. Lins, *Entwicklung eines Auslese- und Triggersystems zur Leptonenidentifizierung mit dem HADES-Flugzeitdetektor*, PhD Thesis, II Physikalisches Institut, Justus Liebig Universität Giessen (2001).

[125] M. Petri, *Entwicklung eines kombinierten Auslese- und Echtzeit-Triggersystems zum Nachweis von Elektronen/Positronen-Signaturen in einem elektromagnetischen Schauerdetektor*, PhD Thesis, II Physikalisches Institut, Justus Liebig Universität Giessen (2000).

[126] M.Traxler, *Real-Time Dilepton Selection for the HADES Spectrometer*, PhD Thesis, II Physikalisches Institut, Justus Liebig Universität Giessen (2001).

[127] M.Sanchez, *Momentum Reconstruction and Pion Production Analysis in the HADES Spectrometer at GSI*, PhD Thesis, Facultad de Fisica, Universitade de Santiago de Compostela (2003).

[128] R.Brun, F.Rademakers, *ROOT - An Object Oriented Data Analysis Framework*, Proceedings AIHENP 96 Workshop, Lausanne, (1996). Nucl. Inst. and Meth. A 389, 81-86 (1997). http://root.cern.ch/

[129] *ORACLE Database*, http://www.oracle.com

[130] *GEANT, Detector Description and Simulation Tool*, http://wwwinfo.cern.ch/asd/geant/index.html

[131] W.Przygoda, *Identyfikacia czastek e^+e^- za pomoca detektora RICH w spektrometrze HADES*, PhD Thesis, Jagellonian University Cracow (2002).

[132] *Mdc Calibration*, http://www-hades.gsi.de/docs/mdc/mdcana/mdc-calib.htm

[133] D.Zovinec, PhD Thesis in prparation, Slovac Academy of Science, Bratislava (2004).

[134] *Shower Analysis*, http://hades.if.uj.edu.pl/hydra/shower/

[135] A.Rustamov, *An Algorithm for Momentum Reconstruction for the HADES Spectrometer*, internal document (2003).

[136] P.Tlusty, *Particle identification in the HADES spectrometer and particle production in C+C at 2 A GeV*, Proceeding of QM04 (2004).

[137] A.Balanda et al., *Performance of the Pre-Shower Detector for HADES*, to be published in Nucl. Inst. and Meth. (2004).

[138] A.Toia et al., *The HADES second level trigger algorithm: principles and first results from experiments with ^{12}C beam*, Procedings of the XL International Winter Meeting on Nuclear Physics; Ricerca Scientifica ed Educazione Permanente Supplemento N. 119, p. 112 (2002).

[139] A. Toia et al., *A Highly Selective Dilepton-Trigger System Based on Ring Recognition*, Nucl. Inst. and Meth. A 502, 270 (2003).

[140] A. Toia, J. Lehnert et al., *The HADES second level trigger: from the concept to the first resutls with C+C reactions Procedings of the XLI International Winter Meeting on Nuclear Physics*, Ricerca Scientifica ed Educazione Permanente Supplemento N. 120, p. 351 (2003).

[141] M. Petri et al., *The Readout and Online Analysis System of the HADES Pre-Shower Detector*, to be published in Nucl. Inst. and Meth. (2004).

[142] V.Metag, *Near-threshold particle production in heavy ion collisions* Nucl. Phys. A553 283c (1993).

[143] F.Balestra et al., *Production of ϕ and ω Mesons in Near-Threshold pp Reactions*, Phys. Rev. Lett. 81(21), 4572-4574 (1998).

[144] W.Koenig, private communication.

[145] J.Aichelin, and H.Stöcker, Phys. Rev. Lett. B176, 14 (1986).

[146] J.Aichelin, A.Rosenhauer, G.Peilert, H.Stöcker, and W.Greiner, Phys. Rev. Lett. 58, 1926 (1987).

[147] J.Aichelin, Phys. Rep. 202, 233 (1991).

[148] J.Cugnon, Phys. Rev. C22, 1885 (1980).

[149] J.Konopka, Thesis, Goethe Universität, Frankfurt am Main, Germany (1996).

[150] S.A.Bass et al., *Microscopic Models for Ultrarelativistic Heavy Ion Collisions*, nulc-th/9803035.

[151] C.Ernst et al., Phys. Rev. C58 447 (1998).

[152] R.Averbeck et al., Z. Phys. A359 65 (1997).

PER FINIRE

Raccomando ai miei posteri
(se ne saranno) in sede letteraria,
il che resta improbabile, di fare
un bel falo´ di tutto che riguardi
la mia vita, i miei fatti, i miei
nonfatti.
Non sono un Leopardi, lascio
poco da ardere
ed e´ gia´ troppo vivere
in percentuale.
Vissi al cinque per cento, non
aumentate la dose.
Troppo spesso invece piove sul
bagnato.

(Eugenio Montale)

FOR THE END

I reccomended that my successors
(if there are any) in the field
of literature,
and that is improbable, make
a lovely bonfire of everything
concerning my life,
of what I did and did not do.
I am not a Leopardi, leave little
for the fire.
It is really too much to live
in percentages.
I lived at five percent, do not
increase the dose.
Too many times when it rains, it
pours.